Réponse des fortes précipitations et des sécheresses météorologiques à un accroissement du CO2 atmosphérique et au réchauffement global associé

Amal John

THÈSE

En vue de l'obtention du
DOCTORAT DE L'UNIVERSITÉ DE TOULOUSE

Délivré par l'Université Toulouse 3 - Paul Sabatier

Présentée et soutenue par

AMAL JOHN

Le 6 octobre 2022

Réponse des fortes précipitations et des sécheresses météorologiques à un accroissement du CO2 atmosphérique et au réchauffement global associé

Ecole doctorale : **SDU2E - Sciences de l'Univers, de l'Environnement et de l'Espace**

Spécialité : **Océan, Atmosphère, Climat**

Unité de recherche :
CNRM - Centre National de Recherches Météorologiques

Thèse dirigée par
Hervé DOUVILLE et PASCAL YIOU

Jury

Mme Sophie BASTIN, Rapporteure
M. Yves TRAMBLAY, Rapporteur
Mme Juliette BLANCHET, Examinatrice
M. Hervé DOUVILLE, Directeur de thèse
M. Pascal YIOU, Co-directeur de thèse
M. Jean-Pierre CHABOUREAU, Président

And I shall have some peace there, for peace comes dropping slow,
Dropping from the veils of the morning to where the cricket sings;
There midnight's all a glimmer, and noon a purple glow,
And evening full of the linnet's wings.

I will arise and go now, for always night and day
I hear lake water lapping with low sounds by the shore;
While I stand on the roadway, or on the pavements grey,
I hear it in the deep heart's core.

— W. B. Yeats (1888)

Acknowledgements

There is a quote that is close to my heart, "if you can read this, then thank your teacher". I would like to express my deepest gratitude to my teachers for leading and helping me to choose the roads less travelled. I owe my parents for culturing a seed of curiosity in me. I owe my friends for believing in my capacity. I thank the love of my life, Jaleena, for being by my side in troubled times.

Heroes do not always wear a cape: sometimes, they wear a reading glass and ask you silly but savvy questions. This thesis grew from dozens of conversations with my supervisors, Hervé Douville and Pascal Yiou. They helped me to identify the key scientific questions, think critically and find rational answers. I owe my academic recognition to the leadership of these two people and, I thank them — the everyday heroes of my thesis.

All successful efforts have a group of unsung stars behind them. My PhD was only possible because of the CAFE consortium and the large group of people behind it. I thank the MSCA ITN Horizon 2020 for coordinating and funding the CAFE project activities. I thank the CAFE family, especially, Arantxa Sanz and Alvaro Corral, for their dedication and extraordinary optimism! I also thank Pedro Lormendez and Jorg Maschulatt for the wonderful collaboration and the scientific discussions during my secondments. I thank Pedro, also for being a super travel companion and for all the trash talks and beers we had, which was fun!

Never will I forget, Aurelien Ribes and his kindness and leadership to take over as my supervisor when Hervé was out of his office. Discussions with him lead to my first published paper. I was lucky enough to work with him and get a different perspective on how to approach a problem. I thank my team CLIMSTAT for the general scientific discussions and attempts to include me in their conversations during the occasional coffee breaks. I also thank the administration, finance department and the director of the CNRM/Météo-France.

Keep in my mind that, who I am. Every day I hold my hand out, flex my fingers and ponder how grateful I am to be a part of this awesome world I live on. This makes me humble and inspires me to live my life as a love letter to my planet.

Sincere thanks to everyone — who taught me to be kind, guided me to make choices, enlightened me to believe in myself and still be able to treasure my character, flawed as it may be — you are my gurus. *Pranaam.*

Summary

Climate change is a challenging and yet a humbling insight provided by science. While the global warming train has left the station with a more than 1K rise in the global mean temperature, we need to ask ourselves the question of what kind of future is up ahead, and what climate "surprises" we have in store? This thesis is a contribution to better quantifying and understanding the global response of extreme daily precipitation intensities to anthropogenic climate change.

The words droughts and floods resonate across our disastrous history and our uncertain collective future. Anticipating, mitigating and adapting to such disasters remains a challenge to our shared humanity. In this thesis, I assess future changes in meteorological dry and mostly wet extremes on regional and global scales. The investigation is primarily based on global projections and more idealised climate change experiments conducted in phase 6 of the Coupled Model Intercomparison Project (CMIP6). The future changes described in the thesis are mostly based on the highest emission scenarios (SSP5-8.5), which maximises the signal-to-noise ratio, but presumably, provides an unfavourably bleak picture of our future climate (although large model uncertainties can lead to a strong overlap between projections derived from moderate to high-emissions scenarios). In the lead of the 6th Assessment Report of IPCC, future changes in extremes are also investigated at different global warming levels. The extremes considered include the annual maximum daily precipitation intensities (RX1DAY) and meteorological droughts described as consecutive dry days and their annual maximum numbers (CDD).

Using some idealised atmosphere-only experiments with the CNRM-CM6-1 and a few other climate models which participated in a CMIP subproject, I first distinguish the various timescales of the annual mean and daily precipitation responses to an abrupt quadrupling of the atmospheric CO_2 concentration, especially the fast response to CO_2 increase from the slower response to the gradual and uniform versus non-uniform components of the global ocean warming. The response of the dry meteorological extremes is particularly complex and involves multiple timescales and processes which can be highly model-dependent.

Even though most CMIP6 models qualitatively agree on the idealized response of RX1DAY to a CO_2 increase, I quantify the related uncertainties in a high-emission scenario using a large subset of CMIP6 models and a large ensemble of a single model. The study pays particular attention to both model uncertainties,

and the irreducible uncertainties related to internal climate variability. The results illustrate an upper bound of the inter-model spread and estimate a large spread. However, there is a robust enhancement of extreme precipitation with more than 90% of models simulating an increase in the precipitation extremes. I also provide a 5-95% confidence range for projected RX1DAY values at the end of the 21st century and highlight the regions (only 17% of the globe surface) where the changes may not be consistent with the widely used assumption of a Clausius-Clapeyron (CC) rate of ≈7%/K when scaled by concomitant changes in global mean surface temperature.

Finally, I investigate the changes in the seasonality of precipitation extremes, focusing on Europe and the potential contribution of regional changes in atmospheric circulation. My analysis documents a sharper seasonal cycle of extreme precipitation and a shift in its seasonality. To better understand the mechanisms that cause the change in seasonality, I analyse the possible role of different synoptic circulation types (CTs) in regulating the frequency of extremes across different seasons. By using a simple decomposition technique, I further explore the role of the projected changes in the CT frequencies to the previously assessed changes in the RX1DAY seasonality and the associated inter-model spread.

Résumé

Le changement climatique est un défi, mais aussi une leçon d'humilité que nous offre la science. Alors que le train du réchauffement climatique a quitté la gare avec une augmentation de plus de 1K de la température moyenne globale, nous devons nous poser la question de savoir quel genre de futur nous attend, et quelles sont les "surprises" climatiques qui nous sont réservées? Cette thèse est une contribution à une meilleure quantification et compréhension de la réponse globale des intensités extrêmes de précipitations quotidiennes au changement climatique d'origine anthropique.

Les mots sécheresses et inondations résonnent à travers notre histoire désastreuse et notre avenir collectif incertain. Anticiper, atténuer et s'adapter à de tels désastres reste un défi pour notre humanité commune. Dans cette thèse, j'évalue les changements futurs des extrêmes météorologiques secs et, surtout, humides à l'échelle régionale et globale. L'analyse est principalement basée sur des projections globales et des expériences de changement climatique plus idéalisées menées dans la phase 6 du Coupled Model Inter Comparison Project (CMIP6). Les changements futurs décrits dans la thèse sont principalement basés sur les scénarios d'émissions les plus élevés (SSP5-8.5), ce qui maximise le rapport signal/bruit, mais fournit une image particulièrement sombre de notre climat futur (bien que les incertitudes de modélisation puissent conduire à un fort chevauchement entre les projections dérivées des scénarios d'émissions modéré à élevé). En suivant l'exemple du 6ème rapport d'évaluation du GIEC, les changements futurs des extrêmes sont également étudiés à différents niveaux de réchauffement global. Les extrêmes considérés comprennent les intensités maximales annuelles de précipitations quotidiennes (RX1DAY) et les sécheresses météorologiques décrites comme des jours secs consécutifs (CDD) et leur nombre maximal annuel.

À l'aide de quelques expériences idéalisées en mode purement atmosphérique, menées avec le modèle CNRM-CM6-1 et quelques autres modèles climatiques qui ont participé à un sous-projet du CMIP, je distingue d'abord les différentes échelles de temps des réponses de la moyenne annuelle et des précipitations quotidiennes à un quadruplement abrupt de la concentration atmosphérique de CO_2, en particulier la réponse rapide à l'augmentation de CO_2 par rapport à la réponse plus lente aux composantes graduelles et uniformes versus non uniformes du réchauffement océanique global. La réponse des extrêmes météorologiques secs est particulièrement complexe et implique de multiples échelles de temps et processus qui peuvent dépendre fortement du modèle.

Même si les modèles CMIP6 sont qualitativement d'accord sur la réponse idéalisée de RX1DAY à une augmentation de CO_2, je quantifie les incertitudes associées dans un scénario de fortes émissions en utilisant un grand sous-ensemble de modèles CMIP6 et un grand ensemble de réalisation d'un seul modèle. L'étude accorde ainsi une attention particulière à la fois aux incertitudes de modélisation et aux incertitudes irréductibles liées à la variabilité climatique interne. Les résultats fournissent une limite supérieure de l'écart inter-modèle, incluant une contribution de la variabilité interne du climat. Cependant, on constate une forte augmentation des précipitations extrêmes, dans plus de 90% des modèles analysés. Je fournis également un intervalle de confiance de 5 à 95% pour les valeurs projetées de RX1DAY à la fin du 21e siècle et je mets en évidence les régions (seulement 17% de la surface du globe) où les changements peuvent ne pas être cohérents avec l'hypothèse largement utilisée d'un taux Clausius-Clapeyron (CC) de ≈7%/K lorsqu'il est mis à l'échelle par les changements concomitants de la température moyenne à la surface du globe.

Enfin, j'étudie les changements de la saisonnalité des précipitations extrêmes, en me concentrant sur l'Europe et sur la contribution potentielle des changements régionaux de la circulation atmosphérique. Mon analyse révèle un cycle saisonnier plus marqué des précipitations extrêmes et un décalage de leur saisonnalité. Pour mieux comprendre les mécanismes à l'origine de ce changement, j'analyse le rôle possible des différents types de circulation synoptique (CT) dans la modulation de la fréquence des extrêmes à travers les différentes saisons. En utilisant une technique de décomposition simple, j'explore le rôle des changements projetés dans les fréquences des CTs dans les changements de saisonnalité de RX1DAY et la dispersion inter-modèle associée.

Table of contents

Introduction

The atmosphere is everywhere. One could argue that it would be more conspicuous. Like the fish, unaware of the water they dwell in, we humans breathe and walk through the atmosphere that is invisible to us. It is the sine qua non for our existence, yet it's a mystery to us. Without the extremes of wind and rain, heat and cold, we would be negligible of the atmosphere's existence. If we are to understand why floods and droughts occur, we must begin with the atmosphere and climate is the fundamental link between the two. Daily we are touched by the vicissitudes of the weather from extreme heat or cold, heavy rain or drought. Storms rage, rivers breach their banks, the skies remain clear for months as animals perish, and reservoirs run empty. Over years and seasons, one learns what to expect from the weather. The cumulative effects of storms, wind, and heat merge into a sense of climate over time. Climate, rather than a smooth continuum of meteorologic possibilities, turns out to be the sum of several processes functioning on different time scales, both regionally and globally.

As individuals and as a society, we are shaped by extreme weather events. Droughts are caused by prolonged dryness spanning months or years, whereas a single summer thunderstorm can cause catastrophic floods. Flooding can also be caused by the rapid melting of heavy winter snow accumulations or soil saturation caused by high seasonal rainfall. Extreme weather events are firmly ingrained in the collective human experience. In 1931 the Huang Ho River in China claimed 3.7 million lives. During the second half of the 20th century, at least 150,000 lives were lost due to the drought in Africa's Sahel Desert. In the present times, we see unprecedented rains and severe flooding throughout Asia and Europe and drought in parts of Africa and South America. In 2021, there were 432 catastrophic incidents, which is much more than the average of 357 yearly catastrophic events from 2001 to 2020. With 223 occurrences, floods dominated these events, up from an average of 163 yearly flood occurrences between 2001 and 2020.

Hydrologists and climatologists have long recognized the relevance of regional climate in flood prediction and drought understanding. With our expanding awareness of a changing climate, it's time to reconsider the thesis concepts of flood and drought as global processes rather than isolated catastrophes. Floods and droughts, traditionally thought to be acts of God, are now more understood as connected events driven by the same forces that shape the oceans and the entire atmosphere. At the same time, the impact of human intervention on the planet's baseline climate condition has become more certain. Anthropogenic climate change is one of humanity's most serious threats, and it has been the subject

of regular assessment reports since the establishment of the Intergovernmental Panel on Climate Change (IPCC) in 1988. The latest and sixth Assessment Report (AR6) from the IPCC underlines that many significant climate-related changes have unfolded worldwide since the publication of the previous Fifth Assessment Report (AR5) in 2014.

Extreme weather events have always occurred and are a natural aspect of climatic variability. However, because the background climate is changing, it is reasonable to wonder about what to anticipate in the future and hence raises the basic question of my PhD;

"How does the extremes (wet/dry) respond to the changing climate states of our planet?"

To begin, Chapter 1 will provide a more extensive foundation to the thesis by summarizing our present knowledge of observed and projected changes in precipitation extremes and the essential mechanisms that underpin them. The observed datasets, available global climate models, and statistical tools and routines used to infer extreme precipitation events' return levels and periods will be described, compared, and evaluated in Chapter 2.

As global temperatures rise, there is ample and robust evidence that the global water cycle will intensify, with precipitation becoming more variable across most land regions within seasons and year to year. Although the response of precipitation extremes at the regional scale is perhaps more robust and better understood than projected changes in annual or seasonal mean precipitation, there is always an impending call to better understand the water cycle changes with a better assessment of model uncertainty; which motivates the main objectives of this thesis.

Chapter 3 distinguishes and compares the inter-model response of precipitation extremes (wet/dry) to the rise in CO_2 emissions and increased global surface temperatures as the fast and slow responses using different idealised climate change experiments. The total uncertainties in projecting the extreme precipitation by the state-of-the-art global climate models are quantified along with the discussion about the contribution of internal variability to this uncertainty in chapter 4. Chapter 5 assess and discusses the potential changes in the seasonality of extreme precipitation events and the possible contribution of large-scale atmospheric circulation anomalies therein. The final section of this thesis wraps up the substance of my PhD and concludes, emphasizes all scientific points and objectives from each chapter and eventually discussing the different avenues it opened for future research.

If you wish to make an apple pie from scratch,
you must first invent the universe.

— Carl Sagan

1

Precipitation extremes in a changing climate

Human influence on the average climate state of our planet, especially global mean surface temperature, is a well-established fact. Anthropogenic emissions of greenhouse gases (GHG) have already warmed the Earth's surface by about 1.1°CC since preindustrial times, altered the global energy and water cycles, and led to more frequent and severe wet and dry events which have undesirable effects on the human life as well as to the ecosystems. This chapter provides a detailed review of extreme precipitation, including its classic definitions, the key physical mechanisms, the projected changes along with the impacts they might have on both societies and the natural world.

1.1 The definition of extremes

According to the AR6, an extreme weather event is defined as "an event that is rare at a specific location and time of year," while an extreme climate event is defined as "a pattern of extreme weather that persists for a period of time, such as a season" (cf. Glossary, IPCC 2022). Rare can be defined in a variety of ways, depending on the context. Some studies classify an event as an extreme if it is unprecedented, whereas others classify events that happen numerous times a year as moderate extreme events (Seneviratne et al., 2021). Under human-induced climate change, the rarity of a fixed-magnitude event changes, making events that are unprecedented so far rather probable under present conditions, but unique in the observational record — and thus often considered as "surprises". Precipitation extremes can be computed in a variety of ways. These are usually calculated using relative (e.g., 90th percentile) or absolute (e.g., 1mm/day for a dry day) thresholds over which conditions are considered extreme.

Changes in extremes can be studied from two angles: changes in frequency for a certain magnitude of extremes, or changes in magnitude for a specific return period (frequency). Extreme probability changes are proportional to the rarity of the extreme event under consideration, with a bigger change in likelihood associated with a rarer event (e.g., Kharin et al. 2018). Changes in the magnitude reflected by the return levels of extreme events, on the other hand, may not be as sensitive to the event's rarity. While the answers to the two different questions are related, their relevance to different audiences may differ. Conclusions on the role of GHG forcing in changes in magnitude vs frequency of extremes may also vary (Otto et al., 2012). Correspondingly, the sensitivity of changes in extremes to rising global warming is determined by the definition of the extremes in question. Changes in the magnitude of precipitation extremes have been found to scale with changes in global mean surface temperature, although changes in frequency are non-linear and can be exponential at increasing global warming levels (Fischer and Knutti, 2015; Kharin et al., 2018). When similar damage occurs once a predefined threshold is exceeded, it's more vital to inquire about frequency changes. However, if exceeding this predetermined threshold becomes a common occurrence in the future, the change in probability may become saturated.

Hydrological extremes and related phenomena occur on a variety of spatial and temporal scales. Convective storms can have spatial scales as small as a few kilometres and temporal scales as short as a few hours. A drought, on the other hand, can last for years and affect vast areas. The complexity of the processes involved varies depending on the type of extreme event, affecting our ability to detect, attribute, and project changes in weather and climate extremes. The extremes of precipitation studied in the literature are frequently based on extremes derived from daily values. Longer time scale studies, or studies of sub-daily extremes, are scarcer, which limits the assessment for such events. However, some research suggests that the effects of GHG emissions on heavy precipitation events may be highly localized, making detection and attribution highly dependent on spatial scale (Angélil et al., 2018).

The joint CCl/WCRP-Clivar/JCOMM Expert Team on Climate Change Detection and Indices (ETCCDI, https://www.clivar.org/organization/etccdi/etccdi.php) has created a core set of descriptive indices of extremes to acquire a uniform viewpoint on observed changes in weather and climate extremes. There are a total of 27 indices that have been designated as core indexes. They are calculated using daily temperature or precipitation data. Some are based on fixed thresholds that are relevant to specific applications (e.g., 0°CC, 1mm/day, 10mm/day). In these circumstances, all stations have the same criteria. Other indices are based on location-specific thresholds. Thresholds are often defined as a percentile of the relevant data series in these circumstances. We can use this set of indices to describe certain aspects of extremes, such as frequency, amplitude, and persistence. We have summarized the most important precipitation indices in Table 2.2 in section 2.2. The annual maximum daily precipitation intensity (RX1DAY) will be the primary emphasis of this thesis, but additional indices will be employed as well, particularly in Chapters 3 and 4.

These station-based indices are frequently interpolated into regular grids

for comparison with model outputs, such as model evaluation and detection-attribution. In order to create such gridded datasets, two alternative methodologies were applied, each involving two separate orders of operation. In some cases, like the HadEX3 dataset (Dunn et al., 2020), extreme indices are estimated first using time series directly obtained from stations, then gridded over the space. The gridded data products are point estimates of the indices averaged over the spatial scale of the grid box because the indices are computed at the station level. In other instances, daily values of station observations are gridded first (e.g., REGEN dataset; Contractor et al. 2020), and then the interpolated values are then used to compute indices. Extremes generated from data gridded this way represent extremes of spatial scales ranging from the size of the grid box to a point, depending on the station density. The gridded values are closer to the extremes of the area means in places with high station density (e.g., North America and Europe), and are thus more appropriate for comparisons with extremes calculated from climate model output, which is often considered to represent areal means. The gridded values are closer to point estimates of extremes in regions with low station density (e.g., Africa).

Some studies have used extreme indices generated from various reanalysis data sets, although reanalysis extreme statistics have not been rigorously compared to observations. For extreme precipitation changes, there was generally minimal agreement across several reanalysis datasets, however temporal and spatial correlations against observations were nonetheless significant. There is often less agreement for extreme precipitation between different reanalysis products in regions with sparse observations (e.g., Africa and parts of South America), indicating a consequence of the lack of an observational constraint in these regions (Donat et al., 2014, 2016a). Recent reanalyses, such as ERA5 (Hersbach et al., 2020), appear to be a step up from past products. Caution is however needed when reanalysis data products are used to provide additional information about past changes in these extremes in regions where observations are generally lacking.

For the sake of comparison across numerous observed datasets, reanalyses, and global climate models, we compute ETCCDI indices from gridded daily precipitation products interpolated (cf section 2.4) onto a common (usually 1° by 1°) horizontal grid. As a result, we necessarily underestimate the maximum precipitation intensities that can be observed at the local scale, but we ensure a consistent approach across models with different horizontal resolutions and, to a lesser extent, between models and observations, due to the limited number of in situ measurements in some regions.

1.2 Observed changes and their attribution

According to the fifth IPCC Assessment Report (AR5, Stocker et al. 2014, further supported by the sixth Assessment Report (AR6, Masson-Delmotte et al. 2021b), there is evidence from observations that precipitation and related extremes have changed since the mid-twentieth century, that some of these changes are the result of a human influence, that some of these changes are anticipated to persist into the future, and that other changes are projected to emerge from natural climate

variability under enhanced global warming. The same sources of weather and climate observations are used in studies of past and future changes in weather and climate extremes and in the mean state of the climate, including in-situ observations (e.g., Dunn et al. 2020), remotely sensed data (e.g., Kanemaru et al. 2017), and derived data products such as reanalyses (e.g., Hersbach et al. 2020). Station-based indices have the same limitations as mean climate indices in terms of data quality, availability, and homogeneity. Despite the employment of a cutting-edge weather forecasting technology, atmospheric reanalyses include significant inhomogeneities due to the constant evolution of the global observation system and the potential for a shift in the water cycle due to the assimilation of fresh satellite data. Although the density of surface in-situ measurements has evolved across the twentieth century and does not severely limit the global water cycle (i.e., no assimilation of humidity), twentieth-century reanalyses products only assimilate surface observations and are less hindered by such inhomogeneities.

In this context, despite significant progress in precipitation extremes analysis over recent years, major disparities remain, particularly in terms of data quality and availability, our ability to regularly monitor these events, and our ability to apply the sophisticated statistical methods necessary to detect and attribute changes in precipitation extremes. When establishing the magnitude of the human contribution to observable changes, observational uncertainty and a poor signal-to-noise ratio can still pose major challenges (Hegerl et al., 2015). Observed changes in several studies are much larger than those simulated by climate models (Dai, 2006; Raäisaänen, 2007; Tapiador et al., 2017). However, these results were not typically resistant to data uncertainty, which could be due in part to the low density of in-situ observations in some areas. The uncertainty arises because the satellite record is short in comparison to decadal climate variability and is affected by calibration uncertainty, as well as because the available in situ record has many gaps, especially in the tropics and subtropics, and is sparse on sub-daily time scales. As a result, while observations can constrain future temperature changes, future precipitation projections cannot yet be constrained.

Long-term monitoring and calibration of satellite datasets rely on in-situ stations. In situ precipitation records over land date back centuries locally and to the early to mid-twentieth century on a global scale. The most recent versions of available datasets differ in their input data, completeness of records, period of record, and gridding procedures, which may result in differences in global and regional estimates due to spatial clustering and the small spatial scales of precipitation. Only since the 1950s has there been a degree of consistency in decadal variations between the various products, with primarily positive precipitation anomalies occurring during the 1950s, 1970s, and after the mid-1990s (AR6 WG1 Chapter 2, Gulev et al. 2021). However, in recent decades, there has been an alarming decline in available in situ data, which must be addressed to fully exploit the longest timeseries and the improving signal-to-noise ratio (Hegerl et al., 2015) since the end of the global dimming decades (decades between 1950-1980 marked by a widespread decrease in the surface solar radiation Wild 2009). Internal climate variability, especially on interannual to multidecadal time scales, has a significant impact on precipitation and delays the detection and emergence of changes driven by human activities.

The number of stations employed, their homogeneity, the method of analysis, quality control measures, and the treatment of changing data coverage over time all affect the gridded products of in-situ precipitation change (Roca et al., 2019). Observations in key regions are still sparse, notably in the tropics, where the monitoring system is insufficient to capture projected water cycle changes (Figure 1.1). Data scarcity for the Asian monsoon is mainly due to practical and administrative challenges with data sharing. It is critical to developing an international capability to monitor all aspects of observed changes. Satellite remote sensing data have also been utilized to provide information on precipitation extremes because various products provide precipitation data at sub-daily resolution (e.g., TRMM; Maggioni et al. 2016). Satellites, on the other hand, do not directly observe the fundamental atmospheric state variables, and polar-orbiting satellites do not observe any one location at all times. As a result, their utility as a replacement for frequent (daily) ground-based observations is restricted. Furthermore, the timeseries are often not long enough to analyze observed trends and detect potential changes caused by human intervention. Nonetheless, in recent years, several initiatives have been made to track precipitation changes more frequently and globally (Dunn et al. 2020; https://www.climdex.org/).

Using an interpolated network of in-situ data, a new global land-based daily precipitation dataset (REGEN, Contractor et al. 2020) covering the period 1950-2016 has been developed. Multiple in-situ data archives have been merged, including two of the largest, the Global Historical Climatology Network - Daily (GHCN-Daily) and the Global Precipitation Climatology Centre (GPCC). When compared to existing datasets, this has resulted in a tremendous increase in station density. The quality-controlled data were interpolated to produce area-averaged estimates of daily precipitation for global land areas with a horizontal resolution of 1° by 1°. A related dataset based on a network of long-term stations that interpolates stations with a record length of at least 40 years was also produced for those interested in a dataset with lower station network variability, more suitable for detection and attribution studies.

In comparison to other similar regional and global gridded datasets, REGEN is now the longest running dataset of daily precipitation based on gauge-only records with global land coverage, making it suitable for any global analysis of changes and variability in several aspects of daily precipitation distributions, including extremes and measures of hydrological intensity (Contractor et al., 2020). Monthly datasets or gridded ETCCDI indices were the only datasets that allowed global climatological scale assessments of precipitation till now. Monthly datasets, on the other hand, have a tendency to average out the extremes, rendering them less effective when it comes to high-impact phenomena like heavy rainfall on shorter durations. This is why the REGEN dataset has frequently been acknowledged as the most appropriate observational reference in the current study's continuation (e.g., Alexander et al. 2019; Wehner et al. 2020; Thackeray et al. 2022).

Since the mid-twentieth century, statistical analysis of accessible observational records has revealed substantial changes over land (Figure 1.2). For example, both in humid and dry regions of the world, the average annual maximum precip-

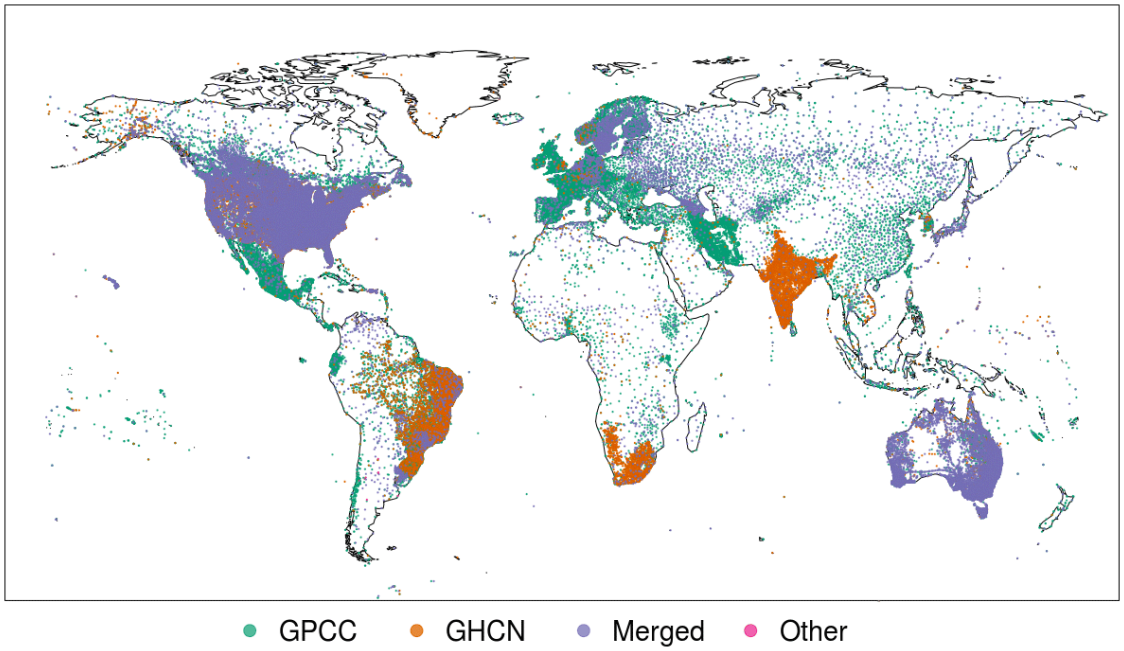

Figure 1.1: Distribution of stations colour coded by source. "GPCC" refers to stations hosted by Deutsche Wetterdienst, "GHCN" refers to stations hosted by the National Centers for Environmental Information (NCEI), and "Merged" refers to stations that have been identified as identical in two or more archives resulting in a merger of the timeseries and finally "Other" refers to the Russian and Argentinian stations that were added in REGEN. Source: Contractor et al. (2020)

itation amount in a day (RX1DAY) has increased dramatically (Dunn et al., 2020). Over the globe continent as a whole, as well as North America, Europe, and Asia, as well as monsoon regions where data coverage is relatively good, the percentage of observing stations with statistically significant increases in RX1DAY is more than predicted by chance, but the percentage of stations with statistically significant drops is smaller than expected by chance. The addition of observational data from the previous decade reveals a more substantial increase in RX1DAY across the global land region.

In the REGEN gridded daily precipitation data set, light, moderate, and heavy daily precipitation have all strengthened (Contractor et al., 2020). In most land regions, daily mean precipitation intensities have increased since the mid-twentieth century. Between 1961 and 2018, the likelihood of precipitation topping 50 millimetres per day increased (Benestad et al., 2019). The global yearly fraction of precipitation from days in the top 5% (R95pTOT) has also increased greatly (Dunn et al., 2020). The magnitude of RX1DAY increased at a rate consistent with Clausius-Clapeyron (CC) scaling with respect to global mean temperature during the twentieth-century (Fischer and Knutti, 2016; Sun et al., 2021b). There is less research on past changes in extreme precipitation lasting more than a day, while there are a few that look at long-term trends in annual maximum five-day precipitation (RX5DAY). Long-term variations in RX5DAY are similar to those in RX1DAY on global and continental scales in many respects (Sun et al., 2021b).

In recent years, new or improved statistical approaches have been developed to attribute changes in weather extremes, such as heavy precipitation events

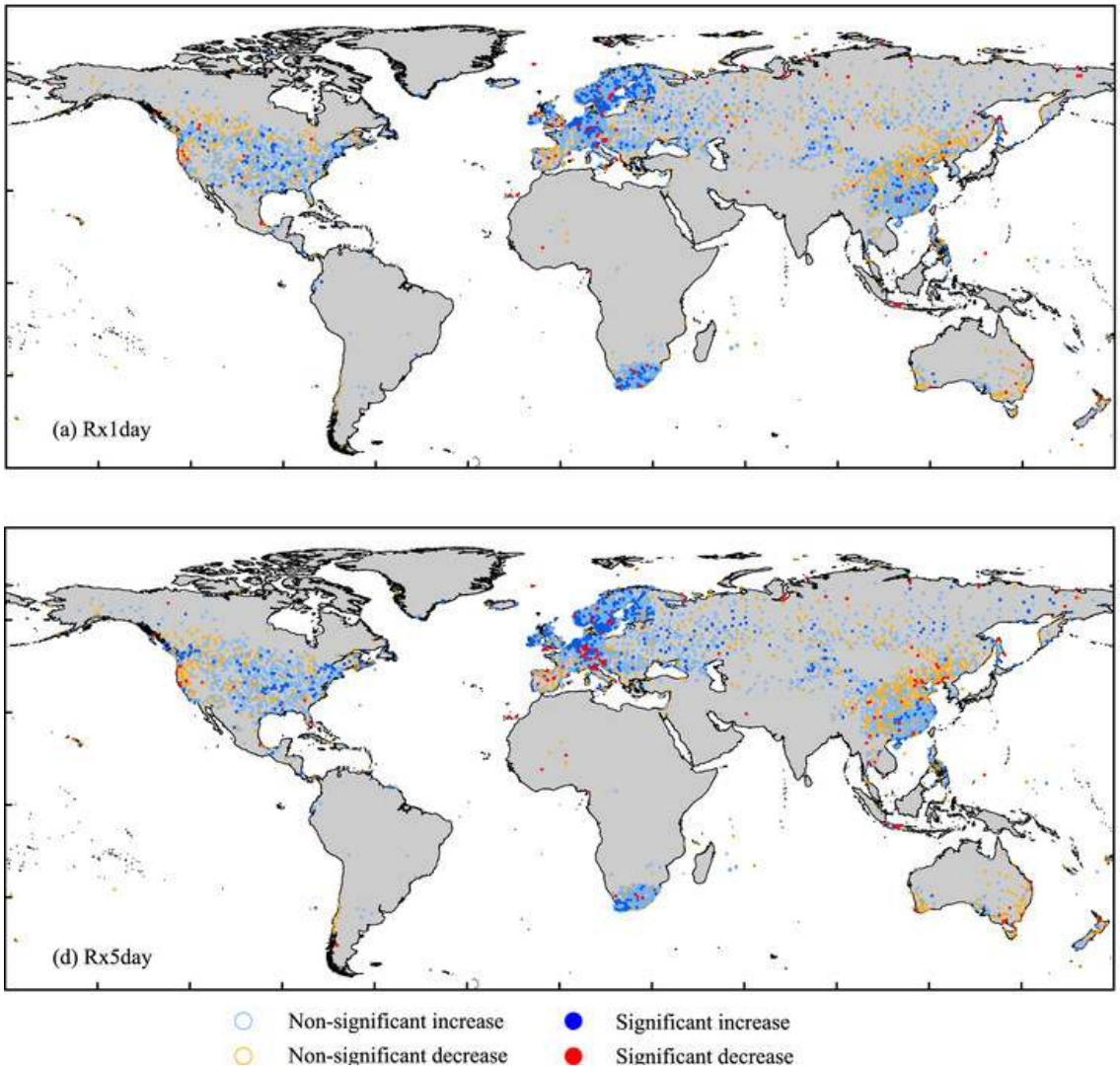

Figure 1.2: Summary of Mann-Kendall trend analyses for the period 1950-2018 for 7293 stations. (a),(d) Maps of locations of stations with trends for RX1DAY and RX5DAY, respectively. Light blue open dots indicate non-significant increasing trends and light red open dots mark non-significant decreasing trends. Dark blue and red filled dots indicate statistically significant trends as determined by a two-sided test conducted at the 5% level. Source: Sun et al. (2021b)

or droughts. With a growing amount of literature (Yiou et al., 2017; Cheng et al., 2018; Du et al., 2019), the attribution of extreme singular events has emerged as a burgeoning topic of climate research. Statements like "anthropogenic climate change made this event type twice as likely" or "anthropogenic climate change made this event 25% more intense" are produced by a commonly used approach, often referred to as the "risk-based approach" in the literature and referred to here as the "probability-based approach." This is done by estimating probability distributions of the index defining the event in today's environment as well as a counterfactual climate (e.g., preindustrial), and comparing intensities for a given occurrence probability or probabilities for a given magnitude (Pall et al., 2011).

The process to answer the question of how has climate change affected the probability of extreme event occurrences, including the interpretation of these changes owing to anthropogenic climate change in other characteristics, such

as the intensity of the event is referred to as extreme event attribution (van Oldenborgh et al., 2021). While there are multiple methods, a key component in any event attribution study is the level of conditioning on the state of the climate system. The combined effect of overall warming and changes in large-scale atmospheric circulation is frequently considered in the least conditional approach, which generally employs fully coupled climate models (Sun et al., 2014). Other, more conditional approaches involve prescribing specific aspects of the climate system. These range from prescribing the pattern of surface ocean change at the time of the event (e.g., Hoerling et al. 2013, 2014) to prescribing large-scale atmospheric circulation and using weather forecasting models or similar methods (e.g., Pall et al. 2017). These "storylines" (Shepherd, 2016) are highly conditional methodologies that can be beneficial when applied to extreme occurrences that are too rare for a more systematic statistical study, or when the local atmospheric conditions are central to the impact. However, the prescribed conditions may limit the assessment of the human influence on an event, as the fixed aspects of the analysis may also have been affected by climate change.

As a result, the outcome of event attribution is determined by the framing, which includes the event's definition (Cattiaux and Ribes, 2018) and spatial scale (Angélil et al., 2014). It's also susceptible to errors in both observations and models. Extreme events defined by atmospheric dynamics (e.g., tropical cyclones, atmospheric rivers) that may put current-generation models to the test limit the applicability of the probability-based approach to event attribution. Early event attribution studies were criticized for lacking model review, which led to scrutiny of this developing area (Trenberth et al., 2015). In the event attribution literature, however, evidence of a human influence on precipitation extremes has grown. Extreme rainfall occurrences in the UK (Schaller et al., 2016; Vautard et al., 2016; Otto et al., 2018), for example, have prompted more research than others, and equivalent research in other regions may be absent due to a lack of observational data and/or reliable climate models (Otto et al., 2020).

Figure 1.3 summarizes the AR6 WG1 evaluation of documented changes in heavy daily or 5-day precipitation occurrences (mainly based on RX1DAY and RX5DAY indices) and agricultural and ecological drought (primarily based on soil moisture observations and simulations) from the mid-20th century. It further supports the hypothesis that human influence, specifically greenhouse gas emissions, is the primary driver of the observed global scale intensification of heavy precipitation in all land regions with a long enough record, including North America, Europe, and Asia. It also shows that human activity has led to reduced water availability throughout the dry season across a large portion of the land, particularly in the northern mid-latitudes (Seneviratne et al., 2021). The spatial aggregation may sometimes obscure the detection of observed changes at a finer scale, such as the increase in RX1DAY over Southeast France (Ribes et al., 2019), which belongs to the Mediterranean AR6 region where other studies found no significant changes over Spain and Italy, implying that the AR6 regions are not necessarily homogeneous in terms of observed changes in precipitation extremes. Many AR6 regions (in grey) continue to lack sufficient evidence to allow for a robust assessment of observed changes. Furthermore, the lack of observed trends does not necessarily imply that regional precipitation, including extremes, has not

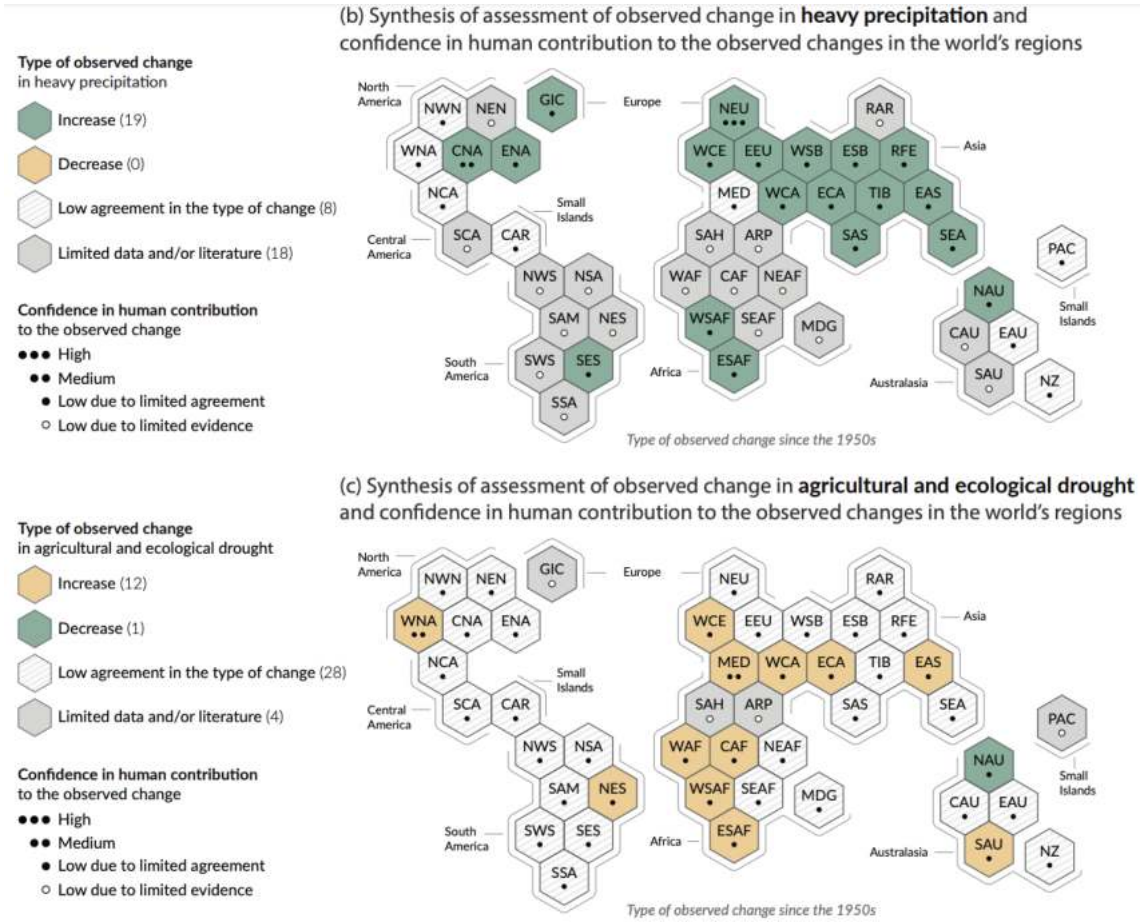

Figure 1.3: Synthesis of assessed observed changes and human influence for (panel b) heavy rainfall and (panel c) agricultural and ecological drought, for the IPCC AR6 regions, displayed as hexagons of identical size. The colours in each panel represent the four outcomes of the assessment of the observed changes: red/green for an observed increase with at least medium confidence; blue/yellow for a decrease with at least medium confidence; white for no significant change for the region as a whole; and grey when the evidence in this region is insufficient due to lack of data and/or literature preventing the assessment of the region as a whole. All assessments have been made for each AR6 region as a whole and for the timeframe from 1950 to the present. A more local assessment made on shorter time scales might differ from what is shown in the figure. The confidence level for the human influence on these changes is based on trend detection and attribution and event attribution literature, and it is indicated by the number of dots: three dots for high confidence; two dots for medium confidence; and one dot for low confidence. Horizontal bars indicate when an assessment is not possible due to insufficient evidence for the specific region. For heavy precipitation, the evidence is mostly drawn from changes in RX1DAY and RX5DAY precipitation indices. Agricultural and ecological droughts are assessed based on observed and simulated changes in total column soil moisture, complemented by evidence of changes in surface soil moisture, water balance (precipitation minus evapotranspiration) and metrics-driven by precipitation and atmospheric evaporative demand. Source: AR6 WG1 SPM, Masson-Delmotte et al. 2021a

already been influenced by human GHG emissions. As previously mentioned, an opposite response to anthropogenic aerosols and their dominant cooling effect at both global and regional scales may have compensated for such an alteration in the water cycle (Salzmann, 2016). Aerosols can also have an impact on precipitation extremes due to their microphysical effects, which are largely unknown

(Heikenfeld et al., 2019).

1.3 Key mechanisms

Beyond detection and attribution, analyses of observed changes are more reliable if they are consistent with the expected changes, given our current understanding of the main physical mechanisms responsible for global or regional water cycle responses. Globally, changes in precipitation extremes are expected as a direct result of global warming and the resulting increase in atmospheric water-holding capacity (Trenberth, 2011; Roderick et al., 2019; Algarra et al., 2020; Allan et al., 2020). On a global scale, column-integrated water vapour content rises roughly in accordance with the CC relationship, at a rate of about 7% for every degree Celsius of global-mean surface warming. Because extreme precipitation events are not often moisture-limited, local to global variations in annual maximum one-day precipitation (RX1DAY) has continuously increased with temperature at roughly 7% per 1°CC, both in observations (Westra et al., 2013; Fischer and Knutti, 2016; Ribes et al., 2019; Sun et al., 2021b) and future climate projections (Kharin et al., 2013; Wehner et al., 2020).

Multiple processes, however, are at work at regional scales, and the extreme precipitation response may deviate from this CC rate for a variety of reasons (Allan et al., 2020). Atmospheric large-scale circulation patterns are important drivers of the regional climate (IPCC AR6 WG1 Chapter 10, Doblas-Reyes et al. 2021). As a result, they're also relevant to extremes' magnitude, frequency, and duration. The extent and strength of the Hadley circulation, for example, have an impact on locations where tropical and extra-tropical cyclones develop, with substantial implications for extreme precipitation and drought characteristics. Global climate models reveal that the dynamic contribution to expected changes in precipitation can be significant and that it can significantly alter the pace of change of extreme precipitation, with vast subtropical regions showing robust decreases and other areas (e.g., equatorial Pacific) showing robust amplification (Figure 1.4). These dynamic contributions can increase or mitigate the relatively uniform thermodynamical response at the regional level, but they are highly model-dependent (Shepherd, 2014; Trenberth et al., 2015; Pfahl et al., 2017). The residual between the positive thermodynamic change owing to increased specific humidity and the decreased convective mass flux due to the weakening of the circulation causes the mean precipitation increase in the tropics. Model disagreement on shifts in convective zones dominates the uncertainty, but the drivers differ across land and ocean. Changes in large-scale circulation can also dominate the seasonal mean precipitation response over land in the mid-latitudes (Chadwick et al., 2014; Kent et al., 2015; Chadwick, 2016).

Dynamic contributions can also arise as a result of changes in temperature distribution vertically and horizontally, affecting the frequency and intensity of synoptic phenomena such as atmospheric rivers, low-level jets, concomitant moisture convergence, tropical cyclones, and extratropical storms (Figure 1.5). Extreme precipitation can also be amplified by mesoscale dynamic responses and feedbacks within storms, which are caused by the extra latent heat released by thermodynamic moisture increases (Molnar et al., 2015; Lenderink et al., 2017; Nie

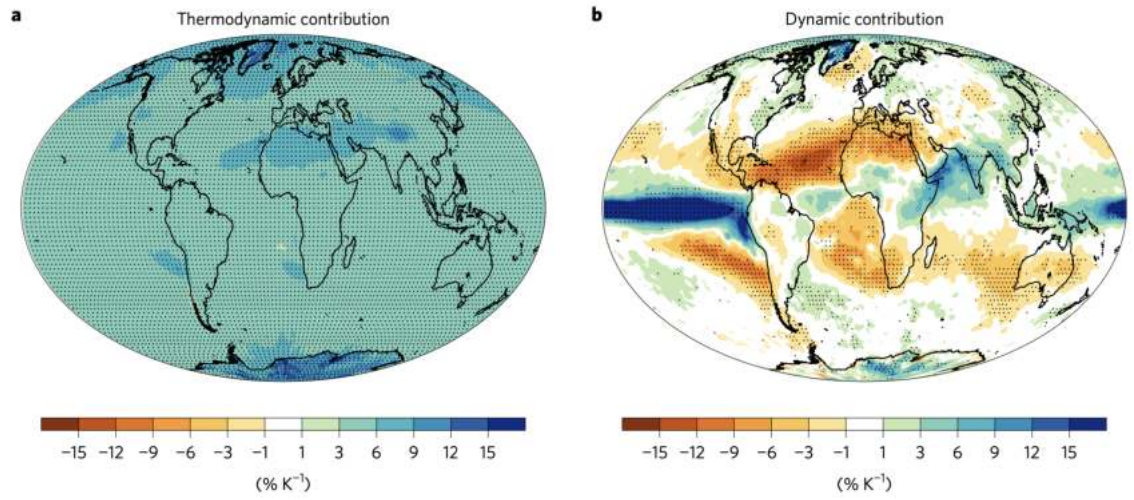

Figure 1.4: a) Multi-model mean fractional changes in thermodynamic scaling of RX1DAY in which the vertical velocity is kept constant (it is replaced with its mean value over the period 1950–2100). b) Difference between changes in full scaling and changes in thermodynamic scaling (full minus thermodynamic). Stippling indicates that at least 80% of the CMIP5 models agree on the sign of signal. Source: Pfahl et al. (2017)

et al., 2018). Because these dynamic impacts are strongly coupled to convective processes, their effective representation in global climate models may necessitate revised parameterizations for both shallow and deep convection (Rio et al., 2019; Douville et al., 2021) and/or the increased use of convective-permitting regional climate models (e.g., Prein et al. 2015; Pichelli et al. 2021). Precipitation formation and the microphysical effects of both natural and anthropogenic aerosols are also empirically parameterized, and they may be responsible for the varying responses of precipitation extremes across global and regional climate models.

External forcing has caused recent alterations in large-scale atmospheric circulation, which are less robust and generally less well understood than thermodynamical changes (Shepherd, 2014). Nonetheless, the AR6 WG1 Chapter 8 has assessed several robust signals (Douville et al., 2021). Since the 1970s, storm paths and associated precipitation in the Southern Hemisphere have shifted polewards, particularly in the austral summer and autumn. The inter-hemispheric temperature response to the time-evolving radiative influence of anthropogenic aerosols and the continued warming influence of GHGs has been linked to recent alterations in the tropical rain belt. Sulphate aerosol cooling in the Northern Hemisphere caused a southern shift in the tropical rain belt, contributing to the Sahel drought from the 1970s to the 1980s. On the other hand, reported changes in regional monsoon precipitation, particularly in South Asia, East Asia, and West Africa, have been limited for much of the twentieth century, due to increases in GHG-induced warming being counteracted by decreases due to anthropogenic aerosol-induced cooling.

Climate variability can be also sensitive to climate change in a wide range of timescales. The AR6 WG1 Chapter 8 emphasizes that water cycle variability and extremes are expected to increase faster than average changes in most regions of the world and across all emission scenarios (Douville et al., 2021). During the summer/warm season, interannual variability of precipitation over land is ex-

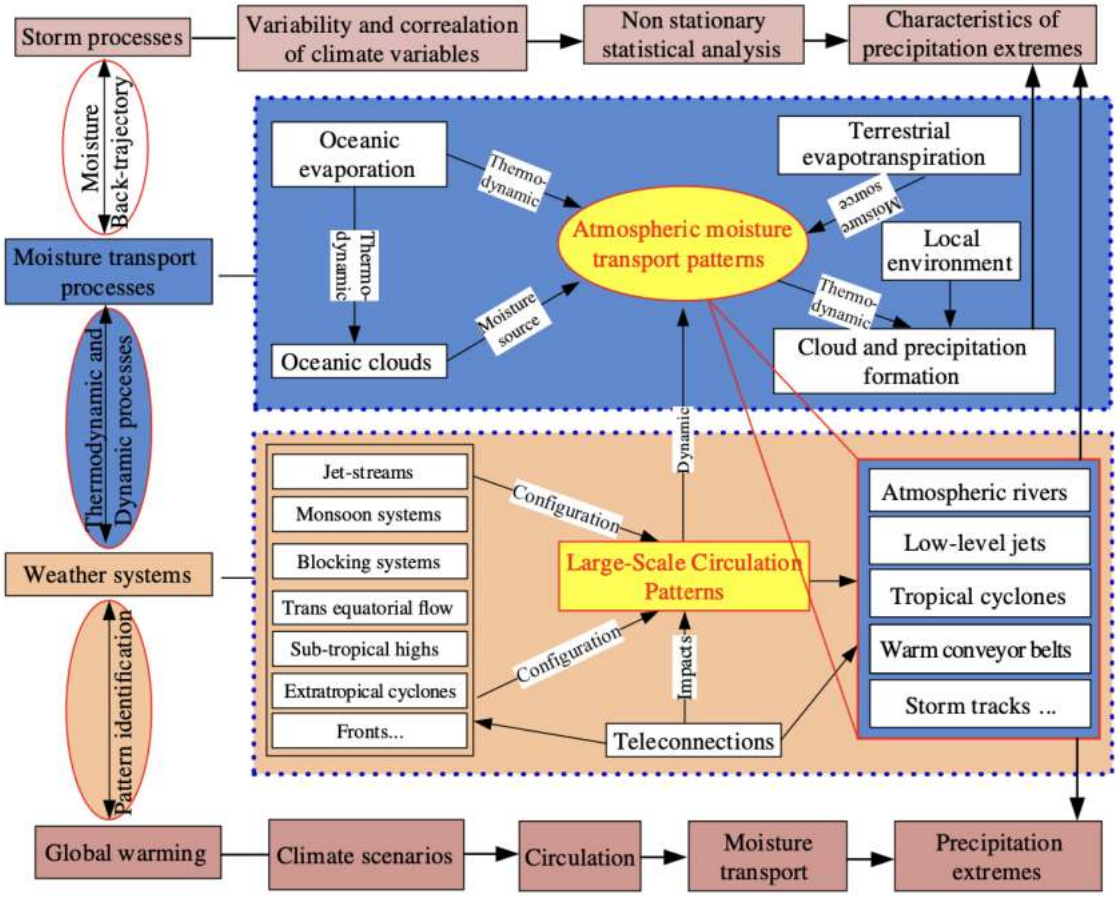

Figure 1.5: Physical processes which control atmospheric moisture transport and the associated precipitation extremes under global warming. Storm processes: the implications of climate change impacts on precipitation extremes suggest to use the non-stationary hydroclimatic frequency analyses for civil engineering design and risk management of water-related natural hazards, in which the variability of precipitation and its correlation to other climate variables should be considered. Moisture transport processes: back trajectory analyses could identify the atmospheric moisture sources and transport pathways that are conducive to particular extreme precipitation events. The analyses of thermodynamic and dynamic conditions are needed to investigate the physical mechanisms of the formation and evolution of atmospheric transport. Weather systems: atmospheric moisture transport patterns are resulting from large-scale circulation patterns that are highly associated with weather systems for occurrences of extreme precipitation events. Source: Liu et al. (2020).

pected to increase faster than changes in seasonal mean precipitation amount in the tropics and extratropics of both hemispheres. Rainfall variability related to the El Nino–Southern Oscillation, in particular, is very likely to be amplified by the end of the twenty-first century. This could have implications for projected changes in ENSO-related extreme events, such as widespread droughts. Over many land regions, sub-seasonal precipitation variability is projected to increase, with fewer wet days but increased daily mean precipitation intensity. Additionally, heavy precipitation events linked with tropical and extratropical cyclones, including atmospheric rivers, are expected to intensify (e.g., Catto et al. 2019; Kodama et al. 2019; Liu et al. 2019. In the observed changes in the primary modes of variability, it is difficult to distinguish the effects of global warming from internal multi-decadal variability (e.g., Austral Oscillation, North Atlantic Oscillation).

Regional forcings, such as deforestation, urbanization, and, mostly aerosols, can modulate changes in extremes at the regional scale (Kawecki et al., 2016; Lin et al., 2018; Souri et al., 2020). Aerosol forcing affects circulation patterns and tropical cyclone activity through changing patterns of sea surface temperatures (SSTs) (Takahashi et al., 2017). Aerosol forcing has a strong regional footprint and can influence precipitation extremes as well (Lin et al., 2018; Zhao et al., 2019). Enhanced aerosol loadings resulted in regional cooling due to reduced global solar radiation ("global dimming") from the 1950s to the 1980s, followed by a period of "global brightening" due to reduced aerosol loadings (AR6 WG1 Chapters 3 and 8, Eyring et al. 2021; Douville et al. 2021). Decreases in atmospheric aerosols result in greater warming and consequently an increase in extreme precipitation in 21st-century scenarios (Samset et al., 2018; Sillmann et al., 2019). Ambiguity in future aerosol emission projections leads to even more uncertainty in heavy precipitation projections (Lin et al., 2016).

Extremes can also be significantly influenced by regional feedback processes (Seneviratne et al., 2021). Droughts can be exacerbated by soil moisture-atmosphere feedbacks in particular (Zhou et al., 2019). There have also been reports of the possible influence of land surface conditions on circulation patterns (Koster et al., 2016; Sato and Nakamura, 2019). Furthermore, there exist feedbacks between soil moisture content and precipitation occurrence, which are often characterized by negative spatial and positive local feedbacks (Taylor et al., 2012; Guillod et al., 2015). These feedbacks appear to be crucial for expected changes in heavy precipitation, according to climate model projections (Seneviratne et al., 2013). However, there is evidence that climate models may not always capture the proper sign of soil moisture-precipitation feedbacks (Taylor et al., 2012; Moon et al., 2019), which could contribute to significant inter-model variability in climate projections. Droughts are driven by thermodynamic and dynamic processes. Droughts are influenced by thermodynamic processes that increase atmospheric evaporative demand (Vicente-Serrano et al., 2020) through changes in air temperature, radiation, wind speed, and relative humidity. Droughts are more affected by changes in the occurrence, length, and intensity of meteorological anomalies, which are related to precipitation and the amount of sunlight, due to their longer timescale than heavy precipitation events. While atmospheric evaporative demand increases with warming, regional changes in aridity are affected by increasing land-ocean warming contrast, vegetation feedbacks and responses to rising CO2 concentrations and dynamic shifts in the location of the wet and dry parts of the atmospheric circulation in response to climate change as well as internal variability (Allan et al., 2020).

1.4 Projected changes and their uncertainties

The AR6 recently examined the global climate response to five hypothetical scenarios that begin in 2015 and cover the range of possible future developments of anthropogenic climate change drivers found in the literature (Figure 1.6). They include scenarios with high and very high GHG emissions (SSP3-7.0 and SSP5-8.5), as well as scenarios with intermediate GHG emissions (SSP2-4.5) and CO2 emissions remaining around current levels until the middle of the century, as well

as scenarios with very low and low GHG emissions and CO2 emissions declining to net-zero around or after 2050, followed by varying levels of net negative CO2 emissions (SSP1-1.9 and SSP1-2.6).

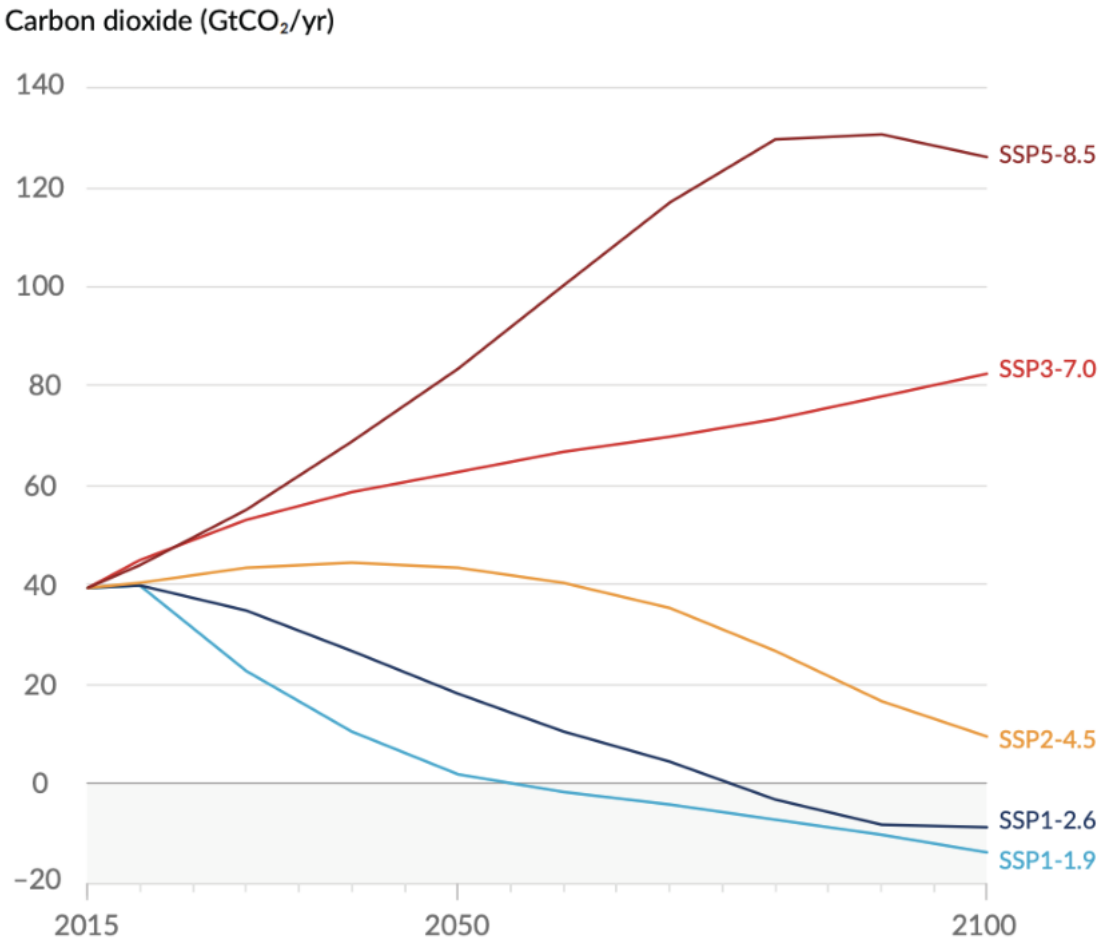

Figure 1.6: Future annual emissions of CO_2 across five illustrative CMIP6 scenarios. Emissions vary between scenarios depending on socio-economic assumptions, levels of climate change mitigation and, for aerosols and non-methane ozone precursors, air pollution controls. Alternative assumptions may result in similar emissions and climate responses, but the socio-economic assumptions and the feasibility or likelihood of individual scenarios are not part of the assessment. Source: IPCC AR6 WGI SPM, Masson-Delmotte et al. (2021a)

Whatever the emissions scenario, there is a high likelihood that average annual precipitation over land will increase as a result of global warming, but with different regional patterns: a large relative increase in the high latitudes and the core of the ITCZ, but a significant relative decrease in the subtropics and over Amazonia, for example. Projected precipitation changes are also seasonally dependent, as shown in Figure 1.7 for the intermediate emissions scenario. We see substantial seasonal contrasts and regional differences over land as well as over the ocean. Increased precipitation is expected across the tropical oceans, northern Africa, the Arabian Peninsula, India, southeastern Asia, and the Polar Areas in the future, whereas decreased precipitation is projected primarily over the subtropical regions, including northern Africa and southern Europe. Precipitation patterns in the tropics differ widely, with wetter wet seasons over South Asia, the central Sahel, and eastern Africa, but less precipitation across Amazonia and coastal West

Africa. These large-scale responses are linked to increased moisture transports in a warmer climate, which are driven by greater warming over land relative to the ocean, atmospheric circulation responses, and land surface feedbacks.

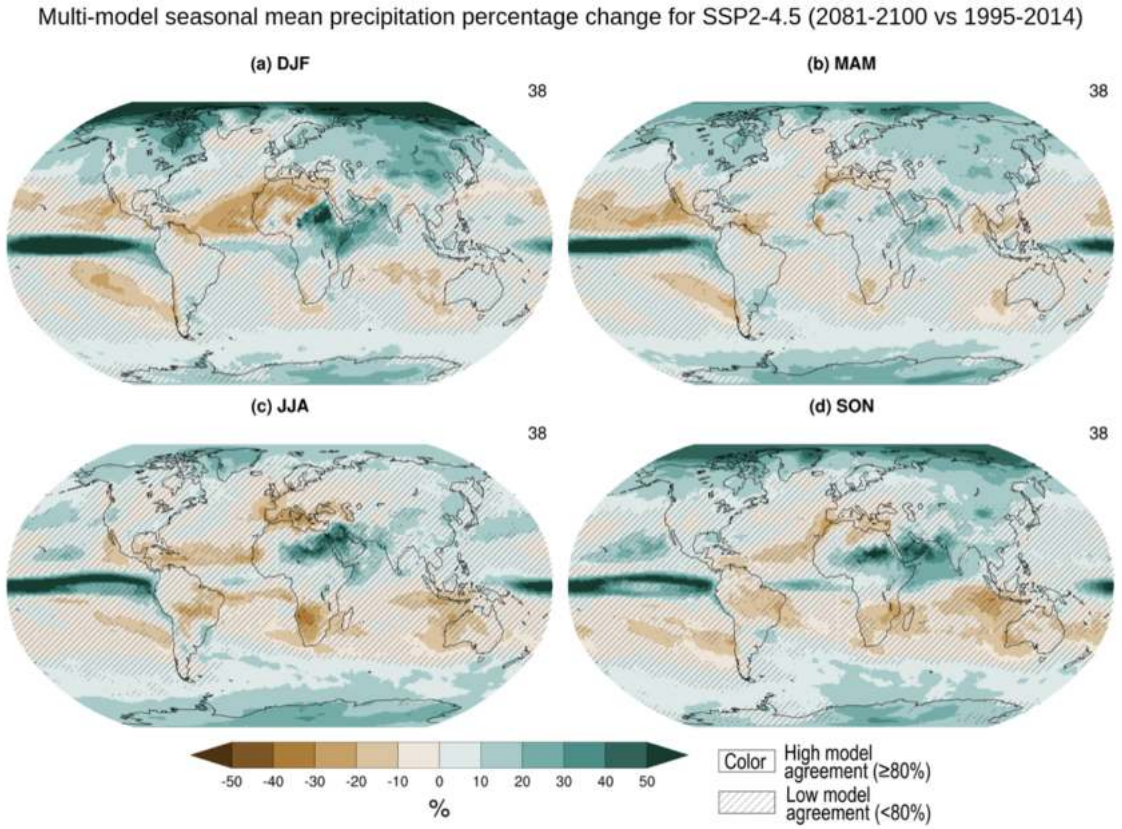

Figure 1.7: Projected long-term relative changes in seasonal mean precipitation. Global maps of projected relative changes (%) in the seasonal mean of precipitation averaged across 29 CMIP6 models in the SSP2-4.5 scenario. All changes are estimated for 2081-2100 relative to the 1995-2014 base period. Uncertainty is represented using the simple approach. No overlay indicates regions with a high model agreement, where more than 80% of models agree on the sign of change; diagonal lines indicate regions with a low model agreement, where <80% of models agree on the sign of change. Source: IPCC AR6 WG1 Chapter 8, Douville et al. (2021)

Over many land regions, sub-seasonal precipitation variability is expected to increase, with fewer wet days but increased daily mean precipitation intensity (Figure 1.8). The figure shows the dry days per year as well as the daily precipitation intensity for the different scenarios in CMIP6. We see that as we go from low to high-emission scenarios, the number of dry days, as well as the precipitation intensity, is significantly changing. The frequency of dry days is decreasing over northern Africa, the Arabian Peninsula, India, Southeast Asia, and the Polar Regions, while it is increasing across Amazonia, Central America, South Africa, the west coast of Africa, Australia, the Mediterranean, and central Europe. However, we also see a widespread increase in the daily mean precipitation intensity (Figure 1.8 b, d and f) as we go up the scenarios. An increase in the number of dry days is projected in several regions of the globe, which can dominate the precipitation change. It is clear that independent of the scenario, in the long term, we can expect more dry days but more intense single events of precipitation. Such changes in the precipitation regimes, as well as the general

increase in the frequency and intensity of precipitation extremes, contribute to an overall increase in precipitation variability.

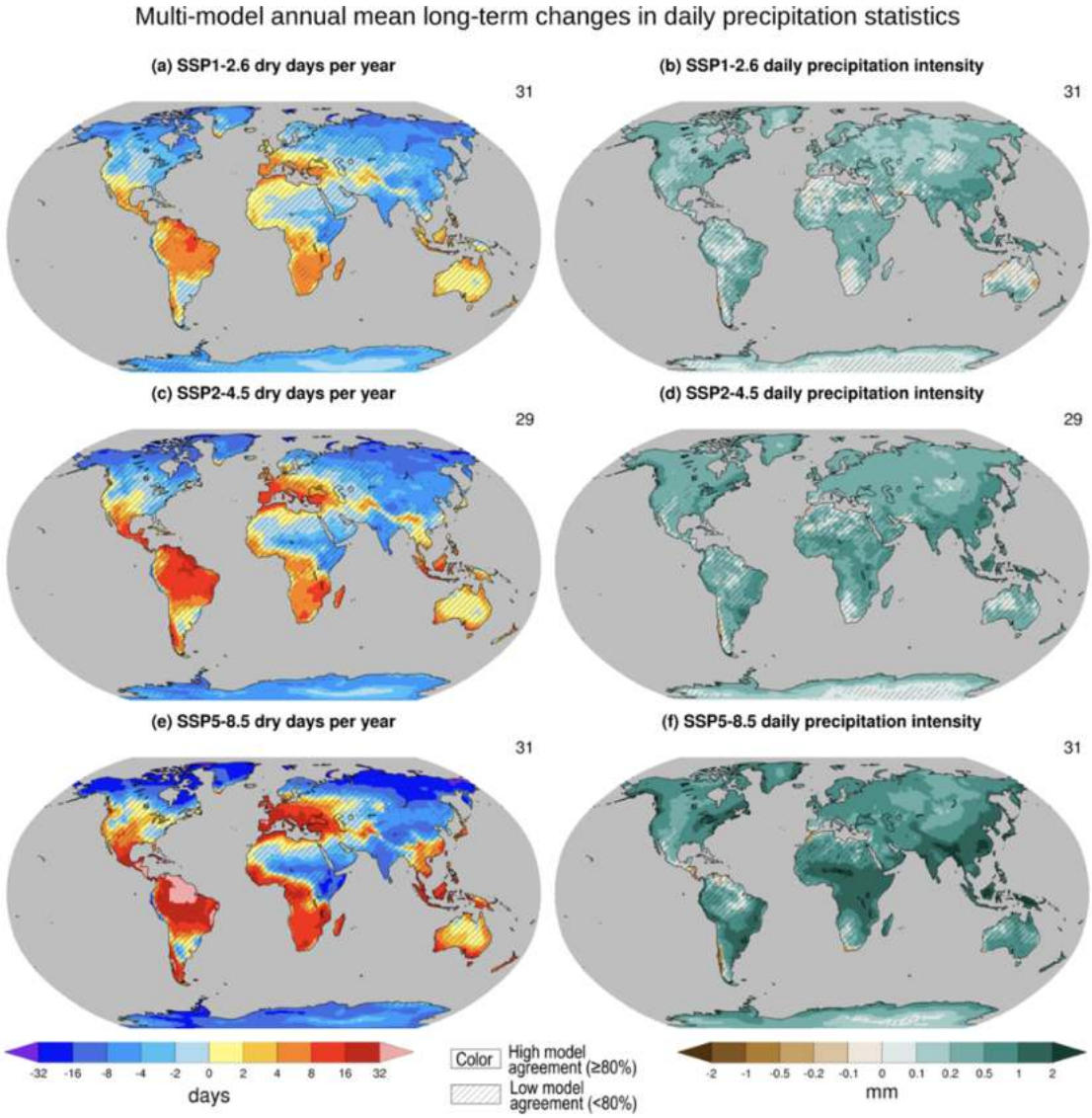

Figure 1.8: Projected long-term relative changes in daily precipitation statistics. Global maps of projected seasonal mean relative changes (%) in the number of dry days (days with less than 1 mm of rain) and daily precipitation intensity (in mm/day, estimated as the mean daily precipitation amount on wet days — i.e., days with intensity above 1 mm/ day) averaged across CMIP6 models in the SSP1-2.6 (a, b), SSP2-4.5 (c, d) and SSP5-8.5 (e, f) scenario respectively. Uncertainty is represented using the simple approach: no overlay indicates regions with a high model agreement, where ≥80% of models agree on the sign of change; diagonal lines indicate regions with a low model agreement, where <80% of models agree on the sign of change. Source: IPCC AR6 WGI Chapter 8, Douville et al. (2021).

There is however a large inter-model spread in the regional precipitation projections (Hawkins and Sutton, 2011; Rowell, 2012; Oueslati et al., 2016; Huang et al., 2018; Lehner et al., 2020), with only a few exceptions such as the robust drying of the Mediterranean (Zappa et al., 2015; Cook et al., 2018; Tang et al., 2018). In the South American and Australian monsoons, for example, there is little confidence in projected precipitation changes, and even the sign of the response is uncertain (Douville et al., 2021). In the extra-tropics, there is a signif-

icant likelihood that precipitation associated with storms and atmospheric rivers would increase in the future in most regions, resulting in more intense precipitation extremes, but the regional pattern and magnitude of projected changes are extremely model-dependent. On the one hand, a persistent poleward shift of storm tracks in the Southern Hemisphere and North Pacific is projected with a moderate confidence and should result in similar shifts in seasonal and extreme precipitation. On the other hand, despite major advances in their present-day climatology, the behaviour of the North Atlantic extratropical jet remains highly varied across CMIP6 models (Oudar et al., 2020). Some models however project a significant decrease in the cyclone occurrences over the Mediterranean, as well as a strong increase in extreme cyclone-related precipitation. The latter is mainly due to thermodynamics as it follows the Clausius-Clapeyron relation. Yet, the relation between temperature and extreme cyclone-related precipitation is not always controlled by the Clausius-Clapeyron relationship, thereby suggesting that dynamical processes can play an important role in generating extreme cyclone-related precipitation (Raible et al., 2018).

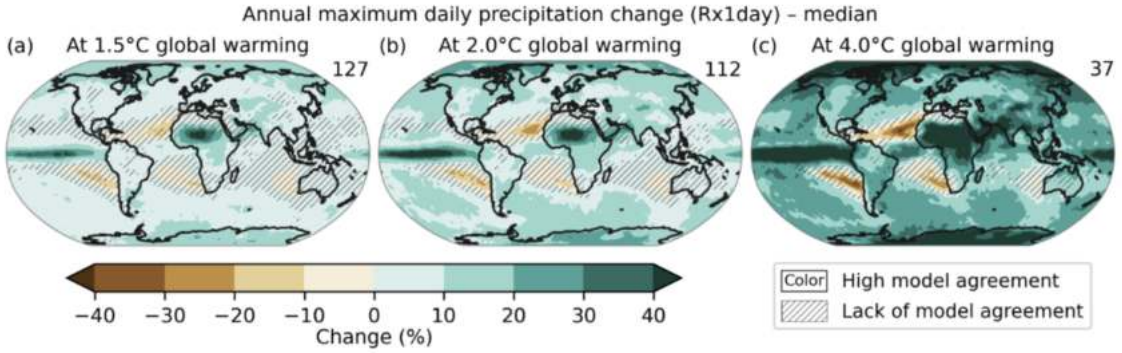

Figure 1.9: Projected changes in annual maximum daily precipitation at (a) 1.5° C, (b) 2° C, and (c) 4° C of global warming compared to the 1850–1900 baseline. Results are based on simulations from the Coupled Model Intercomparison Project Phase 6 (CMIP6) multi-model ensemble under the Shared Socio-economic Pathway (SSP), SSP1-1.9, SSP1-2.6, SSP2-4.5, SSP3-7.0, and SSP5-8.5 scenarios. The numbers on the top right indicate the number of simulations included. Uncertainty is represented using the simple approach: no overlay indicates regions with high model agreement, where ≥80% of models agree on the sign of change; diagonal lines indicate regions with low model agreement, where <80% of models agree on the sign of change. Source: IPCC AR6 WG1 Chapter 11, Seneviratne et al. (2021).

The rate of increase in RX1DAY with global warming was found to be independent of the forcing scenario for precipitation extremes (Pendergrass et al., 2015). This conclusion is backed up by the AR6 WG1 Chapter 11 assessment (Seneviratne et al., 2021). As a result, irrespective of the emissions scenario, projected changes in the intensity of extreme precipitation events have been shown for different global warming levels (GWLs) comparative to the 1851-1900 preindustrial baseline period (Figure 1.9). Different GWLs have fairly similar spatial patterns of projected changes. Except in a few regions, such as southern Europe surrounding the Mediterranean Basin during particular seasons, extreme precipitation almost always increases throughout geographical areas, with larger increases at higher global warming levels. The very likely ranges of the multi-model ensemble changes over all land grid boxes in the 50-year return values for RX1DAY and RX5DAY between 1.5°C and 1°C warming levels are greater than

zero for all continents except Europe, with a likely range greater than zero across Europe (Li et al., 2020). Extreme precipitation decreases are largely confined to subtropical ocean areas and are highly correlated with mean precipitation decreases because of storm track shifts. In some model realizations, these subtropical declines can spread to surrounding land areas.

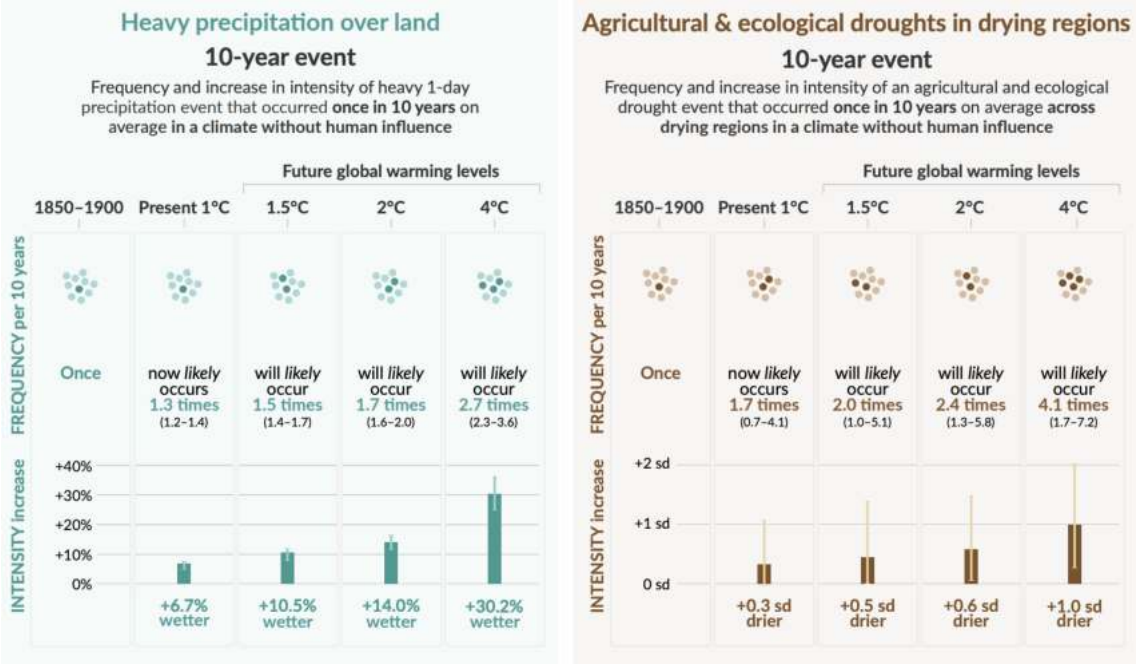

Figure 1.10: Projected changes in the intensity and frequency of extreme precipitation and droughts for global warming levels of 1° C, 1.5° C, 2° C, and 4° C, relative to their respective 1851–1900 reference period (1850–1900 for drought). Extreme precipitation events are defined as the daily precipitation amount that was exceeded on average once in a decade during the 1851–1900 reference period. Drought events are defined as the annual average of total column soil moisture that was below its 10th percentile during the 1850–1900 base period. For extreme precipitation, results are shown for the global land. For drought, results are shown for the AR6 regions in which there is at least medium confidence in a projected increase in agriculture and ecological drought at the 2° C warming level compared to the 1850–1900 base period. The dots and bars show the medians and their respective very likely range based on the multi-model ensemble from simulations of CMIP6 under different SSP scenarios. Dark dots indicate years in which the extreme threshold is exceeded. Light dots are years when the threshold is not exceeded. Changes in the intensity of drought are expressed as fractions of the standard deviation of annual soil moisture. Source: IPCC AR6 WG1 SPM, Masson-Delmotte et al. (2021a).

Projected increases in the likelihood of extreme precipitation of fixed magnitudes have been proven to be non-linear, with larger increases for rarer events (Fischer and Knutti, 2015; Li et al., 2020; Kharin et al., 2018). Increases in the probability of high (99th and 99.9th) percentile precipitation projected by the CMIP5 model between 1.5°C and 2°C warming scenarios are consistent with what might be expected based on observed changes (Fischer and Knutti, 2015), lending confidence to the projections. According to CMIP5 model simulations, the frequency of present-day climate 20-year extreme precipitation is projected to increase by 10% at the 1.5°C global warming level and by 22% at the 2.0°C global warming level, while the frequency of present-day climate 100-year extreme precipitation is projected to increase by 20% and more than 45%, respectively, at the 1.5°C and

2.0°C warming levels (Kharin et al., 2018). At a very high warming level of 4°C, CMIP6 simulations with SSP scenarios show that the frequency of 10-year and 50-year events will be roughly doubled and tripled, respectively (Figure 1.10).

Faced with such uncertainties in water cycle projections, various methods have been proposed to refine these projections based on observations. These range from more or less sophisticated bias correction methods (e.g., Schmidt et al., 2021), generally assuming that the biases diagnosed in the recent period will remain unchanged in the future, to even more empirical statistical methods that seek to constrain the projections on the basis of the performance of the models (e.g., Grose et al. 2017) or of emerging relationships between their recent and future behaviours (e.g., O'Gorman et al. 2012; Shiogama et al. 2022). More recently, direct observational constraints based on the instrumental record have been also applied to both recent and future changes simulated by global climate models (e.g., Brunner et al. 2020). Yet, preliminary results suggest that such methods are more efficient for temperature than for precipitation, given the higher signal-to-noise ratio and the clear emergence of the regional temperature response to anthropogenic forcings over recent decades (e.g., O'Reilly et al. 2022).

1.5 Synthesis

The frequency and severity of heavy precipitation have likely increased at the global scale throughout a majority of land regions with strong observational coverage, according to the AR6 WG1 report (Masson-Delmotte et al., 2021a). Over the land regions with sufficient observational coverage for assessment, the annual maximum amount of precipitation falling in a day or over five consecutive days has likely increased since 1950, with increases in more regions than declines. Heavy precipitation has likely increased on a continental scale across three continents: North America, Europe, and Asia, where observational data is more plentiful.

Although the fundamental mechanisms of precipitation response to rising GHG concentrations are reasonably well understood, some of them remain challenging to capture in global climate models (especially the possible dynamical amplification of precipitation extremes at the mesoscale). They include a fast radiative adjustment, a slower thermodynamical response induced by ocean warming, and large-scale dynamical changes owing to both radiative adjustment and non-uniform warming, among other processes and timescales. At the global scale, thermodynamic changes result in a spatially homogenous fractional increase in the intensity of precipitation extremes, but the dynamic contribution can either accentuate or counteract the reaction at the regional scale, according to multiple analyses.

In current global climate models, the future change in global-mean precipitation per degree of warming still has a significant spread (1-3 %/K). Because the entire distribution of daily precipitation intensities is perturbed, this spread is partly controlled by the response of extreme precipitation, with a model-dependent compensation between increasing extreme precipitation events and decreasing weak-moderate precipitation events (Thackeray et al., 2018). Due to the energy constraint on the latent heat released by water condensation within

the global atmosphere, the range of increase is much less than the increase in global-mean water vapour (around 6-7 %/°C). Regional precipitation changes are dominated by water vapour transport and dynamical processes, particularly at scales less than 4000 km. As a result, they are far more uncertain than the global-mean response.

The thermodynamic contribution to precipitation extremes is more robust than for seasonal mean rainfall. Storm-related extremes are expected to increase in a moister environment because storms are fueled by moisture convergence. Limited moisture availability over land and probable stabilization of atmospheric temperature profiles tend to minimize the empirically derived response in precipitation extremes below the CC based increase in water vapour of 6%-7% per °C, therefore the magnitude of this increase is still unknown. Simulating changes to convective extremes may require accurate modelling of local storm dynamics, especially at sub-daily timescales, which are outside the scope of this study.

Drought projections are also uncertain because precipitation deficits are influenced by dynamic mechanisms operating at various spatial scales, such as synoptic processes like atmospheric rivers and extratropical cyclones, blocking and ridges, dominant large-scale circulation patterns, and global ocean-atmosphere coupled patterns. They're also sensitive to land-atmosphere coupling, which includes moisture feedbacks and a direct CO2 effect on plant transpiration and photosynthesis, which isn't taken into consideration in all models but might be important at the regional scale, particularly over tropical forests.

Given the difficulty for climate models to converge on projected water cycle changes, including extremes, there is a need for both a better understanding of the drivers and mechanisms of simulated changes and better quantifying projection uncertainties and their contributions (i.e., scenario uncertainty, model response uncertainty, internal climate variability). In the continuation of the present study, we will focus primarily on projected changes in heavy precipitation and their seasonality, but we will also pay attention to the maximum number of consecutive dry days (CDD), particularly in Chapter 3.

If I cease searching, then, woe is me, I am lost.
That is how I look at it - keep going,
keep going come what may.

— **Vincent van Gogh**

2

Data, methods and models

There is now a widespread recognition that any increase in the frequency or severity of extreme weather events can have far-reaching consequences for nature and society. As a result, it is critical to assess recent and future changes in extreme events and to quantify related uncertainties. Monitoring, detecting, and attributing recent changes in climate extremes typically necessitate at least daily resolution data (sub-daily data can be even more informative but are generally not available at the global scale or in archived model outputs). This study makes use of diverse daily and monthly observational and global climate model data sets with varying spatial resolution. This chapter describes these multiple datasets, as well as the main methods that have been used to analyze the response of precipitation and related extremes to climate change.

2.1 Daily precipitation datasets

Precipitation is a key variable for assessing changes in both water and energy cycles. Observational records of precipitation have a long history (Park et al., 2017) and have evolved considerably in the recent decades. The advancements in the remote sensing technologies have also made it possible to record continuous observations with a global coverage (Levizzani et al., 2018) and complement the historically available in situ archives and associated gridded products (e.g., Becker et al. 2013; Roca et al. 2019; cf. Table 2.1). Apart from this, rapidly growing archives of reanalysis precipitation are also very useful to document and understand the observed precipitation variability, although the diversity of assimilated observations questions the feasibility or validity of trend analyses using such products (Bosilovich et al., 2008).

Based on the overall assessed performance of the different datasets to capture the relevant climatology of the mean and extreme precipitation (Roca

et al., 2019; Contractor et al., 2020), and the availability of a longer-term gridded product with wide geographical coverage (cf. Table 2.1), we have decided to focus on a limited number of datasets in the continuation of this study. However there is no clear consensus about the single best observational data set to use, especially for model evaluation (Randall et al., 2007; Gleckler et al., 2008; Gómez-Navarro et al., 2012; Kotlarski et al., 2019). We have therefore often selected one reference dataset, but also used other plausible observations and reanalysis that are generally considered reliable for the evaluation of daily precipitation intensities and related extremes. Regarding global climate models (GCMs), we have used a large subset of the latest generation (phase 6) of Coupled Model Intercomparison Project (CMIP6) models (cf. Table A.1).

We have acquired most observational and reanalysis data sets (except two) from the Frequent Rainfall Observations on GridS (FROGS) database (Roca et al., 2019), composed of gridded daily-precipitation products on a common $1° \times 1°$ grid which helps in the intercomparison and assessment exercises. This database includes satellite, ground-based and reanalysis products. Table 2.1 shows the names of the observational and reanalysis datasets along with their native resolution and the range, that we used in the course of our study. Appendix A contains the maps of mean and extreme precipitation captured by these individual datasets (except CHIRPS and EOBs).

Product short name	Period used	Spatial Coverage	Native Horizontal Resolution ($lon \times lat$)	References
MSWEP V1	1979-2015	90°S-90°N	0.25° × 0.25°	Beck et al. (2017)
REGEN	1950-2016	60°S-90°N *(land only)*	1° × 1°	Contractor et al. (2020)
GPCP	1997-2017	90°S-90°N	1° × 1°	Huffman et al. (2001)
GPCC	1982-2016	60°S-90°N	1° × 1°	Ziese et al. (2018)
EOBs	1950-2019	Europe *(land only)*	0.25° × 0.25°	Cornes et al. (2018)
CHIRPS	1981-2016	50°S-50°N *(land only)*	0.05° × 0.05°	Funk et al. (2015)
ERA5	1959 to present	90°S-90°N	0.25° × 0.25°	Hersbach et al. (2018)

Table 2.1: List of the different observational and reanalysis data sets used in this study. Also shows the period available, the spatial coverage, native resolution and the main references to the data set.

2.2 ETCCDI — Extreme precipitation indices

Focusing on temperature and precipitation extremes, the joint Expert Team (ET) on Climate Change Detection and Indices (ETCCDI) was charged with addressing the need for objective measurement and characterization of climate variability and change by providing international coordination and assisting in the organization of collaboration on climate change detection and indices relevant to climate change detection, as well as encouraging the comparison of modelled data and observations. A total of 27 core indices have been considered within the framework of ETCCDI. They are based on daily temperature values or the amount of precipi-

tation that falls on a given day. Some are based on predefined thresholds that are relevant to specific applications. Thresholds are the same for all stations in these cases. Other indices are based on thresholds that vary by location. Thresholds are typically defined in these cases as a percentile of the relevant data series. We used a small subset of the indices as listed in table 2.2.

Index	Indicator Name	Definition	Units
CDD	Consecutive Dry Days	Number of maximum consecutive dry days with RR < 1 mm	Days
CWD	Consecutive Wet Days	Number of maximum consecutive dry days with RR > 1 mm	Days
R10mm	Number of heavy precipitation days	Number of days when RR >10 mm	Days
R20mm	Number of heavy precipitation days	Number of days when RR >20 mm	Days
RX1DAY	Max 1 day precipitation amount	Maximum of total RR in 1 day	mm
RX5DAY	Max 5 day precipitation amount	Maximum of total RR in 5 day	mm
PRCPTOT	Annual total wet-day precipitation	Annual total RR in wet days (when RR > 1 mm)	mm
SDII	Simple daily intensity index	Annual Total RR divided by the number of wet days (when RR > 1 mm)	mm/day
R95p	Very wet days	Annual sum daily of RR >95th percentile	mm
R99p	Extremely wet days	Annual sum daily of RR >99th percentile	mm
R95PTOT	Contribution from very wet days	Fraction of total wet-day rainfall that comes from very wet days	%

Table 2.2: The list of different ETCCDI indices used in the course of this study

There are a plethora of indices based on daily precipitation data (Alexander et al., 2019). Individual studies often choose the different indices to define the extremes (e.g., annual maxima or predefined thresholds such as the 95th, 99th and 99.9th percentile), which lead to unintentional consequences associated with the interpretation of different results. It also makes the intercomparison difficult and causes mismatches across studies that employ various indexes. Furthermore, the indices should only incorporate variations induced by climate processes in order to robustly monitor and detect climate change. When creating these indexes, there are two things to bear in mind. To begin, the original daily data should be homogeneous, meaning that they should be free of non-climate-related volatility. Second, the method for constructing the indices should not introduce any further variation.

ETCCDI have facilitated the analysis of extremes by defining a set of climate indices that provide a comprehensive overview of temperature and precipitation statistics focusing particularly on extreme aspects (Karl and Easterling, 1999; Data, 2009). It has led to the standardisation of the extreme indices (Peterson and Manton, 2008) and now the same indices could be calculated and compared between observations and climate model output (e.g., Sillmann et al. 2013a). Many of the recent studies (e.g., Donat et al. 2013; de los Milagros Skansi et al. 2013; Dunn et al. 2014; Donat et al. 2016a; Herold et al. 2016, 2017; Tangang et al. 2017; Cattani et al. 2018) have concentrated on the set of ETCCDI indices calculated from in situ-based, satellite and reanalysis datasets, and also global climate model outputs on both regional and global scales. Figure A.4 shows an illustration of the RX1DAY (an ETCCDI index) based on a time series of daily precipitation. The indices are computed for the gridded daily precipitation observational datasets which facilitates the comparison with climate models, similar to the previous works mentioned above. It should be noted that the analysis of sub-daily precipitation extremes is beyond the scope of the present study, although dedicated studies suggest that they usually show an even stronger sensitivity to global warming (Barbero et al.,

2017; Poschlod et al., 2021) than the extremes in daily intensities.

2.3 Generalized Extreme Value methods

Statistical extreme values theory (EVT) is a branch of statistics that deals with large deviations from the median of probability distributions, or extreme values (Coles et al., 2001; De Haan et al., 2006). The theory evaluates the type of probability distribution of the extremes that processes generate. The limiting distributions for the minimum and maximum of large collections of independent random variables from the same arbitrary distribution are known as extreme value distributions. In practice, there are two main approaches. The first approach uses a continuous record to determine the block maxima (minima) series, whereas the second method uses a continuous record to extract peak values above (below) a specific threshold. Many studies (e.g., Cunnane 1973; Wang 1991; Madsen et al. 1997b,a; Martins and Stedinger 2001; Caires 2009) have discussed the relative merits of these parallel approaches.

In our thesis, we have employed the block maximum approach to investigate daily extreme precipitation rates. There are many practical reasons for using the block maxima method, like; the only available data may be block maxima (e.g., annual maxima, Kharin et al. 2007); the observations are not exactly independent and identically distributed (e.g., there is seasonality for the maxima, Katz et al. (2002)); the ease of applicability as blocks appear naturally in many situations (Van den Brink et al., 2005; Naveau et al., 2009). The main drawback is that the block maxima method can both miss some high values (within the same block) and consider low values (when blocks do not exhibit high values). Our choice to use the block maxima method was also partly dictated by the possibility to compare our results with the previous studies (e.g., Kharin et al. 2013; Li et al. 2020; Wehner 2020) that had focused on the annual maximum of daily precipitation intensities.

EVT describes the probability distribution of the maxima of sequences from a given ordered sample of random variables $X_1, ..., X_n$ with a common distribution function F. In most applications, the X_i indicates values of a process observed on a regular time scale, like daily values, so that M_n denotes the process's maximum (minimum) across n time units of observation.

$$M_n = \max\{X_1, ..., X_n\},$$

Under general conditions of independence and homoscedasticity (Independent and Identically Distributed: IID), the probability distribution of the block maxima M_n of any random variable X_i converges to a General Value Distribution, hereafter GEV (Coles et al., 2001; De Haan et al., 2006). This GEV does not depend on the detailed analytical formulation of the distribution of X. This result is similar to the Central Limit Theorem, which stipulates that under general conditions, the block average of X_i converges to a Gaussian.

The GEV distribution is a family of continuous probability distributions developed under extreme value theory and was formed by combining the Gumbel, Fréchet, and Weibull families (Coles et al., 2001). The GEV distribution is the distribution toward which the sampling distributions of largest-of-m values converge. According to the extreme value theorem, the GEV distribution is the only conceivable limit distribution of appropriately normalized maxima of a series of independent identically distributed random variables. It's important to note that a limit distribution is necessary, which imposes regularity constraints on the tail of the distribution. Regardless, the GEV distribution is widely used to describe the maxima of lengthy (finite) sequences of random variables as an approximate approximation. In a nutshell, GEV theory outlines how the m biggest values behave.

GEV asserts that G is a non-degenerate limiting cumulative distribution function (CDF) that exits for particular sequences maxima and can be written in the form:

$$G(z) = \exp\left\{-\left[1+\xi\left(\frac{z-\mu}{\sigma}\right)\right]^{\frac{-1}{\xi}}\right\} \tag{2.1}$$

defined on the set $\{z : 1+\xi(z-\mu)/\sigma > 0\}$, where the parameters satisfy $-\infty < \mu < \infty, \sigma > 0$ and $-\infty < \xi < \infty$. There are three parameters for the GEV model: a location parameter, μ; a scale parameter, σ; and a shape parameter, ξ. According to the value of the shape parameter, the GEV simplifies into the different types of distributions (cf. Figure 2.1). The type I and type II classes of extreme values distribution correspond respectively to the cases ξ>0 and ξ <0. The subset of the GEV family with $\xi = 0$ is interpreted as the limit of Eq. (2.1) as $\xi \to 0$, leading to the Gumbel family. The statistical implementation is substantially simplified by the consolidation of the original three families of extreme value distribution into a single family. The data themselves determine the most appropriate type of tail behaviour through inference on ξ.

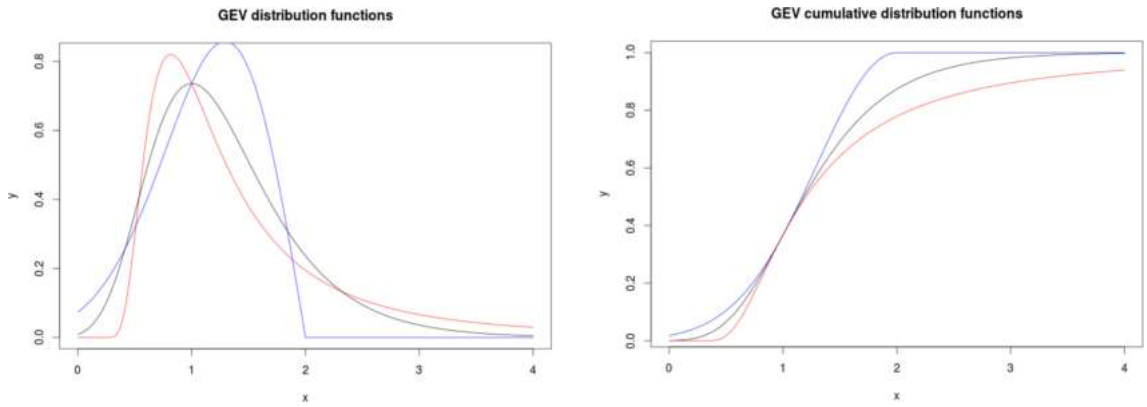

Figure 2.1: PDFs for (left) and CDFs (right) for GEV. For each plot, x and μ=1, σ=0.5. For ξ, blue=-0.5, black=0, and red=0.5

It's important to remember here that the location parameter μ represents the 'centre' of the distribution rather than the mean, and that the scale parameter σ governs the size of the deviations about μ rather than the standard deviation.

Probability density functions (PDFs) and cumulative distribution functions (CDFs)

The probability density function (illustrated in Figure 2.1 (left)) depicts the relative likelihood (on the y-axis) of a variable having value X. (on the x-axis). In contrast, the cumulative distribution function (illustrated in Figure 2.1 (right)) defines the probability of X by integrating the PDF over the range when the variable $\leq$ X. Eq. 2.1 is in CDF format, not PDF.

2.3.1 Return Levels

For modeling extremes of a series of independent observations $X_1, X_2, ...$, data are blocked into sequences of observations of length n, for some large value of n, yielding a series of block maxima, $M_{n,1}, ..., M_{n,m}$, say to which the GEV distribution can be fitted. The blocks are often chosen to correspond to one year, in which case n is the number of observations per year and the block maxima are annual maxima. As previously stated, we compute the annual maximum one-day precipitation (RX1DAY), which are yearly block maxima, for this thesis. Estimates of extreme quantiles of the annual maximum distribution are obtained by inverting Eq. (2.1):

$$z_p = \begin{cases} \mu - \frac{\sigma}{\xi}[1 - \{-\log(1-p)\}^{-\xi}], & for \xi \neq 0, \\ \mu - \sigma log\left\{-\log(1-p)\right\}, & for \xi = 0, \end{cases} \tag{2.2}$$

where $G(z_p)$ = 1 - p. Here z_p is the return level associated with the return period 1/p. The level z_p is expected to be exceeded on average once every 1/p years or in other words, z_p is exceeded by the annual maximum in any particular year with probability p. The return levels were computed using both stationary and non-stationary assumptions, as discussed in the section 2.3.2 (Figure 2.3). In Chapter 4, we also examine the rare extreme precipitation events that we computed as the 20-year return values from the RX1DAY after fitting a non-stationary GEV.

2.3.2 Non-stationary vs. stationary GEV

A stationary process in statistics is a stochastic process whose joint probability distribution does not change with time. When calculating the model fit, it's relevant to see if the model distribution stays the same throughout time. In GEV models, non-stationarity can be introduced by describing one or more parameters as a function of a covariate (e.g., time). Figure 2.2 depicts how the likelihood of extremes may evolve in the future under several climatic scenarios. It's worth noting that the model that was fitted to a 20th-century extreme temperature distribution would not work so well for 21st-century values.

This change can be represented as a function of time in the model; for example, μ, σ and ξ can be represented as a function of time. A non-stationary model is one in which the model parameters are not set to constant, as opposed to a stationary model. If we expect a higher proportion of extremely high temperatures

in the future, the shape of a GEV function fitted to the data may shift toward a more heavy-tailed distribution. As a candidate model for the non-stationary GEV, we can assume a model where linear trends in the location and scale parameter ($\mu(t) = \mu_0 + \mu_1(t), \sigma(t) = \sigma_0 + \sigma_1(t)$) are considered while no trend is considered in the shape parameter ($\xi(t) = \xi$). The parameter μ_1 can be interpreted as the slope of a linear trend in the centre of the distribution, and the parameter σ_1 as the appropriate rate of change in the scale or the size of the distribution.

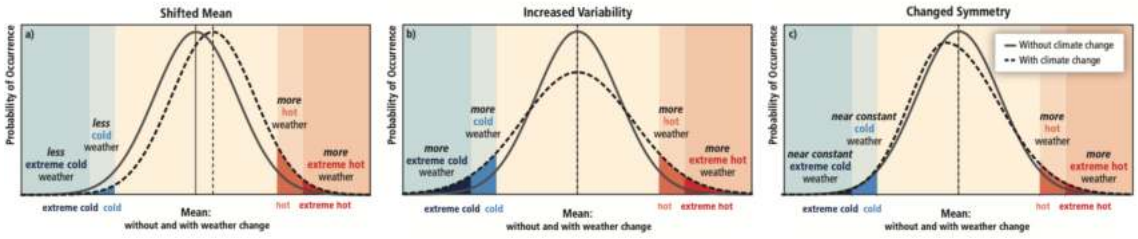

Figure 2.2: Temperature magnitudes and probability of occurrence in the context of a warmer climate. Source: IPCC SPM 2012, Field et al. (2012)

The return level is the same for all years under the assumption of stationarity, or there is a one-to-one relationship between the return level and the return period, as shown in Figure 2.3 (top). In a non-stationary model with linear time trends in the location and/or scale parameters, the effective return level would likewise vary linearly as shown in Figure 2.3 (bottom).

So we can mainly fit three different forms of GEV distributions into our data:

- A stationary GEV in which no parameters are dependent on a covariate.
- A non-stationary GEV in which either μ or σ change with a covariate
- A non-stationary GEV in which both μ and σ change with a covariate

2.4 Interpolation techniques

Interpolation is often employed in climate studies, for example when remapping model output data in post-processing applications or for model intercomparison or model evaluation against gridded observations. Several software libraries have been developed in recent years to apply various, more or less conservative, interpolation techniques. Examples include the ESMF library (Hill et al., 2004), SCRIPS (Jones et al., 1998), and others. Typically, these libraries offer linear, bilinear, multilinear, and conservative interpolation (Jones, 1999). When dealing with water or energy, conservative interpolation, also known as area-weighted interpolation, is commonly used. It is more computationally expensive than linear interpolation because the overlaps between target and source cell regions must be computed. Regardless, conservative interpolation has grown in popularity and is now the most widely used regridding interpolation method (Pletzer and Hayek, 2019).

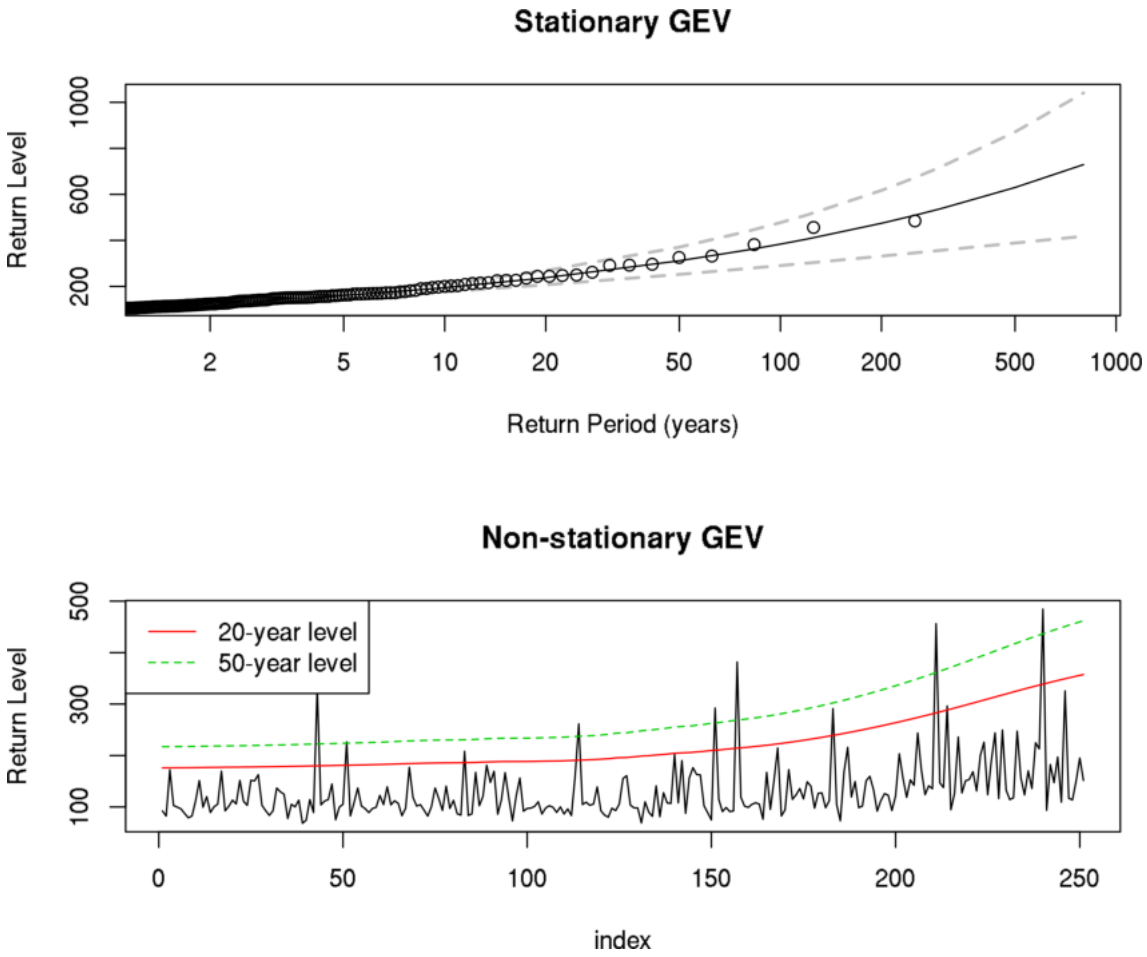

Figure 2.3: Return level plots from a stationary (top) and non-stationary (bottom) GEV analysis of the annual RxlDAY over a single grid point for the period 1850-2100. The non-stationary fit is calculated by ln[CO_2] as a covariate for both location and scale.

Irrespective of the mathematical method used to remap the fields, derived fields such as the daily precipitation temporal standard deviation and other indices can be remapped using two different procedures:

- the final-step procedure, in which statistics and climate indices are calculated directly from fields on the native grid and then interpolated on the target grid, and
- the initial-step procedure, in which the fields are interpolated on the target grid before the statistics and climate indices are calculated.

At the moment, there is no agreement on which procedure is best for evaluating model climate indices. It may appear self-evident that after computing the derived field, the remapping should be done as the last step. In practice, however, it is preferable to interpolate all fields on a common grid before computing statistics and climate indices (the first-step procedure), particularly in intercomparison studies of simulations from several models with different native grids (e.g., Loikith et al. 2015; Mehran et al. 2014). Some studies (e.g., Chen and Knutson 2008; Bootsma et al. 2005; DeAngelis et al. 2013; John et al. 2022) used the initial-step procedure to evaluate climate indices, while others (e.g., Sillmann

et al. 2013a; Bhowmik and Costa 2015; Sunyer et al. 2013; Diaconescu et al. 2015) used the final-step procedure. Other studies (e.g., Tencer et al. 2014; Sylla et al. 2013) make no mention of the procedure at all. Throughout the thesis, we have used the initial-step procedure in all of our analyses.

Figure 2.4 depicts the difference between the aforementioned orders of interpolation. For most of the analysis, we have regridded all the models as well as the observations onto a 1° by 1° latitude-longitude (1° × 1° hereafter) grid using a first-order conservative remapping. This enables us to directly compare the results from a diverse model suit with the observations. The 1° × 1° grid is a finer horizontal grid when compared with most of the CMIP6 model native grids, which are based on an average grid size of 2 degrees or more. In contrast, for some observations, this target grid size is coarser and regridding may smooth out the values. When going to a smaller grid from the coarser one as we do in most of the CMIP6 models, we do not expect to over-estimate the values, but we may be equipped with the analysis of some regional features. We have followed this method consistently throughout the thesis, and there is always a trade-off between the smoothing of intensity and regional analysis.

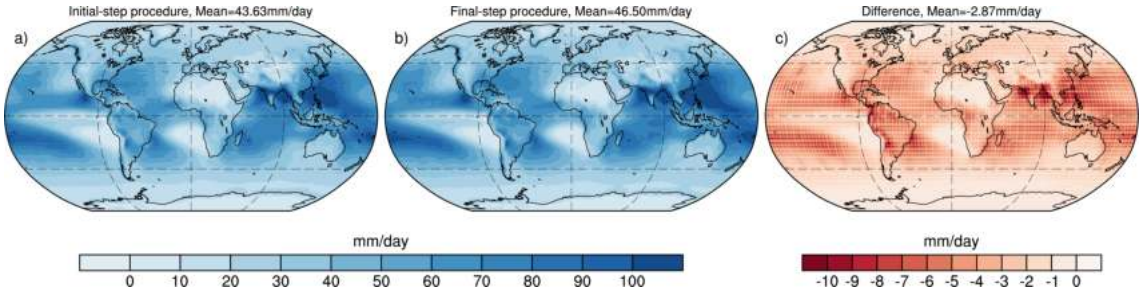

Figure 2.4: Maps showing the multi-model mean climatology of RX1DAY after regridding all models onto a common 1°x1° grid by using the two procedures of interpolation; a) initial-step, b) final-step. The right panel c) shows the difference (b minus a) results obtained using the two procedures.

2.5 Circulation type classifications

Synoptic circulation typing has been routinely used for various purposes throughout the previous few decades. The classification of atmospheric circulation into different types or clusters proves to be an important tool for better understanding the two-way interactions between the atmosphere and the surface climate (e.g., the day-to-day variability of temperature and precipitation). The different classes are collectively called circulation types (CTs) or weather types. There are several circulation classifications utilized in a variety of applications and regions. The synoptic classifications limit the number of representative categories and simplify the atmospheric circulation (Huth et al., 2016). A weather regime approach (e.g., Cassou et al. 2005; Van den Besselaar et al. 2010; Franzke et al. 2011; Cattiaux et al. 2013) can also be used that however usually focus on persistent circulation patterns that are identified either after applying a prefiltering or using a duration criterion a posteriori. Our focus here is on synoptic or day-to-day variability so this common weather regime approach is not considered.

The majority of the CTs have been developed in regions around the globe

where synoptic variability is an important driver of regional weather conditions (Huth et al., 2008). Many studies have addressed synoptic situations around the world, including North America (Sheridan, 2002; Lee, 2015), Australia (Hart et al., 2006), New Zealand (Jiang, 2011), Asia (Chen et al., 2008), and all of Europe (Huth et al., 2016; Otero et al., 2018). This section illustrates how to use a gridded CT categorization based on the classic Lamb weather type (Lamb, 1972), which Jenkinson and Collison (Jenkinson and Collison, 1977) objectively applied (hereinafter JC). This CT classification scheme, which was originally established for the British Isles, has become one of the most widely used in the mid-high latitudes.

Examining the strength and direction of the airflow is the foundation for distinguishing synoptic patterns (cyclonic or anticyclonic). Here we implement the objective JC classification by applying a movable 16-point mask to every grid point from $1° \times 1°$ regridded climate model outputs. We constructed a gridded JC categorization, similar to Otero et al. (2018), by treating each grid-point on the map as the central point, surrounded by the 16 points (cf. Figure A.5) that would represent the synoptic condition for that central point. This approach can be used anywhere in the mid-latitudes (Donat et al., 2010). However, here only the European domain encompassing — 15.5°W - 35.5°E and 30.5°N - 70.5°N was used. These are then used to conduct the additional analysis in chapter 5. Also, this method takes daily mean sea level pressure as an input, which is one of the main advantages because free atmospheric variables are thought to be relatively effectively replicated by GCMs (Goodess and Palutikof, 1998). Before computation, the daily pressure datasets were brought to a standard $1° \times 1°$ resolution using a bilinear interpolation.

By obtaining daily atmospheric synoptic circulations over every grid point of a defined region, the tailored version of the JC classification allows for the direct linkage of the dominant atmospheric pattern with any atmospheric variable over a specific time frame. The JC classification can identify a total of 27 different synoptic patterns (cf Table A.2). These are determined by the dominant atmospheric pressure pattern (cyclonic and anticyclonic) and wind flow directions. For days with very weak pressure gradients that make it difficult to assign to a dominant advection or dominant CT, a "low flow" or "unclassified" type is also assigned. For the sake of simplicity, the 27 CTs have been merged into 11 broader types for this study, which include the Anticyclonic (A) and Cyclonic (C) pressure patterns, the eight dominant directional patterns are named after the direction of advection (NE, E, SW, W, and so on) and the unclassified (U) type (cf. Table A.2). These circulation types are considered sufficient to analyse the influence of circulation on extreme precipitation, as discussed in chapter 5, section 5.5.

2.6 The ARPEGE-Climat 6.3 atmospheric model

The Centre National de Recherches Météorologiques (CNRM) has been developing a spectral global atmospheric general circulation model (AGCM) dubbed ARPEGE (a French acronym for "research project on small and large scales"; Courtier et al. 1991) for both numerical weather prediction (NWP) and climate applications since the 1990s. The model code is jointly developed by Météo-France and the European

Center for Medium-range Weather Forecast (ECMWF, Integrated Forecast System - IFS - project). ARPEGE and IFS hence share the same software system. Derivatives of ARPEGE-IFS, called ARPEGE-Climat, have been tailored for climate studies at a lower resolution than the NWP model but coupled with other climate component models (dynamical ocean, enhanced land surface, carbon cycle, ozone chemistry and aerosols), and longer integrations, which need a "frozen" version for several years. The first-ever version of the ARPEGE-Climat AGCM was described in Déqué et al. (1994). Since then, it has been updated regularly, by including new atmospheric physical packages, improving the representation of the land surface and its coupling with the atmosphere, extending the top of the model beyond the troposphere, and increasing both the vertical and horizontal resolution.

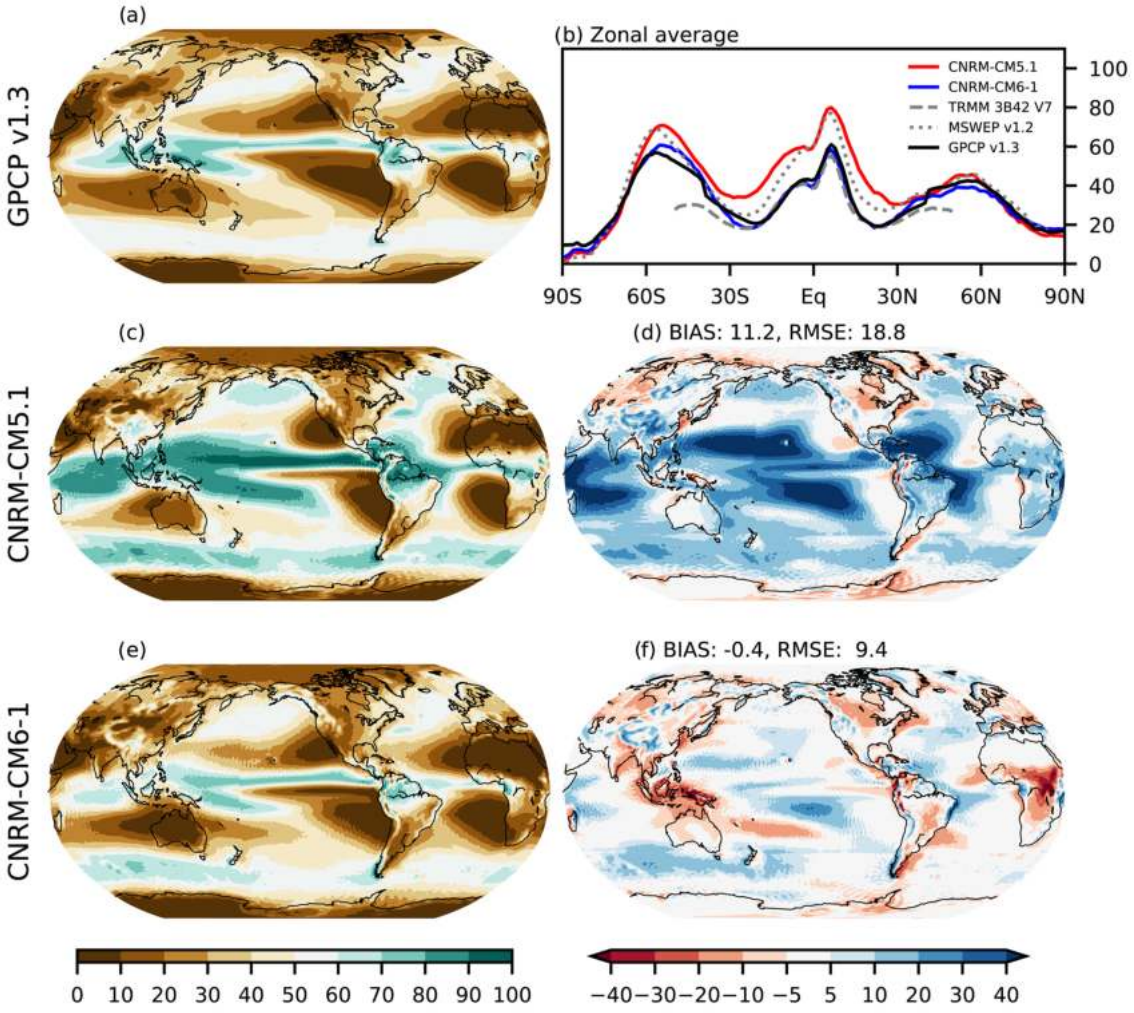

Figure 2.5: Mean annual percentage of rainy days (daily precipitation above 1 mm/day, in %): (a) GPCP Version 1.3,(c) CNRM-CM5.1, and (d) its bias with respect to GPCP Version 1.3, and (e) CNRM-CM6-1 and (f) its bias with respects to GPCP Version 1.3. Zonal averages of these annual percentages are indicated on panel (b) (GPCP Version 1.3:black line; CNRM-CM5.1: red line; CNRM-CM6-1: blue line; MSWEP Version 1.2: dashed grey line; and TRMM 3B42 Version 7: dotted grey line). Only one member is used for CNRM-CM6-1. Source: Roehrig et al. (2020)

ARPEGE-Climat is the atmospheric component of the CNRM-CERFACS (*Centre National de Recherches Météorologiques - Centre Européen de Recherche et de Formation Avancée en Calcul Scientifique*) Climate Model (CNRM-CM; e.g., Voldoire

et al. 2013) and Earth System Model (CNRM-ESM; e.g., Séférian et al. 2016). This model has contributed to the CMIP, including the last two phases CMIP5 and CMIP6. For CMIP6, three model versions have been used: the standard climate model at standard (T127 truncation) resolution, CNRM-CM6-1 (Voldoire et al., 2019), its high-resolution counterpart, CNRM-CM6-1-HR (T359 truncation), and its Earth System version, CNRM-ESM2-1 (Séférian et al., 2019). Here, our focus will be mainly on CNRM-CM6-1 given its participation in the Cloud Feedback Model Intercomparison Project (CFMIP, Webb et al. 2017; Douville and John 2021), with targeted idealized coupled and atmosphere-only experiments aimed at a better understanding of the climate response to increased CO_2.

Like any other atmospheric model, ARPEGE-Climat is made up of a dry dynamical core and a set of physical parameterizations for representing diabatic processes. It also necessitates a numerical grid, coupling to a land surface model, and boundary external parameters (e.g., trace gas and aerosol concentration, gas absorption optical properties, temporal variations in the solar irradiance, land surface properties, and sea surface temperature (SST) and sea ice (SIC)). The most recent version of the ARPEGE-Climat global atmospheric model is 6.3. (Roehrig et al., 2020). Cycle 37 of the ARPEGE/IFS is used to derive the dynamical core of ARPEGE-Climat 6.3. The vorticity and divergence form of the primitive equations were resolved by the dynamical core, with temperature and surface pressure logarithm serving as thermodynamic state variables. All nonlinear terms (including physical tendencies) are computed on the related reduced Gaussian grid, which has a spatial resolution of around 150 km in both latitude and longitude (Hortal and Simmons, 1991), whilst, the linear terms are computed using a spectral transform on the sphere with a T127 triangular truncation. ARPEGE-Climat 6.3 is a "high-top" model that features 91 vertical levels and a progressive hybrid pressure coordinate system (Simmons and Burridge, 1981).

ARPEGE-Climat 6.3 is the atmospheric component of the coupled model CNRM-CM6-1, which we have analysed but also integrated for our idealized sensitivity study in Chapter 3. Voldoire et al. (2013) describe its previous version 5.2. Roehrig et al. (2020) evaluate the present-day precipitation modelled by CNRM-CM6-1 in AMIP (Eyring et al., 2016) atmosphere-only experiments driven by observed SST and observed radiative forcings. Figure 2.5 depicts the mean precipitation greater than 1 mm/day from CNRM-CM6-1 AMIP simulations. The GPCP v1.3 and TRMM 3B42 V7 reference data sets reveal a mean frequency of rainy days of about 60% to 80% in the ITCZ region, while it falls below 20% over much of the subtropics (Figure 2.5 b). It rains roughly half of the time in the mid-latitudes. The reference dataset, MSWEP v1.2, shows a 10 to 20% increase in the frequency of rain occurrences (Figure 2.5 b). Given that this rainfall product incorporates both observational and reanalysis data, such a disparity is to be expected, as numerical models have been found to exaggerate the occurrence of light precipitation (e.g., Dai 2006; Flato et al. 2014). This systematic error was however much more pronounced in the former CNRM-CM5.1 AGCM. The model considerably overestimates the frequency of rainy days across the tropics, other than in the eastern subtropical ocean basins, where it is more consistent with data (Figures 2.5 b and d). Likewise, the model precipitates far too frequently along mid-latitude storm tracks. Except for tropical continental areas and the maritime

continent, CNRM-CM6-1 greatly eliminates these biases over the majority of the globe (Figures 12.5 b, e, f). The frequency of wet days is underestimated there, implying that the dry biases are partly due to a paucity of rainy events.

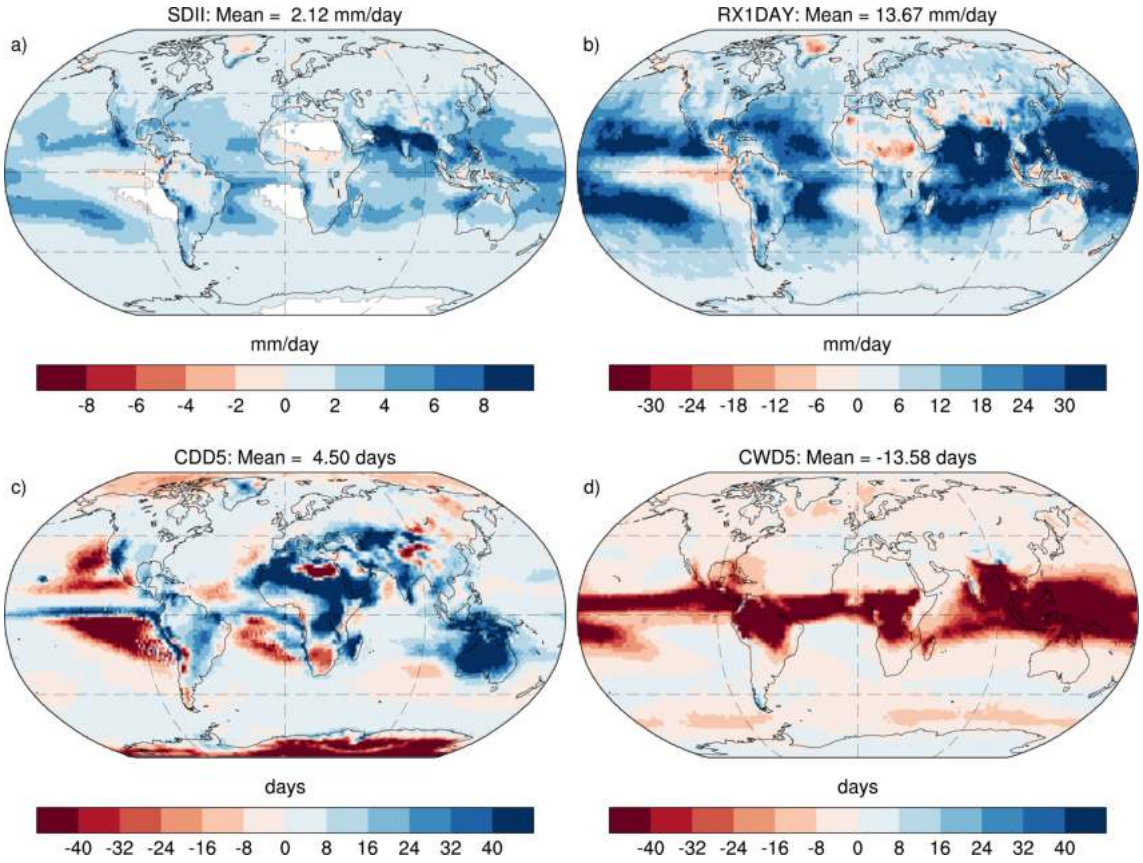

Figure 2.6: Global bias maps for the extreme indices a) SDII, b) RX1DAY, c) CDD, and d) CWD simulated by the CNRM-CM6-1 in the GMMIP experiments for the period 1979-2014 with respect to the MSWEP observations. The maps show the 10-member mean biases for each index.

Figure 2.6 portrays the present-day bias (1979-2014) in the precipitation extreme values simulated by the ensemble mean (10 members) CNRM-CM6-1 using GMMIP experiment framework (ensemble of extended atmospheric only simulations, Zhou et al. 2016) with respect to the MSWEP V1.2 observation dataset. The maps show the present-day biases for extreme indices SDII, RX1DAY, CDD and CWD which are defined in section 2.2. The analysis of the mean values of these extremes (cf. Figure A.3) shows a good general agreement and the model's ability to capture the overall pattern and average intensity of the observed extremes. There are however significant differences between the modelled and observed estimates. We note an overestimation of average and extreme precipitation intensities as indicated by the SDII and RX1DAY maps (Figure 2.6 a and b). The frequency of extreme precipitation, on the other hand, is a different story. The CWD (Figure 2.6 d) shows a deficit in the maximum number of consecutive wet days. There is also an overestimation of the total number of dry days (CDD, (Figure 2.6 c), particularly over land. As a result, the lack of precipitation in some tropical areas (land), particularly the maritime continent, shows an overabundance of moisture convergence along the continent's boundaries and a challenge for humid oceanic air masses to penetrate the continent's interior. This is in line

with the well-known shortcomings of global climate models with parameterized convection, which show difficulties to deal with inland areas where convergence from sea-breeze circulations is critical for convection initiation (Birch et al., 2015).

Taylor Diagram

The Taylor diagram (cf. Figure 2.7) provides a graphical framework for comparing or evaluating a set of models and observations/reanalyses versus a single reference dataset. The reference data can be observational (like reanalysis), or it can refer to a specific model or simulation (for model intercomparison). It is measured in terms of pattern correlation (R), centred root-mean-square-error (RMSE), and the amplitude of their variations, represented by their normalized spatial standard deviations (STD) (Taylor, 2001). The graphic illustrates how to plot three statistics showing how well a pattern matches observations on a two-dimensional graph. The pattern correlation between the models and the observational products is the angular dimension of the Taylor diagram, while the normalized spatial standard deviation is the radial dimension. The centred RMSE is based on a geometric relationship between the basic definitions of a centred root mean square error (RMSE), correlation, and standard deviation. It is a byproduct of the Taylor Diagram that the distance between a model result and the reference data on the abscissa is the centred RMSE. A data point will be on a radial arc of unity when a model has the same spatial variance as the reference data. The data point for a model will be on the abscissa if it is well correlated with the reference data. If both of these conditions are met, the RMSE will be zero, and the model data will coincide with the reference data point on the abscissa. These statistics make it simple to establish how much of a pattern's overall root mean square difference is due to variation and how much is due to poor pattern correlation. Thus, standard deviations and correlations between the values simulated by the models and those from the reanalysis are presented in the same diagram, offering a full picture of the model's ability to reproduce the different variables. It's vital to remember that all variables must be on the same grid, which may necessitate regridding (cf. section 2.4). Taylor diagrams have been employed in several parts of this work (e.g., sections 2.6, 2.7.7), particularly for model evaluations.

Taylor diagrams as shown in Figure 2.7 depict the skill of each ensemble member of CNRM-CM6-1 as well as the multi-ensemble mean and observations in capturing the global geographical distribution of various daily precipitation statistics during the recent period (1979-2014). We see that, in all the panels in Figure 2.7, the individual ensembles are tightly clustered around the ensemble mean, with high pattern correlation values ranging from 0.8 to 0.9, which means that the CNRM-CM6-1 is pretty realistic and that this good performance is not obtained by chance (i.e., not heavily dependent on internal climate variability and the choice of the ensemble member). We also see that the model compares with the MSWEP reference dataset (available over both land and ocean) almost as well as the other observational datasets. For all the indices, the ensemble mean and all individual members fall within the centred RMSE value of 0.75 despite the large

biases of Figure 2.6. Normalized standard deviation values for intensity of the extremes (SDII and RX1DAY) are more than one for the members as well as the mean, however, for the frequency of dry and wet extremes (CDD, CWD cf fig 2.7 c, d) it falls inside unity. To summarize the atmospheric part of CNRM-CM6-1 is capable of capturing the pattern of the intensity and frequency of the extremes to a decent level and the overall model performance is similar across all individual members. However, there is a large bias in the magnitude of these values as depicted by Figure 2.6.

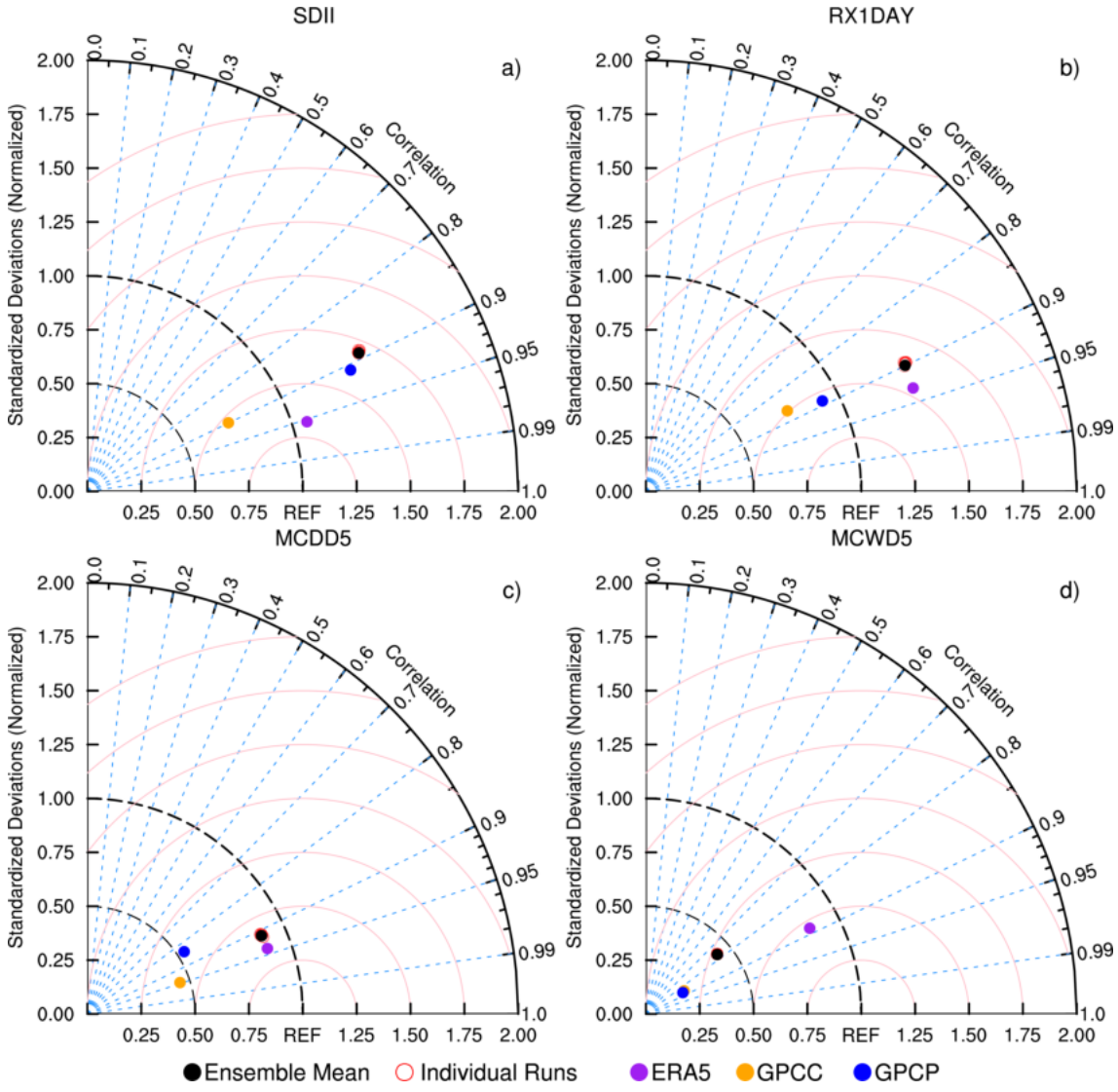

Figure 2.7: Taylor diagram illustrating the model performance of the atmospheric-only CNRM-CM6-1 experiments in simulating the extreme indices; a) SDII, b) RX1DAY, c) CDD and d) CWD for the historical period from 1979-2014. The radial axis is the normalized standard deviation while the angular axis is the centered pattern correlation. The reference data set is MSWEP (REF). The pink concentric circles show the centred RMSE. Individual ensemble members are shown in red (hollow markers) and the ensemble mean in black (solid marker). Other observational products are also marked with colours as mentioned in the legend. The periods analysed for the other observational products depend on the available data during the reference period as mentioned in Table 2.1

2.7 CMIP6 models and experiments

2.7.1 Overview

Climate models are now widely used as a key tool for understanding the climate system, its natural variations as well as its response to human perturbations (emissions of greenhouse gases and aerosols, but also possible changes in land use and land cover). Different simulations provide information on how the climate system has changed over time and what we might expect in the future. These model simulations are increasingly used as a benchmark to develop and implement climate policies, although adaptation policies also need higher resolution climate information that cannot be delivered by the current generation of GCMs.

The Coupled Model Intercomparison Project (CMIP), which began 20 years ago, has brought together a diverse set of climate models under one umbrella, allowing for coordinated model comparisons and climate change assessments on a global scale. CMIP is now in its sixth phase (CMIP6, Eyring et al. 2016), with the goal of continuing to lead the development and evaluation of climate models. It also acts as a framework for open-access climate simulations that adhere to prescribed experimental protocols, greatly expanding our understanding of climate change and related uncertainties, basically divided into three contributions: future emissions of greenhouse gases (as assessed by a small set of illustrative scenarios), model uncertainties (as assessed by a multi-model approach although CMIP models are not entirely independent since they can share common components or structural assumptions), internal variability (as assessed by multiple realizations of the same model at least for global modelling centres that have sufficient computing resources). Furthermore, an important part of CMIP is making the multi-model outputs publicly available in a standardized manner for assessment by the global climate community and users.

2.7.2 Different experiments in CMIP6

Over the course of recent decades, remarkable progress has been made in model evaluation (Randall et al., 2007; Schaller et al., 2011). Many baseline aspects of model evaluation must now be performed much more efficiently in order to allow for a systematic and rapid performance assessment of the large number of models participating in CMIP. In terms of the number of modelling groups involved, the number of future scenarios evaluated, and the number of distinct experiments undertaken, CMIP6 marks a significant increase over CMIP5.

The new CMIP6 structure consists of three major components (Eyring et al., 2016). First, a number of common experiments, the Diagnostic, Evaluation, and Characterization of Klima (DECK) experiments, and CMIP historical simulations are used to evaluate the model properties. Second, is the common standards, coordination, infrastructure, and documentation that facilitate sharing of model outputs and the characterisation of model ensembles. Third, is the implementation of a more decentralized structure based on more independent CMIP-Endorsed MIPs. Idealized "diagnostic" simulations (called DECK) in which CO_2 is increased

by 1% each year, suddenly quadrupled, or the preindustrial radiative forcings are left unaltered for long periods of time are included in the CMIP6 experiments. Historical runs (1850-2014) based on observed CO_2 concentrations and other climate forcings, as well as future emission scenarios for the twenty-first century (2015-2100) and beyond, are also considered by all modelling centres in CMIP6. Other Model Intercomparison Projects, or MIPs, have been also proposed to the global modelling community. These are more specific experiments that provide useful (sometimes process-based) assessments of climate change. This includes the Cloud Feedback Model Intercomparison Project (CFMIP, cf. chapter 3) which aims at a better understanding of cloud feedback, as well as of the role of the SST pattern effect and of the fast (mostly radiative, but also physiological) adjustment to increased CO_2 levels. Other examples are the LS3MIP project (Van den Hurk et al., 2016) dedicated to the land-atmosphere coupling or GeoMIP (Kravitz et al., 2011) that compares the effect of various types of geoengineering techniques. The diagram below (Figure 2.8) depicts the MIPs included in CMIP6.

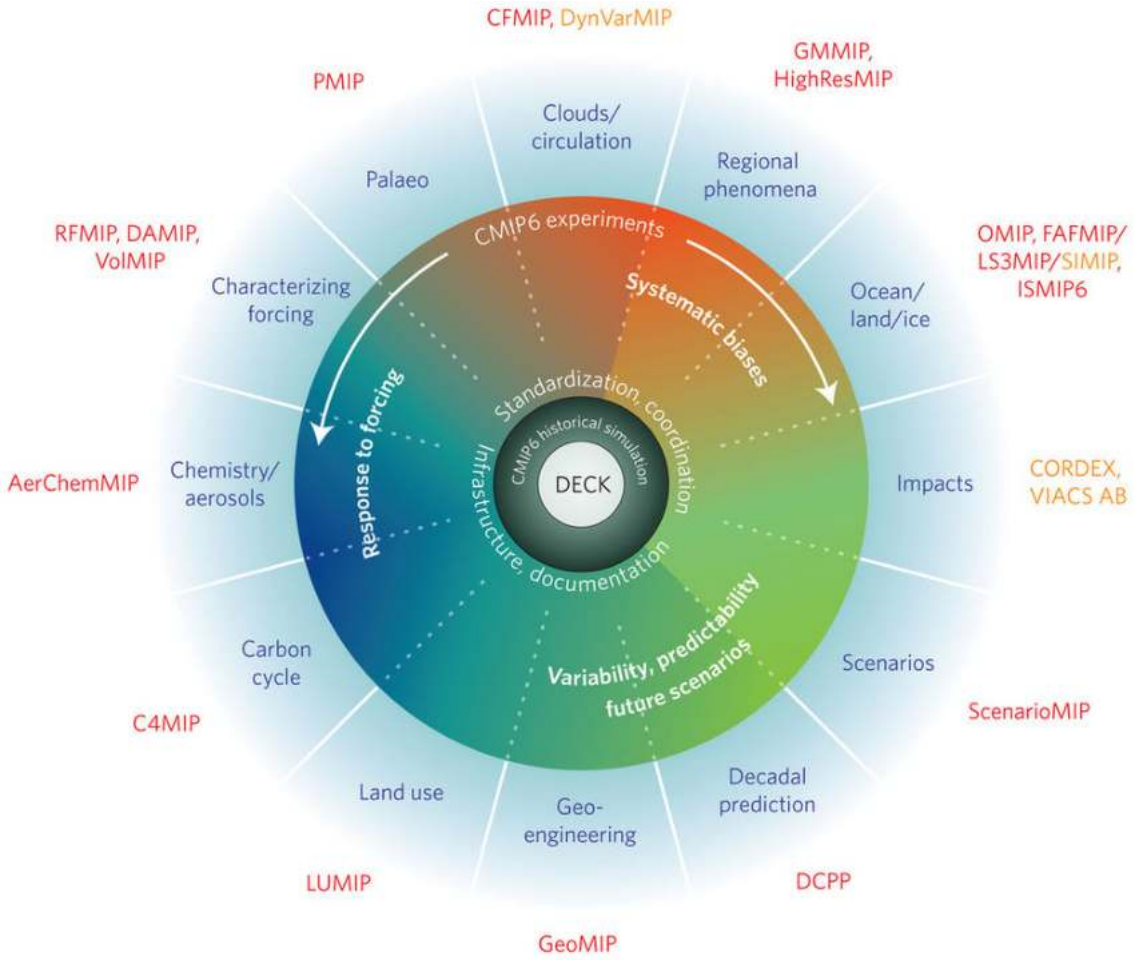

Figure 2.8: Schematic of the CMIP/CMIP6 experimental design and the 21 CMIP6-Endorsed MIPs. Source: Eyring et al. (2016)

Not all modelling groups participate in all the MIPs due to the limited computing resources they might have. The complete list of MIPs and their definition can be obtained from Eyring et al. (2016).

2.7.3 Historical simulations

Historical simulations have been conducted with most if not all CMIP6 models. Unlike the DECK experiments, they are not fully comparable from one generation of CMIP models to the next since (i) the historical period is extended from one CMIP exercise to the next, (ii) the natural (solar, volcanoes) and anthropogenic forcings (GHG, aerosols, land cover and land use) may also slightly evolve between successive CMIP exercises. In CMIP6, the historical period is from 1850 to 2014. Based on observations, these simulations are forced by changing, externally imposed forcings such as solar variability, volcanic aerosols, and changes in atmospheric composition (GHGs and aerosols) caused by human activities. The aim is to assess the models' ability to simulate the recent climate, including its variability and multidecadal trends. These simulations can also be used to see if climate model forcing and sensitivity match the observed record, allowing researchers to better constrain climate sensitivity and/or the scale of aerosol forcing. Furthermore, they, along with the control preindustrial runs, provide the baseline simulations for conducting formal detection and attribution studies (e.g., Stott et al. 2006), which aid in determining the causes of observed climate changes. Despite the fact

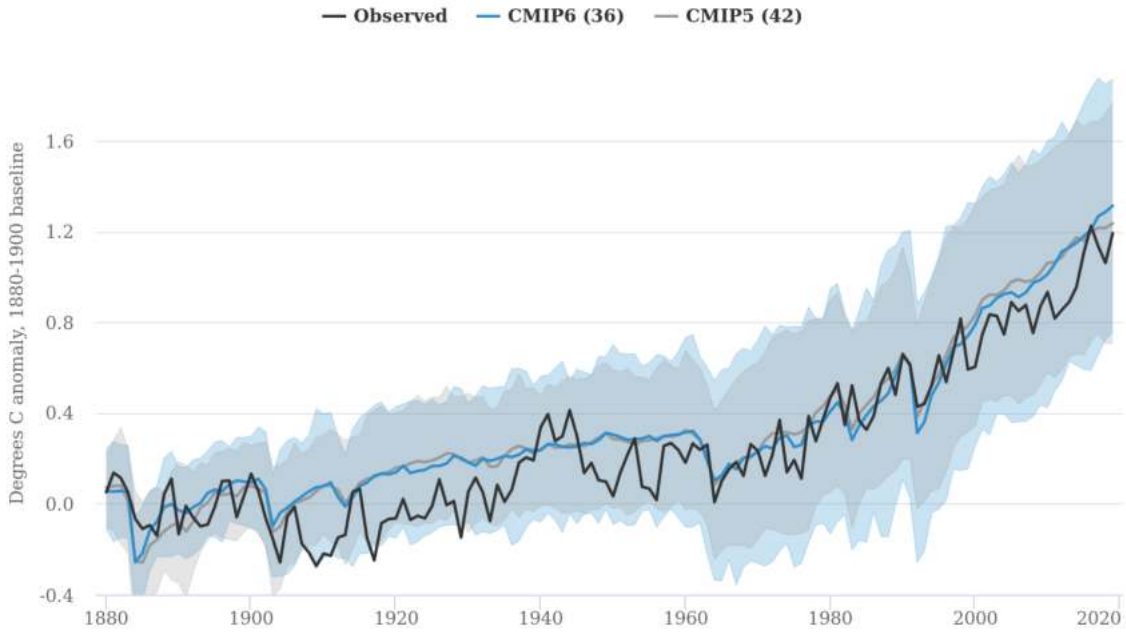

Figure 2.9: Observed temperatures compared to CMIP5 and CMIP5 hindcasts. CMIP6 model historical runs from 1850-2014 are combined with mean projections through 2019 across all available scenarios. One run is used per model. Solid lines show the multi-model mean, while the shaded areas represent the two-sigma range. Values in brackets reflect the number of models used in the analysis. Source: CarbonBrief

that there are dozens of different climate variables, the climate modelling community focuses on global surface temperature as one of the most important variables. The near-surface air temperature gives us a notion of how warm the lower atmosphere has become, as well as the overall picture of the atmosphere's energy budget. When models accurately represent past changes (historical simulations), it gives users confidence that they will accurately represent future changes as well. The graph below (figure 2.9) compares global surface temperature from historical

simulations of the CMIP6 (blue) and CMIP5 (grey) climate models to observations from the NASA GISTEMP dataset. The lines depict the average of 42 CMIP5 and 36 CMIP6 models, while the shaded area depicts the 95% confidence interval of model runs which shows the large uncertainty range associated with the models.

Climate models cannot resolve all of the small-scale physics of the Earth's climate due to their limited spatial resolution. To accurately simulate small-scale processes, such as cloud formation or cloud-aerosol interactions, models include parameterization methods (Anthes, 1977; Pitman, 2003), which provide an empirical surrogate for these processes. The process of determining these characteristics, which are sometimes poorly known or very uncertain, is known as model tuning. While most modellers avoid explicitly adjusting their models to account for past temperature changes, significant mismatches may force them to scramble for a solution. Only a few CMIP6 modelling groups have tuned certain parameters to better match historical temperatures, whereas the bulk do not and only use present-day and preindustrial climatological constraints. As a result, there is a large inter-model spread in terms of recreating past and future climates, a part of this owing to differences in the physical representation of atmospheric process across the models, known as model uncertainty.

Additional uncertainty can also arise from the limited sample size (lack of multiple member ensembles) also called uncertainty due to the internal variability (cf. Chapter 4). This intrinsic variability of the climate system arises from non-linear processes in the atmospheric and oceanic circulation, but also from interactions between the multiple components of the climate system. Emblematic examples include the El Nino-Southern Oscillation (ENSO) in the tropics or, the Atlantic Multidecadal Variability (AMV) in the North Atlantic. Beyond the forced component of the climate evolution, one MIP (DCPP, Decadal Climate Prediction Project Boer et al. 2016) aims at constraining the unforced component (i.e., internal climate variability) by initializing the ocean state and running decadal to multi-decadal hindcasts and forecasts, which show increasing skill (and improved skill compared to uninitialized historical simulations) in predicting surface temperature, but more difficulties to improve the simulation of precipitation over land (Douville et al., 2021).

2.7.4 SSP Scenarios

This set of standard simulations of future climate enables the comparison of the results from different CMIP6 models. This aids researchers in piecing together images of climate change in the near (2021-2040) to long-term (2081-2100 and beyond) future, assessing the most likely responses, but also quantifying related uncertainties. ScenarioMIP (O'Neill et al., 2016) includes the scenario runs and is, therefore, one of the most popular sets of CMIP6 simulations. To estimate future climate, all models employ a common set of future GHG concentrations, aerosols, and other radiative forcings. For CMIP6, a new set of illustrative shared socioeconomic pathways (SSP) have been developed and associated with contrasted emission scenarios ranging from low (e.g., SSP1-2.6) to high (e.g., SSP5-8.5) emissions of greenhouse gases. When compared to their predecessors, Representative Concentration Pathways (RCPs, Van Vuuren et al. 2011), in CMIP5, they take into

account many socioeconomic elements in addition to the radiative forcings. The IPCC AR5 report featured four RCPs, each of which looked at different scenarios for future greenhouse gas emissions. These RCP2.6, RCP4.5, RCP6.0, and RCP8.5 scenarios have been updated in CMIP6. The new scenarios include the SSP1-2.6, SSP2-4.5, SSP4-6.0, and SSP5-8.5 illustrative pathways, and they result in similar 2100 radiative forcing values as their predecessors in AR5.

A variety of new scenarios are also being employed in CMIP6 to enable scientists a larger range of possibilities to simulate. These scenarios are depicted in the Figure 2.10, which displays the estimated annual CO_2 and other GHG emissions (top panel) for each scenario until 2100. The Figure (bottom panel) also illustrates the change in global surface temperature caused by various emissions for each scenario.

A broader study of various baseline "no climate policy" outcomes is one of the primary improvements to CMIP6 scenarios. Only one very high baseline scenario (RCP8.5) and one relatively modest mitigation scenario (RCP6.0) commensurate with baseline outcomes were included in the previous generation of climate models featured in CMIP5. Despite being a worst-case scenario among possible no-policy outcomes, much of the ensuing research focused on RCP8.5 as the only no-policy baseline, often referring to it as "business as usual." SSP3-7.0, a new scenario added to CMIP6, falls in the middle of the spectrum of baseline outcomes generated by models. Researchers can now investigate worst-case (SSP5-8.5), middle-of-the-road (SSP3-7.0), and more optimistic (SSP4-6.0) possibilities while projecting how the planet will warm if no climate policies are implemented. SSP4-3.4 is a new scenario that attempts to bridge the gap between scenarios that restrict warming to below 2 degrees Celsius (RCP2.6 / SSP1-2.6) and approximately 3 degrees Celsius (RCP4.5 / SSP2-4.5) by 2100. It will enable scientists in assessing the effects of warming if countries reduce emissions rapidly but fail to offset them quickly enough to keep temperatures below 2 degrees Celsius. SSP5-3.4OS is an overshoot scenario (OS) in which emissions maintain a worst-case SSP5-8.5 trajectory until 2040, after which they quickly drop with extensive late-century use of negative emissions. Finally, SSP1-1.9 is a scenario that aims to keep warming below 1.5 degrees Celsius over pre-industrial levels by 2100. It was included following the Paris Agreement when countries pledged to undertake efforts to keep global warming to 1.5°C. Energy models and basic climate models built to keep warming to 1.5°C played a key part in the IPCC's special report on 1.5°C, which was issued in 2018. With these new CMIP6 scenarios, full climate models will be able to examine climate change and its consequences at 1.5°C warming. New scenarios in CMIP6 result in 2100 forcing, similar to the RCP scenarios in CMIP5. Regardless of the fact that their end-of-century forcing is identical, their emission trajectories and mix of CO_2 and non-CO_2 emissions differ.

2.7.5 CFMIP experiments

The Cloud Feedback Model Intercomparison Project (CFMIP) has been a part of the CMIP since its third phase (CMIP3) and is one of the important MIPs in the CMIP6 framework. CFMIP experiments are now in their third phase (CFMIP3).

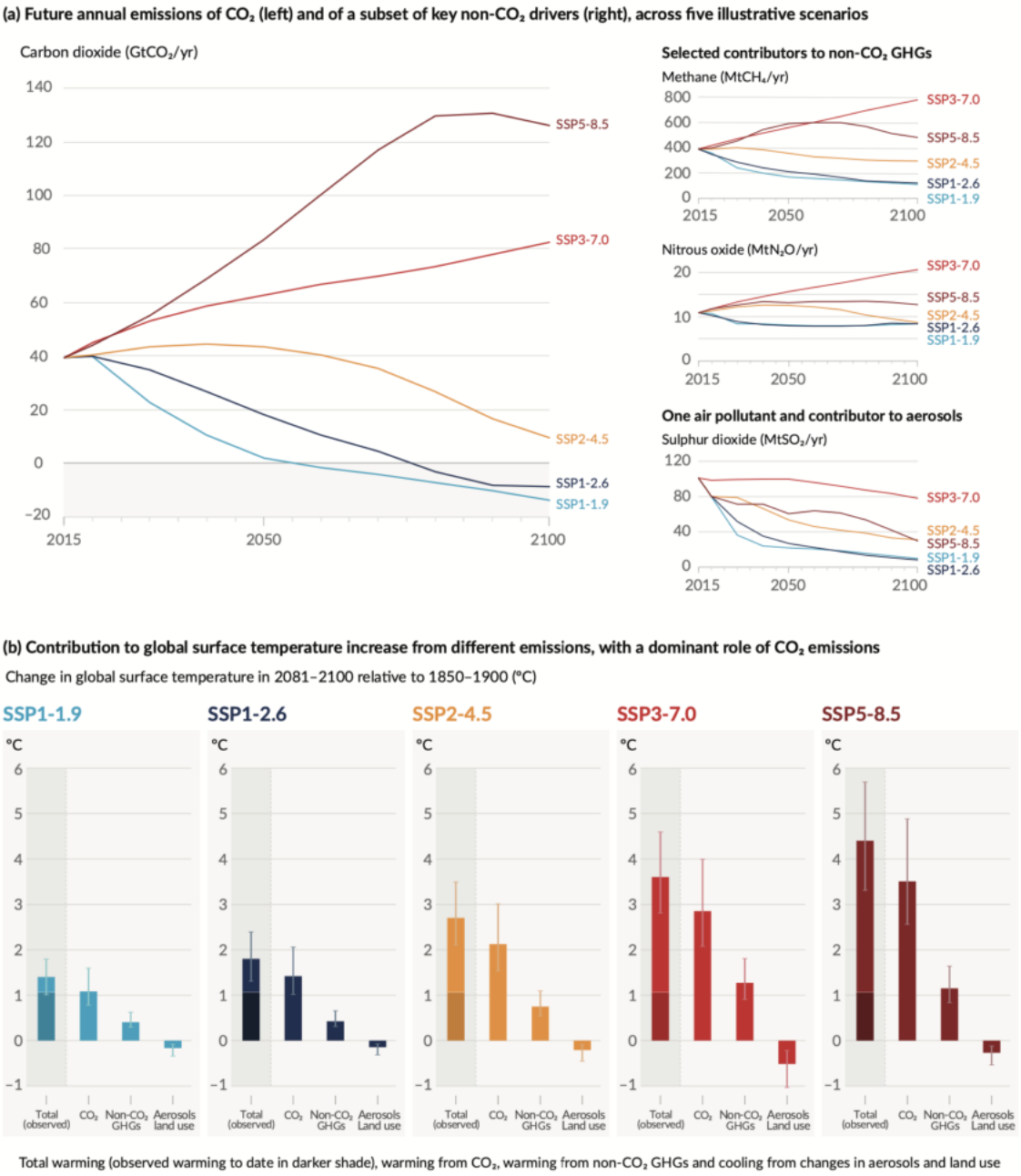

Figure 2.10: Future anthropogenic emissions of key drivers of climate change and warming contributions by groups of drivers for the five illustrative scenarios used in this report. The five scenarios are SSP1-1.9, SSP1-2.6, SSP2-4.5, SSP3-7.0 and SSP5-8.5. Source, Masson-Delmotte et al. (2021a); cf. Figure SPM.4 from the report for detailed caption

The major objective of CFMIP is to improve the understanding of cloud-climate feedback mechanisms and evaluation of cloud processes and cloud feedback in climate models. Other aspects of the climate response, such as changes in circulation, regional-scale precipitation, and non-linear change, can be better understood using the CFMIP experimental hierarchy and process diagnostics. CFMIP contributes to CMIP6 by coordinating a hierarchy of targeted experiments with cloud-related model outputs. How does the Earth system respond to forcing? and What are the origins and consequences of systematic model biases? are two of the primary questions CFMIP addresses within the CMIP6 distribution. It also supports the activities of the World Climate Research Program (WCRP) Grand Challenge

on Clouds, Circulation and Climate Sensitivity. Groups of experiments are divided into Tiers 1 and 2 using the CMIP6 design process, which is inspired by scientific questions CFMIP addresses (Eyring et al., 2016). All Tier 1 experiments must be completed and released through the CMIP6 shared data portal and this is a prerequisite for modelling organizations participating in the CFMIP3/CMIP6 model intercomparison. Tier 2 experiments are optional and address more specific scientific questions which are discussed in Webb et al. (2017). The modelling groups have the freedom to perform any subset of Tier 2 experiments. All the CFMIP3/CMIP6 experiments are summarized in Figure A.6 (adapted from Webb et al. 2017). This thesis has utilised different CFMIP-tier 2 experiments, which are detailed in chapter 3. We have used the tier 2 experiments to investigate the response of the mean and extreme (wet and dry) precipitation to the uniform warming of the SST, increase in the CO_2 concentrations, and also the contribution from the SST patterns.

2.7.6 Climate sensitivity of models

Equilibrium (ECS) and transient (TCR) climate sensitivities to a given abrupt or gradual increase in CO_2 concentration compared to preindustrial levels are key metrics that sit at the heart of climate change science. They are generally intrinsic properties of GCMs that arise from physical and biogeochemical simulated processes, rather than being intentionally tuned by modellers (Flynn and Mauritsen, 2020). These climate sensitivities are typically expressed in terms of the global mean temperature that would follow if atmospheric carbon dioxide concentrations were abruptly (abrupt-4xCO2 experiment) or gradually (1pctCO2 experiment) doubled compared to preindustrial times (piControl experiment). The ECS is therefore an estimate of global warming at doubling CO_2 levels in the long run, while, TCR is the mean global warming anticipated to occur around the time of CO_2 doubling in climate simulations with atmospheric CO_2 concentrations increasing at 1% per year. TCR values are less than ECS values across a suite of models due to the deep-ocean heat uptake leading to a lag in the response of global temperature to increasing CO_2 concentration (Hansen et al., 1985). Moreover, the ratio of TCR over ECS tends to decrease as ECS increases and is influenced by the spatial pattern of the ocean warming (Armour, 2017).

ECS and TCR estimate only need three basic idealized experiments (the so-called DECK experiments: piControl, abrupt-4xCO2 and 1pctCP2) that can be reconducted between successive generations of global climate models. The range of ECS and TCR still remains uncertain even after decades of advancement in climate science. The previous IPCC assessment reports have quoted the likely range of ECS from 1.5 to 4.5 K, with an exception in the fourth assessment report which moved the likely lower range temporarily to 2K. Similarly, the IPCC AR5 gives a plausible range of TCR of 1 to 2.5K based on multiple lines of evidence. Nevertheless, the CMIP6 models have a general upward drift towards higher climate sensitivities with more than one-third of the models estimated to have ECS values over 4.5K (Forster et al., 2020) and a few with TCR values over 2.5K (Nijsse et al., 2020). Also, a quarter of the CMIP6 models have a higher sensitivity than any of the models in CMIP5. The Paris climate targets will be far

more difficult to accomplish if the real climate system is equally sensitive (Tanaka and O'Neill, 2018). A comprehensive investigation of these two sensitivity metrics and how they have changed with successive generations of the climate models to date (CMIP6) is summarised in (Meehl et al., 2020). Figure 2.11 depicts the IPCC AR5 likely ECS range (black bar), the range and individual values for CMIP5 models (grey bar; black dots), and the range and values for CMIP6 models that are currently available (grey bar; black dots) (blue bar; black dots).

Beyond climate sensitivity, other metrics have been proposed to depict the response of the global water cycle (Douville et al., 2021). Hydrological sensitivity (HS) is among such metrics, which represents the rate of increase in global mean surface evaporation and precipitation per degree of warming in a climate change scenario (Webb et al., 2018). HS simply denotes the ratio of the global-mean precipitation changes to the corresponding global-mean surface temperature changes (Fläschner et al., 2016). It can be estimated as differences between the perturbed and control mean states (eg., Held and Soden 2006; Bala et al. 2008; Previdi 2010; Pendergrass and Hartmann 2014) or using a linear regression approach based on the abrupt-4xCO2 experiments (Fläschner et al., 2016). Definition of HS is important for understanding water cycle changes since it depicts the forcing-independent response of global precipitation to any change in global mean surface temperature. Studies like Allen and Ingram (2002), Lambert and Webb (2008), Andrews et al. (2009) incorporate the exception that precipitation not only changes proportionally with surface temperature, but also adjusts directly to radiative forcing agents, whereas, other studies like Mitchell et al. (1987), Andrews et al. (2010), Fläschner et al. (2016) refer HS specifically to the temperature-dependent increase in global precipitation with surface warming, excluding the effects of radiative forcing agents.

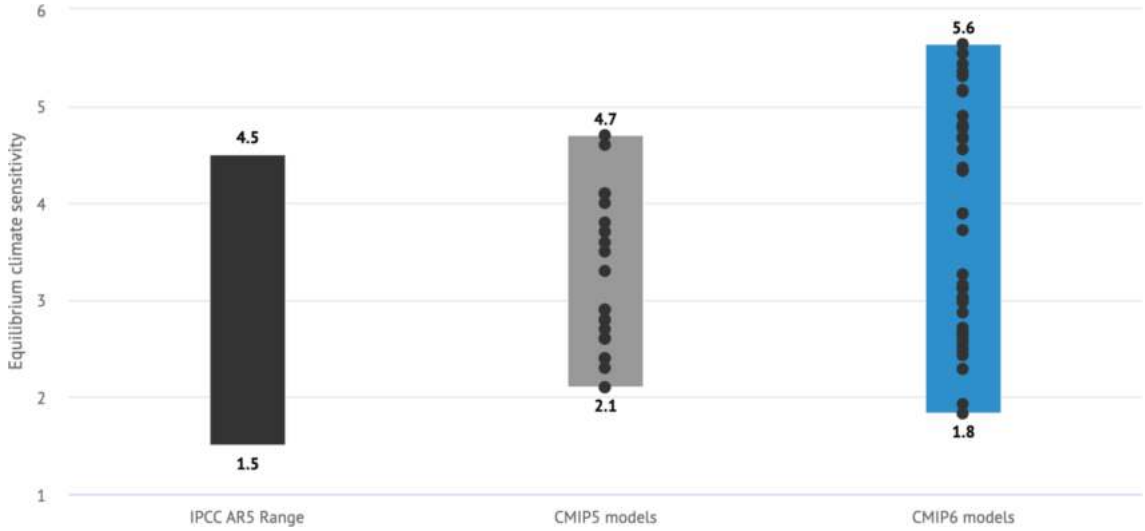

Figure 2.11: Likely ECS range (e.g., with an estimated 66% chance of occurring) from the IPCC AR5 (black bar), CMIP5 model ECS values (grey), and CMIP6 model ECS values (blue). Source: CarbonBrief

Fläschner et al. (2016) has thus introduced a formal terminology analogous to the ECS framework to facilitate the comparison of global precipitation response estimates. According to this study, the slope of temperature-dependent precipitation change, when discarding rapid precipitation changes (adjustment) of the

atmosphere to radiative forcings, is referred to as hydrological sensitivity, while the slope of the total precipitation response to a gradual increase in CO_2 is the apparent hydrological sensitivity. The apparent HS encompasses the contribution from both a fast atmospheric adjustment to the prescribed radiative forcing and slower precipitation response to the induced surface ocean warming. According to the AR6 WGI, the apparent hydrologic sensitivity exhibits a threefold spread (1-3%/K) across the CMIP6 climate models. The term equilibrium hydrological sensitivity was also introduced as the equilibrium change of precipitation due to a doubling of CO_2. Pendergrass (2020) has estimated the multi-model mean HS from the CMIP6 ensemble as 2.5%/K (ranging from 2.1-3.1%/K), very close to the former CMIP5 ensemble mean (2.6%/K). HS is not strongly related to ECS across both CMIP5 and CMIP6 global climate models (Fläschner et al., 2016; Pendergrass, 2020), and other physical processes may thus control the simulated precipitation response.

2.7.7 Taylor diagram — A synthetic tool to assess the model skill

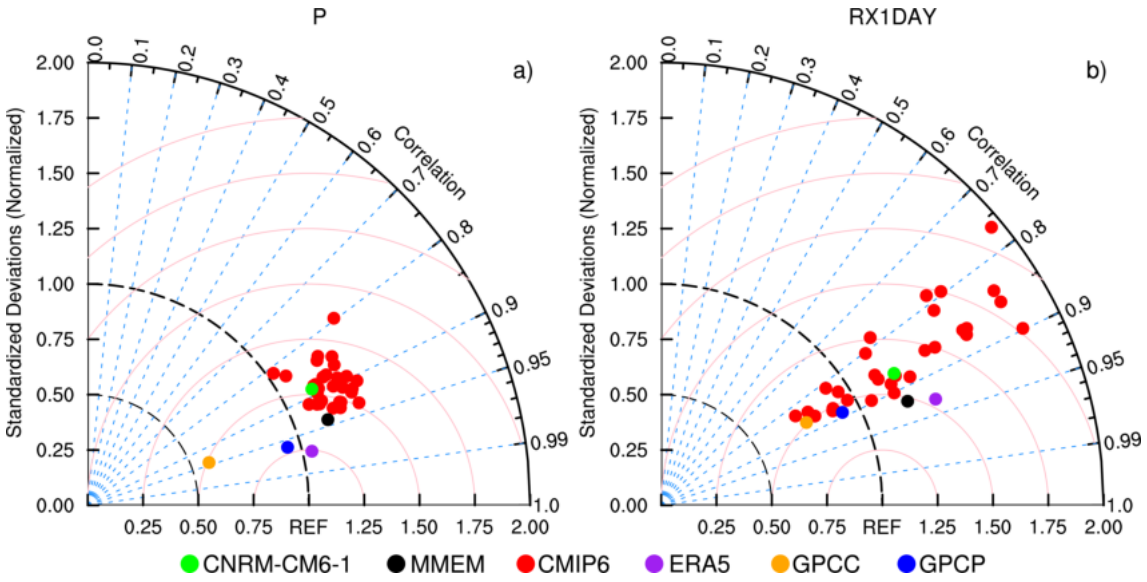

Figure 2.12: Taylor diagram measuring the model performance of each CMIP model (33 here) in simulating the a) annual mean precipitation (P) and b) extremes (RX1DAY) for the historical period from 1979-2014. The radial axis is the normalized standard deviation while the angular axis is the centered pattern correlation. The reference data set is MSWEP (REF). The pink concentric circles show the centred RMSE. Individual models are shown in red and the multi-model ensemble mean is in black. CNRM-CM6-1 is highlighted using green and other observational products are also marked with colours as mentioned in the legend.

The Taylor diagrams (Figure 2.12) show the statistical overview of each CMIP6 model's performance in capturing the mean and extreme precipitation values, as well as the multi-model mean and observational products. The models are tightly clustered for mean precipitation values (Figure 2.12 a), with the spatial standard deviation (radial distance from the origin) of all models being somewhat higher than the reference data. In addition, all models have a high pattern correlation between 0.8 to 0.95, however, some models are at the lower end of this range. Except for one model, the centred RMSE is less than 0.75; nonetheless, the outlier does not surpass unity. However, for extreme precipitation (Figure 2.12 b), the models exhibit wider ranges of Taylor skills than they do for mean

precipitation and are not as densely clustered in the Taylor diagrams. The pattern correlation ranges from 0.75 to 90 with most of the models falling near the upper end of this range. Except for four outliers with centred RMSE values exceeding unity, all models have centred RMSEs of the annual RX1DAY values between 0.5 and 1.0.

The Taylor skills for both the mean and extreme precipitation is not degraded, though the skills for mean precipitation are a bit more than that for the extremes. Needless to say, the spread is large for the extremes, largely due to the considerable cross-model differences in the amplitude of the spatial patterns, with some models substantially underestimating pattern amplitude while others overestimating it. The pattern correlation and Taylor skill for the multi-model averages are better than any single model for both mean and extreme precipitation. The CMIP6 models' overall performance in simulating mean and extreme precipitation is adequate.

2.8 Synthesis

A growing set of global observational datasets, reanalyses and climate simulations is available to understand, assess and quantify climate change and its impact on recent and future precipitation extremes. With the expansion in the number of different products (e.g., Roca et al. 2019), the evaluation of climate model outputs is now being done more carefully, given the potential for observation errors or for compensating errors in global climate models (e.g., too frequent and too light rainy events). We have employed a small fraction of the most reliable observational datasets available for the evaluation of the CMIP6 models we used in this thesis, focusing not only on seasonal and annual mean precipitation but also on the full distribution of daily precipitation rates including extremes. One of the important aspects we came across is the difference in the evaluation of the models based on the reference dataset used. We can see that for some variables, the spread across datasets is as large as the spread across models. This raises the question of which dataset is the most suitable to evaluate the models, depending on spatial and temporal scales, selected domains, and the focus on present-day climatology versus historical variations (highly sensitive to potential inhomogeneities in the timeseries).

Climate models have improved significantly in several respects across successive generations of CMIP intercomparisons (Brunner et al., 2022). The majority of the CMIP6 models are capable of reasonably simulating mean and extreme precipitation. Even at a standard resolution, CNRM-CM6-1 performs well in comparison to the other CMIP6 models. There are significant limitations when using climate models to predict future changes. One example is the models' inability to resolve small-scale atmospheric features. The majority of climate models available today are coarse resolution models, which necessitate the use of various parameterization schemes to resolve and quantify small-scale phenomena occurring within a grid. Because models depict physical processes differently, there is a large degree of spread when computing the mean and extreme precipitation, which we refer to as model uncertainties. Another source of systematic error

or deviations from realistic climatology values can be the irreducible uncertainty caused by internal variability. This is related to the fact that we don't have enough samples when utilizing climate models as most of them do not provide multiple members to analyse the present and the future simulations. While investigating future changes in the mean and extreme precipitation, this results in a deficit of sampling and a significant source of uncertainty, beyond the choice of the CMIP6 model and/or of the illustrative SSP scenario.

Despite their limited resolution and their parametric and structural uncertainties, global climate models are employed as first-hand tools to project future climate. The latest generation of CMIP6 models has been evaluated and shown to be capable of capturing the overall present-day patterns of mean and extreme precipitation, even if they are over or under-estimated at regional scales. We can see that the majority of the CMIP6 models can generate geographical patterns with correlations ranging from 0.8 to 0.95, with the majority of the models falling in the middle of this range. The new set of scenario simulations from the CMIP6 also enables us to understand and investigate a wide range of plausible futures, with varying CO_2 concentration and other radiative forcings.

We are now equipped with different tools and methods to understand and quantify the projected changes in daily precipitation extremes, thanks to the availability of a growing number of global climate models. Regional climate models, including convection-permitting models, are also very useful for this purpose but are beyond the scope of our study. The methods to define extreme events in a changing climate have also advanced. We will use simple ETCCDI indices in our study of extremes, which enable us to compare our results with a large volume of previous studies. The use of a state-of-the-art non-stationary GEV technique will enable us to assess changes in the intensity of rare extreme events based on the 20-year return values of the block maxima RX1DAY. We will also use a simpler stationary GEV analysis to investigate the response of extreme precipitation to different global warming levels (GWLs) or CO_2 concentrations.

Despite the advances in available observations, global climate models, and statistical tools, we still face multiple difficulties in conducting such quantitative analyses. Models and observations are available at different resolutions and must be interpolated onto a common grid before evaluation and comparison, which may lead to a loss of information and smooth the results of the highest-resolution models. Higher-resolution projections can be obtained with dynamical or statistical downscaling techniques that are however beyond the scope of the present study. Another related issue is the limited model's ability to capture the present-day distribution of daily precipitation intensities, including extremes, which may also affect their ability to project precipitation changes. While various bias correction or bias adjustment techniques have been proposed to circumvent this obstacle, they all have shortcomings (Maraun et al., 2017) and will be only briefly discussed in our manuscript. Finally, internal climate variability remains a key contribution to the future climate in the near term, especially for extremes, and may need the use of large ensembles that are still not systematically available for all CMIP6 models. This important limitation will be further discussed in Chapter 4, based on a relatively large ensemble available from one illustrative CMIP6 model.

All intelligent thoughts have already been thought;
what is necessary is only to try to think them again.

— **Johann Wolfgang von Goethe**

3

Fast adjustment versus slow SST-mediated response

The precipitation response to escalating GHG concentrations is now well established to be a combination of a fast atmospheric adjustment to the radiative forcing and a slower response mediated by ocean surface warming (Allen and Ingram, 2002; Andrews et al., 2010; Allan et al., 2020). The temperature-dependent response, or hydrological sensitivity, is about 2-3%/°C and is substantially less forcing-dependent than the fast adjustment (Samset et al., 2016; Myhre et al., 2018). The fast adjustment accounts for a major fraction of the change in tropical precipitation and partly suppresses the global mean precipitation response to increasing SST (Bony et al., 2013). This chapter addresses the response of not only mean but also extreme precipitation to an abrupt quadrupling of atmospheric CO_2 forcing. The analysis is based on dedicated atmospheric-only experiments, first with the global climate model CNRM-CM6-1, then with a few other AGCMs that have also contributed to this component of the Cloud Feedbacks Model Intercomparison Project (CFMIP, cf. sections 2.7.5 in chapter 2 and 3.1). Most of the content discussed in this chapter is adapted from the from Douville and John (2021), with however a stronger focus on precipitation extremes and a preliminary assessment of the model-dependence of our key findings.

3.1 The CFMIP experiment design

As briefly discussed in Chapter 2 (section 2.7.5), The primary objective of the Cloud Feedbacks Model Intercomparison Project (CFMIP) is to improve our understanding of cloud-climate feedback mechanisms (Webb et al., 2017). However, the CFMIP approach is also increasingly being used to explore other aspects of climate change, such as the understanding of changes in large-scale atmospheric circulation and regional precipitation. In particular, original atmosphere-only ex-

periments have been proposed to assess how regional precipitation responses and their uncertainties in coupled global climate models arise from the combination of different aspects of CO_2 forcing and sea surface temperature (SST) warming. A pilot study (Chadwick et al., 2017) was first realized and suggested that the pattern of the non-uniform SST warming is the dominant cause of annual mean precipitation change over the tropical oceans but also contributes to inter-model spread over tropical land regions. The results also revealed that the so-called physiological CO_2 effect (e.g., the effect of atmospheric CO_2 on plant transpiration and photosynthesis) can be the dominant contribution to annual precipitation changes over the tropical rainforests. Yet, limited attention has been paid so far to daily precipitation intensities.

Here, the focus is on the distribution of daily precipitation rates, including extremes. The next section highlights the main results obtained with the ARPEGE-Climat 6.3 atmospheric general circulation model (AGCM) (already described in Chapter 2), which is the atmospheric component of the CNRM-CM6-1 coupled model that has contributed to the sixth phase of the Coupled Model Intercomparison Project (CMIP6). It was highlighted in chapter 2, section 2.6 that this model has been significantly improved compared to its former version (Roehrig et al., 2020) and shows a much more realistic simulation of daily precipitation intensities, with no drizzle syndrome (i.e., too many and too light rainy events) in contrast to most global climate models (Tan et al., 2018). The improved precipitation distribution of ARPEGE-Climat makes it a good candidate to assess changes in daily precipitation to fast adjustment to increasing CO_2 levels versus the slow SST-mediated response (Section 3.2). In addition, a comparison of the results from ARPEGE-Climat with those of other AGCMs participating in CFMIP is included in Section 3.4.

Name of experiment	Monthly mean annually varying SST and SIC boundary conditions	CO_2 forcing
piSST	Years 111-140 of piControl	Preindustrial (1xCO2)
piSST-pxK	As piSST + uniform SST anomaly computed as the climatological global mean difference between years 111-140 of abrupt-4xCO2 and piControl	preindustrial
a4SSTice	Years 111-140 of abrupt-4xCO2	preindustrial
a4SSTice-4xCO2	As a4SSTice	4xCO2 seen by radiation and vegetation

Table 3.1: Summary of the CFMIP atmosphere-only timeslice experiments conducted with ARPEGE-Climat 6.3. All experiments are 30-year integrations after spin-up except amip and amip-a4SST-4xCO2 (36-year long integrations after spin-up)

The CFMIP experiment design is summarized in Table 3.1. The first pair of time-slice simulations, piSST and a4SSTice-4xCO2, aims at replicating the piControl and abrupt-4xCO2 coupled experiments. This is done by prescribing the same atmospheric CO_2 concentrations but also monthly mean annually varying oceanic boundary conditions derived from the SST and sea-ice concentration (SIC) simulated from year 111 to 500 in piControl and abrupt-4xCO2 respectively. Note that this is a much more extended period than the default simulation length (30 years) suggested in CFMIP. Such an extension of the CFMIP simulations was motivated by the analysis of daily precipitation statistics, including wet and dry extremes. Since the coupled model is still not fully at equilibrium after 500 years

of abrupt-4xCO2, a linear trend was removed from all "warm climate" simulations from years 111 to 500 in order to avoid slight inconsistencies with CFMIP results usually shown for years 111 to 140 only.

3.1.1 Coupled vs. Atmospheric only experiments

Despite the lack of coupling, the atmosphere-only experiments capture the annual mean precipitation changes simulated by CNRM-CM6-1 (Figure 3.1 a, b). The geographical pattern of the annual mean precipitation response to abrupt-4xCO2 is well reproduced by the atmosphere-only configuration of CNRM-CM6-1, as revealed by the high spatial anomaly correlation coefficient (ACC=0.97) between the patterns found in the coupled and atmosphere-only configurations. This pattern is broadly consistent with the results of the previous-generation models (e.g., Muller and O'Gorman 2011). It shows significant positive anomalies over the ITCZ and in the high latitudes, but significant negative anomalies in the subtropics. Some features, such as the response of regional monsoons in the tropics, are likely to be model-dependent and can be better understood based on complementary atmosphere-only simulations. Globally averaged and although the model is still not at full equilibrium after 390 years of simulation, the annual mean precipitation increases by 0.3 mm/day after an abrupt quadrupling of atmospheric CO_2. Such a model response corresponds to a global hydrological sensitivity of 2.3%/°C, within the 2-3%/°C range of the previous generation global climate models.

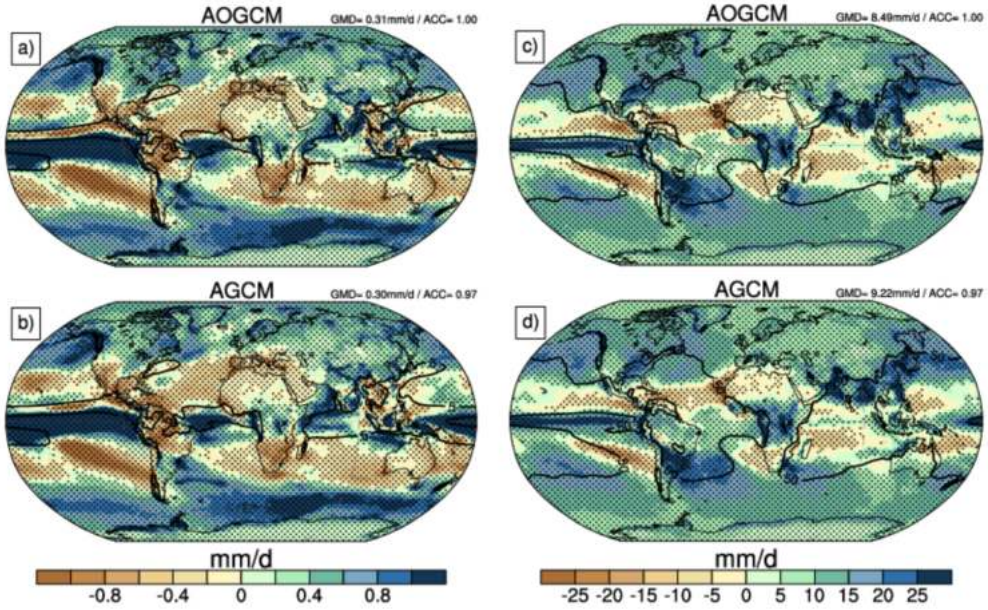

Figure 3.1: Year 111-500 annual mean response to abrupt-4xCO2 of annual mean precipitation (mm/day, left panels) and annual maximum daily precipitation intensity (RX1DAY in mm/day, right panels), as simulated either by CNRM-CM6-1 (panels a,c) or in the piSST and a4SSTice-4xCO2 atmosphere-only experiments (panels b,d). Stippling highlights areas where the differences are significant at the 5% level. GMD denotes the global mean response and ACC denotes the spatial pattern correlation with the coupled model response shown in the upper panel. A single isoline of the control (preindustrial) climatology is shown as a black solid line in each panel, corresponding to 5 mm/day in panels a,b and to 50 mm/day in panels c,d.

The ARPEGE-Climat 6.3 AGCM ability to capture the CNRM-CM6-1 response

to an abrupt quadrupling of CO_2 has been also verified for the daily statistics (Figure 3.1) which are used in the continuation of the study. The sensitivity of extreme precipitation to ocean-atmosphere coupling may depend on the details of the experimental design and deserves careful verification (e.g., Fischer et al. 2018). As for the annual mean precipitation, our atmosphere-only simulations reproduce accurately the coupled model response of the annual maximum of daily precipitation intensity (RX1DAY), both in terms of magnitude and geographical distribution (Figure 3.1 c, d). Note that the SST boundary conditions of ARPEGE-Climat are prescribed on a daily basis, but that the day-to-day SST variability is very weak since daily SSTs are interpolated (conservatively) from the monthly mean SSTs derived from CNRM-CM6-1. The lack of realistic intraseasonal SST variability does not appear to be a major obstacle to simulating the response of extreme rainfall. A small impact of ocean-atmosphere coupling appears over the tropical ocean, with annual maximum daily intensities slightly stronger in the AGCM. This effect is consistent with our understanding of the high-frequency SST feedback but is only slightly enhanced in a warmer climate. The net effect on the response of RX1DAY to abrupt-4xCO2 is therefore weak compared to other potential sources of uncertainty.

3.1.2 Decomposition of total response

The study utilises CFMIP experiments that were extended to 390-year integrations rather than their standard time frame. Various combinations of the different experiments can be used in splitting the atmospheric response to abrupt-4xCO2 into separate responses to different aspects of CO_2 forcing and related ocean warming (uniform SST warming, patterned SST change, sea ice change, radiative and physiological CO_2 effects, cf. Table 3.2). The latter effects can be diagnosed by driving the AGCM with preindustrial SST boundary conditions, but a quadrupling of the atmospheric CO_2 concentration. This CO_2 increase can be seen by either the radiative parameters or the vegetation scheme, to distinguish the radiative versus physiological CO_2 effect.

Component	**Calculation**
All forcings	a4SSTice-4xCO2 - piSST
Uniform SST warming	piSST-pxK - piSST
SST anomaly pattern and SIC change	a4SSTice - piSST-pxK
Radiative and physiological CO_2 effects	a4SSTice-4xCO2 - a4SSTice

Table 3.2: Calculation of the different components of the CNRM-CM6-1 coupled model response to abrupt-4xCO2 based on CFMIP atmosphere-only experiments.

The total response to an abrupt quadrupling of CO_2 concentration can be first decomposed as follows:

$$\begin{aligned} a4SSTice\text{-}4xCO2 - piSST = &(a4SSTice\text{-}4xCO2 - a4SSTice) \\ &+ (a4SSTice - piSST\text{-}pxK) \\ &+ (piSST\text{-}pxK - piSST) \end{aligned} \tag{3.1}$$

where the three right-hand terms represent the fast direct (radiative and physiological) CO_2 effect, the SST anomaly pattern and SIC effects, and the uniform

SST warming effect respectively.

Table 3.2 summarizes how each component of the total response to abrupt-4xCO2 is calculated. As in Figure 3.1 showing the total model response, the statistical significance of the different contributions will be assessed using a two-sided t-test at the 5% level (Wilks, 2016). Such a method adjusts the p values for multiple testing and, thereby, avoids overconfidence in the statistical significance of the results. It does not make here a significant difference with a basic t-test given the large sampling of our extended CFMIP experiments.

3.2 Changes in daily precipitation statistics

3.2.1 Response of Annual mean precipitation

As discussed in section 3.1.2 (cf. Eq 3.1), the total response of the precipitation (mean as well as extreme) can be decomposed as the sum of the contributions from fast direct CO_2 effect, slow uniform SST warming effect and SST anomaly pattern and SIC effects. Figure 3.2 shows the Equation (3.1) decomposition of the annual mean precipitation response to abrupt-4xCO2 in the ARPEGE-Climat 6.3 AGCM. The global-mean response (+0.30 mm/day i.e., about 10%) is dominated by the uniform SST warming (+0.49 mm/day), which is, however, partly cancelled by the CO_2 effect (-0.20 mm/day). The total change in the annual mean precipitation response is globally driven by the uniform SST warming but shows substantial geographical variations which are primarily explained by the non-uniform pattern of the SST warming and may therefore depend on the precipitation sensitivity to local SST.

Regionally speaking, the uniform SST warming (Figure 3.2 b) drives a significant drying in the subtropics, but mostly increased precipitation over the ITCZ and poleward of about 45°N/S. It explains 20% of the spatial variability of the global precipitation response. In contrast, the fast adjustment to the increased CO_2 level (Figure 3.2 d) shows a widespread drying (except over the tropical land areas due to an apparent competition between convection over land versus ocean) and only explains a very limited fraction of the spatial variability in Figure 3.2 a. Despite its negligible contribution to global-mean precipitation changes, this spatial distribution is partly explained by the SST pattern effect (ACC=0.54), which drives contrasting regional changes in the tropics. The results are broadly consistent with former studies based on CMIP5 models, suggesting that the precipitation response to abrupt-4xCO2, especially in the subtropics, does not only depend on the global mean ocean warming and cannot be explained without invoking the fast adjustment to CO_2 forcing and, in certain regions, the pattern of the SST warming (He and Soden, 2017).

3.2.2 Changes in daily precipitation frequency and intensity

Response of daily precipitation intensity

The annual mean daily mean precipitation intensity (SDII, cf. chapter 2, section 2.2) is defined as the average precipitation rate estimated during these

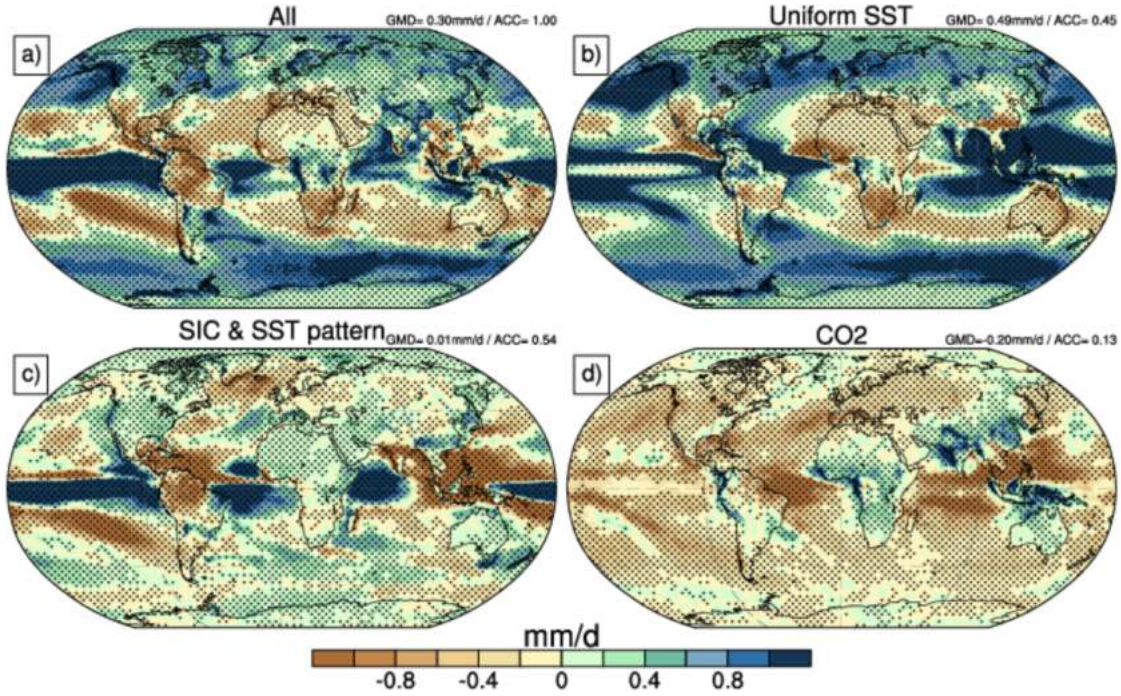

Figure 3.2: Breakdown of the climatological (Year 111-500) annual mean precipitation response (mm/day) to abrupt-4xCO2 in CNRM-CM6-1 using pairs of atmosphere-only timeslice experiments (cf. Tables 3.1 & 3.2): a) total AGCM response, b) response to uniform SST warming, c) response to SST and sea-ice anomaly pattern and d) response to CO2. Stippling highlights areas where the differences are significant at the 5% level. GMD denotes the average global-mean precipitation response and ACC is the spatial continental pattern correlation with the total change shown in a).

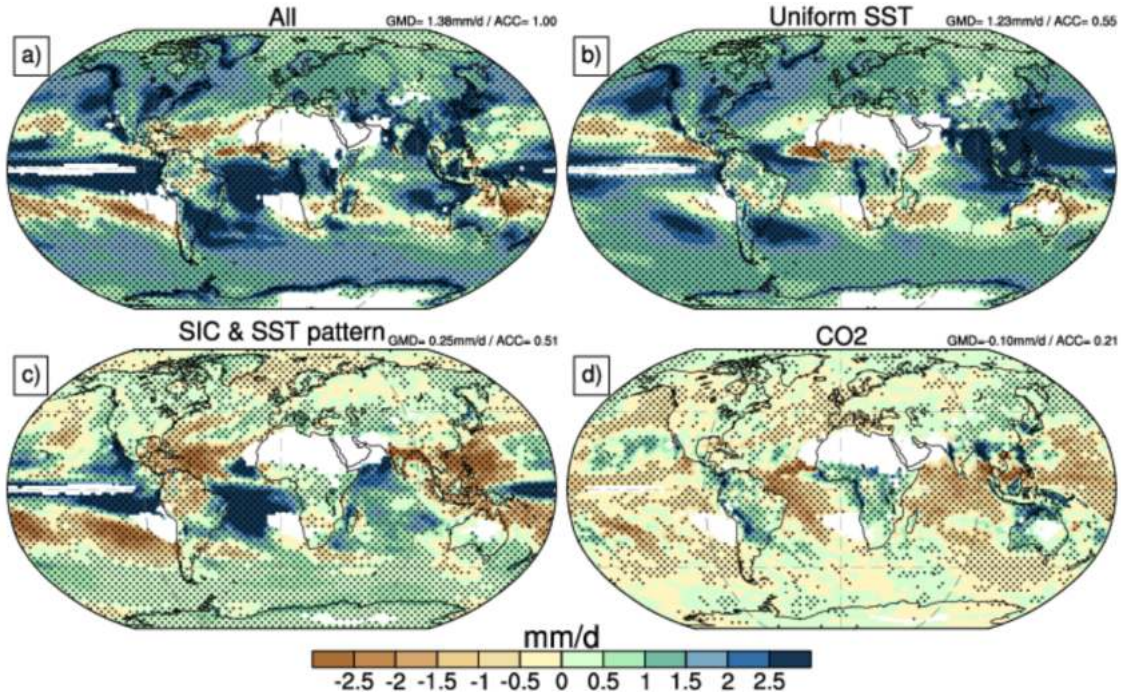

Figure 3.3: Same as Figure 3.2, but for the daily mean precipitation intensity (mm/day)

wet days (i.e., days with precipitation > 1 mm). The annual mean SDII response to abrupt-4xCO2 in ARPEGE-Climat 6.3 is decomposed using the Eq. 3.1 and is quite similar to the annual mean precipitation response. The uniform SST

warming (+1.23mm/day) and the SST warming pattern (+0.25mm/day) contribute positively to the total global-mean response (+1.38mm/day) where the former dominates the latter. The response to uniform SST shows a widespread increase in SDII (except in some regions like the Sahel), while the response to SST warming pattern shows more contrasted geographical patterns with enhanced intensities along the south equatorial Pacific, south tropical Atlantic and north tropical Indian oceans. Poleward of 45°N/S and mostly over land, the uniform SST warming has the upper hand over the SST pattern effect, even though both of these explain the overall spatial variability almost equally. The CO_2 effect shows a dominant decrease in daily precipitation intensities over the tropical ocean. This fast response partly offsets (-0.1mm/day) the slower global-mean increase in annual mean SDII, but only explains a small fraction of the spatial variability in Figure 3.3 a. This drying is the consequence of a weaker net radiative cooling of the atmosphere associated with higher atmospheric carbon dioxide levels, which limits the strength of atmospheric vertical motions (Bony et al., 2013). In contrast, a significant increase in SDII was found over most tropical monsoon regions. This is again consistent with stronger moisture convergence over the rapidly warmed land, mostly due to the fast radiative CO_2 effect.

Response of daily precipitation frequency

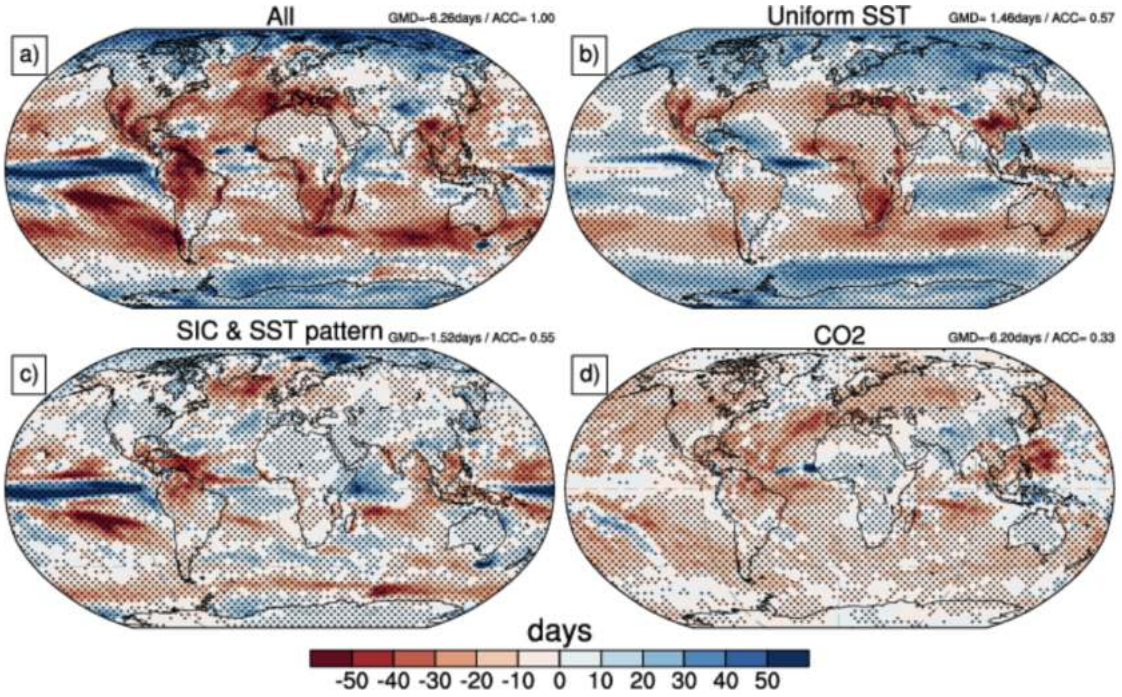

Figure 3.4: Same as Figure 3.2, but for the annual maximum consecutive number of wet days.

From Figure 3.4 a, it is clear that the frequency of wet days (R1mm, cf. chapter 2, section 2.2) can decrease regardless of the general increase in daily precipitation intensity. This overall reduction in the number of wet days (overall annual mean of R1mm is -6.26 days/year) confirms the results from previous studies, in which the recent and projected rainfall days in a year has a clear negative trend (Polade et al., 2014, 2017; Benestad, 2018). Thus, it tends to rain less frequently but more intensely. Figure 3.4 can also be highlighted as the complex

and multi-driver response of the annual mean number of dry days (defined as days with less than 1mm precipitation). Beyond the global mean response and as highlighted by Polade et al. (2014), the pattern of the R1mm response shows a strong similarity with the pattern of changes in interannual variability (cf. Figure A.8) and suggests that the decreased frequency of precipitation events plays a key role in the increased variability of annual mean precipitation. Fast adjustments to increased CO_2 (-6.20 days/year) are the main contributor to the global-mean reduction of wet days. Yet, the signal is relatively smooth and only explains a limited fraction of the geographical pattern in the total response. Both uniform SST warming and SST warming pattern effects almost equally (ACC=0.57 and 0.55 respectively) explain the spatial variability in Figure 3.4 a. They partly cancel out each other at both regional and global scales, which explains the dominant direct CO_2 effect on the global-mean response.

Published article

Douville and John (2021) (cf. Annex A) discusses the response of the mean and extreme precipitation using the ARPEGE-Climat 6.3 AGCM abrupt-4xCO2 experiments. The results discussed are broadly consistent with the study by Chadwick et al. (2017). Nonetheless, the ARPEGE-Climat 6.3 AGCM does not show the same breakdown as the former CNRM AGCM for multiple reasons. Such differences highlight that the precipitation breakdown is model-dependent and that it may be useful to better understand the inter-model spread in the total precipitation response. This model-dependence is also supported by the stronger uniform SST warming contribution to subtropical drying in CNRM-CM6-1 compared to previous studies (He and Soden, 2017), although the fast adjustment to increased CO_2 is also found to dominate the large-scale subtropical precipitation decline.

A major highlight of the paper is that the increase in daily precipitation intensity drives the global-mean magnitude of the annual precipitation change. In contrast, the response of wet day frequency shapes the geographical distribution and interannual variability of the annual mean precipitation, especially in the subtropics, and is more sensitive to changes in near-surface relative humidity than in the total water column over land. Although the annual precipitation response does not seem highly sensitive to the base state, these results deserve further investigation and model intercomparison within CFMIP. By focusing on wet day intensity versus wet day frequency the daily precipitation statistics can be used to reconstruct the annual precipitation response, and may also have a more straightforward connection with the model formulation.

In the following sections of this chapter, I will discuss the response of the extremes (wet/dry) to the abrupt quadrupling of the CO_2 using the AGCM, which is one of the objectives of this PhD. The analysis that was initially done using only CNRM-CM6-1 is now extended with additional available CMIP6 models, which qualifies for the inter-model evaluation of the results. The rest of the chapter will focus on the response of the precipitation extremes to an abrupt increase of CO_2 and will assess the individual contributions from the decomposition based on the Eq. 3.1.

Additional to this, in section 3.5, a preliminary analysis of a stationary GEV fitting for the idealised climate change experiments with CNRM-CM6-1 is discussed.

3.3 Changes in wet and dry extremes

Given the extensive sampling of the day-to-day variability, the extended CFMIP experiments enable the diagnosis of the changes in daily precipitation extremes accurately. Figure 3.5 and 3.6 show the simulated changes in the annual maximum of daily mean precipitation intensity (RX1DAY) and the maximum number of consecutive dry days (CDD, defined as consecutive days with less than 1mm/day intensities), respectively. Wet extremes generally feature a lower spatial coherence than dry extremes (Donat et al., 2016b; Alexander and Arblaster, 2017). Figure 3.5 a however shows a widespread increase in RX1DAY, at least over the regions which roughly coincide with the increase in annual mean precipitation. The uniform SST warming dominates this increase (+8.10 mm/day), which is consistent with the fact that extreme precipitation scales with the global warming level and does not depend on emissions scenario in most global climate models (Pendergrass et al., 2015). The CO_2 effect has very little statistical significance, and the response illustrates relatively moderate extreme events on land. There is a non-negligible contribution (+1.75 mm/day) to the wet precipitation extremes from the SST warming pattern effect, which also contributes to shaping the spatial distribution of the total response (ACC=0.39). It is noticeable that, over the tropics and subtropics, the uniform SST warming and its pattern have almost opposite effects which partly cancel out each other.

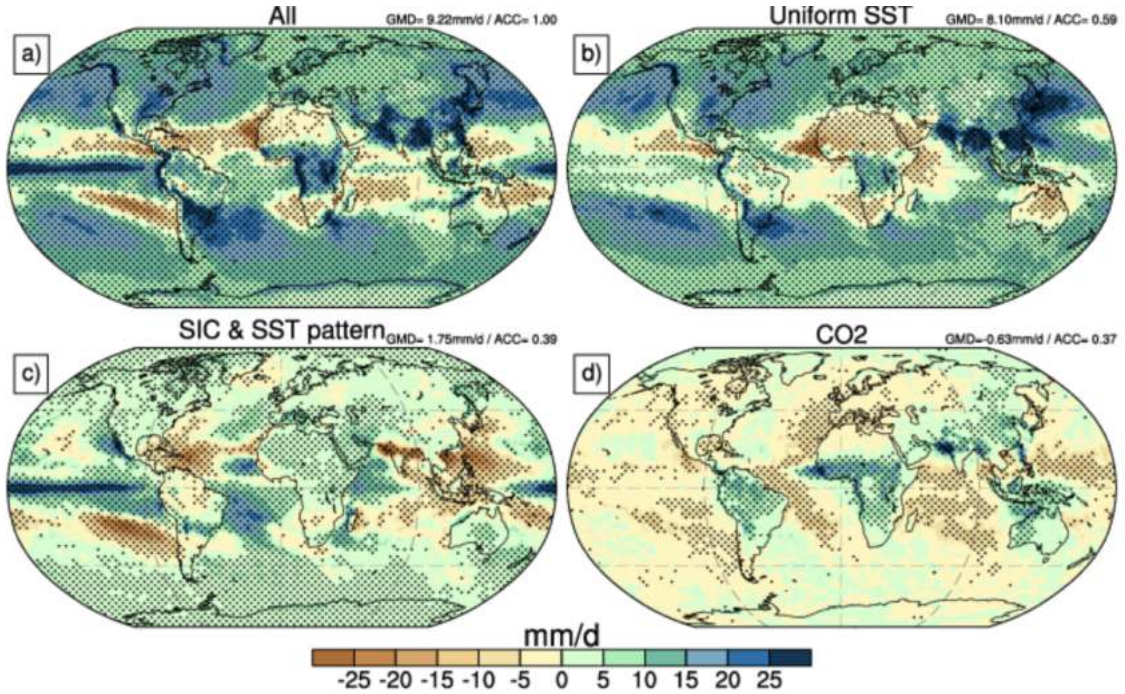

Figure 3.5: Same as Figure 3.2, but for the annual maximum daily mean precipitation intensity (mm/day).

Regions with a significant increase in the annual maximum number of CDD (Figure 3.6 a) coincide with regions affected by a decrease in annual mean precip-

itation. Figure 3.6 a indicates intensified meteorological drought-like conditions over Central America, the Mediterranean, southern Africa as well as Northern Australia with significant positive annual mean anomalies as high as 30 days/year. Both uniform SST warming (+2.29 days/year) and CO_2 effects (+3.72 days/year) contribute to this increase in the total CDD, where the latter plays the dominant role. The increase in CDD over the Mediterranean is reinforced by both uniform SST warming and the CO_2 effect, while these effects partly cancel out each other over South and Southeast Asia. The SST warming pattern effect (+0.91 days/year) contributes least to the global-mean increase in CDD while it limits the amplification of dry extremes, especially over the Mediterranean. Despite being the most significant contributor to the global-mean increase in meteorological droughts, the CO_2 effect only explains a limited fraction of the spatial distribution of CDD changes (ACC=0.47), which is mostly explained by the uniform SST warming (ACC=0.70).

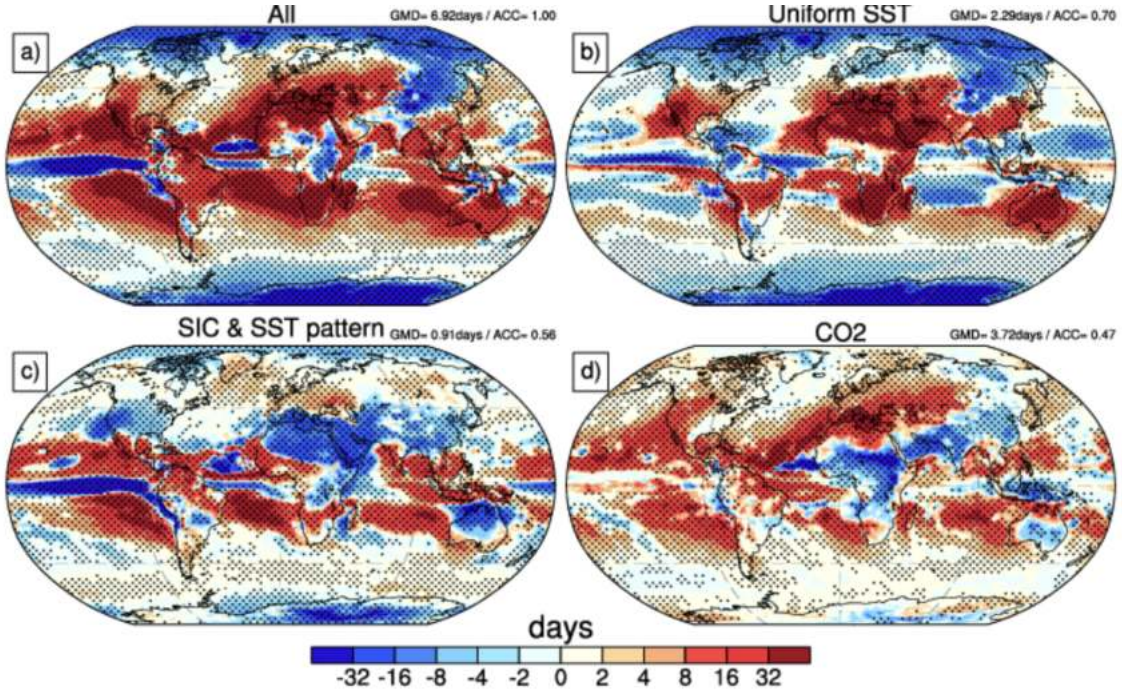

Figure 3.6: Same as Figure 3.2, but but for the annual maximum consecutive number of dry days.

In the northern high latitudes, the projected significant reduction of CDD coincides with an increase in RX1DAY. This is in agreement with many studies showing that these regions are projected to become much wetter in the future (Behrangi and Richardson, 2018), as already detected in the instrumental record (Wan et al., 2015). In contrast, there are many continental regions (Northern Amazonia, Central America, US, Europe, South and Southeast Asia, Southern Australia) where increases in CDD are combined with increases in RX1DAY. Such a strengthening of both wet and dry extremes represents a major challenge for the adaptation to climate change, for instance, an increasing need to derive water resources from floodwater in Mediterranean-like climates where seasonal to annual precipitation accumulation depends on a decreasing number of precipitation events, thus leading to more volatile water resources (Gershunov et al., 2019). The results also suggest that solar radiation modification Jarvis and Leedal (2012)

techniques aimed at cooling the Earth's surface without changing the atmospheric CO_2 level may be more effective reducing wet extremes than dry extremes (e.g., Curry et al. 2014; Adler et al. 2017).

To sum up, the spatial response of annual mean precipitation to an abrupt 4xCO2 is mostly shaped by the simulated changes in wet day frequency. The latter changes are themselves partly governed by changes in near-surface relative humidity (RH, Figure 3.7 a, see also Douville et al. (2020)), which is a crucial driver of convective inhibition over land. Other processes may also contribute to modulating global and regional changes in the annual mean number of wet days. Precipitation is associated with an upward motion and is therefore controlled by atmospheric stratification or static stability. Unstable atmospheric stratification favours upward motion and heavy precipitation, whereas stable atmospheric stratification suppresses upward motion and precipitation. In response to abrupt 4xCO2, our model shows a widespread increase in the low-troposphere (below 700 hPa) static stability (Figure 3.7 b) whose centred anomalies are indeed spatially anti-correlated (ACC=-0.38) with the changes in the number of wet days. Such an anti-correlation remains however limited over land (ACC=-0.18), where precipitation changes are particularly complex and do also depend on orography and its contrasted interaction with different weather types at the regional scale. Nevertheless, the low-troposphere static stability seems less important than the low-troposphere RH for understanding the projected changes in wet day frequency and annual precipitation amount in our model.

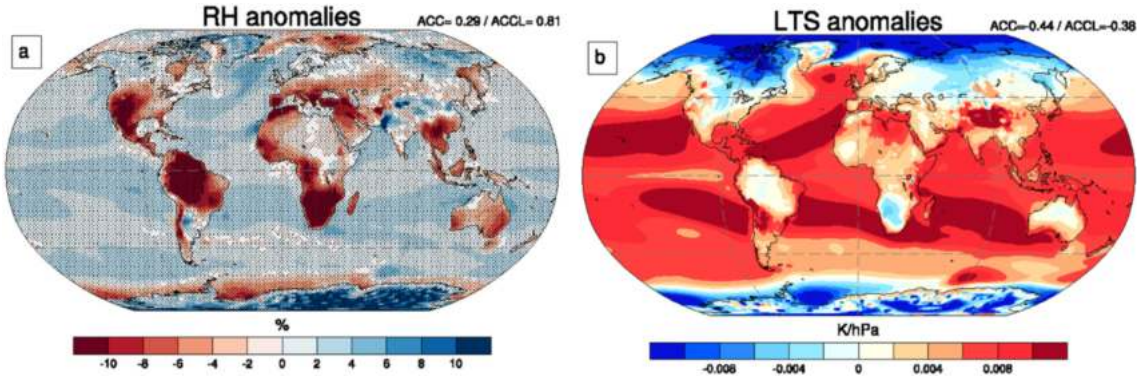

Figure 3.7: Annual mean response to abrupt 4xCO2 simulated in atmosphere-only mode (a4SSTice-4xCO2 minus piSST): a) anomalies in near-surface relative humidity (%) (ACC/ACCL denotes the global/global land spatial anomaly correlation coefficient with the Rlmm anomalies; b) anomalies in the low-troposphere static stability (KhPa) vertically averaged below 700hPa (ACC/ACCL denotes the global/ global land spatial anomaly correlation coefficient with the relative precipitation anomalies. Stippling highlights areas where the differences are significant at the 5% level (the statistical significance has not been assessed but is also high in the last panel given the 390-year sampling

Globally speaking, the SDII and RX1DAY response to abrupt 4xCO2 shows a negligible fast adjustment. This response is therefore primarily driven by the uniform SST warming, which mostly controls the response of atmospheric moisture availability. In contrast, the mean number of wet days and the annual maximum of consecutive dry days (CDD) show a substantial (-6.2 and 3.7 days respectively) fast adjustment to increased CO2. In areas like the Mediterranean basin, where both atmospheric adjustment and SST changes are significant (and additive), the

drying is particularly severe and is associated with a significant increase in the annual maximum of CDD. Total annual precipitation is therefore projected to rely more and more on a limited number of heavy precipitation events in such regions (Polade et al., 2017).

3.4 Comparison with a subset of available CMIP6 coupled models

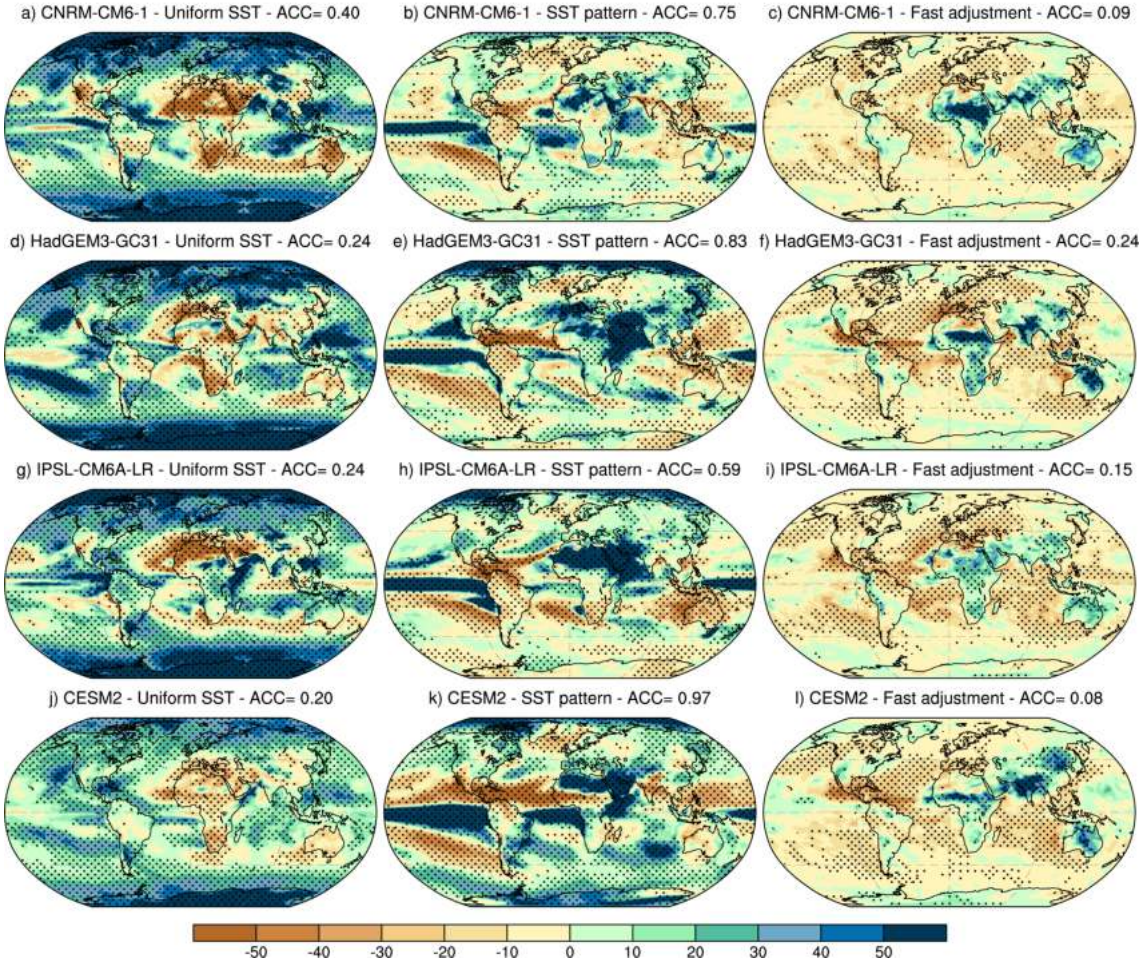

Figure 3.8: Breakdown of relative changes (%) in annual mean precipitation. The total changes are split into three contributions for each of the four selected models: the response to the uniform component of SST warming (left panels a,d,g,j), the response to the geographical pattern of the SST change (also including changes in sea-ice cover, middle panels b,e,h,k), and the radiative and physiological adjustment to increased CO_2 levels (right panels c,f,i,l). In each panel, stippling highlights areas where the difference is significant at the 10% level and ACC denotes the spatial anomaly correlation coefficient with the total AGCM response

While the analysis of daily model outputs using CNRM-CM6-1 allowed us to go one step further in the understanding of the annual mean precipitation response to abrupt 4xCO2, the inadequacy of the sample space by not using a large subset of models is still a drawback. The longer 390-year integration of the simulations has been an advantage as our results are consistent with a previous multi-model study (Polade et al., 2014). Both show that future changes in the number of dry (or wet) days per year can either reinforce or counteract projected increases in daily precipitation intensity as the climate warms, especially in the subtropics where

such changes dominate the projected changes in annual mean precipitation. Not all the CMIP6 models have participated in the CFMIP experiments to date. This section includes the comparison of the finding from CNRM-CM6-1 using additional results with the three (cf. Table 3.3) models now available with CFMIP-Tier2 experiments.

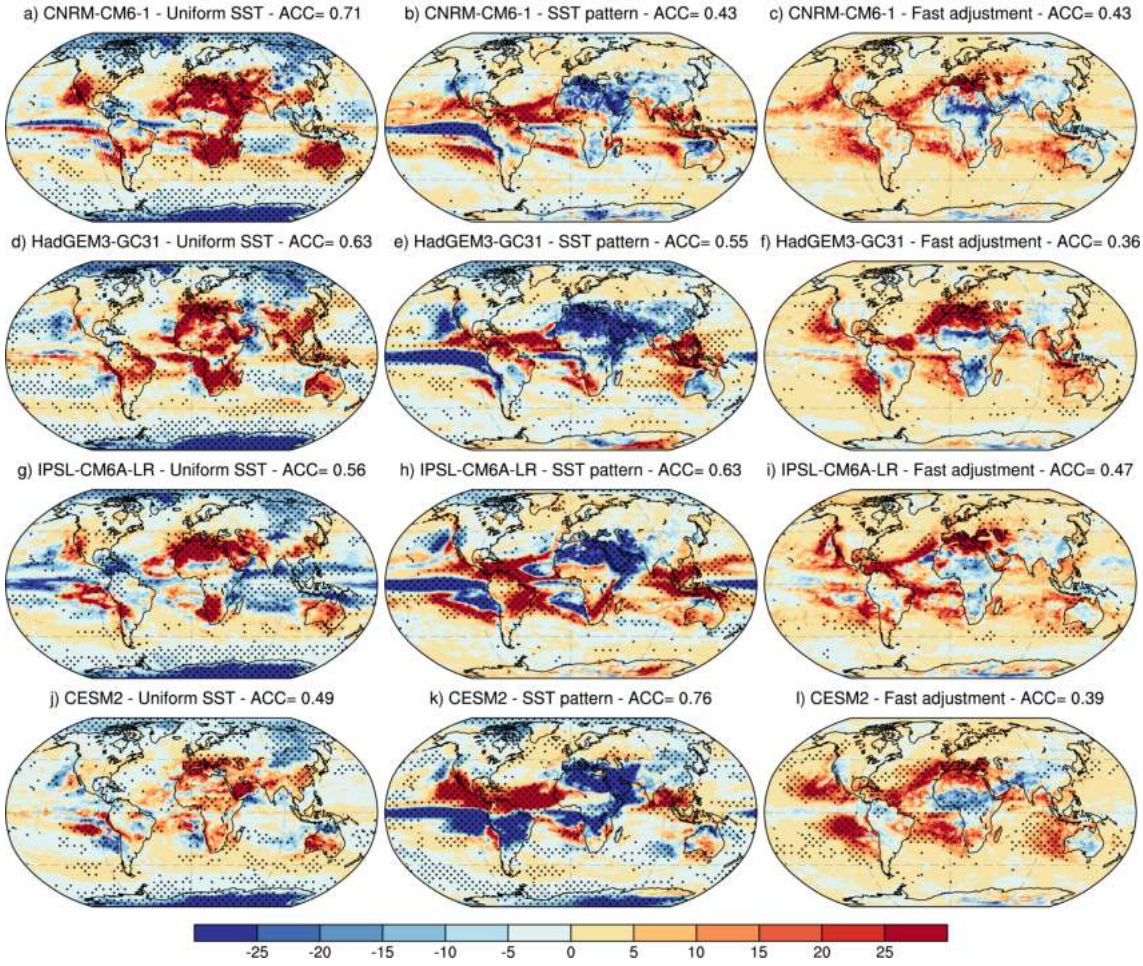

Figure 3.9: Same as Figure 3.8, but for changes in the annual maximum length of dry spells (in days)

Figure 3.8 shows the breakdown of the annual precipitation response to abrupt-4xCO2 using the Eq. 3.1, from the atmospheric-only experiments of the different CMIP6 models. In all the models the global mean response is dominated by the uniform SST warming followed by the SST pattern response and the fast adjustments. Also similar regional features can seen in all four models among all the three contributions. The uniform SST warming drives a significant drying in the subtropics especially over the Saharan desert and the Mediterranean, while it causes increased precipitation over the ITCZ and poleward of about 45N/S. It explains at least 20% of the spatial variability of the global precipitation response in all models. The fast adjustment to increased CO_2 on the other hand, except over the tropical land areas, shows a widespread drying, possibly due to the convective disparities between land and ocean. Moreover, it only explains a very limited fraction of the spatial variability of the total response in most of the models. The contribution of the SST pattern effect in driving the spatial distribution of the mean precipitation is commendable in all four models. Table 3.3 summarises how

much of the spatial variability of the total mean precipitation can be explained by the three individual contributions. Appendix A includes additional Figures (A.10 that illustrate the changes in the total response of annual mean precipitation in all the four models and their multimodel mean.

		CNRM-CM6-1	IPSL-CM6A-LR	HadGEM3-GC31	CESM2
Uniform SST	**P**	0.40	0.24	0.24	0.20
	CDD	0.71	0.56	0.63	0.49
SST pattern	**P**	0.75	0.59	0.83	0.97
	CDD	0.43	0.63	0.55	0.76
Fast adjustment	**P**	0.09	0.15	0.24	0.08
	CDD	0.43	0.47	0.36	0.39

Table 3.3: List of the values of spatial anomaly correlation coefficient (ACC) with the total AGCM response to abrupt-4xCO2 experiments among the four different models analysed. The ACC values indicates the contribution from the uniform SST warming, SST pattern and the fast adjustment to the spatial distribution of the total anomalies. Table summaries the ACC values for the breakdown of annual mean precipitation (P) and annual maximum consecutive dry days (CDD).

Despite a great number of studies, the dry side of the daily precipitation distribution has received less attention. Figure 3.9 compares changes in the annual maximum length of dry periods in four global climate models caused by an abrupt quadrupling of atmospheric CO_2. Similar to the analysis in the previous sections, the total response (cf. Figure 3.6) of the yearly maximum CDD is broken down using Eq. 3.1 to analyze the individual roles of the fast, slow, and SST pattern responses. In all three deconstructed parts, regions with an increase in annual maximum CDD overlap with regions affected by a reduction in annual mean precipitation (cf. Figure 3.8). This is consistent with the previous studies that assessed more intense but less frequent precipitation events throughout several locations (Giorgi et al., 2019; Donat et al., 2019), with projections of a higher incidence of extreme precipitation events associated with prolonged dry spells (Sillmann et al., 2013b; Thackeray et al., 2018). There is a widespread increase in the CO_2 contribution to dry periods, with the exception of a few land regions, such as the Saharan and Sahel regions, Southeast Asia, etc., where it is found to decrease. Over the majority of the continental areas, with the exception of the northern high latitudes, the uniform SST is to account for an overall increase in the CDD. The SST pattern response is clearly distinct from the other two responses, with considerable regional discrepancies in all models. The offsetting effect of the SST pattern and uniform SST warming, particularly over the Mediterranean and North Africa, is an intriguing observation in this case. The patterns of SST anomalies are indeed model-dependent and can contribute to large uncertainty in the regional dry spell response, which requires further investigation. Despite the overall increase in the CDD from the CO_2 effect in all the models, it only explains a limited fraction of the spatial distribution of the CDD changes (with the highest ACC = 0.47, cf. Table 3.3). Moreover, there is no conclusive evidence (at least from

the models available) that either SST warming or SST pattern effects dominate the regional distribution of CDD changes (cf. Table 3.3).

3.5 Stationary GEV analysis of idealised climate change experiments

In the previous sections, I have discussed and compared the response of annual mean and extreme daily precipitation to the fast atmospheric and vegetation adjustment and the slow SST- mediated changes using some CFMIP Tier2 experiments. I have compiled the major results based on the CNRM-CM6-1 model and also have extended the analysis using three more additional CMIP6 models, that took part in the CFMIP intercomparison. In this section, I analyse the response of extreme daily precipitation intensities in complementary idealised, atmospheric-only, climate change experiments consisting of increasing either the CO_2 concentration or the global mean SST. For this purpose, I have used three levels of increased SST (with global mean anomalies of 2K, 3K and XK respectively) or three levels of increased CO_2 concentration (with a factor of 2, 3, and 4 compared to preindustrial level). These idealized experiments allow us to avoid transient responses to variable forcings and thus to analyse changes in precipitation extremes (by comparison with a preindustrial climate) under an assumption of stationarity. For each experiment, the estimation of location, scale and shape parameters (here for RX1DAY) can be computed by fitting the entire time series with a stationary GEV method (cf. section 2.3.2).

Figure 3.10 depicts the obtained changes relative to a preindustrial climate in the experiments pisst-pXK (left panel) and pisst-4XCO2 (right panel). The results clearly highlight that both the fast (mostly radiative) and slower (SST-mediated) responses of daily precipitation intensities are likely to alter the tail of the RX1DAY distribution. This finding further supports our earlier results based on the CFMIP Tier2 experiments (cf. Figure 3.5), but also allow us to quantify more precisely what could be the expected changes in the GEV parameters and thus in specific return levels or return periods. A widespread increase can be seen in the extreme precipitation distribution with the global mean of all location, scale and shape parameters positive, in response to the uniform warming. However, there is an overall decrease in the extreme precipitation location parameter in response to the CO_2 increases, with slight changes in the scale and shape parameters.

The GEV analysis of these different experiments can be used to assess the changes in the extreme precipitation with respect to different levels of increase in the atmospheric CO_2 and global warming. This lead to the question that whether these changes happen linearly as the emissions or temperatures increase? Grid point analysis by taking random separate single grids points over the globe with differing climatologies revealed that there are regions across the globe where the changes in the extremes are not linear even when the experiments are idealized. To identify the regions where extremes follow a non-linear change, an idea of a simple non-linearity matrix is introduced. The matrix is based on a linear fit between the control experiment along with consecutive levelled warming and CO_2 experiments. Initially, a regression curve is fitted for the control, +2K/2X and

+4K/4X experiments and then for the control, +3K/3X and +4K/4X experiments. From the two separate linear fits slopes are computed between the experiments across all the grid points. The ratio of the two slopes is then used to give a crude idea about the linearity of the experiments. An assumption is now considered that the linearity is satisfied when the ratio is between +/-1 and +/-1.15. This assumption is not built on any criteria and will need to be critically reviewed, evaluated, and revised in the future; nonetheless, it is only a simple tool used to indicate the linearity of the changes in extremes. The limits of the ratio used here are not constant and can change with a more focused and oriented design and development of the nonlinearity matrix, which is one of the future prospectuses of the study.

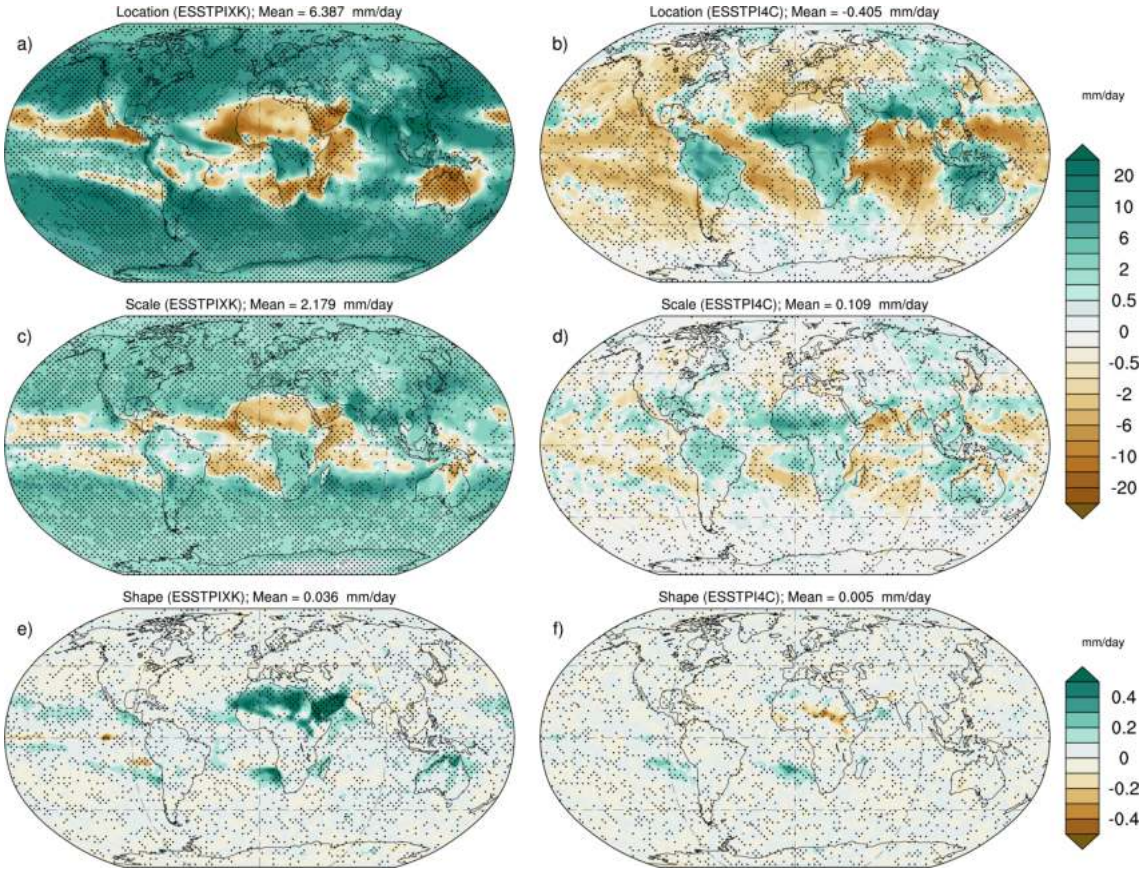

Figure 3.10: Global maps of the anomalies of location, scale and shape parameter obtained by fitting a stationary GEV in the extended CFMIP experiments with CNRM-CM6-1. The anomalies shown here are the difference between the pisst with the pisstXK (a, c, e) and pisst4c (b, d, f) experiments. The stippling highlights the areas where the changes are linear with the different levels of global warming (2K, 3K&XK) and CO_2 concentrations (2×, 3 × &4×). The linearity is calculated using a simple method as detailed in the text.

The stippling that marks all the panels in Figure 3.10 are an approximation of the linearity of the changes in the extremes among the three corresponding experiments of different levels of SST and CO2, using the custom non-linearity matrix. The stippling helps to identify the regions where the changes in the extremes may increase or decrease linearly with the warming and emissions. For the warming experiments, there is a decrease in the linearity of the extremes along the equatorial and tropical regions (Figure 3.10), when compared to the mid and high latitudes, in line with the previously documented results (Pendergrass

et al., 2019). For the CO_2 experiments, the stippling shows no coherent patterns and hence no conclusive results illustrating linear or non-linear regions. This could be a limitation of the nonlinearity matrix used and suggests a refinement of this technique.

3.6 Synthesis

Projected water cycle changes are driven by both fast atmospheric adjustments and slower ocean-mediated responses to increasing concentrations of greenhouse gases. Understanding the relative influence of these multiple drivers is one of the main objectives of the CFMIP. The chapter mainly focuses on the daily precipitation response to an abrupt quadrupling of atmospheric CO_2, as simulated by the CNRM-CM6-1 global climate model. Besides the results already published in the Douville and John (2021) (cf. Annex A), the chapter also discusses the recent intercomparison results using the additional CMIP6 models now available with the CFMIP-Tier 2 experiments along with the analysis of a stationary GEV distribution of the extreme precipitation in different idealised experiments.

Extended atmosphere-only experiments with prescribed SST (cf Table 3.1) are used to decompose the precipitation changes into separate responses to uniform SST warming, the pattern of SST anomalies, as well as fast radiative and physiological CO_2 effects. The combination of the different experiments represents the different individual components as mentioned in Table 3.2. The total response can then be derived (cf. Eq. 3.1) as the sum of the individual responses obtained from the different experiments. Our results highlight that the uniform SST warming dominates the global and regional changes in annual mean and annual maximum daily precipitation intensity. In contrast, the annual mean number of wet days or the response of daily precipitation frequency show a strong fast adjustment. The results state that there is a global-mean reduction in the wet days irrespective of the general increase in the daily precipitation. They are also sensitive to the SST warming pattern that strongly influences changes in large-scale circulation.

Analysis of the extreme (RX1DAY and CDD) precipitation enabled the evaluation of the factors involved in shaping the global total precipitation changes. The total changes in RX1DAY which approximately coincides with the annual mean precipitation changes show a widespread increase. The uniform SST warming is the dominant contributor here responsible for this increase as the extreme precipitation scales with the global warming levels. The contribution from the CO_2 effect to the overall increase in extreme precipitation is modest but non-negligible, demonstrating that extreme precipitation changes do not depend on the emission scenario (Pendergrass et al., 2015). However, for the annual maximum of CDD, both the uniform SST and CO_2 contribute to the total increase with the CO_2 effect being the dominant one. The SST warming pattern effect has the least influence on the global-mean increase in the CDD, although it does limit the amplification of dry extremes, particularly over the Mediterranean.

Insufficiency of the sample space that existed when the analysis was solely done using the CNRM-CM6-1 is resolved by further investigation and model inter-

comparison within CFMIP using the newly accessible additional CMIP6 models. A comparison of the breakdown of total annual mean precipitation and an annual maximum of CDD demonstrates that the models produce fairly similar results. The uniform SST warming effect can account for most of the total mean precipitation changes, whereas the contribution from the CO_2 effect is the least across all models. Furthermore, all the models illustrate that the SST warming pattern effect has an offsetting influence on the uniform SST warming, especially over the Mediterranean, North Africa and the Middle East. Another significant conclusion is that the SST warming pattern makes up the majority of the spatial variability in annual mean precipitation in all the models evaluated. Intercomparison of the annual maximum CDD among the models is a no different story from the findings reached when using only CNRM-CM6-1. The CO_2 effect exhibits a general increase and is a factor for the increase of dry spells in all models. Both uniform SST warming and the SST pattern effects have significant contributions to the increase of the CDD, but with regional heterogeneity from model to model. The uniform SST warming or SST pattern provides the best explanation for the spatial variability of the total annual maximum CDD, and this explanation depends on the model. An increase in the CDD is also detected over the regions with a decrease in the mean annual precipitation, which suggests more intense precipitation with fewer occurrences.

The role played by the warming of the atmosphere and increase in emissions in driving the extreme precipitation is further highlighted by the stationary GEV analysis of the idealized experiments with uniform SST warming anomalies and varying levels of atmospheric CO2 concentrations. There is an overall increase in the location and scale parameters for the warming experiments, which is a widespread decrease in the CO_2 experiments. The spatial variation of the GEV parameters (location and scale, cf. Figure 3.10) from the warming and the CO_2 experiments respectively coincides with the uniform SST warming and CO_2 contributions to the total extreme precipitation change (cf. Figure 3.5). This analysis reaffirms the direct relation of the extreme precipitation to the warming and the non-dependency over the emission scenarios (Pendergrass et al., 2015). In addition, the rudimentary non-linearity matrix adopted (which needs further analysis and evaluation), indicates the regions where changes in the extreme precipitation distribution are not linear.

As far as the laws of mathematics refer to reality,
they are not certain; and as far as they are certain,
they do not refer to reality.

— Albert Einstein

4

Model uncertainty and internal variability

Changes in the magnitude and frequency of extreme weather events are at the nucleus of many climate change discussions. The latest IPCC Assessment Report (AR6) dedicates a whole chapter (Seneviratne et al., 2021) in this regard. Because of a better understanding of the mechanisms, an increasing number of scientific literature incorporating diverse lines of evidence, and easy access to a large suite of global and regional climate models, our confidence in past and future changes in weather and climate extremes has increased over recent years. Although the amplitude of the trends may differ, climate models can reproduce the sign of changes in temperature extremes reported globally and in most locations. In this chapter, I discuss the projected changes in precipitation extremes and their uncertainties using a large subset of CMIP6 global climate models. The extremes are expressed in terms of 20-yr return values (RV20) of annual maximum one-day precipitation by fitting a non-stationary GEV (cf. chapter 2, section 2.3). The extremes are also scaled by corresponding changes either in global mean surface temperature (ΔGSAT) or in local surface temperature (ΔT). By using the scaled extreme changes, I not only quantify the model response uncertainty but also highlight the regions where changes may not be consistent with the widely used assumption of a Clausius-Clapeyron (CC) rate of $\approx$7%/K. Moreover, this chapter also assesses the potential contribution of internal variability to the apparent inter-model spread using a large ensemble of the CanESM5 model in addition to the multi-model ensemble with a single realization for each model. The content of this chapter is largely borrowed from our published paper (John et al., 2022).

4.1 Overview of preliminary studies based on CMIP5 and CMIP6

Today global climate models provide an increasingly comprehensive summary of the climate system. They are used as a primary tool for understanding and projecting changes in climate mean, variability and extremes due to human activities and used as a benchmark to devise and execute different policy changes. In its sixth assessment report (AR6), the IPCC re-estimated a 1.09°C increase in observed global mean surface temperature in the present day (2011-2020) relative to the beginning of the industrial revolution (1850-1900), which can be fully attributed to human influence (IPCC AR6 SPM Masson-Delmotte et al. (2021a)). This anthropogenic global warming is expected to have long-term repercussions on all components of the climate system, including changes in the distribution of daily precipitation. Several generations of multi-model simulations contributing to the CMIP, supported by recent observational evidence, show that both the frequency and intensity of extreme daily precipitation events have increased over recent decades (Allen and Ingram, 2002; Asadieh and Krakauer, 2015; Scherrer et al., 2016; Karl and Easterling, 1999; Kharin et al., 2013; Min et al., 2011; O'Gorman, 2015), owing to the enhanced warming. This is also documented in the IPCC special report on Managing the Risks of Extremes Events to Advance Climate Change Adaptation (SREX, Seneviratne (2012)).

In the absence of moisture constraint and significant dynamical response, the intensity of extreme precipitation is expected to increase exponentially with the atmospheric temperature at a rate determined by the Clausius-Clapeyron (CC) relationship. A robust scaling of daily precipitation extremes with global warming across scenarios was confirmed by Li et al. (2020) who found that changes in precipitation extremes follow changes in global warming at roughly the CC rate of $\approx$ 7%/°C in the latest-generation CMIP6 models. Several studies based on climate model simulations show a future increase of precipitation extremes with the temperature at a rate comparable to or higher than the CC rate (Li et al., 2020; Kharin et al., 2007; Pall et al., 2007; Allan and Soden, 2008; Sugiyama et al., 2010; Kao and Ganguly, 2011; Muller et al., 2011). However, wet extremes are not expected to intensify in all regions (Trenberth, 2011; Pfahl et al., 2017).

Amid the backdrop of a warming climate, both thermodynamic and dynamic effects influence the changes in the extreme precipitation (Pfahl et al., 2017). A sub-CC relation or even negative dependence on global mean temperature has been found for precipitation extremes over some regions, especially over the climatologically dry oceanic regions in the subtropics, presumably as a result of decreasing moisture availability and enhanced large-scale subsidence (Berg et al., 2009; Hardwick Jones et al., 2010; Utsumi et al., 2011; Pfahl et al., 2017). But the question of an appropriate choice of temperature for scaling extreme precipitation is still an open question and the available studies differ in scope (Zhang et al., 2019; Schroeer and Kirchengast, 2018; Sun et al., 2021b). There is a large-scale warming contrast between the continental landmass and the oceans with certain regions over the ocean experiencing a negligible or limited change in the projected surface temperature. The larger warming observed over land may result in a lower scaling with local mean temperature, which may not be considered as a sub-CC scaling rate (Wang et al., 2017). Any departure from the CC rate can be

an indication of a dynamical response which may be either amplified or offset by a thermodynamic response regionally (Pfahl et al., 2017; Sherwood et al., 2010; O'Gorman, 2015).

The strong internal variability of precipitation can obscure the observed changes of precipitation extremes, thereby challenging their detection and attribution (Hegerl et al., 2015). Over recent years, there has been however multiple evidence of a human influence on extreme precipitation. Based on CMIP5 models, the observed increase in RX1DAY over the Northern Hemisphere land area during 1951-2005 has been attributed to the effect of anthropogenic forcing, including both greenhouse gases (GHG) and anthropogenic aerosols, with a rate of intensification consistent with CC scaling (Zhang et al., 2013). This finding has been supported by further studies based on both CMIP5 and CMIP6 models although the relative influence of GHG versus aerosols remains a matter of debate (Lin et al., 2018; Paik et al., 2020). A human influence has been also detected in the fraction of annual precipitation due to extreme events, including over Europe (Dong et al., 2021). Spatial aggregation can be useful to detect changes in the observed extreme rainfall given the limited instrumental record and the low signal-to-noise ratio (Fischer et al., 2013; Ribes et al., 2019).

Beyond the low signal-to-noise ratio of precipitation changes and the limited observational record, the deficiencies of global climate models to simulate realistic precipitation extremes can also hamper the attribution of observed trends and future projections (e.g., Borodina et al. 2017). Despite these limitations, most global climate models are able to capture the large-scale spatial distribution of precipitation extremes over land. The magnitude and frequency of extreme precipitation simulated by CMIP6 models are similar to those simulated by CMIP5 models (Wehner et al., 2020), although an overall increase in horizontal resolution tends to produce larger and more realistic heavy precipitation intensities. Depending on the atmospheric parameterizations, even a model with a medium resolution like the CNRM-CM6-1 model (Voldoire et al., 2019) can produce realistic daily precipitation intensities (Roehrig et al., 2020) although many models still show too frequent too little precipitation events (e.g., Sun et al. 2015). Although convection-permitting simulations now offer considerably more accurate insights into the nature of precipitation extremes and their changes (e.g., Chan et al. 2020), they require large computing resources and are still not suitable for transient climate change simulations covering the whole 21st century.

In CMIP5 global climate models, projected changes in RX1DAY showed a rate of increase with global warming which was found to be independent of the GHG emission scenario (Pendergrass et al., 2015), although some models showed a quadratic rather than linear relationship with global warming (Pendergrass et al., 2019). CMIP5 models also indicated that extreme precipitation could occur later in the year in a warmer climate, shifting in most regions from summer and early fall toward fall and winter although the sign and magnitude of this shift were highly region-dependent (Marelle et al., 2018). The robust scaling of precipitation extremes with global warming across scenarios was confirmed by Li et al. (2020) who found that changes in precipitation extremes follow changes in global warming at roughly the CC rate of 7%/°C in CMIP6 models. Projected long-

period RX1DAY return value changes are larger than changes in mean RX1DAY and increase with increasing rarity (Mizuta and Endo, 2020; Wehner, 2020). Over Europe, the CMIP6 multi-model median projects an overall increase in the 10- and 50-yr return values of RX1DAY (Li et al., 2020). The most intense precipitation events observed today are projected to almost double in occurrence for each additional degree Celsius of global warming (Myhre et al., 2019). There are however regional differences (Rajczak and Schär, 2017; Cardell et al., 2020), with decreases or no change for the southern part of Europe (Tramblay and Somot, 2018; Coppola et al., 2020; Lionello and Scarascia, 2020) but a strong increase over northern Europe (Madsen et al., 2014).

All these studies show changes in either the multi-model mean or median and, *inter alia* have not yet assessed the uncertainties in global precipitation projections. A suite of different model projections often exhibits a large spread (Lehner et al., 2020) and can even disagree on a particular region becoming wetter or drier (sign change in the future). Even where there is an overall consensus among the models on the sign of changes in the projected extremes due to a warmer climate, the magnitude of such changes can differ considerably. Though the climate models have improved over recent decades (Wyser et al., 2020; Zelinka et al., 2020), these improvements do not necessarily result in a reduced spread among the projections (Douville et al., 2021). Thus, the main focus of this Chapter is to quantify the model uncertainties in extreme precipitation projections based on CMIP6 models. I also provide a blueprint for using these projections to identify regions where the projected changes in daily precipitation extremes are consistent with the CC rate and those where they are not.

4.2 Computation of extremes

Daily precipitation data from 35 (cf. Table A.1) global climate models from the CMIP6 repositories (Eyring et al., 2016) are used in this study. I combine the historical simulations (1850–2014) with one shared socioeconomic pathways (SSPs) projections (O'Neill et al., 2016) running from 2015 to 2100. The "end of the road" scenario SSP5-8.5 with the highest emissions is used to get maximum climate change signals and, therefore, better isolate the forced RX1DAY response from internal variability without using large initial conditions ensembles (which are only available for a limited number of models). I use the one-model-one-vote approach i.e., without giving any particular weights, although there are inter-dependencies across models (eg Knutti and Masson (2013); Bador et al. (2018)). For each available CMIP6 model, only one member of the historical and SSP5-8.5 simulations is used — a treatment that is consistent with the recent IPCC AR6, and which ensures that all models are treated equally. As the total uncertainty in the projected changes is the sum of both model uncertainties and internal climate variability, I here also analyze a single model initial condition large ensemble, provided by the CanESM5 model (Swart et al., 2019), with 25 individual members. Hence I can quantify an upper bound for the total uncertainties.

4.2.1 Climate extreme indices and GEV analysis

I first interpolate the daily precipitation data for each model onto a 1°x1° grid using a first-order conservative remapping. This allows us to compare multiple models with different resolutions (typically 1-2°). For each model, grid point and year, I calculate the annual maximum daily precipitation (RX1DAY), which is a widely used extreme index defined by the expert group on Climate Change Detection and Indices (ETCCDI) (Karl et al., 1999; Peterson et al., 2001). I then analyze changes in the return values of RX1DAY, in line with some previous studies of Kharin et al. (2013) and Wehner et al. (2020). To estimate the 20-year return values, I modelled the annual maxima of precipitation at each grid point using a nonstationary Generalized Extreme Value (GEV) distribution using $\ln(CO_2)$ as the covariate for both the location and scale parameters (Coles et al., 2001). The parameters are fitted using the Maximum Likelihood Estimate technique (Easterling et al., 2016). $\ln(CO)_2$ is used as a single co-variate since it has long been recognized to dominate the world mean temperature projections (Arrhenius, 1896) and allows us to use a common co-variate for all models without introducing any internal variability (Wehner et al., 2020).

The cumulative distribution function for a non-stationary GEV distribution for a random variable X is:

$$F(x) = \exp\left\{-\left[1+\xi\frac{(x-\mu(t))}{\sigma(t)}\right]^{\frac{-1}{\xi}}\right\} \tag{4.1}$$

where the co-variate appears linearly in the GEV location parameter as $\mu(t) = \mu_0 + \mu_1 \log(CO_2)$ and in the scale parameter as $\sigma(t) = \sigma_0 + \sigma_1 \log(CO_2)$ while ξ is constant in time. This non-stationary fit is performed for each grid point.

To reduce statistical uncertainty in fitting the GEV distributions, the entire RX1DAY time series from 1850 to 2100 was used for all models. Having fitted GEV distribution, the precipitation extremes of our interest are defined as the 20-year return values. Return values are calculated as the exceedance of the annual extreme with probability p or as the quantiles of a GEV distribution. The changes in the intensity of extreme events can be accordingly estimated for different future periods or periods of different warming levels. Changes in the future (2051-2100) are computed with respect to the historical period (1951-2014), while changes at different warming levels are expressed relative to their intensity during the pre-industrial period (1850-1900).

Comparison of GEV methods

As mentioned earlier, the non-stationary GEV estimates are computed by introducing a linear co-variate into the location and the scale parameters while the shape parameter is fitted as constant in time (but not uniform across models and grid cells). In a warming world, all GEV parameters

may vary between present-day and future climates, but a time-varying shape parameter would not be meaningful because of high estimate uncertainties due to the limited sampling. This assumption was advocated in recent related studies (e.g., Cooley et al. 2007) and widely used since then (Kharin et al., 2013; Wehner et al., 2020). In contrast, non-stationary location and scale parameters may further increase the quality of the fitted RX1DAY distribution in some regions. Figure 4.1 depicts this notion of why I assume both location and scale as non-stationary rather than only considering location parameters to vary with time. It is clear from Figure 4.1 a, b that by the end of the 21st century both location and the scale are supposed to undergo large deviations, hence proving our assumption of non-stationarity for both parameters. While shape parameter (Figure 4.1 c) does not change much, indicating that the shape of the distribution of extremes almost remains a constant

4.2.2 Global warming levels

I frame the projections by considering the changes at a specified global warming target of 1.5, 2 and 3 K above the pre-industrial level. Climate sensitivity, or the simulated global mean surface air temperature response to more comprehensive radiative forcings, is different across different models (Vial et al., 2013; Lee et al., 2021). As a consequence, the point in time when specified global warming levels (GWLs) are achieved differs largely across models. Models with higher climate sensitivity reach specified GWLs earlier than others. However, some models may not even reach the highest specified GWL before 2100. The first year when GWLs is reached for the 35 CMIP6 models used in this study under the scenario SSP5-8.5 is shown in Table 4.1. The extreme precipitation statistics are then calculated for each model individually over 21 years, extending from 10 years before and after the "central year". I have used a moving average of 21 years before computing the central year.

4.2.3 Scaling of extreme precipitation with local and global temperature changes.

I scale changes in extreme precipitation (ΔRV20) with both global mean surface air temperature change (ΔGSAT) and local surface air temperature change (ΔT). ΔGSAT is calculated as the difference between the areal mean surface temperatures for the projected period and reference period (Table 4.1). Similarly, ΔT is estimated as the local change in the climatological surface temperature or the rate of change of mean surface temperature at each grid point for the same periods as above. Instead of considering the linear rate of change ($R_{lin} = \Delta P_{ext}/\Delta T_{surf}$) of the extreme precipitation, I assume a multiplicative rate of change, i.e., $\Delta P_{ext} + 1 = (1 + R_{mul})^{\Delta T_{surf}}$. The multiplicative rate of change is thus calculated as:

$$R_{mul} = (\Delta P_{ext} + 1)^{\frac{1}{\Delta T_{surf}}} - 1, \tag{4.2}$$

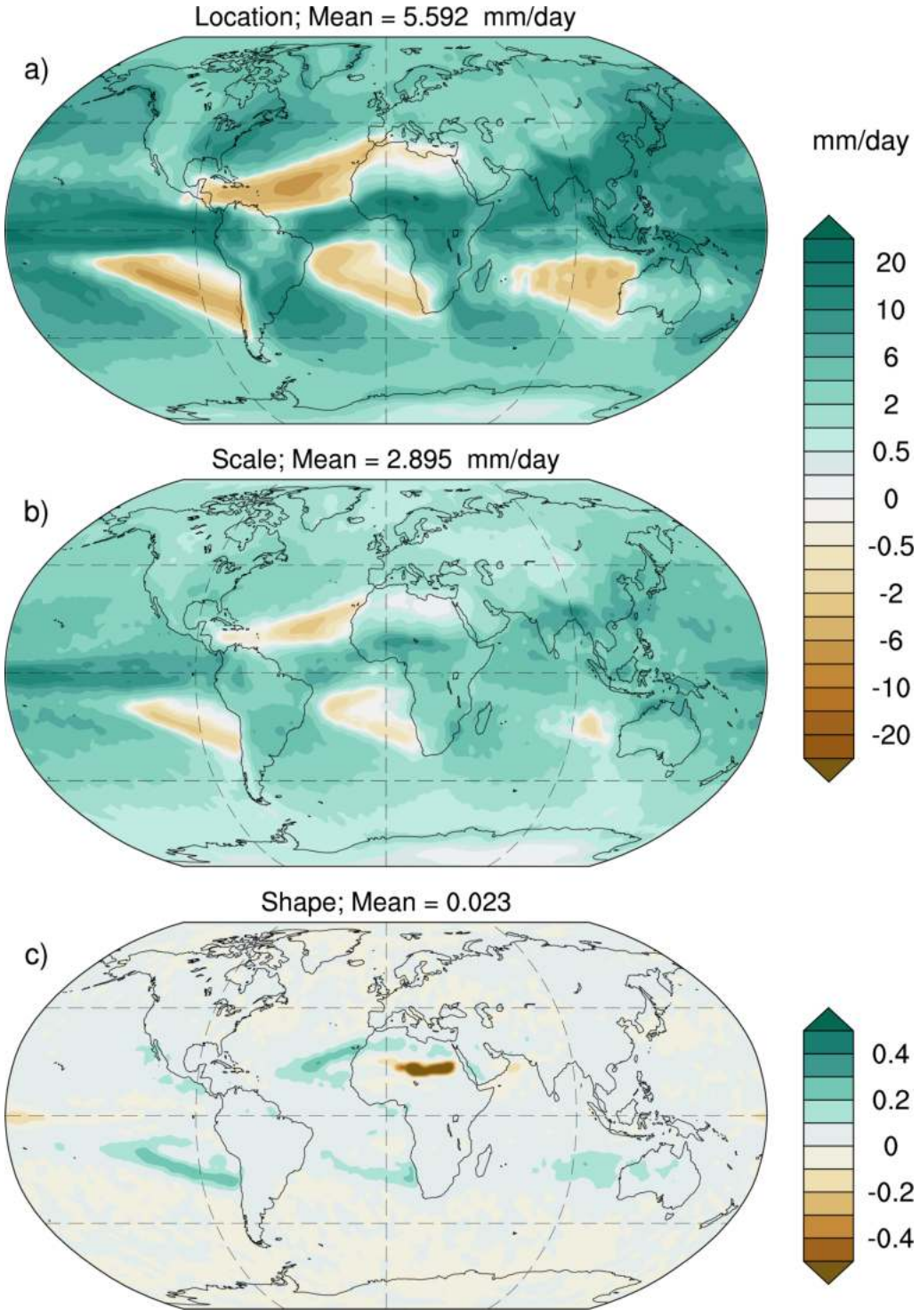

Figure 4.1: Maps showing the changes in the location, scale and shape parameters at the end of the 21st century (2051-2100). The parameters and computed by fitting a stationary GEV distribution to the RXIDAY values.

where ΔP_{ext} is the change in precipitation extremes (here, ΔRV20) and ΔT_{surf} is the change in surface temperature (either ΔGSAT or ΔT). Both the linear and the multiplicative rates become approximately equal ($R_{lin} \approx R_{mul}$) when $\Delta RV20 \ll 1$ mm/day. Another important point to note here is that for scaling with local temperature changes I masked the regions where the temperature changes are too small (i.e., $\Delta T \ll 1$ K) to avoid the infinite scaling while using Eq. 4.2. The

Model	Warming Levels			Model	Warming Levels		
	1.5K	2K	3K		1.5K	2K	3K
CNRM-CM6-1	2028	2040	2058	MIROC6	2040	2052	2076
ACCESS-CM2	2025	2038	2055	MPI-ESM1-2-1	2034	2048	2071
CESM2	2024	2034	2053	NESM3	2021	2034	2054
CanESM5	2012	2022	2040	TaiESM1	2028	2036	2052
FGOALS-g3	2027	2045	2072	IITM-ESM	2035	2048	2075
INM-CM5-0	2030	2046	2074	CMCC-CM2-SR5	2021	2033	2052
KACE-1-0-G	2014	2023	2043	CMCC-ESM2	2028	2039	2054
MPI-ESM1-2-3	2032	2049	2073	CNRM-ESM2-1	2032	2045	2064
MRI-ESM2-0	2026	2038	2064	CNRM-CM6-1-HR	2018	2030	2051
NorESM2-LM	2043	2056	2077	EC-Earth3-CC	2007	2036	2056
ACCESS-ESM10	2027	2039	2060	EC-Earth3-Veg	2011	2027	2050
BCC-CSM2-MR	2030	2043	2065	EC-Earth3-Veg071	2028	2041	2061
EC-Earth3	2024	2035	2057	INM-CM4-8	2030	2046	2069
GFDL-CM4	2029	2041	2059	KIOST-ESM	2017	2037	2064
MIROC-ES2L	2034	2047	2070	UKESM1-0-LL	2023	2031	2046
HadGEM3-GC31-LL	2020	2030	2047	CESM2-WACCM	2021	2033	2053
HadGEM3-GC31-MM	2025	2034	2049	GFDL-ESM4	2039	2053	2075
IPSL-CM6A-LR	2018	2034	2050				

Table 4.1: The year that CMIP6 models reach target warming levels under SSP5.8.8 scenario. Using a 21 year rolling average.

masking is done only for those models which show $\Delta T \ll 1$ K, while I keep the others so that the results are calculated for the models which project a minimum surface warming.

4.2.4 Hypothesis testing

I also aim to identify the regions where the change in extreme precipitation may occur at a super-CC rate or sub-CC rate. The latest IPCC report, (Seneviratne et al., 2021) concludes with high confidence that precipitation extremes are controlled by both thermodynamic and dynamic processes, and that warming-induced thermodynamic change results in an increase in extreme precipitation at a rate that closely follows the CC relationship at the global scale. Any departure from the CC rate could therefore indicate an additional large-scale dynamical response. Attribution studies such as Pall et al. (2017) show the local dynamical responses lead to non-CC rates. Small-scale dynamical responses such as enhanced convection, orographic lifting in atmospheric rivers, or wind intensification in tropical cyclones, can also induce a non-CC rate of change at the local scale. However, our analysis is only based on coarse resolution global CMIP6 models with parameterized convection so the dynamical response here does not account for explicit mesoscale changes in the storm dynamics that could also

modulate the extreme precipitation response (e.g. Chan et al., 2020). Thus, the large-scale dynamics are the only non-thermodynamic mechanisms that can be simulated by these models.

The blueprint I provide will serve as a framework for an extended analysis. This can provide us with much confidence in the areas that are dominated by warming and those regions where changes in the circulation patterns may also matter. For this, I use a simple hypothesis test, where I identify the regions where, e.g., there is no change, using the 80% confidence intervals obtained from the multi-model framework. If the targeted R_{mul} (rate of change of RV20 with temperature) does not fall within the confidence interval calculated from the 35 models, the hypothesis is rejected. When it comes to the range of the confidence interval, the null hypothesis is accepted, and the regions are identified accordingly. To identify the regions with no change, I consider the null-hypothesis R_{mul} = 0%/C, while R_{mul} = 7%/K is used as our second hypothesis to find regions of sub-, super-, or consistent with the CC rate.

4.3 Quantifying CMIP6 model uncertainties in their projection of RX1DAY

4.3.1 Intensification of extreme precipitation

Figure 4.2 shows the analysis for the median, 10th, and 90th percentiles along with the uncertainty range, which is, the difference between the 90th and 10th percentiles, of the extreme precipitation changes scaled by both the global mean (ΔGSAT, left panel) and local mean (ΔT, right panel) surface air temperature changes. The extreme precipitation rate as a function of both ΔGSAT and ΔT shows a clear increase in its intensity with respect to the historical period (1951-2014). The global average of the multi-model median changes is 5.0%/K (Figure 4.2 c) for the scaling with ΔGSAT, while it is 5.3%/K (Figure 4.2 d) for that of ΔT. These close values are slightly smaller than the CC rate of ≈ 7%/K, which suggests some negative dynamical influence at the regional scale in increasingly subsiding regions, but also some water limitation in such dry regions.

From the maps in figure 4.2 c, d, the overall large-scale patterns of change remain similar for both temperature scalings, although changes are a bit more pronounced for the scaling with local temperatures. The largest percentage of increase occurs over the tropical areas followed by the high latitudes for the global temperature scaling. For the local scaling, the largest percentage of changes occurs over the tropics followed by the mid-latitude oceans. The stronger warming over the continental landmass can be a major reason for these differences (Wang et al., 2017). Certain regions over the ocean like the north Atlantic and the Southern Ocean in figure 4.2c are characterized by moderate to high scaled changes in precipitation extremes, which can be linked to the limited changes in the projected local surface temperatures.

Changes in extreme precipitation with ΔGSAT and ΔT scalings vary substantially across the globe. Over most of the mid-latitude land areas, changes do not strongly depend on the scaling method and exhibit a sub-CC rate of 0-4%/K.

Over the subtropics, the assessed rate of change deviates further from the CC rate. In particular, there are high rates (super CC) over the Sahara and the intertropical convergence zone (ITCZ), while the climatological dry areas like the basins of the South Pacific, the north and the south Atlantic, and the south Indian Ocean are marked by reduced, or even negative, rates of change in the extremes. Again, this deviation from the CC rate (≈7%/K) indicates some other factors apart from the thermodynamic features might be at play. Notably, a remarkable property is the increased multi-model spread over these regions (cf. Figure A.13), in line with the less robust dynamical response across global climate models (Pfahl et al., 2017). Large departures, whether it is positive or negative, from the CC rate are associated with a larger inter-model spread, suggesting that these regions may be influenced by less robust changes in atmospheric circulation, possibly related to model-dependent patterns of sea surface temperature anomalies or land-sea temperature contrasts (Douville and John, 2021). Another noticeable feature is the impact of the scaling method over the northern high latitudes. This is partly linked to the Arctic amplification, where the Arctic region gets warm more than twice as fast as the global average (Cohen et al., 2014).

4.3.2 Range of projected responses in extreme precipitation

Figure 4.2 a, b, e and f illustrate the 10th and 90th percentiles of extreme precipitation rates for scalings with global and local warming. The lower and the upper tails of distribution help us to study the worst possible case scenarios and more importantly quantify the uncertainties. The lower tails of extreme precipitation rates are characterized by large-scale features like the negative scaling over the subtropical oceans in the western continental boundaries for both global and local temperature scaling. It is important to note that these regions are predominantly dry areas due to the descending branches of the Hadley cells. The rest of the globe is marked by very small changes either positive or negative that are very close to zero. However, the 90th percentile maps or the upper tail of the distribution show a strong positive increase in precipitation extremes almost everywhere around the globe. These are consistent with super-CC rates (stippling) for the scaling with global warming and, to a large extent, with local warming. Typical to the local warming scaling, the northern mid- and high-latitude land areas are not stippled. This means that the rate of change in extreme precipitation with local warming is sub-CC over these regions even for the 90% quantiles. Moreover, this is consistent across the three maps in the right panel of Figure 4.2 b, d, f. This results directly from a larger and consistent local warming over these areas, especially in the Arctic.

Another noticeable result is the zero or low-density stippling over the tropical Atlantic ocean, Southern Europe, Chilean Coast, Continental North America and South Africa in all maps of both global and local temperature scalings (figure 4.2). This implies a sub-CC rate over these areas irrespective of the scaling choice. One could speculate that the circulation changes, such as a broadening of the subtropical subsidence region, might be responsible for this (Pfahl et al., 2017). Indeed this kind of extension can effectively replace a low-level moisture convergence zone with a regime with low-level divergence where there is

a weaker connection between the projected changes in precipitable water versus temperature.

The bottom panels (g, h) in figure 4.2 show the difference between the 10th and 90th percentile values as simulated by a single realization from 35 CMIP6 models. Large differences between the upper and lower quantiles indicate a substantial spread in the projected extreme precipitation changes. These maps quantify the uncertainties in extreme precipitation response and the pattern is very similar to those of the inter-model standard deviation maps as stated earlier in section 4.3.1 (cf. Figure A.13). As clearly depicted in these figures, the spread is larger over tropical areas than in the rest of the globe. Particularly, over the tropics, the values are notably large in the regions which are climatologically dry or wet, e.g., the subsidence zones of the Hadley cells, the ITCZ, and the Saharan desert. It can be seen that the overall pattern of the inter-model spread is similar for both temperature scalings. Table 4.2 reflects the range of model uncertainty in projected changes in extreme precipitation with respect to both local as well as global warming. It summaries the areal averages of the median, 10%-, 90%-quantiles and their difference for the total (global) area, the global land, and global ocean areas separately. It is clear from this Table that the width of confidence range averaged globally is large, about 10.5%, which is more than the average CC rate.

Several sources of uncertainty can contribute to this spread. The main source is likely due to different representations of the relevant physical processes and related biases in the models' climatology of present-day precipitation. Moreover, the non-homogeneous temperature gradient from the equator to the poles and the land/sea temperature differences are also a source of larger uncertainty in the local temperature scaling maps. Another potential source of uncertainty is the internal climate variability which also gets translated differently into the total uncertainty with the use of different temperatures for scaling. The potential contribution of internal variability is discussed in the next section 4.3.3.

4.3.3 Role of internal variability

The spread among the single realizations of CMIP6 projections has been mainly interpreted so far as model uncertainty. Yet, it can also arise from internal variability given the limited sampling. In the case of historical extreme precipitation changes at a multi-decadal time scale, internal variability was shown to be a significant driver due to the cancellation between different external forcings (Nath et al., 2018). To get more insight into this, I analyzed the rate of change in precipitation extremes in the 25-member ensemble of the CanESM5 model, and assess the spread across members (figure 4.3). A large ensemble from CanESM5 is considered a representative estimate of the internal variability range. It should be noted that CanESM5 is one of the low-resolution CMIP6 models, with moderate skill in simulating global extreme precipitation (Wehner et al., 2020). It is also one of the CMIP6 models with the highest climate sensitivity, but this effect is accounted for by the scaling. The globally averaged median values are thus very close between the CMIP6 ensemble and the CanESM5 ensemble for both scaling with ΔGSAT and ΔT (Table 4.2).

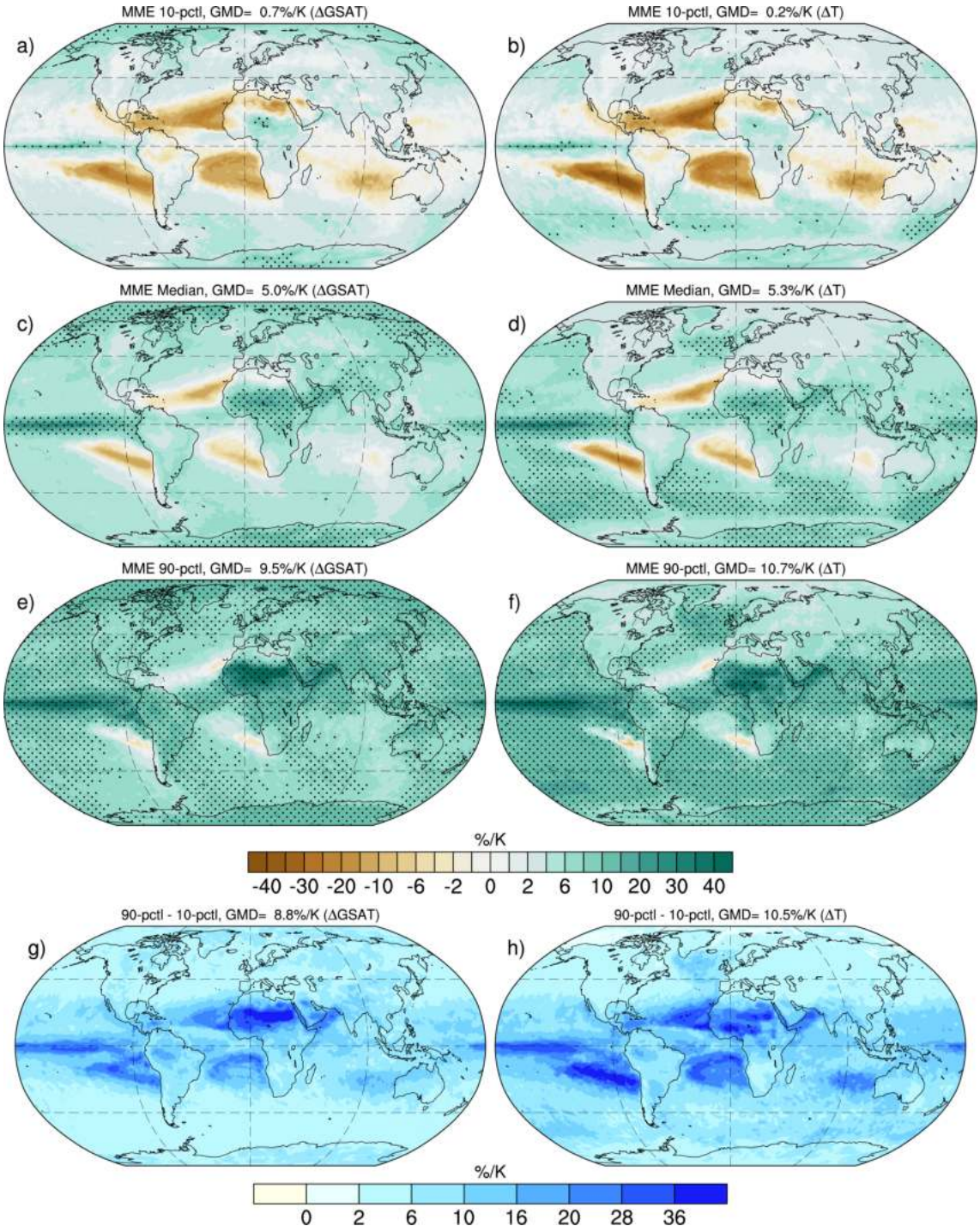

Figure 4.2: Projected relative changes (%/K) in 20-yr return values of RXIDAY scaled by both global mean surface temperature change (ΔGSAT in K, left panel) and local mean surface temperature change (ΔT in K, right panel). The changes are calculated for the future period of 2051-2100 relative to the historical period of 1951-2014 using the SSP5-8.5 scenario. (a),(b) show the 10% quantile maps, (c),(d) shows the median maps and (e),(f) show the 90% quantile maps, calculated from the CMIP6 multimodel ensemble. The bottom panel shows the width of the confidence range of extreme precipitation, computed as the difference between the 90% and 10% quantile maps. Stippling highlights the grid cells where the rate of change is more than 7%/K for respective scalings with ΔGSAT (left panel) and ΔT (right panel). GMD denotes the global mean differences.

			10	med	90	width (90-10)
Total	GSAT	CMIP6	0.7	5.0	9.5	**8.8**
		CanESM5	3.3	4.8	6.2	**2.9**
	T	CMIP6	0.2	5.3	10.7	**10.5**
		CanESM5	3.2	5.0	6.8	**3.6**
Land	GSAT	CMIP6	1.5	5.8	11.1	**9.5**
		CanESM5	4.3	5.9	7.4	**3.1**
	T	CMIP6	1.0	4.6	9.3	**8.3**
		CanESM5	3.4	4.7	6.0	**2.5**
Ocean	GSAT	CMIP6	0.3	4.6	8.8	**8.5**
		CanESM5	2.9	4.3	5.7	**2.8**
	T	CMIP6	-0.1	5.6	11.4	**11.5**
		CanESM5	3.1	5.1	7.1	**4.0**

Table 4.2: Areal mean values (in %/K) of 10%-, 90%- quantiles and median of the extreme precipitation changes scaled by both $\Delta GSAT$ and ΔT over the total global area, global land, and global oceans. The table includes the respective values for both the CMIP6 multi-model changes and CanESM5 multi-ensemble changes.

Figure 4.3 shows the same diagnostics as in figure 4.2, but there are obvious visible differences between them along with a few matching large-scale patterns. For instance, the rates of change for both ΔGSAT and ΔT match over the climatologically dry regions like the north and south tropical Atlantic oceans as well as over primarily wet regions like the inter-tropical convergence zone. Furthermore, the regions like North American inland, Europe and Eurasia, Chilean Coasts, and South Africa are marked by a sub-CC rate of change with both temperature scales, likewise in figure 4.2. Another noticeable result here is the changes in the areas that are stippled. CanESM5 shows areas of super-CC (>7%/K) even for the 10th percentile maps which are not observed in the CMIP6 ensemble. While for 90th percentile maps there is a decrease in the regions that are super-CC rated. The range of uncertainties (2.9%/K for ΔGSAT and 3.6%/K for ΔT) across the CanESM5 ensemble members is evidently less than that across the CMIP6 models. The total uncertainties depicted in Figure 4.3 (bottom panel) are just the result of internal variability. Table 4.2 again summarizes the mean value of median, 10%-, 90%- quantiles and their difference for the total (global) area, the global land, and global ocean areas separately.

The evidenced range of uncertainty for the large ensemble of CanESM5 suggests that internal variability can contribute significantly to the total uncertainty of extreme precipitation rates, when estimated from one single simulation, even in a very high emission scenario. Figure 4.4 depicts the ratio of the width of the confidence range (the difference between 90% and 10% quantiles) of the CanESM5 large ensemble to that of the CMIP6 cross model ensemble. It is clearly seen that for mean extreme precipitation rates scaled by global mean surface temperature, internal variability alone can induce a range of responses about half as large as the CMIP6 multi-model spread (global average of $\approx$40%). For the high- and mid-latitude regions, internal variability is even larger and explains a

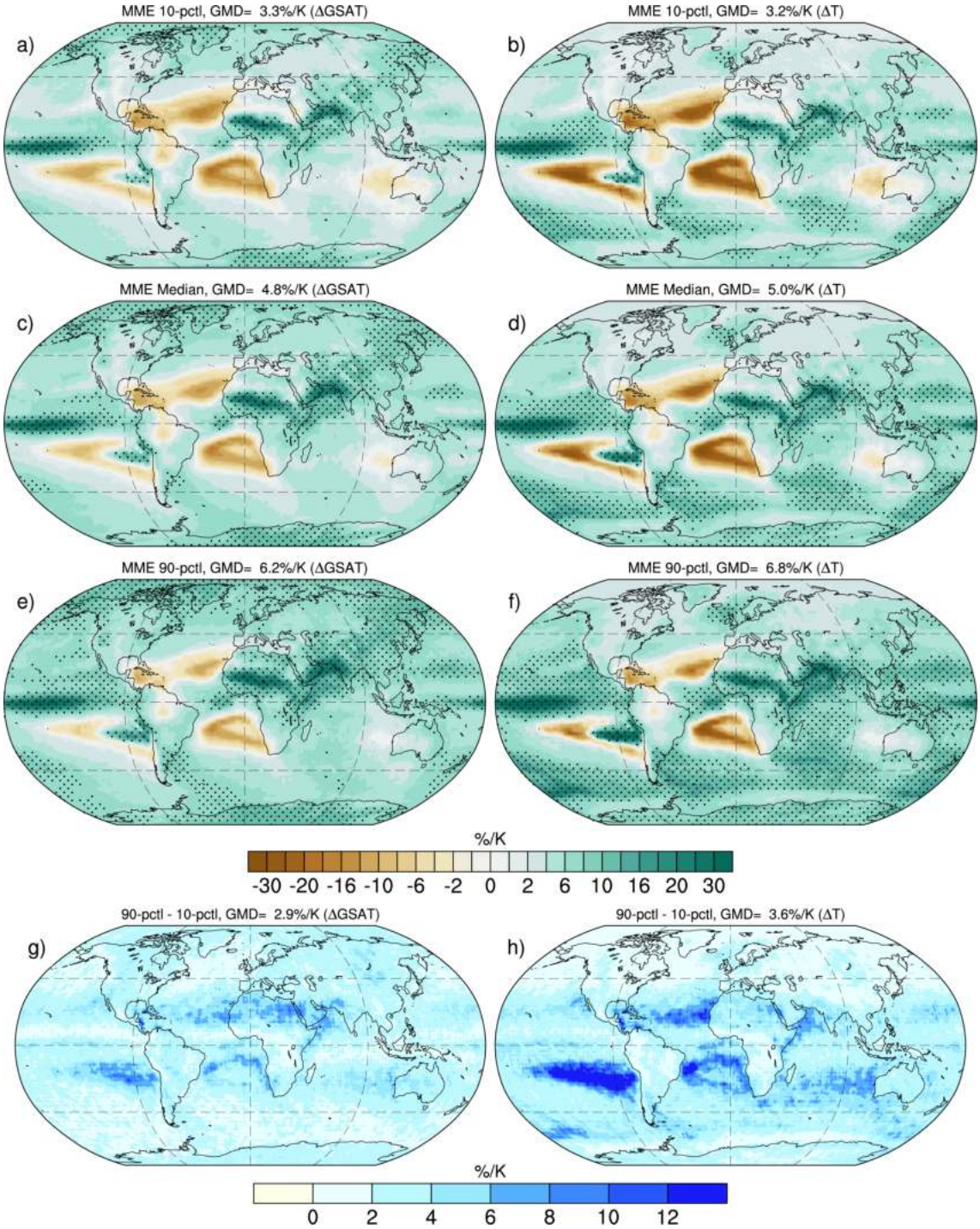

Figure 4.3: Same as figure 4.2, but for the ensemble of 25 individual members of CanESM5 model.

range of response ≈75% (darker shades of blue) as large as the total uncertainty. These regions exhibit a low to moderate increase in the percentage response of the extreme precipitation (as shown in figures 4.2, 4.3) which explains the strong influence that internal variability may have on the extreme precipitation signals. However, throughout the equatorial belt and the adjacent tropical areas, there is a rather less but non-negligible contribution from internal variability. Interestingly, most of these regions fall along with the average position of the ITCZ, which is characterized by high values of extreme precipitation changes. Here, model uncertainty is very likely the major contributor to the assessed inter-model spread,

whereas internal variability only contributes to about 0-20% but is still potentially significant.

Overall, these results suggest that internal variability contributes substantially to the assessed uncertainty (i.e., the width of the 80% confidence range) reported in Figure 4.2. As a consequence, modelling uncertainty alone is probably less than shown in Figure 4.2. Filtering out internal variability could be done by using multiple members for each CMIP6 model involved — but such data are not available for all models so far.

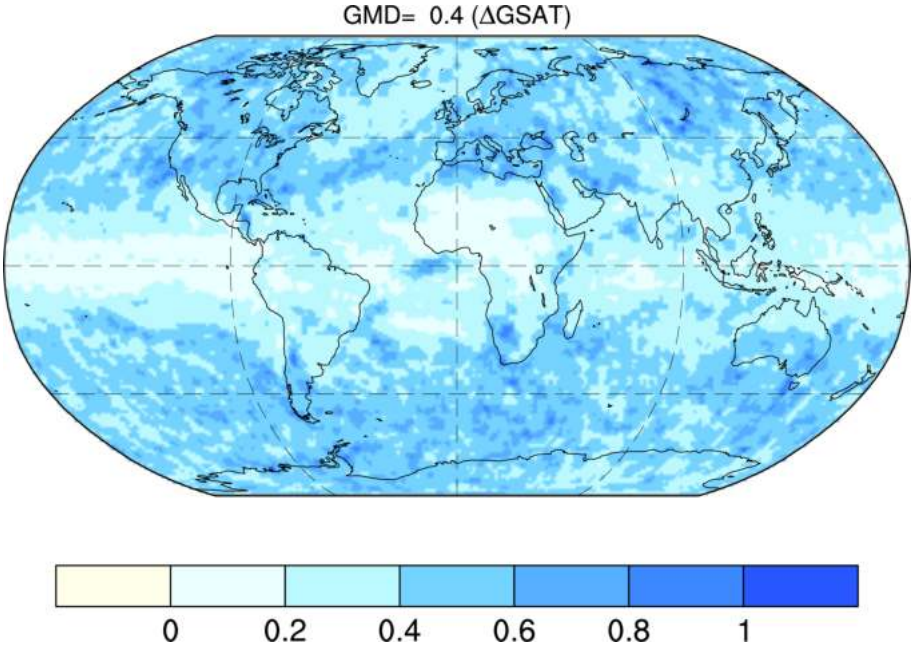

Figure 4.4: Ratio of the width of confidence range of extreme precipitation in large ensemble CanESM5 to the CMIP6 multi-model ensemble. The result shown here is for scaling with global mean surface temperature change (ΔGSAT).

4.3.4 Sensitivity of precipitation extremes at different global warming levels

Figure 4.5 provides analyses of the 10%- and 90%- quantiles of global climate sensitivity of RV20 in the CMIP6 ensembles at GWLs of 1.5 K, 2 K, and 3 K respectively. The median changes (figure not shown) relative to the preindustrial period for all GWLs are close to the CC rate of ≈ 7%/K. Not surprisingly, globally these scaled rates of change in precipitation do not appear to depend on the selected GWL. There is only a slight difference of 0.7%/K in the average multi-model median as the GWL is increased from 1.5K to 3 K possibly due to a non-linear response in some models (e.g., Pendergrass et al. 2019 based on a CMIP5 model), or just a sampling uncertainty. A notable observation as summarized in Table 4.3 is that the inter-model uncertainty range tends to decrease as the GWL increases. The lower-tail of the extreme precipitation rates shown by 10th percentile maps for the three GWLs (figure 4.5 left panel) reveals a very small decrease in the average negative precipitation rate values from 1.2%/K (+1.5K) to 1.1%/K (+2K) and to 1.0%/K (+3K). Also, as seen from the right panel of Figure 4.5, the upper-tail of the distribution or the 90th percentile maps show that the upper bound of extreme precipitation rate moves closer to the median value from 14.9%/K

(+1.5K) to 13.6 %/K (2K) and 12.1%/K (3K). This reduced uncertainty for higher GWLs is consistent with the expected contribution of internal variability. At lower GWLs, the forced response remains limited, and the additional noise resulting from internal variability is proportionally larger. This finding provides support for investigating changes in extreme precipitation at high GWLs. Moreover, the uncertainty at +3K GWL remains larger than that reported in Figure 4.2. Again, this is consistent with a smaller contribution of internal variability in Figure 4.2 compared to a +3K GWL — consistent with the fact that SSP5-8.5 leads to global warming higher than +3K in most CMIP6 models, and that estimating changes over a longer period (50-yr in Fig 4.2, vs 20-yr for GWLs) leads to better filtering of internal variability.

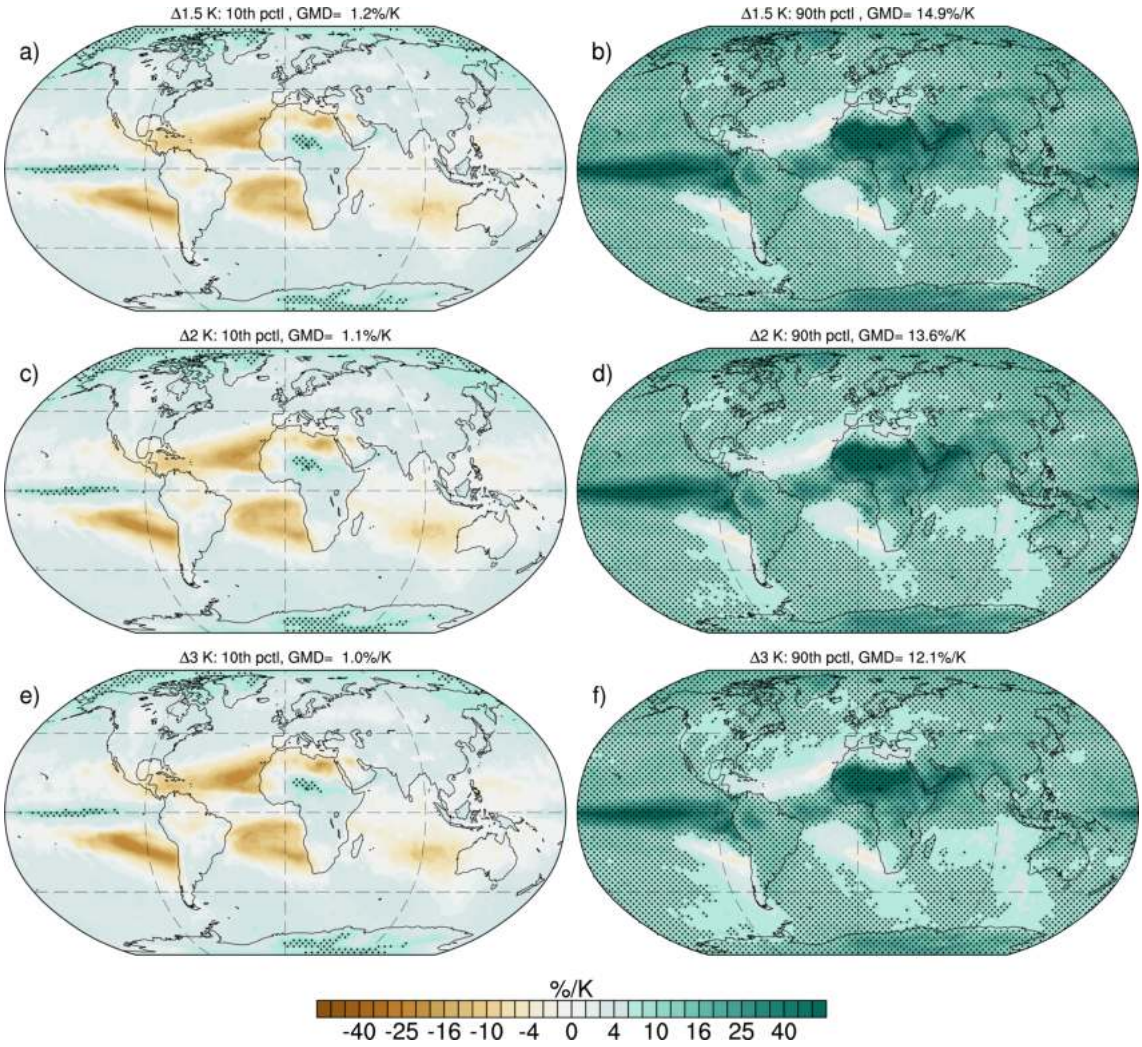

Figure 4.5: Projected relative changes (%/K) in 20-yr return values of RXIDAY scaled by global mean surface temperature change (ΔGSAT in °K) at global warming levels of 1.5, 2 and 3 °K above the preindustrial (1850-1900) average values. The left panel shows the 10% quantile maps and the right panel shows 90% quantile maps for the CMIP6 multimodel changes. Stippling marks the grid cells where the rate of change is more than 7%/K. GMD denotes the global mean differences.

		10	med	90	width (90-10)
Total	1.5K	1.2	6.5	14.9	**13.7**
	2K	1.1	6.2	13.6	**12.5**
	3K	1.0	5.9	12.0	**11.0**
Land	1.5K	2.0	7.5	19.3	**17.4**
	2K	1.9	7.2	17.3	**15.4**
	3K	1.8	6.8	14.8	**13.0**
Ocean	1.5K	0.8	6.0	12.9	**12.1**
	2K	0.8	5.8	12.0	**11.2**
	3K	0.6	5.4	10.8	**10.2**

Table 4.3: Areal mean values (in %/K) of 10%- and 90%- quantiles of the extreme precipitation changes scaled by ΔGSAT over the total global area, global land, and global oceans for three target global warming levels of 1.5, 2, and 3 K.

4.3.5 Regions of hypothesis tests

Using a simple hypothesis test as described in Section 4.2.4, the global areas are classified into three categories. Three general hypotheses that have been considered here are — (H_0) extreme precipitation does not change with global warming, and (H_1, H_2) the change in extreme precipitation follows the CC rate of ≈ 7%/K for ΔGSAT and ΔT scaling, respectively or not. Figure 4.6 shows the regions categorized accordingly to our hypotheses. Red and blue colours are regions where the hypothesis is rejected while yellow represents regions where the hypothesis cannot be rejected. It is important to notice that, not rejecting a hypothesis doesn't mean that it is true. It rather means that the hypothesis is plausible, i.e., there is not enough evidence to reject it.

Figure 4.6 a shows the regions all over the globe where the rate of precipitation change to ΔGSAT is consistent with ≈0%/K (i.e., no significant change, yellow colour). The regions for which H_0 cannot be rejected are limited and these are particularly identified over the global oceans. It is to be noted that over these regions the median values of the projected precipitation changes are consistently low and close to zero. The same results are found for the local temperature scaling (with a correlation ≈99%). Over these regions, the cohort of CMIP6 models does not provide robust evidence that global warming will intensify extreme precipitation. While the small patches of red-coloured regions over the subtropical ocean west to the continents indicate that the hypothesis is rejected but the changes are negative. Another notable feature over the yellow and red-coloured regions is the similarity of negative scaling the figure 4.6a to the patterns of negative dynamic contribution as observed in figure 3 of Pfahl et al. (2017) for the CMIP5 models. This implies a consistency between the CMIP5 and CMIP6 projections of extreme precipitation, possibly for a common reason, perhaps, a less robust dynamical response. The negative dynamic factors may perchance responsible for keeping

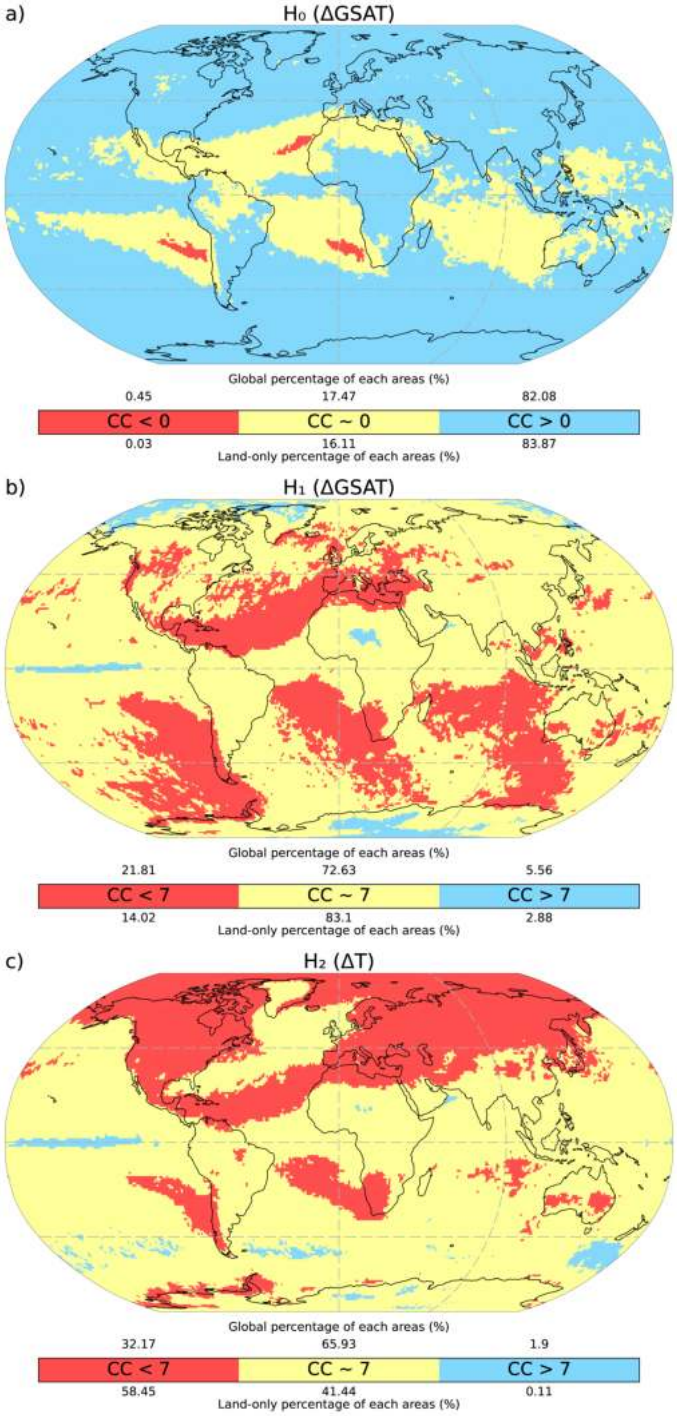

Figure 4.6: Global maps of confidence areas (80% confidence interval) for the CMIP6 using 35 individual models with a single realization. The maps show where the rate of extreme precipitation changes is consistent with constant rates of ≈0%/K or ≈7%/K. Red colour denotes the regions where the changes are always less than the constant, yellow denotes areas where the constant falls within the confidence interval and blue denotes areas where the rates are always greater than the constant. Map (a) shows the areas where the rate of changes in extreme precipitation remains unchanged or consistent to 0%/K when scaled with ΔGSAT. Maps (b), (c) show the global areas where the rate of changes are consistent with the CC rate of ≈7%/K with respect to ΔGSAT and ΔT. The values on top of colourbar show the percentage of each coloured area over the global land surface, while the values at the bottom indicate the same over the total global surface.

the extreme precipitation not to increasing at large as it does with moisture increase in the rest of the globe. Remarkably, there is no land region where extreme precipitation is robustly expected to decrease in response to global warming.

Figure 4.6 b, c shows the regions where the hypotheses H_1, H_2 are accepted or rejected. Both H_1 and H_2 are used for identifying the regions where the extreme precipitation changes are consistent with the CC rate of ≈7%/K with respect to ΔGSAT and ΔT respectively. These maps can be used as a blueprint to identify the regions which are consistent with the CC rate and those which are not. The first outcome is that a vast majority of places on Earth, about 83% of the global land area, are expected to undergo a change in extreme precipitation that is consistent with the CC rate, particularly with the ΔGSAT scaling. This doesn't mean that these regions will experience a change of exactly +7%/K. It means that, over these regions, the expected change in RX1d is not robustly sub-CC or super-CC, i.e., not inconsistent with CC. The majority of regions that follow a sub-CC rate of change for both temperature scalings are over the oceans, especially at the western continental boundaries, which are climatologically dry regions. A few continental regions like the North American continent, South and Central Eastern Europe, Chilean Coast, South Africa and South Australia are also marked by the sub-CC rate for both scaling temperatures. There are also patches of consistent super-CC rates over the equatorial Pacific and the Sahel region. Scaling with two different temperatures displays different areas of consistency with CC, especially over the high Northern latitudes. The map for the local temperature scaling shows a significant increase in the sub-CC areas, especially over the Arctic and most of the mid-latitude landmasses. This indicates that the expected increase in extreme precipitation over these regions does not follow the local warming at the CC rate. This result is consistent with the enhanced warming expected over these regions, while the surrounding oceans (the main source of moisture) are warming less quickly.

4.4 Sensitivity to model biases

Bias correction or bias adjustment of global or regional climate models has become a common and quasi-mandatory step before using model simulations in impact studies context. Indeed, most of the "raw" climate model outputs suffer from biases with respect to reality (or at least to what is measured) in the sense that their statistical distribution and properties differ from those of the observations (e.g., Vrac and Friederichs 2015). Bias correction adjusts or corrects model outputs by transforming them in order to have adjusted values with statistical properties/distribution similar to those of observations used as a reference that can be employed as input into impact (or more generally subsequent) models.

In the previous sections 4.3.2 and 4.3.5), I have quantified the upper bound of the total uncertainty in projecting extremes along with the classification of the global areas which follow the CC rate or not. In addition, I am interested in understanding the potential sensitivity of the estimated changes in precipitation extremes to bias correction of the daily precipitation intensities. Therefore, I computed the RV20 from the RX1DAY values of five CMIP6 models, as obtained after applying a daily bias correction using the method called "Singularity Stochastic

Removal", as described in Vrac et al. (2016). By using this method, it is possible to handle cases in which the proportion of dry days in the model is higher than that in the reference data and instances in which the converse is true and the proportion of dry days in the model is lower than that in the reference data in the same way. Here, the daily ERA5-Land data from 1981 to present (Muñoz Sabater et al., 2019) is used as the reference dataset for the bias correction.

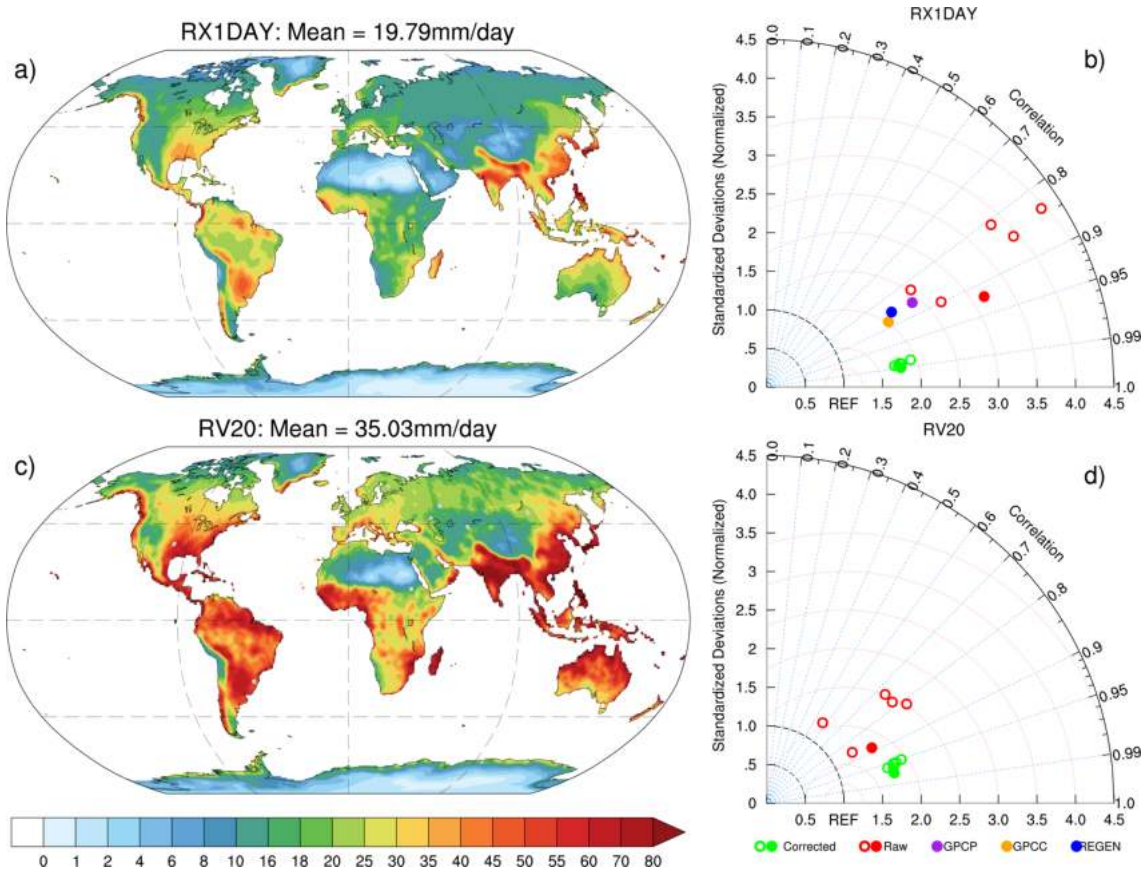

Figure 4.7: Comparison of the bias corrected model outputs with the raw model outputs using Taylor diagrams. The maps in the left panels depict the observed a) RX1DAY, c) RV20 from a non-stationary GEV analysis. The Taylor (b, d) diagrams illustrate the model skills before (red) and after bias-corrections (green) for the variable as illustrated by the maps respectively. The solid markers indicate the multi-model means and circles are individual models. Red is for raw outputs, while green is for bias-corrected outputs. Panel b) depicting the Taylor skill in RX1DAY also consists of other observational data sets as indicated by the coloured legends. The reference data set for the Taylor diagrams in ERA5-Land and the period analysed is 1981-2014.

As a preliminary step, a comparison of the bias-corrected data with the raw data is made by regridding both onto a common $1° \times 1°$ grid. This assesses how the bias correction improves the data, i.e., will the corrected data be better at capturing precipitation extremes than the raw outputs? I used the observational dataset, daily ERA5-Land, same as the bias correction reference dataset for the comparison. The maps in Figure 4.7 (a, c) depict the mean values of RX1DAY and the RV20 from a stationary GEV analysis (stationarity is assumed due to a shorter period of analysis) on the RX1DAY values for the period 1981-2014 from the ERA5-Land. Both RX1DAY and the RV20 maps are marked by very similar spatial characteristics with regional variations in the magnitude of the intensity

of the corresponding values. The RV20 values are more intense than the RX1DAY as illustrated by the colours at the high end of the colour bar spectrum. Now I compare the different models' ability to capture these spatial patterns of the observed extremes for the same period as above using the Taylor diagrams (cf. chapter 2) as illustrated in Figure 4.7 b and d. Within the diagram red markers indicate the raw outputs, while green markers are for the bias-corrected ones. The filled circles (both red and green) are the corresponding multi-model means of the models considered. Other observational datasets, although with different periods, are also included in Figure 4.7 b, marked by respective colours as in the legend.

The bias-corrected outputs exhibit a very noticeable improvement in the skill to capture the historical extremes similar to the observations, as illustrated by the Taylor diagrams. For RX1DAY, the green markers are tightly packed, all falling between 0.5 to 1.0 centred RMSE curves. The values of pattern correlation are appreciably high and are very close to 0.99 indicating a high Taylor skill after bias correction. The raw model outputs on the other hand have a reasonable Taylor skill with a range of 08 to 0.9 and >0.9 for the multi-model mean. However, the values largely spread across the spectrum with the centred RMSEs from 1.5 to 3.5.

Improvement in the bias-corrected RX1DAY is also reflected in the calculations of the historical RV20 values (cf. Figure 4.7 d). The model's competence for bias-corrected outputs (RV20) as illustrated in Figure 4.7 d and shows a significant improvement relative to the raw outputs. The raw model outputs have Taylor skills ranging below 0.8 up to even 0.55. The spread in the RV20 for the raw outputs is reduced when compared to the raw values of the RX1DAY but is still large and should be accounted for. The spread in the bias-corrected models is narrowed and falls between the centred RMSE curves of range 0.5 to 1.0. The Taylor skills for the raw model outputs are under 0.85 and even degrade to about 0.55, however, the multi-model mean skill is about 0.9. It is important to notice that the Taylor skills of the bias-corrected models have substantially improved, where all models have a very high pattern correlation value of $\geq$0.95 with the skill for the multi-model mean close to about 0.99.

The Taylor skills of the raw vs. bias corrected outputs also depend on the reference dataset used. However, it is clear that with bias correction the models can capture the extremes more efficiently and are close to the observational dataset used. An increase in the Taylor skill of RV20 boils down to a very basic question of does all the GEV parameters have improved after bias correction. Figure 4.8 illustrates the Taylor diagrams for the location (a) and scale (b) parameters before and after bias corrections. The Taylor skills for the shape parameter are not computed here as the spatial values of the shape parameter are highly non-coherent and do not seem to show any particular pattern. This makes it meaningless to compare the shape parameters for the Taylor skill, which is based on pattern correlation. As depicted in Figure 4.8, one could understand that the improvement in the Taylor skills of RV20 can be owed to the improvement in the location parameter rather than the scale. Skills of scale parameters are very much degraded for both the raw and bias corrected outputs. There is no visible improvement in the bias corrected scale parameter, at least which, can be

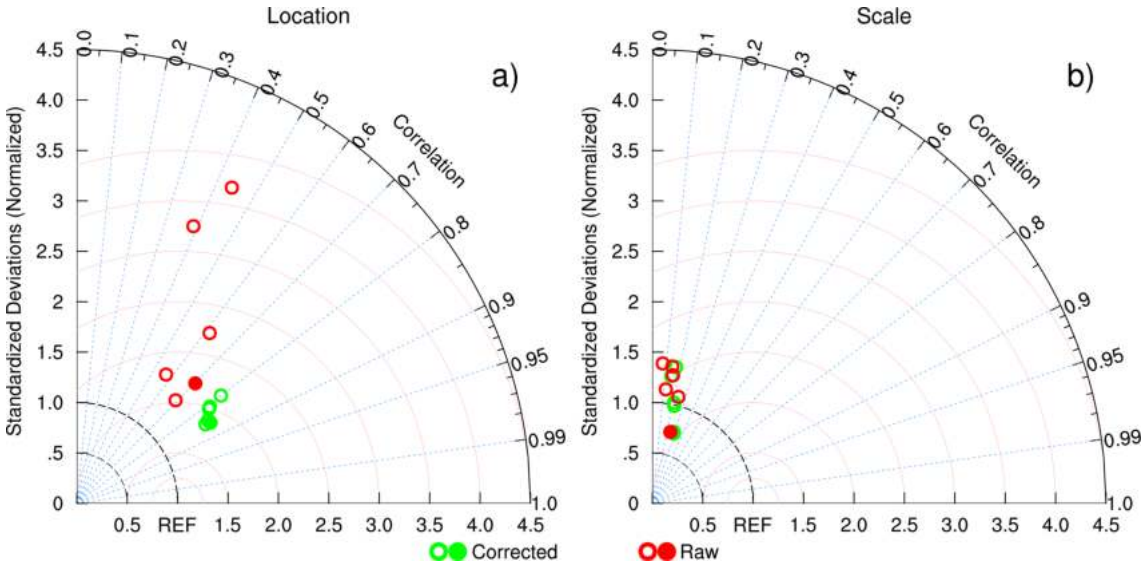

Figure 4.8: Taylor diagrams illustrating the same as in the Figure 4.7b ,d; but for the location and scale parameters from the stationary GEV fit on the RX1DAY values for the period 1971-2014.

obtained by using Taylor diagrams. For the bias-corrected location parameter, the correlation is between 0.8 and 0.9, which is good, however for the raw data the Taylor skills are degraded with correlation values for most of the models less than 0.6. A larger spread in the raw values is another noticeable feature while the bias-corrected outputs are clustered tightly. The improvement in the bias-corrected RV20 is mainly contributed by the improvement in the corresponding location parameter — while keeping in mind that further analysis is required to fully comprehend this.

Note that the spread in the raw outputs as illustrated by the Taylor diagrams is largely due to large inter-model differences in the amplitude of the spatial pattern, with some models substantially underestimating the pattern amplitude while others it is overestimated. A simple comparison of the red and green markers in the Taylor diagram demonstrates that when biases are accounted for by utilizing observational constraints, the models perform more efficiently with a significant reduction in the inter-model spread. This means that the large difference in the amplitude of the spatial patterns of the extremes can be reduced by bias correction and can produce outputs which are more genuine to the observed data.

Provided the improvements in the bias-corrected outputs, it was intriguing to revisit the changes in the extreme precipitation that were already analysed with the raw outputs. So I analysed the changes in the RV20 values of the bias-corrected models and compare them with the respective raw outputs. Maps in the figure 4.9 depict (raw model outputs in left panels; bias-corrected in middle panels) the changes in mean RV20 at the end of the 21st century (2051-2100) relative to the historical period (1951-2014) for the 5 different individual models. The overall large-scale geographical patterns of the relative changes in the extreme precipitation remain the same for both the raw and bias-corrected outputs. In all the models except one (MPI-ESM1-2-HR), the bias correction enhances the relative

changes in extreme precipitation. This is indicated by the areal mean values given at the top of each panel. However, there are many regional dissimilarities between the two, which are illustrated by the right panels in the figure 4.9 showing the difference between the bias-corrected and raw outputs. The highest disparities between the two are seen mostly over North and Equatorial Africa in all models. Nevertheless, the global average values indicated on the top of the difference maps indicate a reasonably small difference between the mean of raw and bias-corrected values. This in turn shows a limited sensitivity of the extreme changes to bias correction when averaged globally, but the regional differences are worth further studies and analysis.

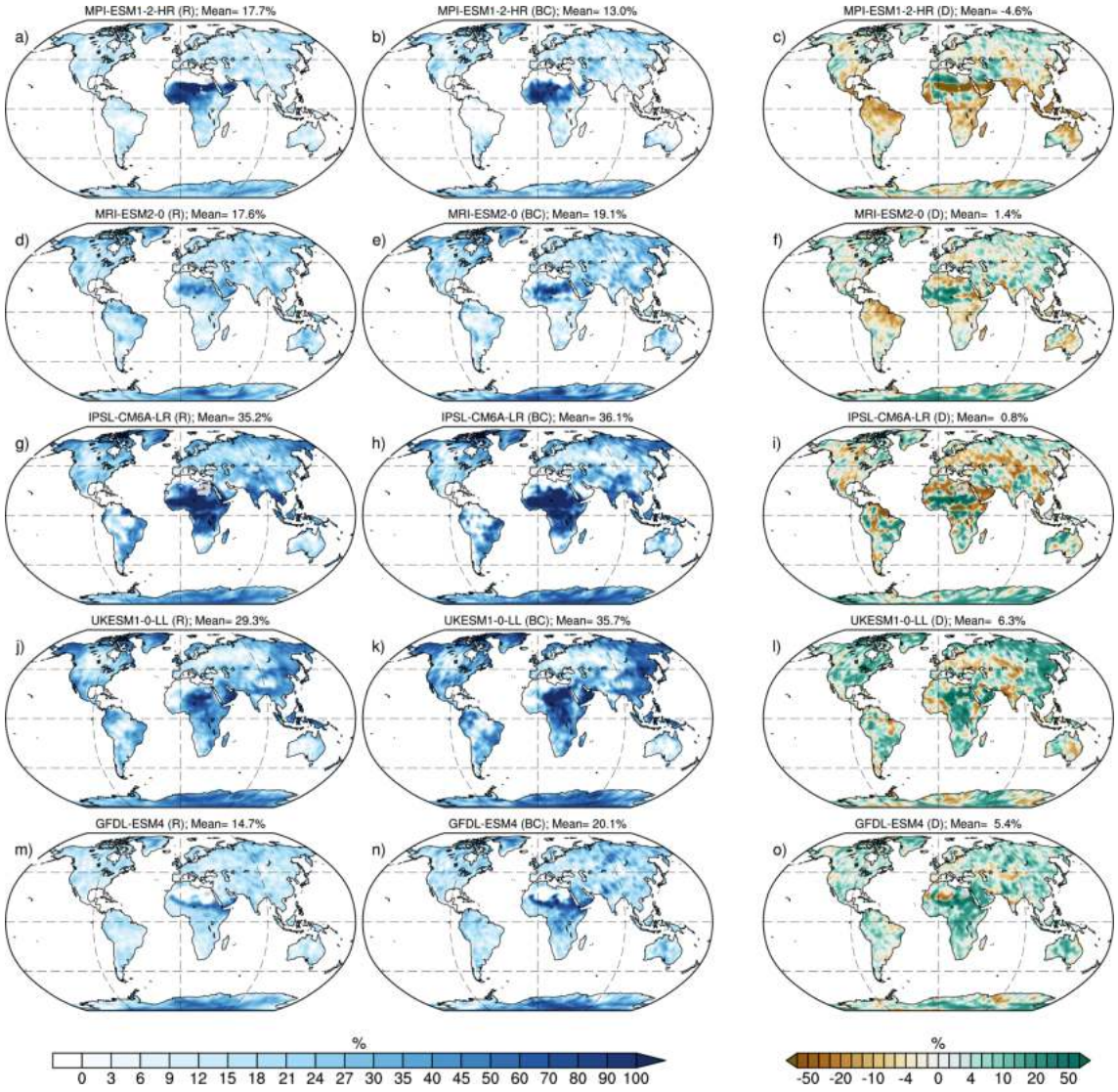

Figure 4.9: Maps showing the future (2051-2100; SSP5-8.5) changes in the RV20 relative to the historical period (1951-2014) for the raw model outputs (left panels) and the bias corrected outputs (middle panels) and the difference between the bias corrected and the raw outputs. The name of individual models is indicated on each panel with the corresponding global mean values.

Four out of the five models assessed here show an overall increase in the extreme precipitation changes after bias correction. Figure 4.10 depicts the ensemble mean of the changes from these five models shown in Figure 4.9 (right panel). The map's stippling highlights the areas where more than 80% of the

models (in this case, four out of five) exhibit a sign change that is similar to the mean value, confirming the locations where the majority of models exhibit a similar difference (either positive or negative) between the bias-corrected and the raw data. The contours illustrate that the average values are a bit smoother when compared to the individual model differences, however, the regional differences are very evident. High model agreement and the substantial differences between the two (bias corrected vs. raw) are primarily seen over the Saharan region, the North and South high latitudes, Central India, etc. The global average value (1.9%) shown at the top of the mean difference map does, however, point to a relatively negligible difference between the means of raw and bias-corrected values. In turn, this demonstrates that, when averaged globally, the extreme changes are only moderately sensitive to bias correction, but the regional variations deserve additional research and analysis using a broader group of models.

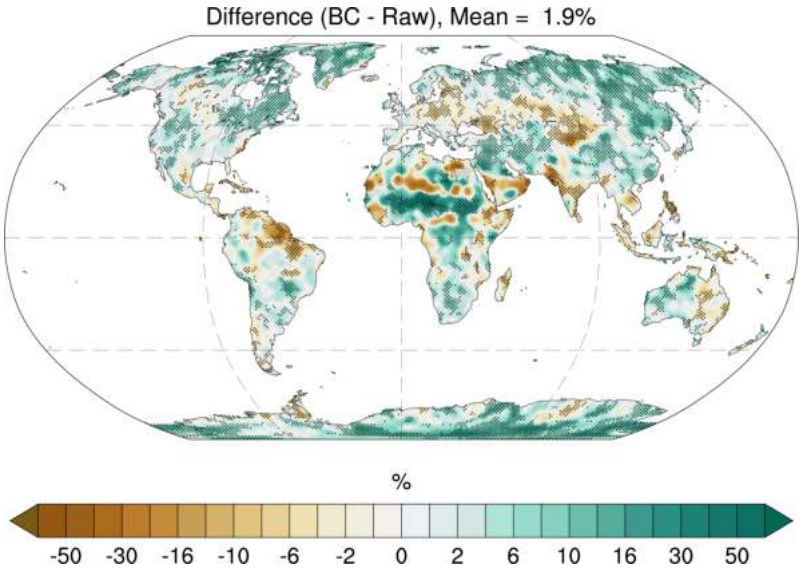

Figure 4.10: The multi-model mean of the difference between the bias corrected (BC) and the raw projected relative changes (in %) in RV20. The stippling indicates the regions where more than 80% of the models agree with the sign change of the multi-model mean. The mean value indicated at the top is the global average of the difference.

By limiting model biases against ERA5-Land data, one can get better and more accurate findings. However, there are a variety of bias correction techniques available today (e.g., Panofsky et al. 1958; Haddad and Rosenfeld 1997; Graham et al. 2007; Sperna Weiland et al. 2010; Watanabe et al. 2012; Wong et al. 2014; Eden et al. 2014; Vrac and Friederichs 2015; Vaittinada Ayar et al. 2016; Xu et al. 2021), and the outcomes of each technique may differ. One difference between bias-correction strategies is the difference between simulated and observed data in the baseline period Graham et al. (2007); Sperna Weiland et al. (2010)). Here I have only considered one among many available bias correction techniques to compare the GEV parameter and RL20 estimates derived from raw versus adjusted daily precipitation outputs. The results need to be further discussed and analysed using more global (e.g., CMIP6) or regional (e.g., CORDEX, Giorgi et al. 2009) climate models and other bias-adjustment methods to fully comprehend the models' sensitivity to such corrections. This will be the main objective of my last secondment during this PhD, which could not be organized before the submission of this manuscript.

4.5 Synthesis

Despite an overall agreement that extreme precipitation follows a ≈7%/K rate of increase at the global scale, projected changes in the intensity of extreme precipitation are influenced by multiple factors, including large-scale and mesoscale dynamics, that can lead to large uncertainties at the regional scale. This study quantifies the uncertainty in the projected changes in extreme precipitation — while most studies look at the mean or median change across an ensemble of models — using a large subset of CMIP6 global climate models and a single high-emission scenario. I provide a first assessment of the 10-90% range in the RV20 responses at the grid-point scale and a global picture of the regions where changes in extreme precipitation are consistent with the CC rate. Our results suggest that uncertainty remains usually quite large (and has not decreased compared to the results of the former generation GCMs). Averaged globally, GSAT scaling ranges extend from about 0 up to a super-CC rate, with a median close to the CC rate. Uncertainty can be larger if changes in extreme precipitation are investigated for a given GWL. This may be an artefact of internal variability due to the lack of sampling which has a stronger relative contribution at lower GWLs compared to our selected very-high emissions scenario.

Our assessed CMIP6 uncertainty arises both from model uncertainty and internal variability, as only a few CMIP6 models provide large ensembles and our calculations are based on single runs from each CMIP6 model. Internal variability can be seen as a basic sampling uncertainty, which could be overcome by averaging across multiple members for each global climate model. Model uncertainty alone would lead to narrower ranges than those reported in this study. However, despite the widening induced by a non-negligible contribution of internal variability, our results show that the intensification of extreme daily precipitation is robust over most regions, with more than 90% of models simulating an increase of 20-yr RVs. I believe that this study helps strengthen our confidence in the intensification of extreme precipitation.

Most regions around the world exhibit a RV20 change consistent with the CC rate of ≈7%/K. Remarkably, about 83% of the global land fraction is consistent with this rate of change when scaled by ΔGSAT. Exceptions to this include limited areas over subtropical oceans (showing a significantly sub-CC rate), and parts of the equatorial Pacific and Sahelian ITCZ (showing a significantly super-CC rate). These findings are consistent with well-known projected changes in large-scale atmospheric circulation, i.e., strengthened subsidence over the subtropics and enhanced convection over the core of the ITCZ (Douville et al., 2021). Not surprisingly, the rate of change in the Arctic is particularly sensitive to the scaling applied, since this region is warming much faster than the global average. This example suggests that the spatial distribution of the warming (e.g., Arctic amplification, land-sea contrast) can be also responsible for changes in the low-level atmospheric circulation and, therefore, for the departure from the CC rate of intensification.

Due to the multiple uncertainties, the rate of change in extreme precipitation depicted here only represents a plausible 21st-century scenario. This hints at

the fact that we cannot produce a more accurate projection as long as we are faced with both strong model uncertainty and substantial (potentially irreducible) internal variability (not to mention uncertainties about future GHG emissions). Better filtering of internal variability would require using multiple ensemble members for each CMIP model. Therefore, I suggest to the modelling community consider producing a minimum number (at least 9 according to O'Neill et al. (2016)) of realizations for each selected emissions scenario in the forthcoming CMIP7 exercise.

Beyond internal variability, evidence suggests that modelling uncertainty also contributes to a large fraction of the reported uncertainty. This source of uncertainty is related to our limited knowledge of the key physical processes controlling the response of extreme precipitation that is simulated by both global and regional climate models. Thus the improvement of the current-generation GCMs and RCMs, along with the development and wider use of convection-permitting models (Lucas-Picher et al., 2021), could increase the reliability of projected changes in extreme precipitation. Bias adjustment on the raw model outputs can help reduce the model uncertainty, however, keeping in mind that different bias correction techniques have different limitations which makes it difficult to choose the optimum method Maraun et al. (2017). Other methods such as the development and application of observational constraints (Ribes et al., 2021) could be also very useful to constrain the response of both global and regional climate models.

In the middle of winter, I was finally learning
that there was an invincible summer inside me.

— Albert Camus

5

Changes in seasonality and circulation types

As quantified in Chapter 4, the intensification of extreme precipitation is a well-known consequence of global warming, which could have devastating consequences on human societies and the environment. Yet, beyond the increase in the magnitude and frequency of heavy precipitation events, and the related uncertainties in global climate projections, better quantifying and understanding the potential changes in the seasonality of such events is also a key question for adaptation strategies (Bevacqua et al., 2020). This chapter builds on a preliminary study based on CMIP5 models by Marelle et al. (2018) and further explores the seasonal shifts in the occurrence of extreme precipitation in the future, with a particular emphasis on Europe. The mechanisms behind these shifts are briefly explored based on an analysis of the dominant circulation types and their projected changes in an illustrative high-emissions scenario. The inter-model spread in the circulation response is also quantified, as well as its contribution to model uncertainties in the assessed seasonality changes.

5.1 The relevance of seasonality

The seasonality of the extremes and how it changes in the future is a relevant but rather less explored topic. Heavy precipitation events have intensified and occurred more frequently under a warming climate (Masson-Delmotte et al., 2021a). It has been shown that in a warmer world, where the atmosphere can hold more moisture and precipitable water, the global hydrological cycle becomes more active (Folland et al., 2001) and thus results in more frequent and severe precipitation events (Trenberth, 2005; Min et al., 2011; Stocker et al., 2014; Roderick et al., 2019; Myhre et al., 2019). Both observations and historical model simulations show that extreme daily precipitation has increased in many regions across the globe since

the mid-20th century (Du et al., 2019; Dunn et al., 2020; Sun et al., 2021b). More specifically, a significant increase in RX1DAY (cf. chapter 2, section 2.2) was observed from 1950 to 2018 over Europe (Sun et al., 2021b), where the 5 to 20-year events of RX1DAY during 1951-1960 became more common over recent decades (Van den Besselaar et al., 2013). Although the evidence is weaker over the Mediterranean (cf. Figure SPM.3 b, Masson-Delmotte et al. 2021a), recent studies also support such an observed intensification over Southeast France (Ribes et al., 2019).

However, there can be significant discrepancies among regions and seasons, with more evidence for increasing extreme precipitation in given seasons than in others (Madsen et al., 2014). Trends in the mean intensity of Mediterranean extreme rainfall are not always positive (e.g., Serrano-Notivoli et al. 2018). Positive trends in extreme precipitation intensity are more evident over northern Europe, although extreme rainfall trends may differ in different seasons (Irannezhad et al., 2017). Furthermore, the increase of extreme daily precipitation varies throughout the year, with regional simulations indicating that extreme precipitation increases faster in winter than in summer across Europe and that it may even decrease slightly in southern Europe during summer. The rain gauge observations in Australia from 1966-2012 (Zheng et al., 2015) also show that the extreme precipitation has increased significantly during summer but decreased during fall.

Climate change is likely to alter the annual cycle of extreme precipitation with regional shifts in extreme rainfall seasons around the globe where both the thermodynamic and dynamic effects contribute to changes in the frequency and intensity of heavy precipitation (e.g., Pfahl et al. 2017). The thermodynamic influence can be positive and relatively homogeneous globally, although the dynamical contribution varies significantly between regions and the pattern and size of the dynamic contribution differ between summer and winter. Pfahl et al. (2017) also indicate a possible global "shift of the seasonality of precipitation extremes towards the cold seasons". Among other things, precipitation extremes with high intensity and widespread geographical spread could contribute to extensive flooding, which potentially causes transportation disruption, infrastructure damage (Kendon and McCarthy, 2015), and a great deal of personnel casualty (Rappaport, 2014) and thus bring about immense socio-economic (Tebaldi et al., 2006; Schmitt et al., 2016; Stocker et al., 2013) and ecological (Mullan et al., 2012; Woodward et al., 2016; Paerl, 2018) impacts. Hence to understand the future risks of flooding, understanding the future seasonality of extreme precipitation is essential.

5.2 Projected changes in the seasonality of extreme precipitation

5.2.1 Seasonal Classification of RX1DAY

Along with calculations of RX1DAY, I also computed the particular day in a year when the extremes are occurring for each grid point and every year. Then I calculated the median day of the year for each CMIP6 model for relatively long periods of the historical simulations (1951-2014) and SSP5-8.5 projections (2051-2100) (cf. section 2.7.4). Instead of the empirical median, the circular median was

calculated using the algorithm developed by Berens (2009). A circular median was used as the date values are always cyclic, and using an empirical median will produce a different result from the expected as the date values may be spread throughout the year. This narrows down the distribution of RX1DAY in each grid cell and period to one representative median day. I then classify the median day as seasons based on the month of the year to which it belongs. The median day occurrences (of RX1DAY) are also used to quantify the number of days the extremes can be shifted, i.e. is there an early occurrence of extremes or a delayed occurrence? Furthermore, the day of the year is used to compute the seasonal frequency of occurrence of RX1DAY for each model and each time period, which is also used to analyse how the seasonal frequency of extreme precipitation will change over time.

5.2.2 Seasonality in CMIP6 models

Observations vs. CMIP6

Using the seasonal classification technique discussed in section 5.2.1, maps of extreme precipitation seasonality were produced for the historical period using the CMIP6 ensemble mean and the global observation data REGEN (cf. Chapter 2, section 2.1). Figure 5.1 depicts that the models can recreate the seasonality of heavy precipitation. Different colours in the maps represent four seasons; December-January-February (DJF), March-April-May (MAM), July-August-September (JJA) and September-October-November (SON). A good agreement is seen between the two maps. The multi-model median map is a bit smoother when compared to that of observation, which is expected as the median is estimated independently for each grid cell. There are slight regional differences between the maps (especially over Greenland), but over the rest of the globe performance of models in simulating the seasonality similar to the observation is notable. Even the areas covered by the different seasonal colours (as indicated by the colour bars) are comparable and close.

CMIP5 v/s CMIP6

The similarity and robustness of models in simulating the seasonality of extreme precipitation can be found by comparing our results with the previous works of Marelle et al. (2018). Our analysis using the CMIP6 models is almost identical to the already reported results using the CMIP5 models. There are subtle differences due to the different time periods and smaller sample sizes used in the two studies (Marelle et al. (2018) included 18 models, while here 30 models were analysed).

Comparison of the Figures 5.2 (Figure 3 a from Marelle et al. (2018)), which showcased the seasonality of the extremes in CMIP5 models and 5.1 b, indicates the ability of the CMIP6 models to capture the seasonality of RX1DAY has not much changed from the previous generation of models. During the historical period, a large percentage of extreme precipitation events in the tropics and the mid-latitudes tend to occur during the summer and fall (JJA and SON in the Northern Hemisphere; DJF and MAM in the Southern Hemisphere). Also, in

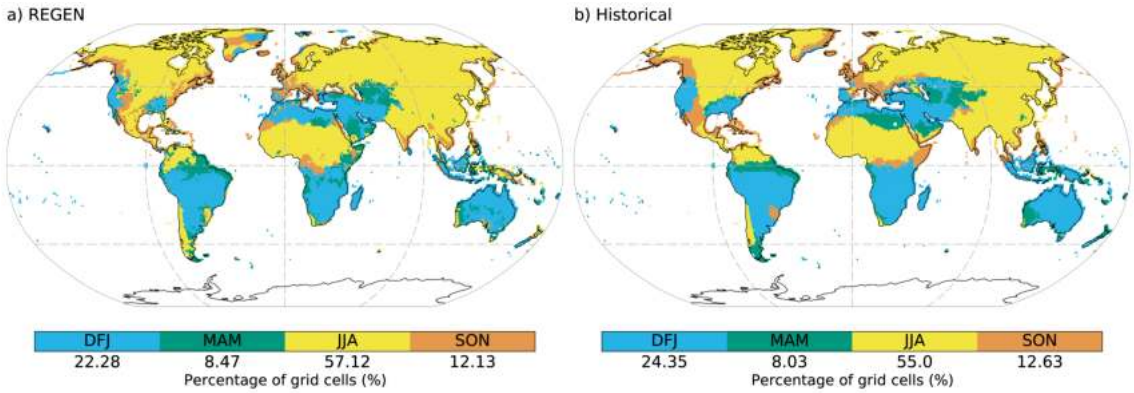

Figure 5.1: Season of the median day of the year of extreme daily precipitation in observational dataset REGEN (a) and in the multi-model CMIP6 ensemble (b) for the historical period (1951-2014). Four colours in the colourbar represent four different seasons; blue for DJF = December-January-February; green for MAM = March-April-May; yellow for JJA = June-July-August; orange for SON = September-October-November. The numbers provided below the colourbar indicate the percentage of the total land areas covered by each season when the extremes occur.

the northern hemispheric subtropics, the extremes tend to occur during winter (DJF)and spring (MAM).

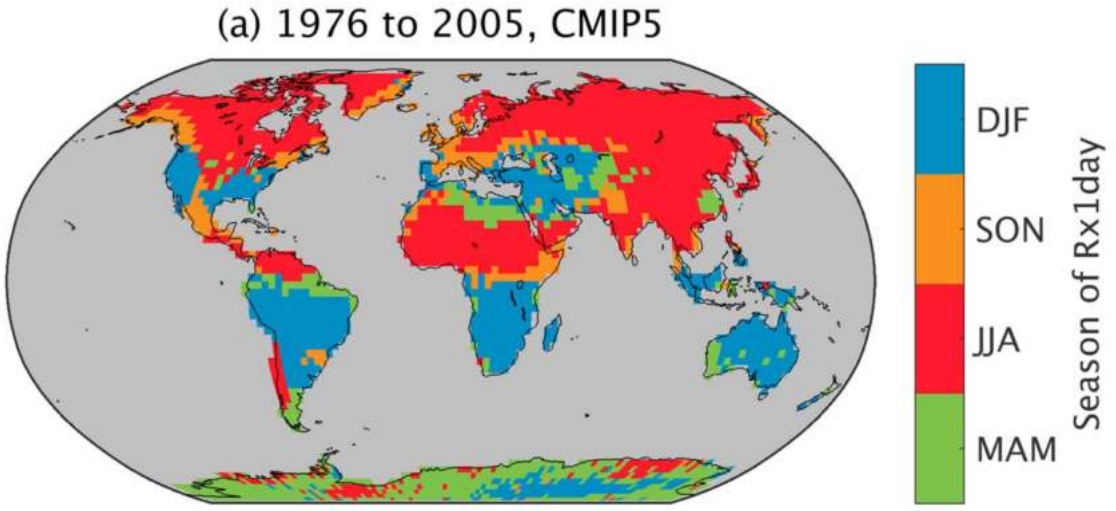

Figure 5.2: Same as Figure 5.1, but using the CMIP5 ensemble for the period 1976-2005. Source: Marelle et al. (2018), Figure 3 a

5.3 Global and regional changes in the seasonality of RX1DAY

The extreme precipitation changes at the end of the 21st century, using the highest emission scenario (here SSP5-8.5), are not expected to be homogeneous across the globe (Pfahl et al., 2017). Different regions exhibit different responses, with some marked by significant seasonal shifts. During the end of the 21st century, the seasonality can change significantly, as shown in Figure 5.3, in several regions by more than a month. There is a delayed occurrence of extreme precipitation over most continental areas, which means that extreme precipitation occurs later in the year. Some regions where the delay in the extreme precipitation can be clearly seen are over the Northern Hemisphere's polar regions, Africa, and Central and South America. Contrarily, RX1DAY happens earlier in Central and Southwest

Asia and large parts of North America. Several regions show small or inconsistent changes in combination with a low model agreement, as seen over South and East Asia, the equatorial regions, most of the United States, and Oceania. Over Europe, the CMIP6 models show a mixture of responses. Over the Mediterranean, many parts of central Europe, the UK and Scandinavia, a delayed occurrence of extremes is seen, while over the north Scandinavian coast and Eastern Europe, there are early occurrences of extremes. Figure 5.3 helps to infer that the seasonality of the extremes in the future is expected to change, but this change is not homogeneous across the globe.

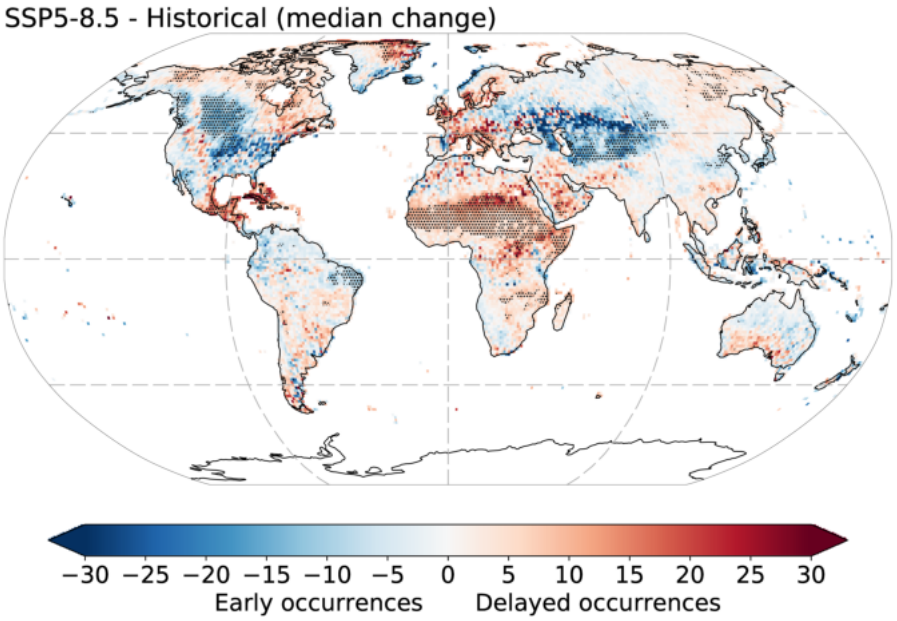

Figure 5.3: The multi-model median change in the median day of the year of extreme daily precipitation between the end of the 21st century (2051-2100) using the SSP5-8.8 scenario and the historical period (1951-2014). Stippling indicates the areas where more than 66% of the models agree on the sign change. Blue shades represent an early occurrence and the red shades show areas marked with the delayed occurrences of extreme precipitation.

To go a step further, I have also investigated the spread in the median day changes of extremes. Figure 5.4 shows the spread in the distribution of median day changes in the RX1DAY. There are widespread areas with a large spread in the seasonality changes, although most of the northern hemisphere poles, Asia, the Saharan and Sahel region, North America and the equatorial regions are characterised by a low spread. In particular, a large spread is found over Europe, north and south Africa, Arabia, South-Western Asia, South and Central America and the maritime continents. It is to be noted that the areas with a relatively small spread also coincide with the areas where the historical and future extreme season is JJA, indicating that there are no significant shifts in the seasons of extremes over these areas in the future (cf. Figure 5.1 b; also see appendix Figure A.16 for future seasonality). The large spread in the seasonality changes coincides with the areas where the extreme season is either of any other three seasons except JJA. This partly indicates that most models are good at simulating the wet seasons, especially the monsoon, in the northern hemisphere. While over other regions, different models simulate different peak seasons, some in fall while others in winter.

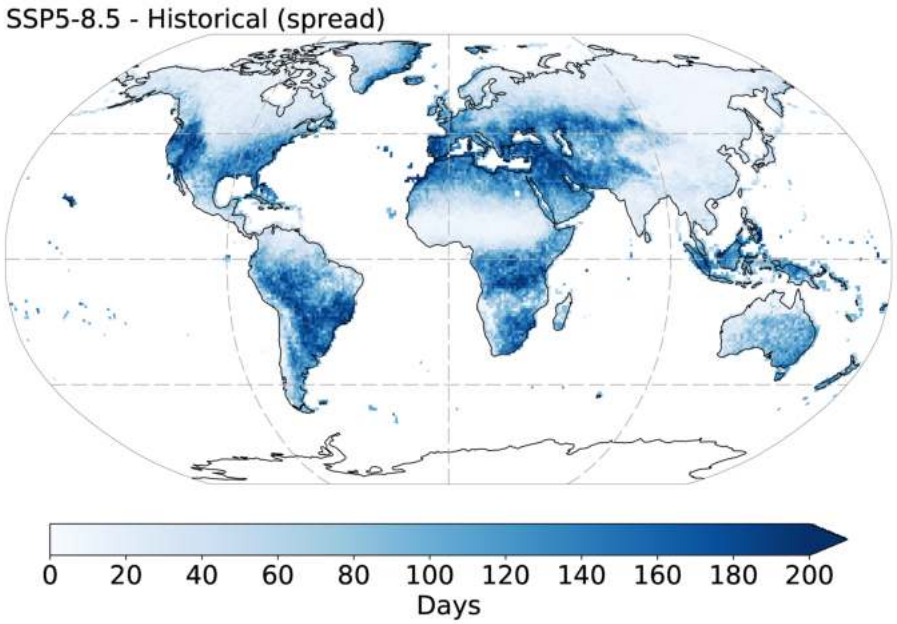

Figure 5.4: The multi-model spread of change in the median day of the year of extreme daily precipitation between the end of the 21st century (2051-2100) using the SSP5-8.8 scenario and the historical period (1951-2014). Darker shades of blue indicate a large multi-model spread.

The North American continental region and the central Sahel region are two regions that I say with much confidence that the extreme seasons will occur early or delayed (respectively) due to the low spread and high model agreement over these areas. Here I choose to focus on Europe and three different subdomains. Europe is chosen for further analysis due to the mixed response to the changes in the seasonality of extremes and the large spread of these changes (Figure 5.3 and 5.4). The choice is also partly made by the influence of a collaborative work (Lormendez et al., 2022, *to be submitted*) that will focus on the dry extremes over Europe. The subdomains that were chosen over Europe have different climatologies and seasonalities, and they are 1) North-West Mediterranean (NWM), 2) Scandinavia (SCD) and Central Europe (CEU). They also represent three different responses to the seasonality changes and their spread.

5.3.1 Seasonal Frequency changes of RX1DAY over Europe

As discussed in the earlier section, the present-day preferential seasons of extreme precipitation can shift to a different one in the future. I have evaluated the changes in the seasonal frequency of the extreme precipitation and found that the changes in the annual cycle of the extremes have definite seasonal differences. Figure 5.5 depicts the seasonal frequency changes of the extreme precipitation. The summer (JJA) decrease in the occurrence of RX1DAY events is balanced by a limited increase across all other seasons, with +2.64, +0.51, and +1.51 % increases in DJF, MAM, and SON, respectively. Summer extremes are found to reduce in numbers, with a -4.68 % decrease in frequency. There are substantial regional fluctuations in the frequency changes over Europe. Summer and fall witness an increase in the frequency of extremes over Scandinavia's north coast, while winter and spring show a decrease in the frequency. In the Mediterranean, the frequency is higher in

the winter and lower in the summer. Similarly, in Central Europe, the frequency of extremes in the JJA season has decreased while the DJF season has increased. Delayed and early occurrence of the extremes in a year, as illustrated in Figure 5.3, is linked to changes in the frequency of the extremes. This is also linked to other physical aspects, such as changes in the water cycle and circulation (Pall et al., 2007; Norris et al., 2019), which I will examine in the following sections. It should be emphasized that a decrease in the frequency of extremes (Trenberth, 1999; Allen and Ingram, 2002; Trenberth et al., 2003; Stephens and Hu, 2010; Trenberth, 2011) does not always imply a decrease in their maximum intensity.

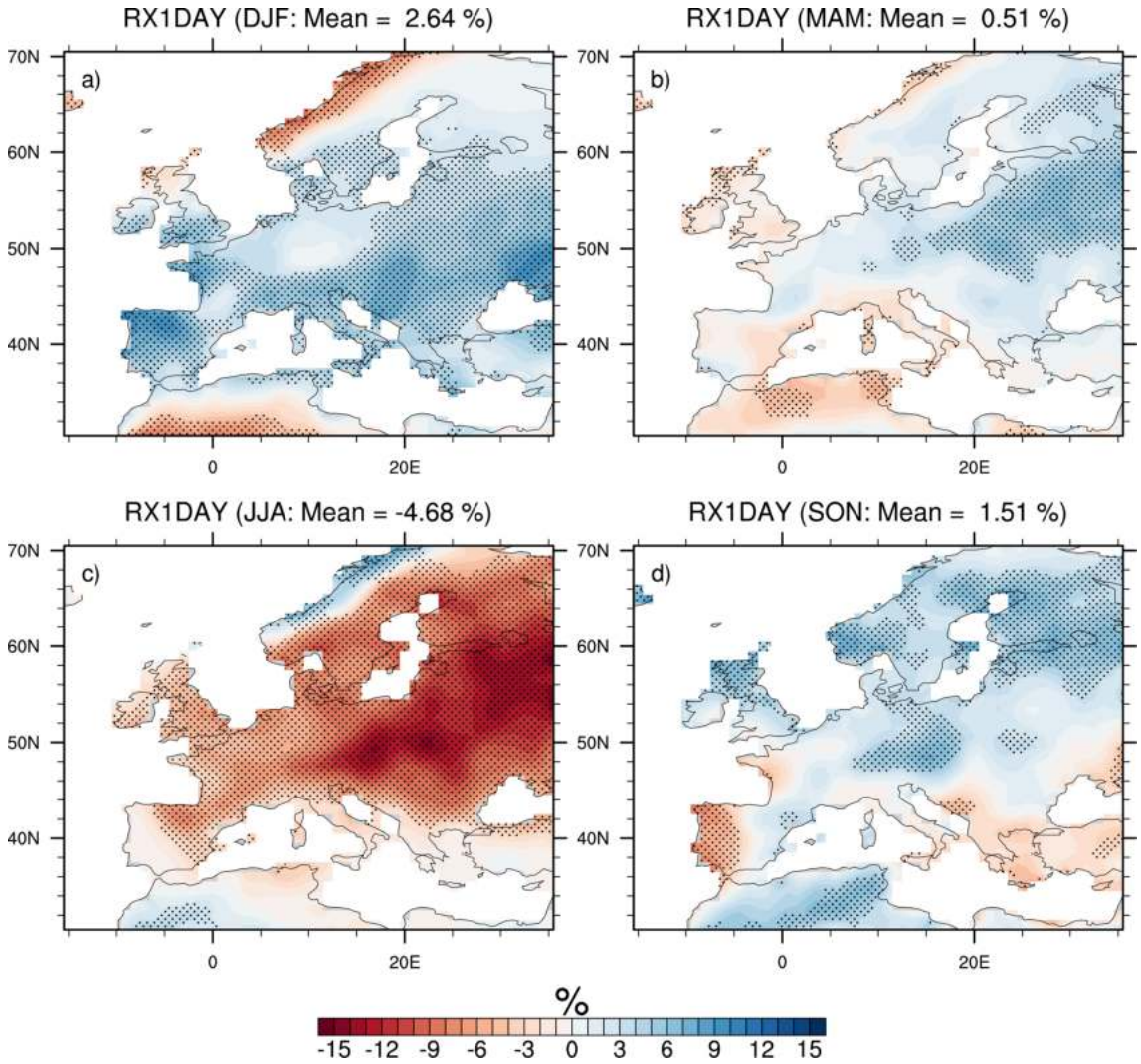

Figure 5.5: Maps depicting the multi-model median changes in the frequency of RX1DAY in different seasons over Europe. Stippling indicates the areas where at least 66% of the models agree on the sign change. The mean values given above each panel indicate the areal average of the changes over the domain for each season. The changes are calculated in percentage.

I have examined the annual cycle of extreme precipitation occurrences across Europe to determine whether there is a shift in the frequency of extreme precipitation. Similar to the maps in Figure 5.5, the annual cycle of the extremes follows a seasonal pattern (cf. Figure 5.6). Except for June, July, and August, all of the months' monthly median values of extreme frequency are positive. September has a negative median value as well. A sharp decrease in the frequency of extremes

can be witnessed from May to August, followed by a sharp increase from August. The blue and red bars in the figure indicate the same thing, but red shows the annual cycle of extreme frequency after removing a possible climatological bias by shifting the peak month to a fixed peak month (M_0), which in this case is October. Thus, aligning the months according to M_0 allows us to evaluate the results relative to a peak month and may be useful to avoid possible discrepancies in the model responses associated with the different model ability to replicate the observed annual cycle in the present-day climate. However, our expectation of a decrease in the spread appears to be false. This result indicates that the annual seasonal cycle response is not much sensitive to the model bias over the historical period. A comparison of the results before and after shifting reveals that the red curve is smoother and shows an increase in the frequency of the extremes from August to September. This increase is also visible in the blue curve. This suggests that the extreme occurrence has shifted from JJA to SON or that the seasonality has indeed been delayed to later in the year.

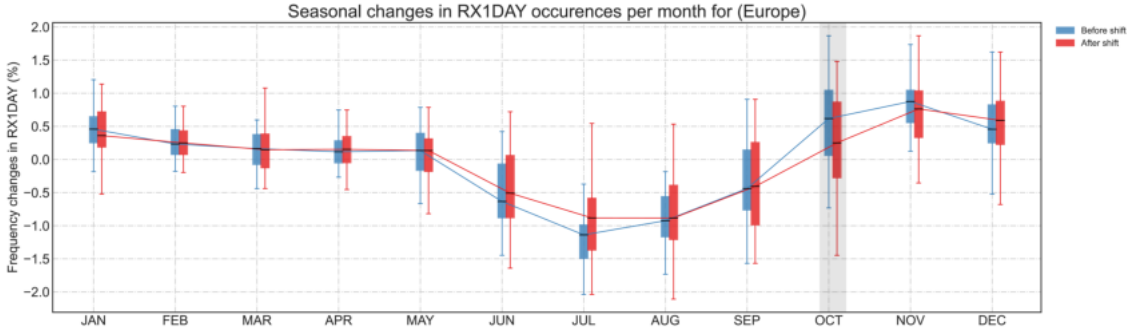

Figure 5.6: Box plots represent the annual cycle of the changes in the frequency of extreme precipitation. Each box represents the frequency change values for a specific month from the 30 CMIP6 models used in the study. The blue boxes show the annual cycle of the extreme where the values of the frequency change correspond to the models' peak months. The red boxes depict the annual cycle after shifting peak months of each model to a fixed month (M_0) based on the climatological peak month. The peak month used in this example is October, marked by light grey colour in the plot. Each whisker represents the spread in the monthly values; the box ends are the 25th and 75 percentile; the back horizontal line in each box shows the median values.

Understanding the projected Seasonality Changes

From the previous sections, it is now clear that the seasonality of the extreme precipitation events is projected to shift in the future. Our seasonality classification technique only tracks an overall displacement sooner or later in the year and has limitations in that it is not intended to capture more complicated changes in the shape of the distribution of heavy precipitation events given the use of the RX1DAY statistics. Additionally, there is a significant regional spread for the shifts in seasonality. Hence, one question at the heart of this study is, what are the mechanisms that are potentially responsible for the seasonality changes and the consequent large spread? To better understand the projected changes, more research with a regional focus is required. I extended our inquiry into the causes

and mechanisms of extreme seasonality shifts in precipitation. To do so, I narrowed the scope of our investigation from a global to a regional one, emphasising Europe. As described in section 5.3, I divide the European domain into subdomains based on their various climatologies and dominating circulation patterns to better comprehend the regional shifts. Changes in the atmospheric circulation turned out to be one of the plausible candidate variables that could be analysed to explain the seasonality changes. Analyzing changes in future circulation patterns relative to the past or current day can provide crucial information on the state of the future atmosphere. The direction of moisture transport in a given season can be determined by the mean anomalous wind flow patterns, which can either promote or prevent excessive precipitation.

5.4 Use of Circulation types

Given the strong relationship between synoptic patterns and local climate variables, atmospheric circulation is often described as one key driver of the day-to-day variability of most surface meteorological parameters including extreme precipitation. The joint research with Lormendez et al., (2022, *to be submitted*) has led to the computation and analysis of the dominant synoptic circulation types (CTs; cf. section 2.5) over Europe, as observed according to the ERA5 reanalyses and as derived from the historical (1951-2014) and future climate (2051-2100; SSP5-8.5 scenario) simulations of a large subset of CMIP6 models. The objective of this collaborative work is to understand the interplay between the frequency changes of the CTs and the dry extremes over Europe. This led to the idea that the CTs have the potential to prove to be a good framework that can be utilized to better understand the seasonality shifts in projected extreme precipitation and their model dependence, especially the relation of the atmospheric circulation in changing the seasons of extremes. The simplicity in terms of the input data (mean sea level pressure), the relatively easy interpretation of the underlying airflow indices for the resulting circulation types and its transferability to other regions with a simple implementation also support our choice to use this classification. In the subsequent sections changes in the frequency of CTs and extreme precipitation during the JJA and SON seasons will be discussed, primarily because they are the seasons when most of the extreme occurs in Europe, as illustrated by Figure 5.1.

5.4.1 Evaluation of circulation types in CMIP6

The models are evaluated according to their ability to reproduce the seasonal frequencies averaged over the historical period (1951-2014). Assessing the skill of CMIP6 models in classifying and reproducing the realistic frequencies of different circulation types is based on the comparison with the state-of-the-art ERA5 reanalysis (Hersbach et al., 2020). This is considered a very reliable dataset for this purpose given the assimilation of both in situ and satellite observations over Europe. Our focus is on two seasons, JJA and SON, as previously mentioned. In the following subsections, I look at the seasonal spatial differences between the

frequencies derived from the reanalysis and models for each CT (only cyclonic type is shown) at each grid point and the average values of the historical frequencies of each CT. The performance of CMIP6 models is assessed through the spatial correlations between reanalysis and models' frequencies of CT derived from the seasonal average over the historical period. Taylor diagram (Taylor (2001), cf. Chapter 2) are employed to assess this spatial distribution.

Present day frequency of CTs in models

The absolute frequencies throughout the entire European domain and three different subdomains for relevant JJA and SON seasons during the historical period are compared to see how accurately the models reflect the circulation patterns compared to the ERA5 reanalyses. The seasonal frequencies for each CT are depicted in Figure 5.7. Overall, models can reproduce CT seasonal frequencies, and reanalyses and the multi-model mean (MMEM) have a reasonable agreement. The frequency distribution averaged over the entire domain for reanalyses, and the MMEM shows that the most common types of CTs are anticyclonic (A) and unclassified (U). The least frequent types vary with season, and the models also agree on this distribution. Aside from the A and U, the cyclonic (C) type dominates throughout summer and fall. The Northeasterly (NE) and Easterly (E) types appear to be more common in summer. On the contrary, these are less common in autumn, while the South Westerly (SW) and Westerly (W) varieties become more common.

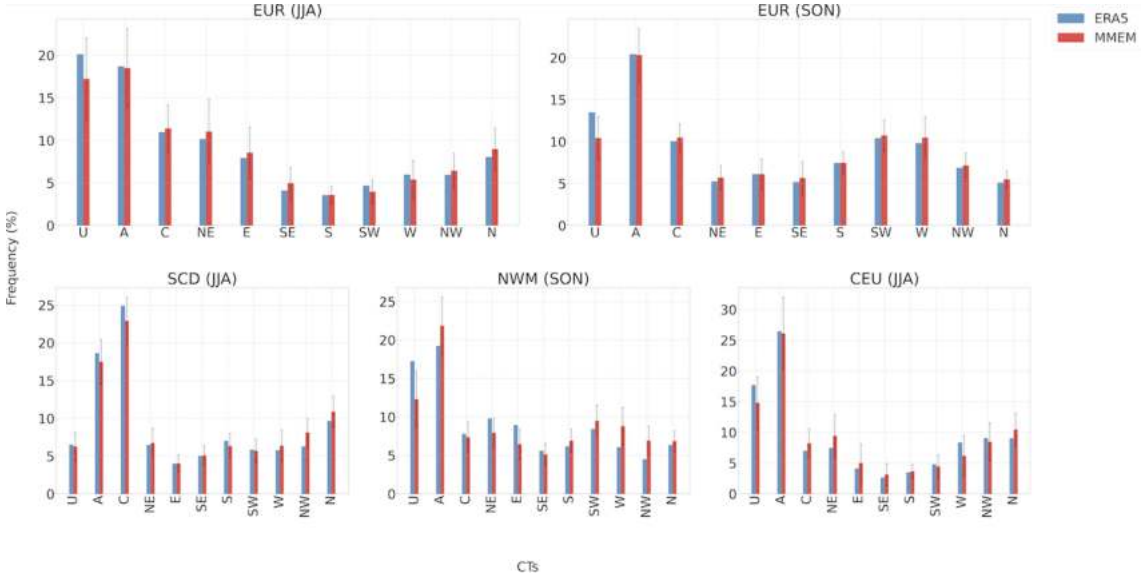

Figure 5.7: The present-day values of frequency (in %) of the combined 11 circulation types (CTs) for ERA5 and the CMIP6 ensemble. The error bars represent the multi-model spread in the present-day values of the frequency. Different panels illustrate the evaluation of the CTs for different seasons and subdomains as indicated by the subtitles. EUR = Europe; SCD = Scandinavia; NWM = North-West Mediterranean; CEU = Central Europe.

However, the relative frequencies are different for the various subdomains. The C type is the most common in the Scandinavian (SCD) subdomain during the summer, followed by the A and the Northerly (N) types. Whereas in the North-West Mediterranean (NWM) and Central European (CEU) subdomains, A is the most prominent in autumn and summer. The U type follows the A type in occurrence

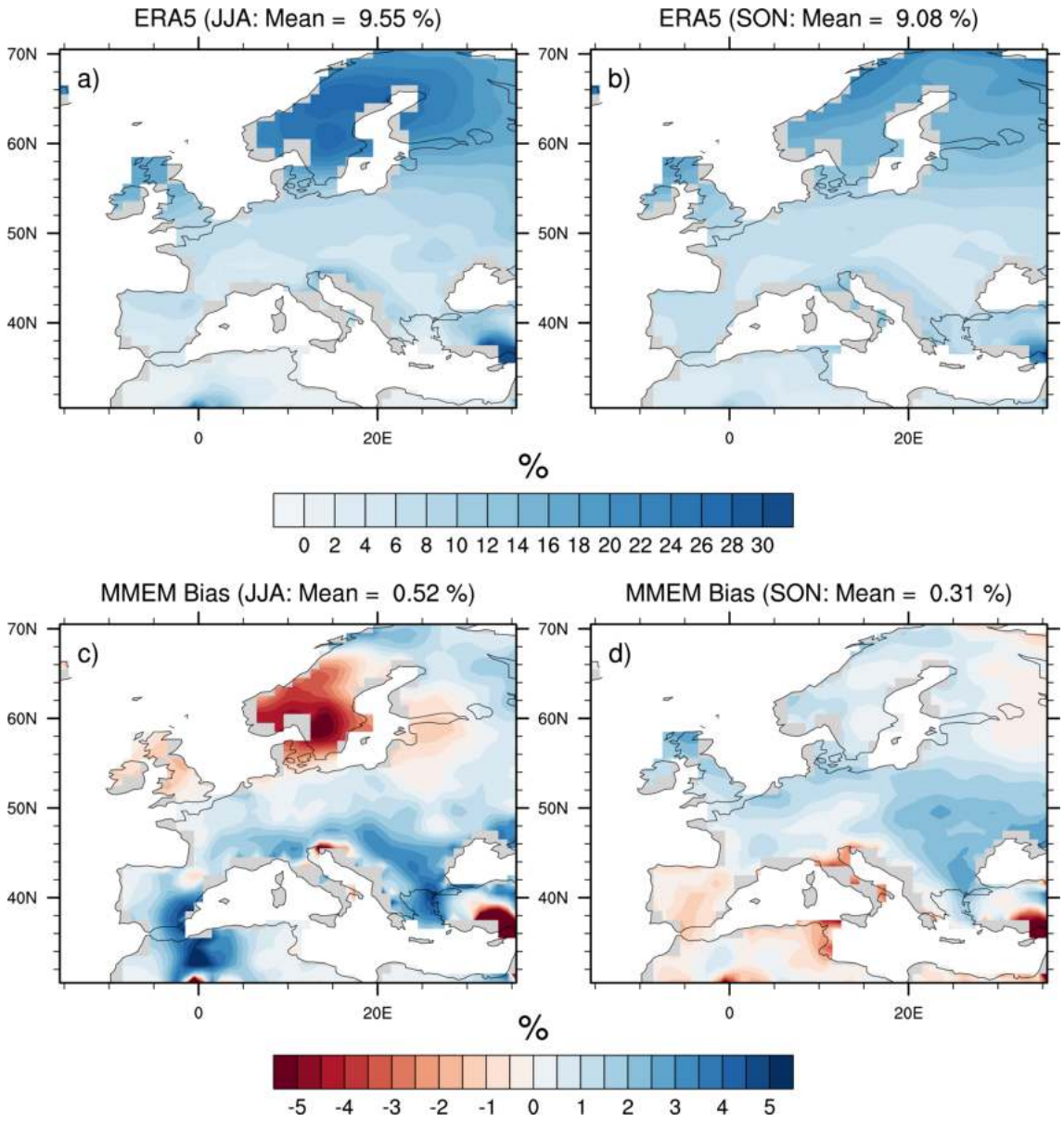

Figure 5.8: Maps illustrating the historical values of the seasonal frequencies (a, b) of the cyclonic type from ERA5 reanalysis and the corresponding biases (c, d) of the CMIP6 multi-model mean. The frequencies are calculated in %, and the maps illustrate the bias and the observed values for JJA and SON seasons. The mean values given above each panel indicate the areal averages.

throughout these subdomains, although it is the least common CT across the SCD in summer.

The ability of models to capture the spatial patterns of relative CT frequencies over Europe is evaluated by comparing them to corresponding CT from ERA5 over the same recent period. Although any CT can be used for comparison, I chose first to evaluate the cyclonic type. The MMEM was calculated for the CMIP6 models to compare the CT over Europe with the reanalysis data. Figure 5.8 illustrates the historical values (panels a, b) of the seasonal (JJA, SON) frequencies for cyclonic type from the ERA5 reanalysis and the corresponding biases (panels c, d) of the MMEM. Although the model can simulate most geographical features of CT frequencies as detailed by the ERA5, there are disparities in spatial repre-

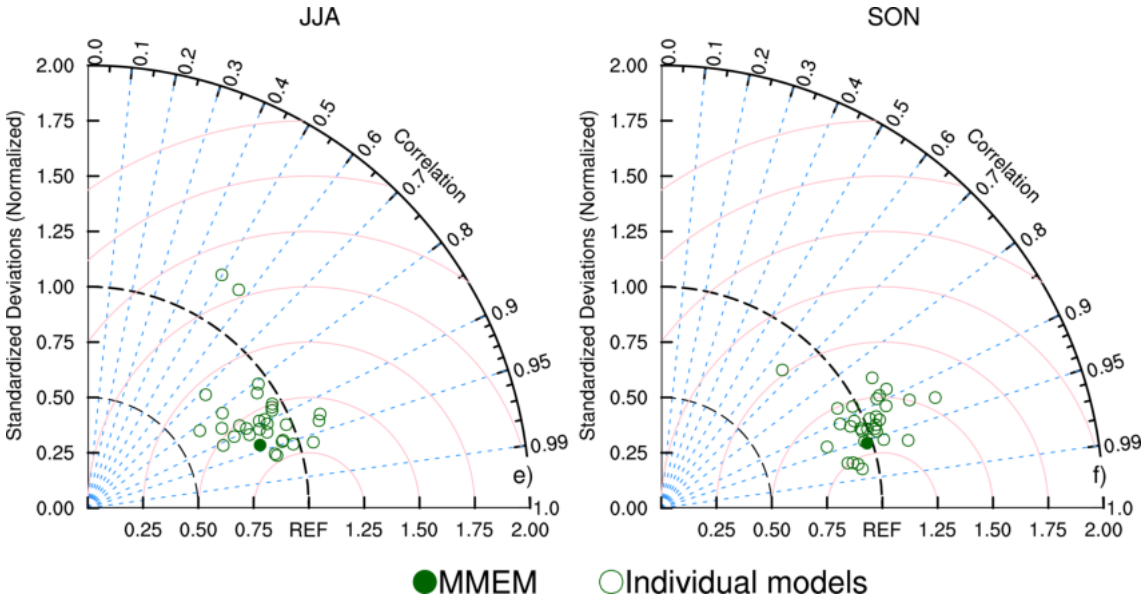

Figure 5.9: Taylor diagram measuring the performance of each CMIP6 model (30 here) in simulating the seasonal frequency of cyclonic type for JJA (a) and SON (b) over Europe for the historical period from 1951-2014. The radial axis is the normalized standard deviation while the angular axis is the centred pattern correlation. The reference data set is ERA5 (REF). The pink concentric circles show the centred RMSE. Individual models are marked in green circles and the multi-model ensemble mean is in the solid green circle.

sentation among the models when replicating the CT frequencies (Figure 5.8 c, d). Models overestimate the C type throughout the land in both seasons. A few places are under-estimated, particularly across the Scandinavian peninsula and the United Kingdom in JJA and Spain and the Mediterranean in SON. It is worth noting that the total average bias is relatively low (0.52% for JJA; 0.31 % for SON), demonstrating the realistic behaviour of the CMIP6 multi-model ensemble.

Figure 5.9 shows the Taylor diagrams for seasonal frequencies of the cyclonic type over Europe and allows us to assess the performance of individual CMIP6 models. For both seasons, there is an overall good correlation among the models with the reanalysis, with the MMEM with ≈95% correlation for both the seasons. For JJA, the correlation of individual models is low, and the spread in the normalized standard deviation is larger than that in SON. This suggests a poorer performance when comparing the summer to the fall. Indeed there are evident differences among the models. For example, the lower correlation and large spread (greater than unity) in two models in the JJA season indicate poor agreement. During SON, most of the models fall outside the 1 standard deviation curve but have a high correlation value to the reanalysis. While for the JJA season, 25 out of the 30 models used are within the 1 standard deviation curve and the correlation is a bit lower than the SON. Overall, most of the models can simulate the patterns of the CT frequencies reasonably well with a few differences between the seasons.

5.5 Linking changes in seasonality to circulation types

The seasonality changes in extreme precipitation have been explored in the previous section 5.3.1. Here I was interested in knowing to what extent the CT changes

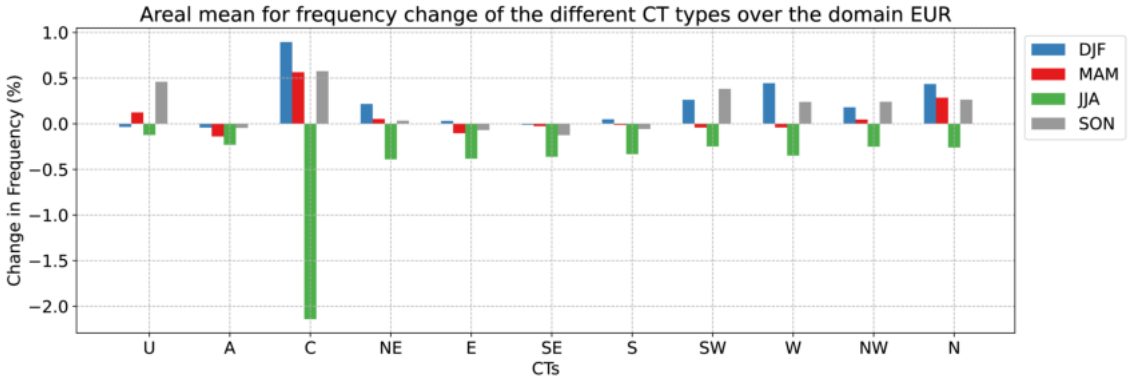

Figure 5.10: CMIP6 multi-model mean changes in the seasonal frequency of the 11 different circulation types (CTs) that occurred for the RX1DAY days during the period 1951-2014 relative to 2051-2100. The bars indicate the average values of the occurrences of CTs over the European domain. Different seasons are indicated by the colours as shown in the legend.

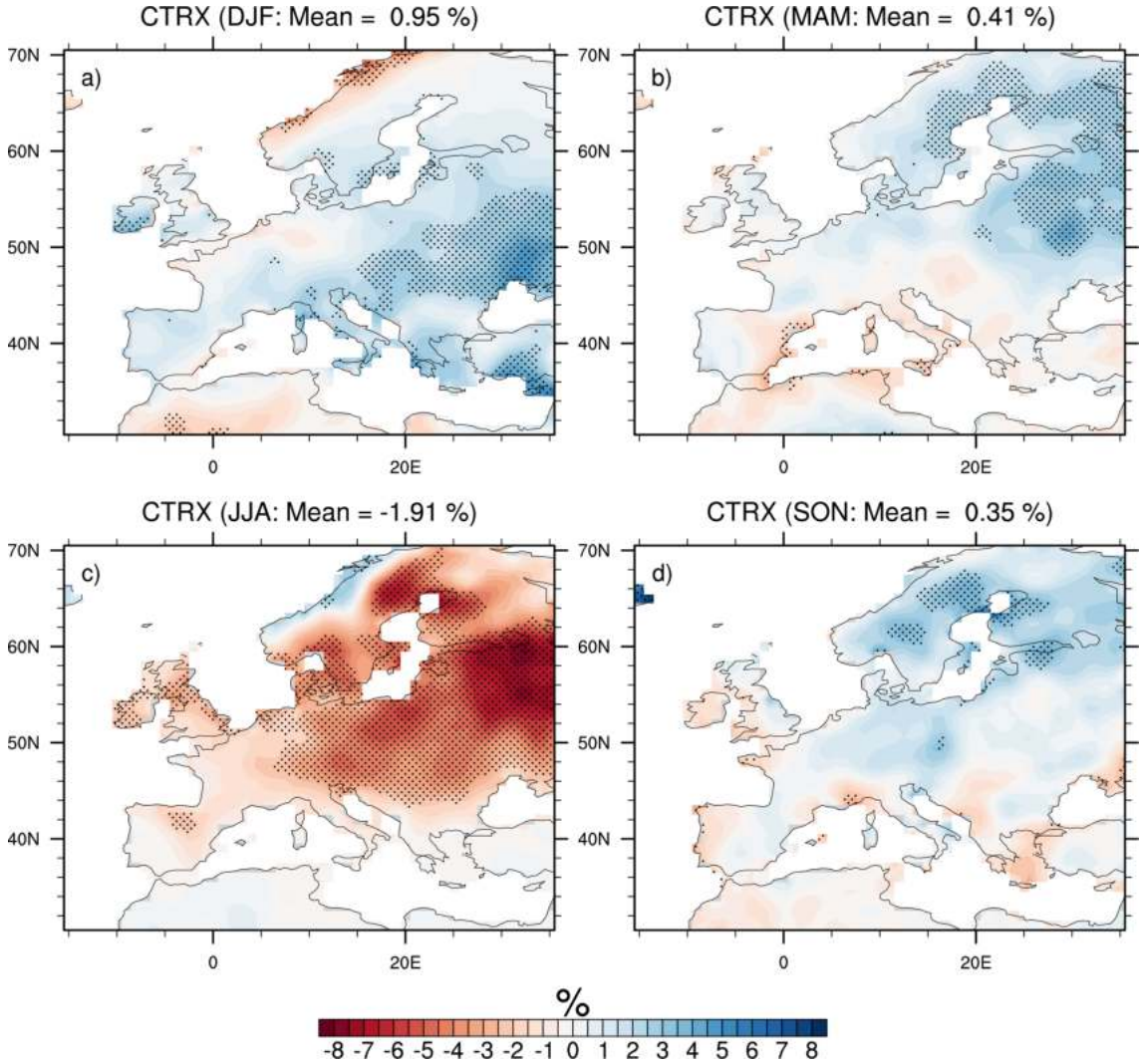

Figure 5.11: Maps depicting the multi-model mean changes in the frequency of cyclonic circulation type for the RX1DAY days (CTRX) for different seasons over Europe. Stippling indicates the areas where at least 66% of the models agree on the sign change. The mean values given above each panel indicate the areal average of the changes over the domain for each season. The changes are calculated in percentage.

account for the changes in RX1DAY seasonality and the inter-model spread in this response. I begin by looking at how the average frequency of each circulation type has changed over time for each season. The change in each circulation type that occurred just for the RX1DAY days is depicted in Figure 5.10. Because the values only show changes in the CT during RX1DAY days, they are directly tied to changes in extreme precipitation. The changes in the cyclonic type are the most during all seasons. A key point to note is that for the JJA season, all CTs changes are expected to decrease, with the cyclonic type experiencing the most significant decline. The cyclonic type shows the largest changes in all seasons when indexed by RX1DAY days, suggesting that it is one of the dominant CTs that causes changes to the seasonality of the extremes over Europe. Obviously, there are local variations, with some types being more sensitive in specific domains (Figure A.17).

The projections based on the SSP5-8.5 scenario point that the cyclonic type may be subjected to substantial changes in the future, with increased frequency in all seasons except summer. The regional patterns of these changes for the cyclonic type during different seasons are depicted in Figure 5.11. The map illustrates that regional changes are not uniform across the European continent. Even if the overall frequency of DJF, MAM, and SON is projected to increase, there are areas with a reduction in cyclonic type frequency, notably over the Mediterranean, Scandinavian coast, etc. Moreover, JJA exhibits a widespread decline in frequency throughout except for the Scandinavian coast, which may suggest a potential dynamical contribution to a future summer drying (increased precipitation deficit) over much of the European continent. Although it is beyond the scope of the study to assess whether such a change is already discernible in ERA5, it should be emphasized that a former study has reported a decrease in the Northern Hemisphere summer extratropical cyclone activity over the last 35 years (Chang et al., 2016).

	U	A	C	NE	E	SE	S	SW	W	NW	N
DJF	0.36	0.07	0.73	0.28	0.28	0.16	0.19	0.41	0.64	0.61	0.28
MAM	0.09	0.31	0.76	0.44	-0.04	-0.13	0.14	0.47	0.48	0.68	0.63
JJA	0.61	0.46	0.91	0.45	0.42	0.55	0.57	0.64	0.59	0.56	0.51
SON	0.24	0.2	0.59	0.04	0.17	0.2	0.39	0.63	0.6	0.31	0.23

Table 5.1: Spatial correlation values between the frequency of the RX1DAY and different circulation types for all seasons.

Also noticeable is the similarity of Figure 5.11 with changes in extreme precipitation frequency, as indicated in Figure 5.5 in section 5.3.1. There are remarkably similar spatial features between the two maps in all four seasons. The decrease in the frequency of extremes in summer corresponds to a decrease in the frequency of the cyclonic type circulation, and the rest of the seasons are marked by an increase in the frequency of extremes and cyclonic type. As shown in Table 5.1, the high correlation values state that the mean regional frequency changes

of extremes are closely related to the regional frequency changes of cyclonic types (other CTs are also related, but the cyclonic type is the dominant one). The following section will assess the CT influence on frequency variations in extremes as a possible purely dynamic contribution that should be distinguished from additional frequency changes that may occur within a given CT category.

5.5.1 Decomposition of precipitation extremes based on conditional probabilities

In order to assess the link between CTs and extreme precipitation, I consider using a linear decomposition (Cattiaux et al., 2013) of a mean variable X($\overline{X}$) as the mean of conditional probabilities x_k weighted by the frequencies of occurrence f_k:

$$\overline{X} = \sum_k f_k x_k \tag{5.1}$$

where $f_k = N_k/N$ the frequency of occurrence of the kth CT and x_k the conditional mean of the CT k.

Using Eq. (5.1) the large scale dynamics to a difference of $\overline{X}$ can be estimated. Taking the difference between the future (index F) and the historical (index P) climates, Eq. (5.1) becomes:

$$\begin{aligned}
\Delta^{F-P} =& \overline{X}^F - \overline{X}^P = \sum_k f_k^F x_k^F - \sum_k f_k^P x_k^P \\
&= \sum_k (f_k^F - f_k^P) x_k^P + \sum_k f_k^P (x_k^F - x_k^P) \\
&+ \sum_k (f_k^F - f_k^P)(x_k^F - x_k^P) \\
&= \underbrace{\sum_k \Delta f_k \cdot x_k^P}_{BC} + \underbrace{\sum_k f_k^P \cdot \Delta x_k}_{WC} + \underbrace{\sum_k \Delta f_k \cdot \Delta x_k}_{RES}
\end{aligned} \tag{5.2}$$

where BC (between class) represents the part of the total difference which is due to the differences in frequencies of occurrence of CTs, and WC (within-class) the contribution of differences within the CTs, while RES (Residual) is a mixing term.

5.5.2 Physical understanding of decomposed components

The proposed WC/BC framework is aimed at quantifying two distinct components of changes in the frequency of extremes. The WC class describes the changes within a specific CT category, whereas the BC class describes the changes that occur relative to changes in the occurrence of the various CTs. The WC effect can be related to both thermodynamic and mesoscale dynamic processes. The thermodynamic factors include the temperature and the moisture content in the vicinity of the storms, which can cause the changes in the storm dynamics as-

sociated with a particular CT at the regional scales. In contrast, the BC effect is primarily related to changes in the large-scale dynamics, namely changes in the frequency of the dominant CTs.

For the JJA and SON seasons, Figure 5.12 depicts the individual contributions of the WC, BC, and RES components for each CT over the EUR and subdomains. Better identification of the primary circulation type responsible for extremes' seasonality changes is possible by splitting changes in the seasonal extremes based on their contributions from the CT. Further deconstruction of the extremes associated with individual CTs such as WC, BC, and RES allows us to understand better the factors that may contribute to an increase or decrease in the seasonal frequency of extreme precipitation. Figure 5.12 shows that the cyclonic type is the dominant type across Europe and all subdomains, except for central Europe, resulting in seasonally changes in extremes. The interplay between the BC and WC components balances the total change in extreme precipitation frequency. The effects from the individual components counteract the total occurrences of extremes for the cyclonic type, especially over the entire European domain during the SON season and the subdomains SCD and NWM for the JJA and SON seasons, respectively. This suggests that severe events are linked to the interaction of dynamic and thermodynamic factors at both the local and regional scales. In contrast, there are instances where the individual components add to each other, particularly in the Central European domain and throughout Europe during the JJA season. It is worth mentioning that, in addition to the cyclonic type, other CTs can play a significant role, particularly when focused on a smaller domain.

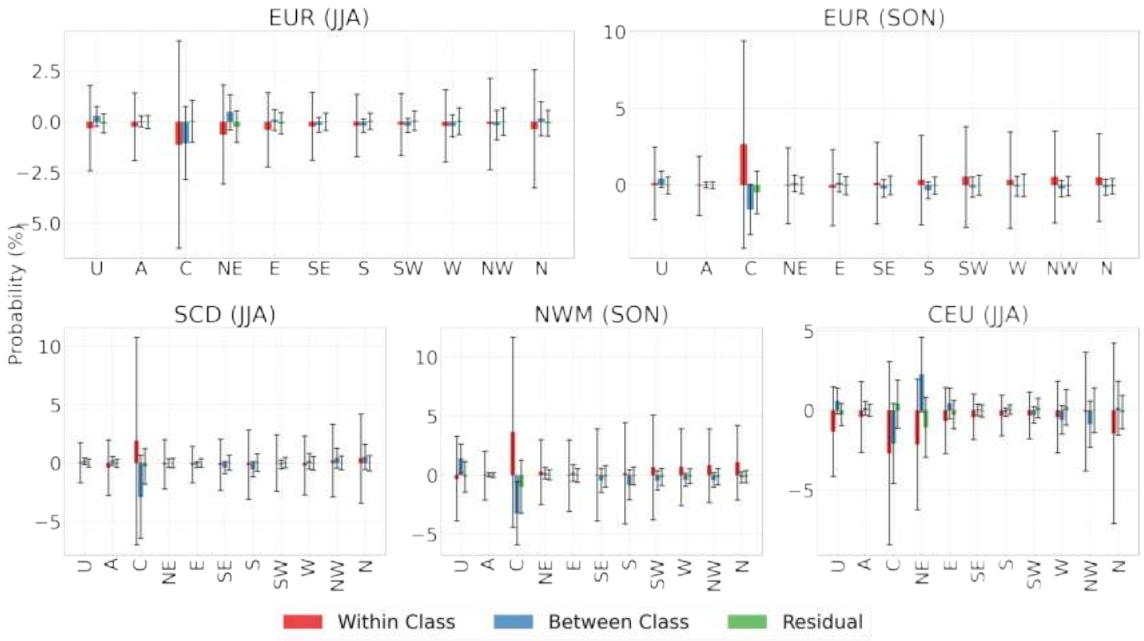

Figure 5.12: Bar plots illustrating the multi-model mean and spread of the probability of three decomposed classes for all the 11 circulation types (CTs). Each panel depicts the figures for different seasons and subdomains as indicated by the subtitles. The decomposed classes include within class (red), between class (blue), and residual (green).

Our method to split the changes in the total frequency of extremes into three contributions (WC, BC and residual) is depicted in Figure 5.13. The further

decomposition of the influence from different CTs gives us an idea about the different forces that underplay leading to the changes in seasonality. Figure 5.13 d, h depicts the sum of three decomposed components from all circulation types at all grid points across Europe for the JJA and SON seasons, based on Eq. 5.2. The WC makes the most significant (positive or negative) contribution for both seasons. A striking contrast can be seen between the seasons. For summer, the average contribution from all components is negative, implying that the frequency of summer extremes will decrease in the future. In autumn, however, the picture is evidently different and well established, with a consistent negative contribution from the BC and a widespread positive contribution from the WC, with average values of -2.26 % and 4.65 %, respectively. The sum of the three components (5.13 d and h) for both seasons is essentially the same as the seasonal frequency of RX1DAY, as shown in Figure 5.5, acknowledging our calculations are accurate. A meaningful result here is that the contribution of the WC and BC can be linked to the respective decrease and increase in the frequency of extremes in the summer and autumn. In both seasons the value of within-class changes is most dominant and could be controlling the total changes. In the summer, negative WC values suggest a possible decrease in the occurrence of favourable thermodynamic conditions leading to extreme precipitation. This may include a model-dependent near-surface drying (Douville and Plazzotta, 2017; Douville et al., 2020) associated with a stronger convective inhibition (Chen et al., 2020). The BC contribution is likewise negative but low, similar to the residual component, indicating that during JJA, changes in CT frequency and hence large-scale dynamic contributions are limited but non-negligible. The negative signals in all components point to a future (high emission scenario, SSP5-8.5) with fewer extreme precipitation occurrences. However, as seen in Figures 5.13 and 5.5, the SON season experiences an increase in the occurrence of extreme precipitation.

During SON, WC is the primary contributor to the total change (increase) in the frequency. In addition, BC contributes a net negative and significant amount to the total frequency. The BC and WC have an overall offsetting effect in SON, but their contributions complement each other in selected locations, like Spain and the Scandinavian coast. The rise in extreme precipitation events in the autumn can be linked to an increase in the thermodynamic feature associated with specific CTs, allowing for more extremes. In the future, the alteration of the mesoscale storm dynamic specific to the CT regime may promote an increase in extremes during SON. While BC, as seen earlier, is also a significant contributor but leading to a decrease in the extremes. Hence from the preceding two examples, it is evident that large-scale dynamics contribute significantly to overall changes in the frequency of extremes; nevertheless, total changes are more dependent on WC changes.

5.6 Exploring the possible reasons for the inter-model spread

By the end of the twenty-first century, the seasonality of extreme precipitation is projected to shift, but there is a considerable inter-model spread in this transition. Previous studies (e.g., Marelle et al. 2018; Brönnimann et al. 2018) have not delved into the reasons for the shift and subsequently the significant inter-model spread

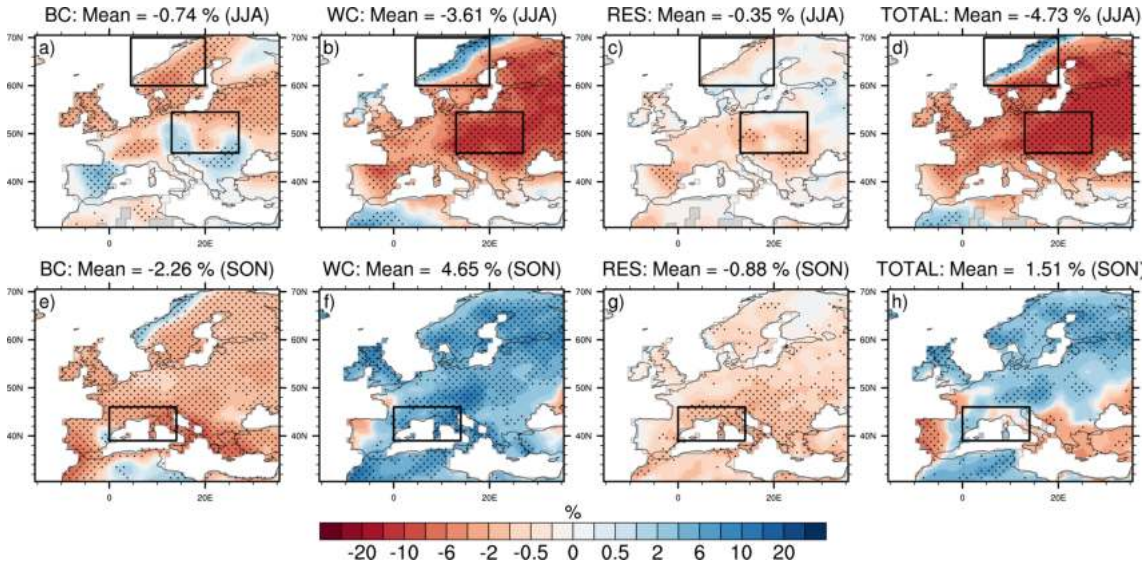

Figure 5.13: Maps illustrating individual contributions from three decomposed classes; within (WC), between (BC) and residual (RES); to the total extreme precipitation changes. The stippling indicates areas where 66% of the models agree on the sign change of the multi-model mean. Panels d and h show the sum of the three classes and are identical to Figures 5.5 c and d. Black boxes are drawn in corresponding panels to showcase the subdomains - Scandinavia (SCD) and Central Europe (CEU) are marked for the JJA while for SON only the North-West Mediterranean (NWM) is considered.

associated with them. Section 5.3 discusses the spread observed in the shift of the median day of extreme precipitation in detail. In section 5.3.1, I confined our focus to Europe in order to investigate the processes behind these changes. I investigated the relationship between the seasonal frequency of extreme precipitation and of dominant CTs, which provided insight into whether or not changes in atmospheric flow patterns can alter the occurrence of extremes. The Eq. 5.2 decomposition of the total frequency of extremes by seasons also provided additional information about the individual contributions of frequency changes of CTs to the frequency changes of extremes. The role played by WC and BC in shaping the distribution of extreme precipitation is also discussed. Nonetheless, the analysis of the individual components also proved to have a significant spread associated with them. One hypothesis is that the spread in the WC and BC can get translated into the total spread found in the shift of the seasonality. Hence assessing the spread in the individual components of decomposition can shed light on the total uncertainty associated with the seasonal shift of extreme precipitation.

5.6.1 Spread in the components of decomposition

As discussed earlier, I identified a large spread in the changes in the frequency of the different CTs. Particularly when analyzing the components of decomposition, the spread is much larger for the within class than the rest for all domains and CTs (Figure 5.12). To assess the variation of the WC and BC among the models and how it contributes to the large spread, I performed a cross-model regression of the average WC and BC values with different monthly variables (note that daily model outputs for variables, such as total precipitable water, for instance, are not available in the CMIP6 archive). I conducted this investigation using monthly

relative anomalies (after removing the annual mean) of surface temperature (T2M), total precipitable water (TPW), and low-level (850 hPa) wind circulations (cf. Figures 5.14 and A.18). The objective is to look for a possible coherent structure or pattern explaining why there is such a spread among the CMIP6 models.

Any change in global and large-scale T2M can be linked to changes in regional TPW, while large-scale circulation patterns can alter the moisture advection. The cross-model regression coefficient values illustrate how T2M or TPW is related to WC or BC changes. At the same time, their slopes indicate the percentage of the changes that these variables can address. I evaluate the subsequent investigation by focusing on a single subdomain (over NWM) to ensure a methodical approach. NWM is opted for further analysis mainly because of the more extensive spread in the individual components (cf. Figure 5.12) than the other subdomains and our interest in further understanding the changes in this area. The regression is performed on a global scale due to our assumption of the involvement of large-scale features that contribute to the spread. This assumption is partially correct, as the significant regions identified were not just in the immediate neighbourhood of the subdomain under study, but also far away.

Figure 5.14 depicts the correlation and slope maps obtained by regressing the average WC values over the NWM across the models used in our analysis. The coloured contours in the top panel represent the regressed TPW results, while the bottom panel represents the corresponding T2M results. Stippled areas on the correlation maps represent significant areas, whereas the vectors on the slope maps represent wind flow slopes obtained using the same method as the contours. As expected, both the correlation and the slopes of T2M and TPW show coinciding patterns of positive and negative values. The stippling illustrates that the areas displaying a significant correlation are not widespread; however, the significant areas in T2M and TPW coincide for most regions. One explanation for the large spread is in the definition of WC, as it is a combination of both thermodynamic and mesoscale dynamic factors leading to extreme precipitation. In the T2M and TPW maps, we see cross-Atlantic positive correlation values (darker blue shades), indicating that any changes in the WC can be linked to changes in the surface temperature and thus related to the precipitable water available at lower levels. Or, to put it another way, most models have positive TPW and T2M anomalies, which are linked to positive WC values across the board. Hence, we may assume that the part of the WC contributed by the thermodynamic factors (over the significant areas) may not be responsible at large for the spread. This leaves us to investigate the dynamic factors, which are explained using the wind flux anomalies.

The cross-model wind flow vectors, when regressed with the WC, are shown in Figures 5.14 b and d. We see wind flow vectors forming regional or mesoscale structures rather than large-scale flow structures or patterns. The TPW (figure 5.14 a) map shows a cyclonic wind anomaly related to the WC values across the models that bring in the moisture, particularly over the NWM. An anticyclonic low-level wind structure originates over the Arctic Sea and expands across most of northern Europe, eventually merging with the cyclonic pattern in the NWM domain. This dipole-like wind flux could explain the significant spread

in the WC across Europe. The various wind flow configurations generated by the different models lead to considerable differences in the moisture convergence to the region of concern, resulting in a large spread in the WC. The thermodynamic factors are explained by the significant TPW with warmer T2M, while the dynamic contribution and most of the WC spread are explained by the different mesoscale wind fluxes seen across the models.

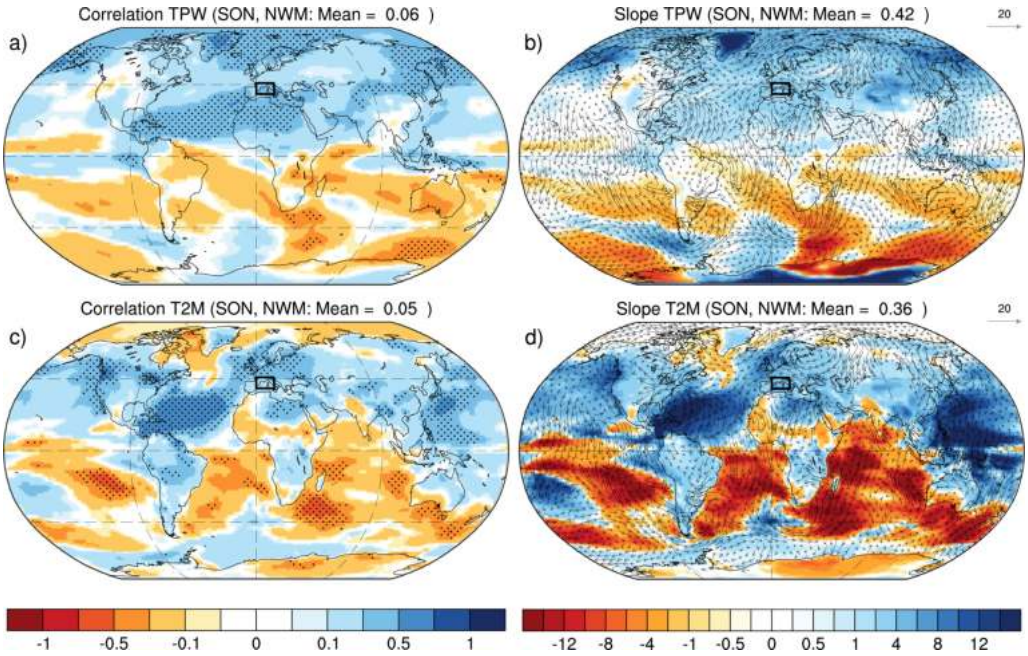

Figure 5.14: Maps showing the correlation (a, c) and slope (b, d) from the cross-model regression of the within class values across models from the North-West Mediterranean (NWM) subdomain with the global anomalies (with annual mean removed) of total precipitable water (TPW; a and b), near-surface temperature (T2M; c and d) and low-level wind flux (overlayed vectors in b and d). The top panel is for the TPW and the bottom panel is for the T2M. The stippling over the correlation maps indicates the significant areas with P-value less than 0.05. The vectors overlayed over panels b and d are the 850 hPa wind flux slopes.

By regressing the average values of both WC (cf. 5.14) and BC (cf. A.18) with the relative monthly anomalies of T2M, TPW and circulation patterns across all the models, a crude perspective of the different factors that may be leading to the large inter-model spread in the seasonal frequency of the extremes can be obtained. However, it is difficult to draw any conclusions from the results until now due to their complexity and shortcomings to explain various factors leading to the spread. Yet, this gives us a picture of how the different variables are associated with the seasonality changes and the accompanying spread. Figure 5.14 illustrates only the initial findings for the WC and requires further analysis. I also have analysed the anomalies in the T2M, TPW, and wind patterns across the extreme models, i.e, the models with the largest and the lowest values of the components of decomposition (only for WC, cf. A.19), and looked for the dissimilarities, which further help in understanding the spread (cf. Figure 5.14). Constructing composites based on the different values of the WC and BC can also be a way to distinguish between the models with distinct physical representations, which could be analysed in future studies.

As previously stated, this preliminary analysis of the inter-model spread requires further investigation and evaluation to reach a solid conclusion. Furthermore, the unavailability of relevant daily variables in the CMIP6 archive is a challenge, as the basic climatology seems to smooth various features and is insufficient to explain the entire picture. As suggested by Chen et al. 2020, additional diagnostics such as the atmospheric convective inhibition (CIN) and available potential energy (CAPE) would be particularly interesting to better understand the response of daily precipitation intensities, including for RX1DAY events in a warmer climate.

5.7 Synthesis

This chapter focuses on the projected changes in the seasonality of the annual maxima of daily precipitation intensities (RX1DAY). The global atmospheric warming associated with climate change increases the RX1DAY intensities, but it may be also associated with a seasonal modulation of the RX1DAY occurrences given the projected seasonal and regional variations in the atmospheric warming and the related circulation changes. Quantifying the future changes in the seasonality of extremes allows us to get better prepared to handle the risks that may accompany them.

In most parts of the world, daily precipitation extremes follow a predictable seasonal pattern (Marelle et al., 2018). Both the latest CMIP6 and the previous CMIP5 generation of climate models likewise capture the observed seasonality of extreme precipitation. In a scenario with unabated emissions (SSP5-8.5), the seasonality of extreme precipitation is projected to change in many places by the end of the twenty-first century. The later occurrence of the extremes, i.e., from summer and early fall towards fall and winter, with no regional uniformity, is a characteristic of this change. Across Africa, South America, Europe, and the high latitudes, there is a definite later shift. However, an early change is also detected in central Europe, North America, and other parts of the world. Significant inter-model spread in the seasonality shifts was also identified, particularly in areas where the historical extreme season is not summer.

One of the questions was whether the inter-model spread identified in the seasonality shift was an artefact of model biases. To alleviate this bias, which may be diluting our findings, an adjustment of the peak month of RX1DAY occurrence in the future to a fixed peak month was done. The fixed peak month is determined by calculating the peak month from the historical period. By aligning the model peak month to a fixed one, I compare the shifts in the seasonality relative to this month, which smooths the seasonal cycle. The apparent shift that was observed before and after this adjustment confirms a clear change in the extremes' seasonality.

To better understand what causes these seasonal shifts in extremes, I narrowed our analysis region to Europe. The European domain is intriguing since it shows an overall later occurrence of extremes, but with a large inter-model spread. To get insights into the underlying mechanisms, I analyzed the frequency changes of 11 circulation types (defined using a simplified version of the JC classification) across the whole European domain. The frequency changes of the various

circulation types are related to changes in extreme precipitation across various seasons. Not surprisingly, the cyclonic type is the most dominant contributor to RX1DAY events across Europe (there is a regional difference over different subdomains in the order of contribution) and thus accounts for significant changes in RX1DAY occurrences. In addition, I computed strong seasonal correlations between the frequency changes of the cyclonic type and the RX1DAY.

Using a simple decomposition technique, I further analyzed the total change in RX1DAY occurrences as a sum of three individual contributions. The three classes, WC, BC and residual, explain the different features of the extremes precipitation and its link to the circulation types. The breakdown revealed the offsetting or common nature of the WC and BC effects depending on the subdomains and seasons. WC, which includes the thermodynamic and the mesoscale dynamic factors, is the dominant contributor to the change in the seasonality of the extremes. BC, which describes the role of the large-scale dynamics or the changes in the frequency of a circulation type relative to others, was not found to be a large contributor (but non-negligible) to the total changes in the seasonal frequency of the extremes. The contribution of both WC and BC changes according to the season analysed and the total change in the frequency of the extreme is dependent on their interplay.

The study was also a preliminary attempt to address the large inter-model spread in the decomposed classes. The drivers that may be responsible for the significant spread, particularly large in the WC, were explored by cross-model regression of the T2M, TPW, and wind flow vectors. The large spread can be related to the varying representation of wind fluxes among the various models, pointing to the distinct dynamical representations implemented. The investigation also showed that the temperature and moisture features, indicating the thermodynamic factors, are consistent with the cross-model regression and in extreme models, leaving us with the differences in the circulation patterns produced by the different models (cf. section 5.6.1).

Conclusion and prospects

Take home messages

Today, googling "climate change" will get you about 1.7 billion hits. A multitude of threads has emerged over the course last few decades on many climate policy blogs and peer-reviewed journals, in which most of them are the gloom-and-doom variety. Among them, many studies have analysed and documented different aspects of the changes in the mean water cycle of our planet. This thesis focuses on the hydrological consequences of increased GHG concentrations and related global warming, with an emphasis on wet and dry meteorological extremes. The primary goal here was to quantify and better understand the response of daily precipitation extremes to increased CO_2 concentrations and across various global warming levels using global projections and idealised climate change experiments undertaken as part of the CMIP6.

The synthesis section at the end of each chapter summarizes the key findings of the corresponding chapters. This concluding chapter is a wrap-up of all the chapter summaries. In chapter 1, I reviewed the science of extreme events and the recent literature available today on the analysis of the extremes. The chapter also discusses the key mechanisms along with shedding light on the projected changes and the uncertainties which are further discussed in the later chapters. The chapter 2 deals with a variety of data and the methods I used to approach the main question of the PhD scientifically. The chapter also highlights the different choices as a researcher I made to conduct and achieve the results. Dynamical methods include the use of a hierarchy of climate change experiments, ranging from idealized abrupt-4xCO2 simulations and their AGCM breakdown, to more realistic projections, here mostly based on a high-emission scenario to limit the confounding effect of internal climate variability. Statistical methods include the use of non-stationary GEV analysis for diagnosing robust changes in the 20-year return level of RX1DAY intensities and classification of daily synoptic circulation types for a better understanding of changes in RX1DAY seasonality.

In chapter 3, I have assessed the relative contributions of fast atmospheric adjustment to increased CO2, slow SST-mediated warming, and SST pattern change to projected daily precipitation extremes. More specifically, I summarised and identified the role of precipitation extremes' frequency and intensity in modulating annual precipitation changes, particularly the differentiation between the fast and slow responses leading to non-homogeneous regional spatial features depending on the wet/dry extremes. The fast adjustment was also shown to trigger

an overall increase in atmospheric stability and thus an increase in the number of dry days and in the annual maximum duration of meteorological droughts (as evaluated as the number of consecutive dry days).

Using a non-stationary GEV approach for both location and scale parameters, I have then quantified projected changes in the 20-year return value (RV20) of annual maximum daily precipitation intensities (RX1DAY), as well as the related uncertainties across different CMIP6 models or different realizations of the same model (Chapter 4). This original study has been published in Weather and Climate Extremes and highlights the need for larger ensembles (than in CMIP6) for individual models and scenarios so that a better distinction can be made between model uncertainty and internal climate variability. Yet, our results suggest that most models show an increase in RX1DAY and RV20 values that are consistent with the Clausius-Clapeyron relationship when scaled by the corresponding global warming.

In chapter 5, I have investigated changes in the seasonality of extreme precipitation and briefly explored the physical mechanisms that underpin this change. In line with the former-generation global climate models, the ensemble mean results of CMIP6 highlight possible changes in the seasonal cycle of the RX1DAY events, that can sometimes be interpreted as a shift towards a later season, potentially related to more favourable thermodynamical conditions. Yet, the use of a circulation type classification over Europe has also enabled the identification of potential dynamical contributions, such as a decrease in the occurrence of cyclonic synoptic conditions in summer that could deserve further analysis and a better understanding of the regional inter-model spread.

If I am asked to sum up this thesis in a single statement, I would say, —
"Learning from the past, reasoning about the future, and making sense of the projections in a warming world"

In this thesis I have complied various aspects of the response of extreme precipitation to climate change, utilising the now available state-of-the-art climate model projections and observations. I have utilised the end-of-the-road scenarios (high emission, low mitigation; SSP5-8.5) to represent the future, and analysed the extreme precipitation changes relative to the historical period. This PhD provided me with the opportunity to strengthen my general appreciation of human-induced climate change and increased my knowledge in the field by enabling me to practice and comprehend different dynamic and statistical tools. This also provided me with a chance exhaustively learn and think about the investigation rationalities and disentangle the results. Furthermore, the opportunity to manage and run a few extended climate simulations with CNRM-CM6-1 that require a lot of effort in designing allowed me to find an optimal configuration to save computing resources and monitor the experiments. As this PhD comes to an end, after three years of dedicated work and a global pandemic, I have gained confidence and energy to seek after my future research and has given me some new perspectives to direct my focus which are discussed in the next section.

Perspectives

This thesis has explored in detail several drivers and mechanisms that contribute to ongoing and future changes in the intensity and frequency of extreme precipitation events under enhanced atmospheric GHG concentrations. It exhaustively covers the role played by the different atmospheric CO_2 concentrations and global warming levels that influence the extreme precipitation response; the uncertainty related to the projections; and the change in the seasonality of the extremes. I can say that this thesis has given me many insights to extend and proceed with my research in the future. Among the several perspectives I acquired from this PhD, a few are my personal favourites and I discuss them in this section. There are a few short-term studies that I would like to pursue in the coming years, while others are long-term research projects that I am considering.

Building on my PhD experience and on the CMIP6 archive, one of my near-term goals is to better understand the underlying mechanisms that lead to extreme precipitation using the different idealised experiments from the CFMIP (Webb et al., 2017). By coding different process-oriented diagnostics like evaluation of the dry static energy, CAPE and CIN analysis (e.g. Cheng et al. 2018; Chadwick et al. 2022) in the CFMIP model outputs, I would like to assess their robustness across the different current-generation global climate models. Moreover, the advancements in climate modelling, especially the development of very high resolution (HighResMIP, Haarsma et al. 2016) and convection-permitting models (Lucas-Picher et al., 2021), represent a good opportunity to assess the effect of model resolution on the response of precipitation extremes. While higher horizontal resolution and explicit convection are expected to improve the simulation of heavy precipitation intensities, I would like to assess whether they also alter the magnitude of the relative changes, particularly do they lead to super-CC rates (Bador et al., 2020; Pichelli et al., 2021) that are generally not found in the coarser-resolution CMIP6 models? Beyond the standard scenarioMIP simulations from the CMIP, I would also like to explore additional MIPs, for instance, the DAMIP (Gillett et al., 2016). The objective would be to distinguish the contribution of GHG and other anthropogenic forcings, particularly aerosols, as well as the combination of both (eg., Baek and Lora 2021; Dong et al. 2021) on the RX1DAY response. So doing, it could be possible to detect and attribute observed changes, at least in regions with sufficiently long and reliable records, and, ultimately, to constrain the model-dependent projections with these observations. One of the other near-term future projects that I would like to pursue (maybe during my latest secondment at Predictia after the PhD manuscript submission) is a comparison of different bias adjustment techniques and their potential quantitative impacts on heavy precipitation projections (Vrac et al., 2016).

A few longer-term objectives are also on my to-do list. The assessment of potential non-linear changes in extreme precipitation (e.g., Pendergrass et al. 2019) has tremendous implications for adaptation and deserves further analysis in a multi-model (structural uncertainties) and/or multi-parameter (parametric uncertainties) ensemble framework. Dry extremes should be also assessed more comprehensively, using a larger set of metrics (not only consecutive dry days) and going beyond meteorological droughts (e.g., Cook et al. 2020; Ukkola et al. 2020;

Sun et al. 2021a). I am particularly intrigued by the changes in the South Asian Monsoon domain, mainly due to my longstanding interest in the tropical agrarian society that I come from. I would like to investigate the relevant regional changes over this domain utilising a potential storyline approach (e.g., Shepherd et al. 2018) by identifying and distinguishing the interplay of the large-scale dynamics and the thermodynamics in influencing the wet and dry extremes (e.g., Allan et al. 2020; Sudharsan et al. 2020). What effect emissions and global warming have on the fundamental mechanisms and structure of mesoscale convective systems and related heavy precipitation events is another key question I would like to address (e.g., Fowler et al. 2021) if I have the opportunity to run a convective-permitting climate model.

References

Adler, R. F., G. Gu, M. Sapiano, J.-J. Wang, and G. J. Huffman, Global precipitation: Means, variations and trends during the satellite era (1979–2014), Surveys in Geophysics, 38(4), 679–699, 2017.

Alexander, L. V., and J. M. Arblaster, Historical and projected trends in temperature and precipitation extremes in australia in observations and cmip5, Weather and Climate Extremes, 15, 34–56, 2017.

Alexander, L. V., H. J. Fowler, M. Bador, A. Behrangi, M. G. Donat, R. Dunn, C. Funk, J. Goldie, E. Lewis, M. Rogé, et al., On the use of indices to study extreme precipitation on sub-daily and daily timescales, Environmental Research Letters, 14(12), 125,008, 2019.

Algarra, I., R. Nieto, A. M. Ramos, J. Eiras-Barca, R. M. Trigo, and L. Gimeno, Significant increase of global anomalous moisture uptake feeding landfalling atmospheric rivers, Nature communications, 11(1), 1–7, 2020.

Allan, R. P., and B. J. Soden, Atmospheric warming and the amplification of precipitation extremes, Science, 321(5895), 1481–1484, 2008.

Allan, R. P., M. Barlow, M. P. Byrne, A. Cherchi, H. Douville, H. J. Fowler, T. Y. Gan, A. G. Pendergrass, D. Rosenfeld, A. L. Swann, et al., Advances in understanding large-scale responses of the water cycle to climate change, Annals of the New York Academy of Sciences, 1472(1), 49–75, 2020.

Allen, M. R., and W. J. Ingram, Constraints on future changes in climate and the hydrologic cycle, Nature, 419(6903), 228–232, 2002.

Andrews, T., P. M. Forster, and J. M. Gregory, A surface energy perspective on climate change, Journal of Climate, 22(10), 2557–2570, 2009.

Andrews, T., P. M. Forster, O. Boucher, N. Bellouin, and A. Jones, Precipitation, radiative forcing and global temperature change, Geophysical research letters, 37(14), 2010.

Angélil, O., D. A. Stone, M. Tadross, F. Tummon, M. Wehner, and R. Knutti, Attribution of extreme weather to anthropogenic greenhouse gas emissions: sensitivity to spatial and temporal scales, Geophysical Research Letters, 41(6), 2150–2155, 2014.

Angélil, O., D. Stone, S. Perkins-Kirkpatrick, L. V. Alexander, M. Wehner, H. Shiogama, P. Wolski, A. Ciavarella, and N. Christidis, On the nonlinearity of spatial scales in extreme weather attribution statements, Climate Dynamics, 50(7), 2739–2752, 2018.

Anthes, R. A., A cumulus parameterization scheme utilizing a one-dimensional cloud model, Monthly Weather Review, 105(3), 270–286, 1977.

Armour, K. C., Energy budget constraints on climate sensitivity in light of inconstant climate feedbacks, Nature Climate Change, 7(5), 331–335, 2017.

Arrhenius, S., Xxxi. on the influence of carbonic acid in the air upon the temperature of the ground, The London, Edinburgh, and Dublin Philosophical Magazine and Journal of Science, 41(251), 237–276, 1896.

Asadieh, B., and N. Y. Krakauer, Global trends in extreme precipitation: climate models versus observations, Hydrology and Earth System Sciences, 19(2), 877–891, 2015.

Bador, M., M. G. Donat, O. Geoffroy, and L. V. Alexander, Assessing the robustness of future extreme precipitation intensification in the cmip5 ensemble, Journal of Climate, 31(16), 6505–6525, 2018.

Bador, M., J. Boé, L. Terray, L. V. Alexander, A. Baker, A. Bellucci, R. Haarsma, T. Koenigk, M.-P. Moine, K. Lohmann, et al., Impact of higher spatial atmospheric resolution on precipitation extremes over land in global climate models, Journal of Geophysical Research: Atmospheres, 125(13), e2019JD032,184, 2020.

Baek, S. H., and J. M. Lora, Counterbalancing influences of aerosols and greenhouse gases on atmospheric rivers, Nature Climate Change, 11(11), 958–965, 2021.

Bala, G., P. Duffy, and K. Taylor, Impact of geoengineering schemes on the global hydrological cycle, Proceedings of the National Academy of Sciences, 105(22), 7664–7669, 2008.

Barbero, R., H. Fowler, G. Lenderink, and S. Blenkinsop, Is the intensification of precipitation extremes with global warming better detected at hourly than daily resolutions?, Geophysical Research Letters, 44(2), 974–983, 2017.

Beck, H. E., N. Vergopolan, M. Pan, V. Levizzani, A. I. Van Dijk, G. P. Weedon, L. Brocca, F. Pappenberger, G. J. Huffman, and E. F. Wood, Global-scale evaluation of 22 precipitation datasets using gauge observations and hydrological modeling, Hydrology and Earth System Sciences, 21(12), 6201–6217, 2017.

Becker, A., P. Finger, A. Meyer-Christoffer, B. Rudolf, K. Schamm, U. Schneider, and M. Ziese, A description of the global land-surface precipitation data products of the global precipitation climatology centre with sample applications including centennial (trend) analysis from 1901-present, Earth System Science Data, 5(1), 71–99, 2013.

Behrangi, A., and M. Richardson, Observed high-latitude precipitation amount and pattern and cmip5 model projections, Remote Sensing, 10(10), 1583, 2018.

Benestad, R. E., Implications of a decrease in the precipitation area for the past and the future, Environmental Research Letters, 13(4), 044,022, 2018.

Benestad, R. E., K. M. Parding, H. B. Erlandsen, and A. Mezghani, A simple equation to study changes in rainfall statistics, Environmental Research Letters, 14(8), 084,017, 2019.

Berens, P., Circstat: a matlab toolbox for circular statistics, Journal of statistical software, 31, 1–21, 2009.

Berg, P., J. Haerter, P. Thejll, C. Piani, S. Hagemann, and J. Christensen, Seasonal characteristics of the relationship between daily precipitation intensity and surface temperature, Journal of Geophysical Research: Atmospheres, 114(D18), 2009.

Bevacqua, E., M. I. Vousdoukas, G. Zappa, K. Hodges, T. G. Shepherd, D. Maraun, L. Mentaschi, and L. Feyen, More meteorological events that drive compound coastal flooding are projected under climate change, Communications earth & environment, 1(1), 1–11, 2020.

Bhowmik, A. K., and A. C. Costa, Representativeness impacts on accuracy and precision of climate spatial interpolation in data-scarce regions, Meteorological Applications, 22(3), 368–377, 2015.

Birch, C. E., M. J. Roberts, L. Garcia-Carreras, D. Ackerley, M. J. Reeder, A. P. Lock, and R. Schiemann, Sea-breeze dynamics and convection initiation: The influence of convective parameterization in weather and climate model biases, Journal of Climate, 28(20), 8093–8108, 2015.

Boer, G. J., D. M. Smith, C. Cassou, F. Doblas-Reyes, G. Danabasoglu, B. Kirtman, Y. Kushnir, M. Kimoto, G. A. Meehl, R. Msadek, et al., The decadal climate prediction project (dcpp) contribution to cmip6, Geoscientific Model Development, 9(10), 3751–3777, 2016.

Bony, S., G. Bellon, D. Klocke, S. Sherwood, S. Fermepin, and S. Denvil, Robust direct effect of carbon dioxide on tropical circulation and regional precipitation, Nature Geoscience, 6(6), 447–451, 2013.

Bootsma, A., Gameda, and S. DW McKenney, Impacts of potential climate change on selected agroclimatic indices in atlantic canada, Canadian Journal of soil science, 85(2), 329–343, 2005.

Borodina, A., E. M. Fischer, and R. Knutti, Models are likely to underestimate increase in heavy rainfall in the extratropical regions with high rainfall intensity, Geophysical Research Letters, 44(14), 7401–7409, 2017.

Bosilovich, M. G., J. Chen, F. R. Robertson, and R. F. Adler, Evaluation of global precipitation in reanalyses, Journal of applied meteorology and climatology, 47(9), 2279–2299, 2008.

Brönnimann, S., J. Rajczak, E. M. Fischer, C. C. Raible, M. Rohrer, and C. Schär, Changing seasonality of moderate and extreme precipitation events in the alps, Natural Hazards and Earth System Sciences, 18(7), 2047–2056, 2018.

Brunner, L., C. McSweeney, A. P. Ballinger, D. J. Befort, M. Benassi, B. Booth, E. Coppola, H. De Vries, G. Harris, G. C. Hegerl, et al., Comparing methods to constrain future european climate projections using a consistent framework, Journal of Climate, 33(20), 8671–8692, 2020.

Brunner, L., R. Lorenz, E. M. Fischer, and R. Knutti, Investigating 25 years of coupled climate modeling, Tech. rep., Copernicus Meetings, 2022.

Caires, S., A comparative simulation study of the annual maxima and the peaks-over-threshold methods, Deltares report 1200264-002 for Rijkswaterstaat, Waterdienst, 2009.

Cardell, M. F., A. Amengual, R. Romero, and C. Ramis, Future extremes of temperature and precipitation in europe derived from a combination of dynamical and statistical approaches, International Journal of Climatology, 40(11), 4800–4827, 2020.

Cassou, C., L. Terray, and A. S. Phillips, Tropical atlantic influence on european heat waves, Journal of climate, 18(15), 2805–2811, 2005.

Cattani, E., A. Merino, J. A. Guijarro, and V. Levizzani, East africa rainfall trends and variability 1983–2015 using three long-term satellite products, Remote Sensing, 10(6), 931, 2018.

Cattiaux, J., and A. Ribes, Defining single extreme weather events in a climate perspective, Bulletin of the American Meteorological Society, 99(8), 1557–1568, 2018.

Cattiaux, J., H. Douville, A. Ribes, F. Chauvin, and C. Plante, Towards a better understanding of changes in wintertime cold extremes over europe: a pilot study with cnrm and ipsl atmospheric models, Climate dynamics, 40(9), 2433–2445, 2013.

Catto, J. L., D. Ackerley, J. F. Booth, A. J. Champion, B. A. Colle, S. Pfahl, J. G. Pinto, J. F. Quinting, and C. Seiler, The future of midlatitude cyclones, Current Climate Change Reports, 5(4), 407–420, 2019.

Chadwick, R., Which aspects of co 2 forcing and sst warming cause most uncertainty in projections of tropical rainfall change over land and ocean?, Journal of Climate, 29(7), 2493–2509, 2016.

Chadwick, R., P. Good, T. Andrews, and G. Martin, Surface warming patterns drive tropical rainfall pattern responses to co2 forcing on all timescales, Geophysical Research Letters, 41(2), 610–615, 2014.

Chadwick, R., H. Douville, and C. B. Skinner, Timeslice experiments for understanding regional climate projections: applications to the tropical hydrological cycle and european winter circulation, Climate Dynamics, 49(9), 3011–3029, 2017.

Chadwick, R., A. G. Pendergrass, L. M. Alves, and A. Moise, How do regional distributions of daily precipitation change under warming?, Journal of Climate, 35(11), 3243–3260, 2022.

Chan, S. C., E. J. Kendon, S. Berthou, G. Fosser, E. Lewis, and H. J. Fowler, Europe-wide precipitation projections at convection permitting scale with the unified model, Climate Dynamics, 55(3), 409–428, 2020.

Chang, E. K., C.-G. Ma, C. Zheng, and A. M. Yau, Observed and projected decrease in northern hemisphere extratropical cyclone activity in summer and its impacts on maximum temperature, Geophysical Research Letters, 43(5), 2200–2208, 2016.

Chen, C.-T., and T. Knutson, On the verification and comparison of extreme rainfall indices from climate models, Journal of Climate, 21(7), 1605–1621, 2008.

Chen, J., A. Dai, Y. Zhang, and K. L. Rasmussen, Changes in convective available potential energy and convective inhibition under global warming, Journal of Climate, 33(6), 2025–2050, 2020.

Chen, Z., S. Cheng, J. Li, X. Guo, W. Wang, and D. Chen, Relationship between atmospheric pollution processes and synoptic pressure patterns in northern china, Atmospheric Environment, 42(24), 6078–6087, 2008.

Cheng, L., M. Hoerling, L. Smith, and J. Eischeid, Diagnosing human-induced dynamic and thermodynamic drivers of extreme rainfall, Journal of Climate, 31(3), 1029–1051, 2018.

Cohen, J., J. Screen, J. Furtado, M. Barlow, D. Whittleston, D. Coumou, J. Francis, K. Dethloff, D. Entekhabi, J. Overland, et al., Recent arctic amplification and extreme mid-latitude weather, Nature Geosci., 7, 627–637, 2014.

Coles, S., J. Bawa, L. Trenner, and P. Dorazio, An introduction to statistical modeling of extreme values, vol. 208, Springer, 2001.

Contractor, S., M. G. Donat, L. V. Alexander, M. Ziese, A. Meyer-Christoffer, U. Schneider, E. Rustemeier, A. Becker, I. Durre, and R. S. Vose, Rainfall estimates on a gridded network (regen)–a global land-based gridded dataset of daily precipitation from 1950 to 2016, Hydrology and Earth System Sciences, 24(2), 919–943, 2020.

Cook, B. I., J. S. Mankin, and K. J. Anchukaitis, Climate change and drought: From past to future, Current Climate Change Reports, 4(2), 164–179, 2018.

Cook, B. I., J. S. Mankin, K. Marvel, A. P. Williams, J. E. Smerdon, and K. J. Anchukaitis, Twenty-first century drought projections in the cmip6 forcing scenarios, Earth's Future, 8(6), e2019EF001,461, 2020.

Cooley, D., D. Nychka, and P. Naveau, Bayesian spatial modeling of extreme precipitation return levels, Journal of the American Statistical Association, 102(479), 824–840, 2007.

Coppola, E., S. Sobolowski, E. Pichelli, F. Raffaele, B. Ahrens, I. Anders, N. Ban, S. Bastin, M. Belda, D. Belusic, et al., A first-of-its-kind multi-model convection permitting ensemble for investigating convective phenomena over europe and the mediterranean, Climate Dynamics, 55(1), 3–34, 2020.

Cornes, R. C., G. van der Schrier, E. J. van den Besselaar, and P. D. Jones, An ensemble version of the e-obs temperature and precipitation data sets, Journal of Geophysical Research: Atmospheres, 123(17), 9391–9409, 2018.

Courtier, P., C. Freydier, J. Geleyn, F. Rabier, and M. Rochas, The arpege project at météo-france, ecmwf workshop, european center for medium-range weather forecast, Reading, England, 1991.

Cunnane, C., A particular comparison of annual maxima and partial duration series methods of flood frequency prediction, Journal of hydrology, 18(3-4), 257–271, 1973.

Curry, C. L., J. Sillmann, D. Bronaugh, K. Alterskjaer, J. N. Cole, D. Ji, B. Kravitz, J. E. Kristjansson, J. C. Moore, H. Muri, et al., A multimodel examination of climate extremes in an idealized geoengineering experiment, Journal of Geophysical Research: Atmospheres, 119(7), 3900–3923, 2014.

Dai, A., Precipitation characteristics in eighteen coupled climate models, Journal of climate, 19(18), 4605–4630, 2006.

Data, C., Guidelines on analysis of extremes in a changing climate in support of informed decisions for adaptation, World Meteorological Organization, 2009.

De Haan, L., A. Ferreira, and A. Ferreira, Extreme value theory: an introduction, vol. 21, Springer, 2006.

de los Milagros Skansi, M., M. Brunet, J. Sigró, E. Aguilar, J. A. A. Groening, O. J. Bentancur, Y. R. C. Geier, R. L. C. Amaya, H. Jácome, A. M. Ramos, et al., Warming and wetting signals emerging from analysis of changes in climate extreme indices over south america, Global and Planetary Change, 100, 295–307, 2013.

DeAngelis, A. M., A. J. Broccoli, and S. G. Decker, A comparison of cmip3 simulations of precipitation over north america with observations: Daily statistics and circulation features accompanying extreme events, Journal of climate, 26(10), 3209–3230, 2013.

Déqué, M., C. Dreveton, A. Braun, and D. Cariolle, The arpege/ifs atmosphere model: a contribution to the french community climate modelling, Climate Dynamics, 10(4), 249–266, 1994.

Diaconescu, E. P., P. Gachon, J. Scinocca, and R. Laprise, Evaluation of daily precipitation statistics and monsoon onset/retreat over western sahel in multiple data sets, Climate Dynamics, 45(5), 1325–1354, 2015.

Doblas-Reyes, F. J., A. A. Sorensson, M. Almazroui, A. Dosio, W. J. Gutowski, R. Haarsma, R. Hamdi, B. Hewitson, W.-T. Kwon, B. L. Lamptey, D. Maraun, T. S. Stephenson, I. Takayabu, L. Terray, A. Turner, and Z. Zuo, Linking global to regional climate change, in Climate Change 2021: The Physical Science Basis. Contribution of Working Group I to the Sixth Assessment Report of the Intergovernmental Panel on Climate Change, edited by V. Masson-Delmotte, P. Zhai, A. Pirani, S. L. Connors, C. Pean, S. Berger, N. Caud, Y. Chen, L. Goldfarb, M. I. Gomis, M. Huang, K. Leitzell, E. Lonnoy, J. B. R. Matthews, T. K. Maycock, T. Waterfield, O. Yelekci, R. Yu, and B. Zhou, Cambridge University Press, 2021.

Donat, M. G., G. C. Leckebusch, J. G. Pinto, and U. Ulbrich, Examination of wind storms over central europe with respect to circulation weather types and nao phases, International Journal of Climatology, 30(9), 1289–1300, 2010.

Donat, M. G., L. V. Alexander, H. Yang, I. Durre, R. Vose, and J. Caesar, Global land-based datasets for monitoring climatic extremes, Bulletin of the American Meteorological Society, 94(7), 997–1006, 2013.

Donat, M. G., J. Sillmann, S. Wild, L. V. Alexander, T. Lippmann, and F. W. Zwiers, Consistency of temperature and precipitation extremes across various global gridded in situ and reanalysis datasets, Journal of Climate, 27(13), 5019–5035, 2014.

Donat, M. G., L. V. Alexander, N. Herold, and A. J. Dittus, Temperature and precipitation extremes in century-long gridded observations, reanalyses, and atmospheric model simulations, Journal of Geophysical Research: Atmospheres, 121(19), 11–174, 2016a.

Donat, M. G., A. L. Lowry, L. V. Alexander, P. A. O'Gorman, and N. Maher, More extreme precipitation in the world's dry and wet regions, Nature Climate Change, 6(5), 508–513, 2016b.

Donat, M. G., O. Angélil, and A. M. Ukkola, Intensification of precipitation extremes in the world's humid and water-limited regions, Environmental Research Letters, 14(6), 065,003, 2019.

Dong, S., Y. Sun, C. Li, X. Zhang, S.-K. Min, and Y.-H. Kim, Attribution of extreme precipitation with updated observations and cmip6 simulations, Journal of Climate, 34(3), 871–881, 2021.

Douville, H., and A. John, Fast adjustment versus slow sst-mediated response of daily precipitation statistics to abrupt 4xco 2, Climate Dynamics, 56(3), 1083–1104, 2021.

Douville, H., and M. Plazzotta, Midlatitude summer drying: an underestimated threat in cmip5 models?, Geophysical Research Letters, 44(19), 9967–9975, 2017.

Douville, H., B. Decharme, C. Delire, J. Colin, E. Joetzjer, R. Roehrig, D. Saint-Martin, T. Oudar, R. Stchepounoff, and A. Voldoire, Drivers of the enhanced decline of land near-surface relative humidity to abrupt 4xco2 in cnrm-cm6-1, Climate Dynamics, 55(5), 1613–1629, 2020.

Douville, H., K. Raghavan, J. Renwick, R. Allan, P. Arias, M. Barlow, R. Cerezo-Mota, A. Cherchi, T. Gan, J. Gergis, D. Jiang, A. Khan, W. Pokam Mba, D. Rosenfeld, J. Tierney, and O. Zolina, Water cycle changes., in Climate Change 2021: The Physical Science Basis. Contribution of Working Group I to the Sixth Assessment Report of the Intergovernmental Panel on Climate Change, edited by Masson-Delmotte, V., P. Zhai, A. Pirani, S. L. Connors, C. Péan, S. Berger, N. Caud, Y. Chen, L. Goldfarb, M. I. Gomis, M. Huang, K. Leitzell, E. Lonnoy, J. B. R. Matthews, T. K. Maycock, T. Waterfield, O. Yelekçi, R. Yu, and B. Zhou, chap. 11, Cambridge University Press, 2021.

Du, H., L. V. Alexander, M. G. Donat, T. Lippmann, A. Srivastava, J. Salinger, A. Kruger, G. Choi, H. S. He, F. Fujibe, et al., Precipitation from persistent extremes is increasing in most regions and globally, Geophysical Research Letters, 46(11), 6041–6049, 2019.

Dunn, R., M. Donat, and L. Alexander, Investigating uncertainties in global gridded datasets of climate extremes, Climate of the Past, 10(6), 2171–2199, 2014.

Dunn, R. J., L. V. Alexander, M. G. Donat, X. Zhang, M. Bador, N. Herold, T. Lippmann, R. Allan, E. Aguilar, A. A. Barry, et al., Development of an updated global land in situ-based data set of temperature and precipitation extremes: Hadex3, Journal of Geophysical Research: Atmospheres, 125(16), e2019JD032,263, 2020.

Easterling, D. R., K. E. Kunkel, M. F. Wehner, and L. Sun, Detection and attribution of climate extremes in the observed record, Weather and Climate Extremes, 11, 17–27, 2016.

Eden, J. M., M. Widmann, D. Maraun, and M. Vrac, Comparison of gcm-and rcm-simulated precipitation following stochastic postprocessing, Journal of Geophysical Research: Atmospheres, 119(19), 11–040, 2014.

Eyring, V., S. Bony, G. A. Meehl, C. A. Senior, B. Stevens, R. J. Stouffer, and K. E. Taylor, Overview of the coupled model intercomparison project phase 6 (cmip6) experimental design and organization, Geoscientific Model Development, 9(5), 1937–1958, 2016.

Eyring, V., N. Gillett, K. Achutarao, R. Barimalala, M. Barreiro Parrillo, N. Bellouin, C. Cassou, P. Durack, Y. Kosaka, S. McGregor, et al., Human influence on the climate system: Contribution of working group i to the sixth assessment report of the intergovernmental panel on climate change, IPCC Sixth Assessment Report, 2021.

Field, C. B., V. Barros, T. F. Stocker, and Q. Dahe, Managing the risks of extreme events and disasters to advance climate change adaptation: special report of the intergovernmental panel on climate change, Cambridge University Press, 2012.

Fischer, E. M., and R. Knutti, Anthropogenic contribution to global occurrence of heavy-precipitation and high-temperature extremes, Nature climate change, 5(6), 560–564, 2015.

Fischer, E. M., and R. Knutti, Observed heavy precipitation increase confirms theory and early models, Nature Climate Change, 6(11), 986–991, 2016.

Fischer, E. M., U. Beyerle, and R. Knutti, Robust spatially aggregated projections of climate extremes, Nature Climate Change, 3(12), 1033–1038, 2013.

Fischer, E. M., U. Beyerle, C.-F. Schleussner, A. D. King, and R. Knutti, Biased estimates of changes in climate extremes from prescribed sst simulations, Geophysical Research Letters, 45(16), 8500–8509, 2018.

Fläschner, D., T. Mauritsen, and B. Stevens, Understanding the intermodel spread in global-mean hydrological sensitivity, Journal of Climate, 29(2), 801–817, 2016.

Flato, G., J. Marotzke, B. Abiodun, P. Braconnot, S. C. Chou, W. Collins, P. Cox, F. Driouech, S. Emori, V. Eyring, et al., Evaluation of climate models, in Climate change 2013: the physical science basis. Contribution of Working Group I to the Fifth Assessment Report of the Intergovernmental Panel on Climate Change, pp. 741–866, Cambridge University Press, 2014.

Flynn, C. M., and T. Mauritsen, On the climate sensitivity and historical warming evolution in recent coupled model ensembles, Atmospheric Chemistry and Physics, 20(13), 7829–7842, 2020.

Folland, C., T. Karl, J. Christy, R. Clarke, G. Gruza, J. Jouzel, M. Mann, J. Oerlemans, M. Salinger, S. Wang, et al., Observed climate variability and change, Climate change, 2001, 99, 2001.

Forster, P. M., A. C. Maycock, C. M. McKenna, and C. J. Smith, Latest climate models confirm need for urgent mitigation, Nature Climate Change, 10(1), 7–10, 2020.

Fowler, H. J., H. Ali, R. P. Allan, N. Ban, R. Barbero, P. Berg, S. Blenkinsop, N. S. Cabi, S. Chan, M. Dale, et al., Towards advancing scientific knowledge of climate change impacts on short-duration rainfall extremes, Philosophical Transactions of the Royal Society A, 379(2195), 20190,542, 2021.

Franzke, C., T. Woollings, and O. Martius, Persistent circulation regimes and preferred regime transitions in the north atlantic, Journal of the Atmospheric Sciences, 68(12), 2809–2825, 2011.

Funk, C., P. Peterson, M. Landsfeld, D. Pedreros, J. Verdin, S. Shukla, G. Husak, J. Rowland, L. Harrison, A. Hoell, et al., The climate hazards infrared precipitation with stations—a new environmental record for monitoring extremes, Scientific data, 2(1), 1–21, 2015.

Gershunov, A., T. Shulgina, R. E. Clemesha, K. Guirguis, D. W. Pierce, M. D. Dettinger, D. A. Lavers, D. R. Cayan, S. D. Polade, J. Kalansky, et al., Precipitation regime change in western north america: the role of atmospheric rivers, Scientific reports, 9(1), 1–11, 2019.

Gillett, N. P., H. Shiogama, B. Funke, G. Hegerl, R. Knutti, K. Matthes, B. D. Santer, D. Stone, and C. Tebaldi, The detection and attribution model intercomparison project (damip v1. 0) contribution to cmip6, Geoscientific Model Development, 9(10), 3685–3697, 2016.

Giorgi, F., C. Jones, G. R. Asrar, et al., Addressing climate information needs at the regional level: the cordex framework, World Meteorological Organization (WMO) Bulletin, 58(3), 175, 2009.

Giorgi, F., F. Raffaele, and E. Coppola, The response of precipitation characteristics to global warming from climate projections, Earth System Dynamics, 10(1), 73–89, 2019.

Gleckler, P. J., K. E. Taylor, and C. Doutriaux, Performance metrics for climate models, Journal of Geophysical Research: Atmospheres, 113(D6), 2008.

Gómez-Navarro, J., J. Montávez, S. Jerez, P. Jiménez-Guerrero, and E. Zorita, What is the role of the observational dataset in the evaluation and scoring of climate models?, Geophysical Research Letters, 39(24), 2012.

Goodess, C. M., and J. P. Palutikof, Development of daily rainfall scenarios for southeast spain using a circulation-type approach to downscaling, International Journal of Climatology: A Journal of the Royal Meteorological Society, 18(10), 1051–1083, 1998.

Graham, L., J. Andréasson, and B. Carlsson, Assessing climate change impacts on hydrology from an ensemble of regional climate models, model scales and linking methods–a case study on the lule river basin, Climatic Change, 81(1), 293–307, 2007.

Grose, M. R., J. S. Risbey, A. F. Moise, S. Osbrough, C. Heady, L. Wilson, and T. Erwin, Constraints on southern australian rainfall change based on atmospheric circulation in cmip5 simulations, Journal of Climate, 30(1), 225–242, 2017.

Guillod, B. P., B. Orlowsky, D. G. Miralles, A. J. Teuling, and S. I. Seneviratne, Reconciling spatial and temporal soil moisture effects on afternoon rainfall, Nature communications, 6(1), 1–6, 2015.

Gulev, S. K., P. W. Thorne, J. Ahn, F. J. Dentener, C. M. Domingues, S. Gerland, D. Gong, D. S. Kaufman, H. C. Nnamchi, J. Quaas, et al., Changing state of the climate system, Climate change, pp. 287–422, 2021.

Haarsma, R. J., M. J. Roberts, P. L. Vidale, C. A. Senior, A. Bellucci, Q. Bao, P. Chang, S. Corti, N. S. Fukar, V. Guemas, et al., High resolution model intercomparison project (highresmip v1. 0) for cmip6, Geoscientific Model Development, 9(11), 4185–4208, 2016.

Haddad, Z. S., and D. Rosenfeld, Optimality of empirical z-r relations, Quarterly Journal of the Royal Meteorological Society, 123(541), 1283–1293, 1997.

Hansen, J., G. Russell, A. Lacis, I. Fung, D. Rind, and P. Stone, Climate response times: Dependence on climate sensitivity and ocean mixing, Science, 229(4716), 857–859, 1985.

Hardwick Jones, R., S. Westra, and A. Sharma, Observed relationships between extreme sub-daily precipitation, surface temperature, and relative humidity, Geophysical Research Letters, 37(22), 2010.

Hart, M., R. De Dear, and R. Hyde, A synoptic climatology of tropospheric ozone episodes in sydney, australia, International Journal of Climatology: A Journal of the Royal Meteorological Society, 26(12), 1635–1649, 2006.

Hawkins, E., and R. Sutton, The potential to narrow uncertainty in projections of regional precipitation change, Climate dynamics, 37(1), 407–418, 2011.

He, J., and B. J. Soden, A re-examination of the projected subtropical precipitation decline, Nature Climate Change, 7(1), 53–57, 2017.

Hegerl, G. C., E. Black, R. P. Allan, W. J. Ingram, D. Polson, K. E. Trenberth, R. S. Chadwick, P. A. Arkin, B. B. Sarojini, A. Becker, et al., Challenges in quantifying changes in the global water cycle, Bulletin of the American Meteorological Society, 96(7), 1097–1115, 2015.

Heikenfeld, M., B. White, L. Labbouz, and P. Stier, Aerosol effects on deep convection: the propagation of aerosol perturbations through convective cloud microphysics, Atmospheric Chemistry and Physics, 19(4), 2601–2627, 2019.

Held, I. M., and B. J. Soden, Robust responses of the hydrological cycle to global warming, Journal of climate, 19(21), 5686–5699, 2006.

Herold, N., L. Alexander, M. Donat, S. Contractor, and A. Becker, How much does it rain over land?, Geophysical Research Letters, 43(1), 341–348, 2016.

Herold, N., A. Behrangi, and L. V. Alexander, Large uncertainties in observed daily precipitation extremes over land, Journal of Geophysical Research: Atmospheres, 122(2), 668–681, 2017.

Hersbach, H., B. Bell, P. Berrisford, G. Biavati, A. Horányi, J. Muñoz Sabater, J. Nicolas, C. Peubey, R. Radu, I. Rozum, et al., Era5 hourly data on single levels from 1979 to present, Copernicus Climate Change Service (C3S) Climate Data Store (CDS), 10, 2018.

Hersbach, H., B. Bell, P. Berrisford, S. Hirahara, A. Horányi, J. Muñoz-Sabater, J. Nicolas, C. Peubey, R. Radu, D. Schepers, et al., The era5 global reanalysis, Quarterly Journal of the Royal Meteorological Society, 146(730), 1999–2049, 2020.

Hill, C., C. DeLuca, M. Suarez, A. Da Silva, et al., The architecture of the earth system modeling framework, Computing in Science & Engineering, 6(1), 18–28, 2004.

Hoerling, M., A. Kumar, R. Dole, J. W. Nielsen-Gammon, J. Eischeid, J. Perlwitz, X.-W. Quan, T. Zhang, P. Pegion, and M. Chen, Anatomy of an extreme event, Journal of Climate, 26(9), 2811–2832, 2013.

Hoerling, M., J. Eischeid, A. Kumar, R. Leung, A. Mariotti, K. Mo, S. Schubert, and R. Seager, Causes and predictability of the 2012 great plains drought, Bulletin of the American Meteorological Society, 95(2), 269–282, 2014.

Hortal, M., and A. Simmons, Use of reduced gaussian grids in spectral models, Monthly Weather Review, 119(4), 1057–1074, 1991.

Huang, D., P. Yan, J. Zhu, Y. Zhang, X. Kuang, and J. Cheng, Uncertainty of global summer precipitation in the cmip5 models: A comparison between high-resolution and low-resolution models, Theoretical and applied climatology, 132(1), 55–69, 2018.

Huffman, G. J., R. F. Adler, M. M. Morrissey, D. T. Bolvin, S. Curtis, R. Joyce, B. McGavock, and J. Susskind, Global precipitation at one-degree daily resolution from multisatellite observations, Journal of hydrometeorology, 2(1), 36–50, 2001.

Huth, R., C. Beck, A. Philipp, M. Demuzere, Z. Ustrnul, M. Cahynová, J. Kyselỳ, and O. E. Tveito, Classifications of atmospheric circulation patterns: recent advances and applications, Annals of the New York Academy of Sciences, 1146(1), 105–152, 2008.

Huth, R., C. Beck, and M. Kuerová, Synoptic-climatological evaluation of the classifications of atmospheric circulation patterns over europe, International Journal of Climatology, 36(7), 2710–2726, 2016.

IPCC, Annex I: Glossary, p. 541–562, Cambridge University Press, doi:10.1017/9781009157940.008, 2022.

Irannezhad, M., D. Chen, B. Kløve, and H. Moradkhani, Analysing the variability and trends of precipitation extremes in finland and their connection to atmospheric circulation patterns, International journal of climatology, 37, 1053–1066, 2017.

Jarvis, A., and D. Leedal, The geoengineering model intercomparison project (geomip): A control perspective, Atmospheric Science Letters, 13(3), 157–163, 2012.

Jenkinson, A., and F. Collison, An initial climatology of gales over the north sea, Synoptic climatology branch memorandum, 62, 18, 1977.

Jiang, N., A new objective procedure for classifying new zealand synoptic weather types during 1958–2008, International Journal of Climatology, 31(6), 863–879, 2011.

John, A., H. Douville, A. Ribes, and P. Yiou, Quantifying cmip6 model uncertainties in extreme precipitation projections, Weather and Climate Extremes, 36, 100,435, 2022.

Jones, P. W., First-and second-order conservative remapping schemes for grids in spherical coordinates, Monthly Weather Review, 127(9), 2204–2210, 1999.

Jones, P. W., et al., A user's guide for scrip: A spherical coordinate remapping and interpolation package, Los Alamos National Laboratory, Los Alamos, NM, 1998.

Kanemaru, K., T. Kubota, T. Iguchi, Y. N. Takayabu, and R. Oki, Development of a precipitation climate record from spaceborne precipitation radar data. part i: Mitigation of the effects of switching to redundancy electronics in the trmm precipitation radar, Journal of Atmospheric and Oceanic Technology, 34(9), 2043–2057, 2017.

Kao, S.-C., and A. R. Ganguly, Intensity, duration, and frequency of precipitation extremes under 21st-century warming scenarios, Journal of Geophysical Research: Atmospheres, 116(D16), 2011.

Karl, T. R., and D. R. Easterling, Climate extremes: Selected review and future research directions, Climatic change, 42(1), 309–325, 1999.

Karl, T. R., N. Nicholls, and A. Ghazi, Clivar/gcos/wmo workshop on indices and indicators for climate extremes workshop summary, in Weather and climate extremes, pp. 3–7, Springer, 1999.

Katz, R. W., M. B. Parlange, and P. Naveau, Statistics of extremes in hydrology, Advances in water resources, 25(8-12), 1287-1304, 2002.

Kawecki, S., G. M. Henebry, and A. L. Steiner, Effects of urban plume aerosols on a mesoscale convective system, Journal of the Atmospheric Sciences, 73(12), 4641-4660, 2016.

Kendon, M., and M. McCarthy, The uk's wet and stormy winter of 2013/2014, Weather, 70(2), 40-47, 2015.

Kent, C., R. Chadwick, and D. P. Rowell, Understanding uncertainties in future projections of seasonal tropical precipitation, Journal of Climate, 28(11), 4390-4413, 2015.

Kharin, V., G. Flato, X. Zhang, N. Gillett, F. Zwiers, and K. Anderson, Risks from climate extremes change differently from 1.5 c to 2.0 c depending on rarity, Earth's Future, 6(5), 704-715, 2018.

Kharin, V. V., F. W. Zwiers, X. Zhang, and G. C. Hegerl, Changes in temperature and precipitation extremes in the ipcc ensemble of global coupled model simulations, Journal of Climate, 20(8), 1419-1444, 2007.

Kharin, V. V., F. Zwiers, X. Zhang, and M. Wehner, Changes in temperature and precipitation extremes in the cmip5 ensemble, Climatic change, 119(2), 345-357, 2013.

Knutti, R., and D. Masson, D. & a. gettelman (2013), Climate Model Genealogy: Generation CMIP5 and How we got there, pp. 1194-1199, 2013.

Kodama, C., B. Stevens, T. Mauritsen, T. Seiki, and M. Satoh, A new perspective for future precipitation change from intense extratropical cyclones, Geophysical Research Letters, 46(21), 12,435-12,444, 2019.

Koster, R. D., Y. Chang, H. Wang, and S. D. Schubert, Impacts of local soil moisture anomalies on the atmospheric circulation and on remote surface meteorological fields during boreal summer: A comprehensive analysis over north america, Journal of Climate, 29(20), 7345-7364, 2016.

Kotlarski, S., P. Szabó, S. Herrera, O. Räty, K. Keuler, P. M. Soares, R. M. Cardoso, T. Bosshard, C. Pagé, F. Boberg, et al., Observational uncertainty and regional climate model evaluation: a pan-european perspective, International Journal of Climatology, 39(9), 3730-3749, 2019.

Kravitz, B., A. Robock, O. Boucher, H. Schmidt, K. E. Taylor, G. Stenchikov, and M. Schulz, The geoengineering model intercomparison project (geomip), Atmospheric Science Letters, 12(2), 162-167, 2011.

Lamb, H. H., British isles weather types and a register of the daily sequence of circu lation patterns 1861-1971, Geophysical Memoirs, 1972.

Lambert, F. H., and M. J. Webb, Dependency of global mean precipitation on surface temperature, Geophysical Research Letters, 35(16), 2008.

Lee, C. C., The development of a gridded weather typing classification scheme, International Journal of Climatology, 35(5), 641-659, 2015.

Lee, J., J. Marotzke, G. Bala, L. Cao, S. Corti, J. Dunne, F. Engelbrecht, E. Fischer, J. Fyfe, C. Jones, et al., Future global climate: scenariobased projections and near-term information, Climate change, 2021.

Lehner, F., C. Deser, N. Maher, J. Marotzke, E. M. Fischer, L. Brunner, R. Knutti, and E. Hawkins, Partitioning climate projection uncertainty with multiple large ensembles and cmip5/6, Earth System Dynamics, 11(2), 491-508, 2020.

Lenderink, G., R. Barbero, J. Loriaux, and H. Fowler, Super-clausius-clapeyron scaling of extreme hourly convective precipitation and its relation to large-scale atmospheric conditions, Journal of Climate, 30(15), 6037-6052, 2017.

Levizzani, V., C. Kidd, K. Aonashi, R. Bennartz, R. Ferraro, G. Huffman, R. Roca, F. Turk, and N.-Y. Wang, The activities of the international precipitation working group, Quarterly Journal of the Royal Meteorological Society, 144, 3–15, 2018.

Li, C., F. Zwiers, X. Zhang, G. Li, Y. Sun, and M. Wehner, Changes in annual extremes of daily temperature and precipitation in cmip6 models, Journal of Climate, pp. 1–61, 2020.

Lin, L., Z. Wang, Y. Xu, and Q. Fu, Sensitivity of precipitation extremes to radiative forcing of greenhouse gases and aerosols, Geophysical Research Letters, 43(18), 9860–9868, 2016.

Lin, L., Z. Wang, Y. Xu, Q. Fu, and W. Dong, Larger sensitivity of precipitation extremes to aerosol than greenhouse gas forcing in cmip5 models, Journal of Geophysical Research: Atmospheres, 123(15), 8062–8073, 2018.

Lionello, P., and L. Scarascia, The relation of climate extremes with global warming in the mediterranean region and its north versus south contrast, Regional Environmental Change, 20(1), 1–16, 2020.

Liu, B., X. Tan, T. Y. Gan, X. Chen, K. Lin, M. Lu, and Z. Liu, Global atmospheric moisture transport associated with precipitation extremes: Mechanisms and climate change impacts, Wiley Interdisciplinary Reviews: Water, 7(2), e1412, 2020.

Liu, M., G. A. Vecchi, J. A. Smith, and T. R. Knutson, Causes of large projected increases in hurricane precipitation rates with global warming, npj Climate and Atmospheric Science, 2(1), 1–5, 2019.

Loikith, P. C., D. E. Waliser, H. Lee, J. Kim, J. D. Neelin, B. R. Lintner, S. McGinnis, C. A. Mattmann, and L. O. Mearns, Surface temperature probability distributions in the narccap hindcast experiment: Evaluation methodology, metrics, and results, Journal of Climate, 28(3), 978–997, 2015.

Lucas-Picher, P., D. Argüeso, E. Brisson, Y. Tramblay, P. Berg, A. Lemonsu, S. Kotlarski, and C. Caillaud, Convection-permitting modeling with regional climate models: Latest developments and next steps, Wiley Interdisciplinary Reviews: Climate Change, p. e731, 2021.

Madsen, H., C. P. Pearson, and D. Rosbjerg, Comparison of annual maximum series and partial duration series methods for modeling extreme hydrologic events: 2. regional modeling, Water Resources Research, 33(4), 759–769, 1997a.

Madsen, H., P. F. Rasmussen, and D. Rosbjerg, Comparison of annual maximum series and partial duration series methods for modeling extreme hydrologic events: 1. at-site modeling, Water resources research, 33(4), 747–757, 1997b.

Madsen, H., D. Lawrence, M. Lang, M. Martinkova, and T. Kjeldsen, Review of trend analysis and climate change projections of extreme precipitation and floods in europe, Journal of Hydrology, 519, 3634–3650, 2014.

Maggioni, V., P. C. Meyers, and M. D. Robinson, A review of merged high-resolution satellite precipitation product accuracy during the tropical rainfall measuring mission (trmm) era, Journal of Hydrometeorology, 17(4), 1101–1117, 2016.

Maraun, D., T. G. Shepherd, M. Widmann, G. Zappa, D. Walton, J. M. Gutiérrez, S. Hagemann, I. Richter, P. M. Soares, A. Hall, et al., Towards process-informed bias correction of climate change simulations, Nature Climate Change, 7(11), 764–773, 2017.

Marelle, L., G. Myhre, Ø. Hodnebrog, J. Sillmann, and B. H. Samset, The changing seasonality of extreme daily precipitation, Geophysical Research Letters, 45(20), 11–352, 2018.

Martins, E. S., and J. R. Stedinger, Historical information in a generalized maximum likelihood framework with partial duration and annual maximum series, Water resources research, 37(10), 2559–2567, 2001.

Masson-Delmotte, V., P. Zhai, A. Pirani, S. L. Connors, C. Péan, S. Berger, N. Caud, Y. Chen, L. Goldfarb, M. I. Gomis, M. Huang, K. Leitzell, E. Lonnoy, J. B. R. Matthews, T. K. Maycock, T. Waterfield, O. Yelekçi, R. Yu, B. Zhou, and (eds.), Ipcc, 2021: Summary for policymakers., in Climate Change 2021: The Physical Science Basis. Contribution of Working Group I to the Sixth Assessment Report of the Intergovernmental Panel on Climate Change, Cambridge University Press, 2021a.

Masson-Delmotte, V., P. Zhai, A. Pirani, S. L. Connors, C. Péan, S. Berger, N. Caud, Y. Chen, L. Goldfarb, M. Gomis, et al., Climate change 2021: the physical science basis, Contribution of working group I to the sixth assessment report of the intergovernmental panel on climate change, p. 2, 2021b.

Meehl, G. A., C. A. Senior, V. Eyring, G. Flato, J.-F. Lamarque, R. J. Stouffer, K. E. Taylor, and M. Schlund, Context for interpreting equilibrium climate sensitivity and transient climate response from the cmip6 earth system models, Science Advances, 6(26), eaba1981, 2020.

Mehran, A., A. AghaKouchak, and T. J. Phillips, Evaluation of cmip5 continental precipitation simulations relative to satellite-based gauge-adjusted observations, Journal of Geophysical Research: Atmospheres, 119(4), 1695–1707, 2014.

Min, S.-K., X. Zhang, F. W. Zwiers, and G. C. Hegerl, Human contribution to more-intense precipitation extremes, Nature, 470(7334), 378–381, 2011.

Mitchell, J. F., C. Wilson, and W. Cunnington, On co2 climate sensitivity and model dependence of results, Quarterly Journal of the Royal Meteorological Society, 113(475), 293–322, 1987.

Mizuta, R., and H. Endo, Projected changes in extreme precipitation in a 60-km agcm large ensemble and their dependence on return periods, Geophysical Research Letters, 47(13), e2019GL086,855, 2020.

Molnar, P., S. Fatichi, L. Gaál, J. Szolgay, and P. Burlando, Storm type effects on super clausius-clapeyron scaling of intense rainstorm properties with air temperature, Hydrology and Earth System Sciences, 19(4), 1753–1766, 2015.

Moon, H., B. P. Guillod, L. Gudmundsson, and S. I. Seneviratne, Soil moisture effects on afternoon precipitation occurrence in current climate models, Geophysical research letters, 46(3), 1861–1869, 2019.

Mullan, D., D. Favis-Mortlock, and R. Fealy, Addressing key limitations associated with modelling soil erosion under the impacts of future climate change, Agricultural and Forest Meteorology, 156, 18–30, 2012.

Muller, C. J., and P. O'Gorman, An energetic perspective on the regional response of precipitation to climate change, Nature Climate Change, 1(5), 266–271, 2011.

Muller, C. J., P. A. O'Gorman, and L. E. Back, Intensification of precipitation extremes with warming in a cloud-resolving model, Journal of Climate, 24(11), 2784–2800, 2011.

Muñoz Sabater, J., et al., Era5-land hourly data from 1981 to present, Copernicus Climate Change Service (C3S) Climate Data Store (CDS), 10, 2019.

Myhre, G., R. Kramer, C. Smith, Ø. Hodnebrog, P. Forster, B. Soden, B. Samset, C. Stjern, T. Andrews, O. Boucher, et al., Quantifying the importance of rapid adjustments for global precipitation changes, Geophysical research letters, 45(20), 11–399, 2018.

Myhre, G., K. Alterskjær, C. W. Stjern, Ø. Hodnebrog, L. Marelle, B. H. Samset, J. Sillmann, N. Schaller, E. Fischer, M. Schulz, et al., Frequency of extreme precipitation increases extensively with event rareness under global warming, Scientific reports, 9(1), 1–10, 2019.

Nath, R., Y. Luo, W. Chen, and X. Cui, On the contribution of internal variability and external forcing factors to the cooling trend over the humid subtropical indo-gangetic plain in india, Scientific reports, 8(1), 1–11, 2018.

Naveau, P., A. Guillou, D. Cooley, and J. Diebolt, Modelling pairwise dependence of maxima in space, Biometrika, 96(1), 1–17, 2009.

Nie, J., A. H. Sobel, D. A. Shaevitz, and S. Wang, Dynamic amplification of extreme precipitation sensitivity, Proceedings of the National Academy of Sciences, 115(38), 9467–9472, 2018.

Nijsse, F. J., P. M. Cox, and M. S. Williamson, Emergent constraints on transient climate response (tcr) and equilibrium climate sensitivity (ecs) from historical warming in cmip5 and cmip6 models, Earth System Dynamics, 11(3), 737–750, 2020.

Norris, J., G. Chen, and J. D. Neelin, Changes in frequency of large precipitation accumulations over land in a warming climate from the cesm large ensemble: The roles of moisture, circulation, and duration, Journal of Climate, 32(17), 5397–5416, 2019.

O'Neill, B. C., C. Tebaldi, D. P. v. Vuuren, V. Eyring, P. Friedlingstein, G. Hurtt, R. Knutti, E. Kriegler, J.-F. Lamarque, J. Lowe, et al., The scenario model intercomparison project (scenariomip) for cmip6, Geoscientific Model Development, 9(9), 3461–3482, 2016.

O'Reilly, C., B. Booth, L. Brunner, S. Qasmi, R. Nogherotto, A. Ballinger, D. Befort, and A. Weisheimer, Testing methods to constrain future european climate projections in an "out-of-sample" framework, Tech. rep., Copernicus Meetings, 2022.

Otero, N., J. Sillmann, and T. Butler, Assessment of an extended version of the jenkinson–collison classification on cmip5 models over europe, Climate dynamics, 50(5), 1559–1579, 2018.

Otto, F. E., N. Massey, G. J. Van Oldenborgh, R. G. Jones, and M. R. Allen, Reconciling two approaches to attribution of the 2010 russian heat wave, Geophysical Research Letters, 39(4), 2012.

Otto, F. E., K. van der Wiel, G. J. van Oldenborgh, S. Philip, S. F. Kew, P. Uhe, and H. Cullen, Climate change increases the probability of heavy rains in northern england/southern scotland like those of storm desmond—a real-time event attribution revisited, Environmental Research Letters, 13(2), 024,006, 2018.

Otto, F. E., L. Harrington, K. Schmitt, S. Philip, S. Kew, G. J. van Oldenborgh, R. Singh, J. Kimutai, and P. Wolski, Challenges to understanding extreme weather changes in lower income countries, Bulletin of the American Meteorological Society, 101(10), E1851–E1860, 2020.

Oudar, T., J. Cattiaux, and H. Douville, Drivers of the northern extratropical eddy-driven jet change in cmip5 and cmip6 models, Geophysical Research Letters, 47(8), e2019GL086,695, 2020.

Oueslati, B., S. Bony, C. Risi, and J.-L. Dufresne, Interpreting the inter-model spread in regional precipitation projections in the tropics: role of surface evaporation and cloud radiative effects, Climate dynamics, 47(9), 2801–2815, 2016.

O'Gorman, P. A., Precipitation extremes under climate change, Current climate change reports, 1(2), 49–59, 2015.

O'Gorman, P. A., R. P. Allan, M. P. Byrne, and M. Previdi, Energetic constraints on precipitation under climate change, Surveys in geophysics, 33(3), 585–608, 2012.

Paerl, H. W., Mitigating toxic planktonic cyanobacterial blooms in aquatic ecosystems facing increasing anthropogenic and climatic pressures, Toxins, 10(2), 76, 2018.

Paik, S., S.-K. Min, X. Zhang, M. G. Donat, A. D. King, and Q. Sun, Determining the anthropogenic greenhouse gas contribution to the observed intensification of extreme precipitation, Geophysical Research Letters, 47(12), e2019GL086,875, 2020.

Pall, P., M. Allen, and D. A. Stone, Testing the clausius–clapeyron constraint on changes in extreme precipitation under co 2 warming, Climate Dynamics, 28(4), 351–363, 2007.

Pall, P., T. Aina, D. A. Stone, P. A. Stott, T. Nozawa, A. G. Hilberts, D. Lohmann, and M. R. Allen, Anthropogenic greenhouse gas contribution to flood risk in england and wales in autumn 2000, Nature, 470(7334), 382–385, 2011.

Pall, P., C. M. Patricola, M. F. Wehner, D. A. Stone, C. J. Paciorek, and W. D. Collins, Diagnosing conditional anthropogenic contributions to heavy colorado rainfall in september 2013, Weather and Climate Extremes, 17, 1–6, 2017.

Panofsky, H. A., G. W. Brier, and W. H. Best, Some application of statistics to meteorology, 1958.

Park, K. J., K. Yoshimura, H. Kim, and T. Oki, Chronological development of terrestrial mean precipitation, Bulletin of the American Meteorological Society, 98(11), 2411–2428, 2017.

Pendergrass, A., D. Coleman, C. Deser, F. Lehner, N. Rosenbloom, and I. Simpson, Nonlinear response of extreme precipitation to warming in cesm1, Geophysical research letters, 46(17-18), 10,551–10,560, 2019.

Pendergrass, A. G., The global-mean precipitation response to co2-induced warming in cmip6 models, Geophysical Research Letters, 47(17), e2020GL089,964, 2020.

Pendergrass, A. G., and D. L. Hartmann, The atmospheric energy constraint on global-mean precipitation change, Journal of climate, 27(2), 757–768, 2014.

Pendergrass, A. G., F. Lehner, B. M. Sanderson, and Y. Xu, Does extreme precipitation intensity depend on the emissions scenario?, Geophysical Research Letters, 42(20), 8767–8774, 2015.

Peterson, T., C. Folland, G. Gruza, W. Hogg, A. Mokssit, and N. Plummer, Report on the activities of the working group on climate change detection and related rapporteurs, Citeseer, 2001.

Peterson, T. C., and M. J. Manton, Monitoring changes in climate extremes: a tale of international collaboration, Bulletin of the American Meteorological Society, 89(9), 1266–1271, 2008.

Pfahl, S., P. A. O'Gorman, and E. M. Fischer, Understanding the regional pattern of projected future changes in extreme precipitation, Nature Climate Change, 7(6), 423–427, 2017.

Pichelli, E., E. Coppola, S. Sobolowski, N. Ban, F. Giorgi, P. Stocchi, A. Alias, D. Belušić, S. Berthou, C. Caillaud, et al., The first multi-model ensemble of regional climate simulations at kilometer-scale resolution part 2: historical and future simulations of precipitation, Climate Dynamics, 56(11), 3581–3602, 2021.

Pitman, A. J., The evolution of, and revolution in, land surface schemes designed for climate models, International Journal of Climatology: A Journal of the Royal Meteorological Society, 23(5), 479–510, 2003.

Pletzer, A., and W. Hayek, Mimetic interpolation of vector fields on arakawa c/d grids, Monthly Weather Review, 147(1), 3–16, 2019.

Polade, S. D., D. W. Pierce, D. R. Cayan, A. Gershunov, and M. D. Dettinger, The key role of dry days in changing regional climate and precipitation regimes, Scientific reports, 4(1), 1–8, 2014.

Polade, S. D., A. Gershunov, D. R. Cayan, M. D. Dettinger, and D. W. Pierce, Precipitation in a warming world: Assessing projected hydro-climate changes in california and other mediterranean climate regions, Scientific reports, 7(1), 1–10, 2017.

Poschlod, B., R. Ludwig, and J. Sillmann, Ten-year return levels of sub-daily extreme precipitation over europe, Earth System Science Data, 13(3), 983–1003, 2021.

Prein, A. F., W. Langhans, G. Fosser, A. Ferrone, N. Ban, K. Goergen, M. Keller, M. Tölle, O. Gutjahr, F. Feser, et al., A review on regional convection-permitting climate modeling: Demonstrations, prospects, and challenges, Reviews of geophysics, 53(2), 323–361, 2015.

Previdi, M., Radiative feedbacks on global precipitation, Environmental Research Letters, 5(2), 025,211, 2010.

Raäisaänen, J., How reliable are climate models?, Tellus A: Dynamic Meteorology and Oceanography, 59(1), 2–29, 2007.

Raible, C. C., M. Messmer, F. Lehner, T. F. Stocker, and R. Blender, Extratropical cyclone statistics during the last millennium and the 21st century, Climate of the Past, 14(10), 1499–1514, 2018.

Rajczak, J., and C. Schär, Projections of future precipitation extremes over europe: a multimodel assessment of climate simulations, Journal of Geophysical Research: Atmospheres, 122(20), 10–773, 2017.

Randall, D. A., R. A. Wood, S. Bony, R. Colman, T. Fichefet, J. Fyfe, V. Kattsov, A. Pitman, J. Shukla, J. Srinivasan, et al., Climate models and their evaluation, in Climate change 2007: The physical science basis. Contribution of Working Group I to the Fourth Assessment Report of the IPCC (FAR), pp. 589–662, Cambridge University Press, 2007.

Rappaport, E. N., Fatalities in the united states from atlantic tropical cyclones: New data and interpretation, Bulletin of the American Meteorological Society, 95(3), 341–346, 2014.

Ribes, A., S. Thao, R. Vautard, B. Dubuisson, S. Somot, J. Colin, S. Planton, and J.-M. Soubeyroux, Observed increase in extreme daily rainfall in the french mediterranean, Climate dynamics, 52(1), 1095–1114, 2019.

Ribes, A., S. Qasmi, and N. P. Gillett, Making climate projections conditional on historical observations, Science Advances, 7(4), eabc0671, 2021.

Rio, C., A. D. Del Genio, and F. Hourdin, Ongoing breakthroughs in convective parameterization, Current Climate Change Reports, 5(2), 95–111, 2019.

Roca, R., L. V. Alexander, G. Potter, M. Bador, R. Jucá, S. Contractor, M. G. Bosilovich, and S. Cloché, Frogs: a daily 1°× 1° gridded precipitation database of rain gauge, satellite and reanalysis products, Earth System Science Data, 11(3), 1017–1035, 2019.

Roderick, T. P., C. Wasko, and A. Sharma, Atmospheric moisture measurements explain increases in tropical rainfall extremes, Geophysical Research Letters, 46(3), 1375–1382, 2019.

Roehrig, R., I. Beau, D. Saint-Martin, A. Alias, B. Decharme, J.-F. Guérémy, A. Voldoire, A. Y. Abdel-Lathif, E. Bazile, S. Belamari, et al., The cnrm global atmosphere model arpege-climat 6.3: Description and evaluation, Journal of Advances in Modeling Earth Systems, 12(7), e2020MS002,075, 2020.

Rowell, D. P., Sources of uncertainty in future changes in local precipitation, Climate dynamics, 39(7), 1929–1950, 2012.

Salzmann, M., Global warming without global mean precipitation increase?, Science advances, 2(6), e1501,572, 2016.

Samset, B., G. Myhre, P. Forster, Ø. Hodnebrog, T. Andrews, G. Faluvegi, D. Flaeschner, M. Kasoar, V. Kharin, A. Kirkevåg, et al., Fast and slow precipitation responses to individual climate forcers: A pdrmip multimodel study, Geophysical research letters, 43(6), 2782–2791, 2016.

Samset, B. H., M. Sand, C. J. Smith, S. E. Bauer, P. M. Forster, J. S. Fuglestvedt, S. Osprey, and C.-F. Schleussner, Climate impacts from a removal of anthropogenic aerosol emissions, Geophysical Research Letters, 45(2), 1020–1029, 2018.

Sato, T., and T. Nakamura, Intensification of hot eurasian summers by climate change and land-atmosphere interactions, Scientific reports, 9(1), 1–8, 2019.

Schaller, N., I. Mahlstein, J. Cermak, and R. Knutti, Analyzing precipitation projections: A comparison of different approaches to climate model evaluation, Journal of Geophysical Research: Atmospheres, 116(D10), 2011.

Schaller, N., A. L. Kay, R. Lamb, N. R. Massey, G. J. Van Oldenborgh, F. E. Otto, S. N. Sparrow, R. Vautard, P. Yiou, I. Ashpole, et al., Human influence on climate in the 2014 southern england winter floods and their impacts, Nature Climate Change, 6(6), 627–634, 2016.

Scherrer, S. C., E. M. Fischer, R. Posselt, M. A. Liniger, M. Croci-Maspoli, and R. Knutti, Emerging trends in heavy precipitation and hot temperature extremes in switzerland, Journal of Geophysical Research: Atmospheres, 121(6), 2626–2637, 2016.

Schmitt, L. H., H. M. Graham, and P. C. White, Economic evaluations of the health impacts of weather-related extreme events: a scoping review, International journal of environmental research and public health, 13(11), 1105, 2016.

Schroeer, K., and G. Kirchengast, Sensitivity of extreme precipitation to temperature: the variability of scaling factors from a regional to local perspective, Climate Dynamics, 50(11), 3981–3994, 2018.

Séférian, R., C. Delire, B. Decharme, A. Voldoire, D. Salas y Melia, M. Chevallier, D. Saint-Martin, O. Aumont, J.-C. Calvet, D. Carrer, et al., Development and evaluation of cnrm earth system model-cnrm-esml, Geoscientific Model Development, 9(4), 1423–1453, 2016.

Séférian, R., P. Nabat, M. Michou, D. Saint-Martin, A. Voldoire, J. Colin, B. Decharme, C. Delire, S. Berthet, M. Chevallier, et al., Evaluation of cnrm earth system model, cnrm-esm2-1: Role of earth system processes in present-day and future climate, Journal of Advances in Modeling Earth Systems, 11(12), 4182–4227, 2019.

Seneviratne, S., X. Zhang, M. Adnan, W. Badi, C. Dereczynski, A. Di Luca, S. Ghosh, I. Iskandar, J. Kossin, S. Lewis, F. Otto, I. Pinto, M. Satoh, S. M. Vicente-Serrano, M. Wehner, and B. Zhou, Weather and climate extreme events in a changing climate, in Climate Change 2021: The Physical Science Basis. Contribution of Working Group I to the Sixth Assessment Report of the Intergovernmental Panel on Climate Change, edited by Masson-Delmotte, V., P. Zhai, A. Pirani, S. L. Connors, C. Péan, S. Berger, N. Caud, Y. Chen, L. Goldfarb, M. I. Gomis, M. Huang, K. Leitzell, E. Lonnoy, J. B. R. Matthews, T. K. Maycock, T. Waterfield, O. Yelekçi, R. Yu, and B. Zhou, chap. 11, Cambridge University Press. In Press., 2021.

Seneviratne, S. I., Historical drought trends revisited, Nature, 491(7424), 338–339, 2012.

Seneviratne, S. I., M. Wilhelm, T. Stanelle, B. van den Hurk, S. Hagemann, A. Berg, F. Cheruy, M. E. Higgins, A. Meier, V. Brovkin, et al., Impact of soil moisture-climate feedbacks on cmip5 projections: First results from the glace-cmip5 experiment, Geophysical Research Letters, 40(19), 5212–5217, 2013.

Serrano-Notivoli, R., S. Beguería, M. Á. Saz, and M. de Luis, Recent trends reveal decreasing intensity of daily precipitation in spain, International Journal of Climatology, 38(11), 4211–4224, 2018.

Shepherd, T. G., Atmospheric circulation as a source of uncertainty in climate change projections, Nature Geoscience, 7(10), 703–708, 2014.

Shepherd, T. G., A common framework for approaches to extreme event attribution, Current Climate Change Reports, 2(1), 28–38, 2016.

Shepherd, T. G., E. Boyd, R. A. Calel, S. C. Chapman, S. Dessai, I. M. Dima-West, H. J. Fowler, R. James, D. Maraun, O. Martius, et al., Storylines: an alternative approach to representing uncertainty in physical aspects of climate change, Climatic change, 151(3), 555–571, 2018.

Sheridan, S. C., The redevelopment of a weather-type classification scheme for north america, International Journal of Climatology: A Journal of the Royal Meteorological Society, 22(1), 51–68, 2002.

Sherwood, S., R. Roca, T. Weckwerth, and N. Andronova, Tropospheric water vapor, convection, and climate, Reviews of Geophysics, 48(2), 2010.

Shiogama, H., M. Watanabe, H. Kim, and N. Hirota, Emergent constraints on future precipitation changes, Nature, 602(7898), 612–616, 2022.

Sillmann, J., V. Kharin, X. Zhang, F. Zwiers, and D. Bronaugh, Climate extremes indices in the cmip5 multimodel ensemble: Part 1. model evaluation in the present climate, Journal of Geophysical Research: Atmospheres, 118(4), 1716–1733, 2013a.

Sillmann, J., V. V. Kharin, F. Zwiers, X. Zhang, and D. Bronaugh, Climate extremes indices in the cmip5 multimodel ensemble: Part 2. future climate projections, Journal of Geophysical Research: Atmospheres, 118(6), 2473–2493, 2013b.

Sillmann, J., C. W. Stjern, G. Myhre, B. H. Samset, Ø. Hodnebrog, T. Andrews, O. Boucher, G. Faluvegi, P. Forster, M. R. Kasoar, et al., Extreme wet and dry conditions affected differently by greenhouse gases and aerosols, npj climate and atmospheric science, 2(1), 1–7, 2019.

Simmons, A. J., and D. M. Burridge, An energy and angular-momentum conserving vertical finite-difference scheme and hybrid vertical coordinates, Monthly Weather Review, 109(4), 758–766, 1981.

Souri, A. H., Y. Choi, J. K. Kodros, J. Jung, J. Shpund, J. R. Pierce, B. H. Lynn, A. Khain, and K. Chance, Response of hurricane harvey's rainfall to anthropogenic aerosols: A sensitivity study based on spectral bin microphysics with simulated aerosols, Atmospheric Research, 242, 104,965, 2020.

Sperna Weiland, F., L. Van Beek, J. Kwadijk, and M. Bierkens, The ability of a gcm-forced hydrological model to reproduce global discharge variability, Hydrology and Earth System Sciences, 14(8), 1595–1621, 2010.

Stephens, G. L., and Y. Hu, Are climate-related changes to the character of global-mean precipitation predictable?, Environmental Research Letters, 5(2), 025,209, 2010.

Stocker, T. F., D. Qin, G.-K. Plattner, L. V. Alexander, S. K. Allen, N. L. Bindoff, F.-M. Bréon, J. A. Church, U. Cubasch, S. Emori, et al., Technical summary, in Climate change 2013: the physical science basis. Contribution of Working Group I to the Fifth Assessment Report of the Intergovernmental Panel on Climate Change, pp. 33–115, Cambridge University Press, 2013.

Stocker, T. F., D. Qin, G.-K. Plattner, M. M. Tignor, S. K. Allen, J. Boschung, A. Nauels, Y. Xia, V. Bex, and P. M. Midgley, Climate Change 2013: The physical science basis. contribution of working group I to the fifth assessment report of IPCC the intergovernmental panel on climate change, Cambridge University Press, 2014.

Stott, P. A., J. F. Mitchell, M. R. Allen, T. L. Delworth, J. M. Gregory, G. A. Meehl, and B. D. Santer, Observational constraints on past attributable warming and predictions of future global warming, Journal of Climate, 19(13), 3055–3069, 2006.

Sudharsan, N., S. Karmakar, H. J. Fowler, and V. Hari, Large-scale dynamics have greater role than thermodynamics in driving precipitation extremes over india, Climate dynamics, 55(9), 2603–2614, 2020.

Sugiyama, M., H. Shiogama, and S. Emori, Precipitation extreme changes exceeding moisture content increases in miroc and ipcc climate models, Proceedings of the National Academy of Sciences, 107(2), 571–575, 2010.

Sun, C., L. Zhu, Y. Liu, Z. Hao, and J. Zhang, Changes in the drought condition over northern east asia and the connections with extreme temperature and precipitation indices, Global and Planetary Change, 207, 103,645, 2021a.

Sun, Q., C. Miao, and Q. Duan, Comparative analysis of cmip3 and cmip5 global climate models for simulating the daily mean, maximum, and minimum temperatures and daily precipitation over china, Journal of Geophysical Research: Atmospheres, 120(10), 4806–4824, 2015.

Sun, Q., X. Zhang, F. Zwiers, S. Westra, and L. V. Alexander, A global, continental, and regional analysis of changes in extreme precipitation, Journal of Climate, 34(1), 243–258, 2021b.

Sun, Y., X. Zhang, F. W. Zwiers, L. Song, H. Wan, T. Hu, H. Yin, and G. Ren, Rapid increase in the risk of extreme summer heat in eastern china, Nature Climate Change, 4(12), 1082–1085, 2014.

Sunyer, M. A., H. Madsen, D. Rosbjerg, and K. Arnbjerg-Nielsen, Regional interdependency of precipitation indices across denmark in two ensembles of high-resolution rcms, Journal of Climate, 26(20), 7912–7928, 2013.

Swart, N. C., J. N. Cole, V. V. Kharin, M. Lazare, J. F. Scinocca, N. P. Gillett, J. Anstey, V. Arora, J. R. Christian, S. Hanna, et al., The canadian earth system model version 5 (canesm5. 0.3), Geoscientific Model Development, 12(11), 4823–4873, 2019.

Sylla, M., F. Giorgi, E. Coppola, and L. Mariotti, Uncertainties in daily rainfall over africa: assessment of gridded observation products and evaluation of a regional climate model simulation, International Journal of Climatology, 33(7), 1805–1817, 2013.

Takahashi, C., M. Watanabe, and M. Mori, Significant aerosol influence on the recent decadal decrease in tropical cyclone activity over the western north pacific, Geophysical Research Letters, 44(18), 9496–9504, 2017.

Tan, J., L. Oreopoulos, C. Jakob, and D. Jin, Evaluating rainfall errors in global climate models through cloud regimes, Climate Dynamics, 50(9), 3301–3314, 2018.

Tanaka, K., and B. C. O'Neill, The paris agreement zero-emissions goal is not always consistent with the 1.5° c and 2° c temperature targets, Nature Climate Change, 8(4), 319–324, 2018.

Tang, T., D. Shindell, B. H. Samset, O. Boucher, P. M. Forster, Ø. Hodnebrog, G. Myhre, J. Sillmann, A. Voulgarakis, T. Andrews, et al., Dynamical response of mediterranean precipitation to greenhouse gases and aerosols, Atmospheric Chemistry and Physics, 18(11), 8439–8452, 2018.

Tangang, F., L. Juneng, and E. Aldrian, Observed changes in extreme temperature and precipitation over indonesia, International Journal of Climatology, 37(4), 1979–1997, 2017.

Tapiador, F., A. Navarro, V. Levizzani, E. García-Ortega, G. Huffman, C. Kidd, P. Kucera, C. Kummerow, H. Masunaga, W. Petersen, et al., Global precipitation measurements for validating climate models, Atmospheric Research, 197, 1–20, 2017.

Taylor, C. M., R. A. de Jeu, F. Guichard, P. P. Harris, and W. A. Dorigo, Afternoon rain more likely over drier soils, Nature, 489(7416), 423–426, 2012.

Taylor, K. E., Summarizing multiple aspects of model performance in a single diagram, Journal of Geophysical Research: Atmospheres, 106(D7), 7183–7192, 2001.

Tebaldi, C., K. Hayhoe, J. M. Arblaster, and G. A. Meehl, Going to the extremes, Climatic change, 79(3), 185–211, 2006.

Tencer, B., A. Weaver, and F. Zwiers, Joint occurrence of daily temperature and precipitation extreme events over canada, Journal of Applied Meteorology and Climatology, 53(9), 2148–2162, 2014.

Thackeray, C. W., A. M. DeAngelis, A. Hall, D. L. Swain, and X. Qu, On the connection between global hydrologic sensitivity and regional wet extremes, Geophysical Research Letters, 45(20), 11–343, 2018.

Thackeray, C. W., A. Hall, J. Norris, and D. Chen, Constraining the increased frequency of global precipitation extremes under warming, Nature Climate Change, 12(5), 441–448, 2022.

Tramblay, Y., and S. Somot, Future evolution of extreme precipitation in the mediterranean, Climatic Change, 151(2), 289–302, 2018.

Trenberth, K., J. Fasulli, and T. Shepherd, Attribution of extreme climate event, Nat. Climate Change, 5, 725–730, 2015.

Trenberth, K. E., The extreme weather events of 1997 and 1998, Consequences, 5(1), 3–15, 1999.

Trenberth, K. E., The impact of climate change and variability on heavy precipitation, floods, and droughts, Encyclopedia of hydrological sciences, 17, 2005.

Trenberth, K. E., Changes in precipitation with climate change, Climate Research, 47(1–2), 123–138, 2011.

Trenberth, K. E., A. Dai, R. M. Rasmussen, and D. B. Parsons, The changing character of precipitation, Bulletin of the American Meteorological Society, 84(9), 1205–1218, 2003.

Ukkola, A. M., M. G. De Kauwe, M. L. Roderick, G. Abramowitz, and A. J. Pitman, Robust future changes in meteorological drought in cmip6 projections despite uncertainty in precipitation, Geophysical Research Letters, 47(11), e2020GL087,820, 2020.

Utsumi, N., S. Seto, S. Kanae, E. E. Maeda, and T. Oki, Does higher surface temperature intensify extreme precipitation?, Geophysical research letters, 38(16), 2011.

Vaittinada Ayar, P., M. Vrac, S. Bastin, J. Carreau, M. Déqué, and C. Gallardo, Intercomparison of statistical and dynamical downscaling models under the euro-and med-cordex initiative framework: present climate evaluations, Climate dynamics, 46(3), 1301–1329, 2016.

Van den Besselaar, E., A. Klein Tank, and T. Buishand, Trends in european precipitation extremes over 1951–2010, International Journal of Climatology, 33(12), 2682–2689, 2013.

Van den Besselaar, E. J., A. Klein Tank, and G. Van der Schrier, Influence of circulation types on temperature extremes in europe, Theoretical and Applied Climatology, 99(3), 431–439, 2010.

Van den Brink, H., G. Können, and J. Opsteegh, Uncertainties in extreme surge level estimates from observational records, Philosophical Transactions of the Royal Society A: Mathematical, Physical and Engineering Sciences, 363(1831), 1377–1386, 2005.

Van den Hurk, B., H. Kim, G. Krinner, S. I. Seneviratne, C. Derksen, T. Oki, H. Douville, J. Colin, A. Ducharne, F. Cheruy, et al., Ls3mip (v1. 0) contribution to cmip6: the land surface, snow and soil moisture model intercomparison project–aims, setup and expected outcome, Geoscientific Model Development, 9(8), 2809–2832, 2016.

van Oldenborgh, G. J., K. van der Wiel, S. Kew, S. Philip, F. Otto, R. Vautard, A. King, F. Lott, J. Arrighi, R. Singh, et al., Pathways and pitfalls in extreme event attribution, Climatic Change, 166(1), 1–27, 2021.

Van Vuuren, D. P., J. Edmonds, M. Kainuma, K. Riahi, A. Thomson, K. Hibbard, G. C. Hurtt, T. Kram, V. Krey, J.-F. Lamarque, et al., The representative concentration pathways: an overview, Climatic change, 109(1), 5–31, 2011.

Vautard, R., P. Yiou, F. Otto, P. Stott, N. Christidis, G. J. Van Oldenborgh, and N. Schaller, Attribution of human-induced dynamical and thermodynamical contributions in extreme weather events, Environmental Research Letters, 11(11), 114,009, 2016.

Vial, J., J.-L. Dufresne, and S. Bony, On the interpretation of inter-model spread in cmip5 climate sensitivity estimates, Climate Dynamics, 41(11–12), 3339–3362, 2013.

Vicente-Serrano, S. M., T. R. McVicar, D. G. Miralles, Y. Yang, and M. Tomas-Burguera, Unraveling the influence of atmospheric evaporative demand on drought and its response to climate change, Wiley Interdisciplinary Reviews: Climate Change, 11(2), e632, 2020.

Voldoire, A., E. Sanchez-Gomez, D. Salas y Mélia, B. Decharme, C. Cassou, S. Sénési, S. Valcke, I. Beau, A. Alias, M. Chevallier, et al., The cnrm-cm5. 1 global climate model: description and basic evaluation, Climate dynamics, 40(9), 2091–2121, 2013.

Voldoire, A., D. Saint-Martin, S. Sénési, B. Decharme, A. Alias, M. Chevallier, J. Colin, J.-F. Guérémy, M. Michou, M.-P. Moine, et al., Evaluation of cmip6 deck experiments with cnrm-cm6-1, Journal of Advances in Modeling Earth Systems, 11(7), 2177–2213, 2019.

Vrac, M., and P. Friederichs, Multivariate—intervariable, spatial, and temporal—bias correction, Journal of Climate, 28(1), 218–237, 2015.

Vrac, M., T. Noël, and R. Vautard, Bias correction of precipitation through singularity stochastic removal: Because occurrences matter, Journal of Geophysical Research: Atmospheres, 121(10), 5237–5258, 2016.

Wan, H., X. Zhang, F. Zwiers, and S.-K. Min, Attributing northern high-latitude precipitation change over the period 1966–2005 to human influence, Climate Dynamics, 45(7), 1713–1726, 2015.

Wang, G., D. Wang, K. E. Trenberth, A. Erfanian, M. Yu, M. G. Bosilovich, and D. T. Parr, The peak structure and future changes of the relationships between extreme precipitation and temperature, Nature Climate Change, 7(4), 268–274, 2017.

Wang, Q., The pot model described by the generalized pareto distribution with poisson arrival rate, Journal of Hydrology, 129(1-4), 263–280, 1991.

Watanabe, S., S. Kanae, S. Seto, P. J.-F. Yeh, Y. Hirabayashi, and T. Oki, Intercomparison of bias-correction methods for monthly temperature and precipitation simulated by multiple climate models, Journal of Geophysical Research: Atmospheres, 117(D23), 2012.

Webb, M. J., T. Andrews, A. Bodas-Salcedo, S. Bony, C. S. Bretherton, R. Chadwick, H. Chepfer, H. Douville, P. Good, J. E. Kay, et al., The cloud feedback model intercomparison project (cfmip) contribution to cmip6, Geoscientific Model Development, 10(1), 359–384, 2017.

Webb, M. J., A. P. Lock, and F. H. Lambert, Interactions between hydrological sensitivity, radiative cooling, stability, and low-level cloud amount feedback, Journal of Climate, 31(5), 1833–1850, 2018.

Wehner, M., P. Gleckler, and J. Lee, Characterization of long period return values of extreme daily temperature and precipitation in the cmip6 models: Part 1, model evaluation, Weather and Climate Extremes, 30, 100,283, 2020.

Wehner, M. F., Characterization of long period return values of extreme daily temperature and precipitation in the cmip6 models: Part 2, projections of future change, Weather and Climate Extremes, 30, 100,284, 2020.

Westra, S., L. V. Alexander, and F. W. Zwiers, Global increasing trends in annual maximum daily precipitation, Journal of climate, 26(11), 3904–3918, 2013.

Wild, M., Global dimming and brightening: A review, Journal of Geophysical Research: Atmospheres, 114(D10), 2009.

Wilks, D., "the stippling shows statistically significant grid points": How research results are routinely overstated and overinterpreted, and what to do about it, Bulletin of the American Meteorological Society, 97(12), 2263–2273, 2016.

Wong, G., D. Maraun, M. Vrac, M. Widmann, J. M. Eden, and T. Kent, Stochastic model output statistics for bias correcting and downscaling precipitation including extremes, Journal of Climate, 27(18), 6940–6959, 2014.

Woodward, G., N. Bonada, L. E. Brown, R. G. Death, I. Durance, C. Gray, S. Hladyz, M. E. Ledger, A. M. Milner, S. J. Ormerod, et al., The effects of climatic fluctuations and extreme events on running water ecosystems, Philosophical Transactions of the Royal Society B: Biological Sciences, 371(1694), 20150,274, 2016.

Wyser, K., T. v. Noije, S. Yang, J. v. Hardenberg, D. O'Donnell, and R. Döscher, On the increased climate sensitivity in the ec-earth model from cmip5 to cmip6, Geoscientific Model Development, 13(8), 3465–3474, 2020.

Xu, Z., Y. Han, C.-Y. Tam, Z.-L. Yang, and C. Fu, Bias-corrected cmip6 global dataset for dynamical downscaling of the historical and future climate (1979–2100), Scientific Data, 8(1), 1–11, 2021.

Yiou, P., A. Jézéquel, P. Naveau, F. E. Otto, R. Vautard, and M. Vrac, A statistical framework for conditional extreme event attribution, Advances in Statistical Climatology, Meteorology and Oceanography, 3(1), 17–31, 2017.

Zappa, G., M. K. Hawcroft, L. Shaffrey, E. Black, and D. J. Brayshaw, Extratropical cyclones and the projected decline of winter mediterranean precipitation in the cmip5 models, Climate Dynamics, 45(7), 1727–1738, 2015.

Zelinka, M. D., T. A. Myers, D. T. McCoy, S. Po-Chedley, P. M. Caldwell, P. Ceppi, S. A. Klein, and K. E. Taylor, Causes of higher climate sensitivity in cmip6 models, Geophysical Research Letters, 47(1), e2019GL085,782, 2020.

Zhang, W., G. Villarini, and M. Wehner, Contrasting the responses of extreme precipitation to changes in surface air and dew point temperatures, Climatic change, 154(1), 257–271, 2019.

Zhang, X., H. Wan, F. W. Zwiers, G. C. Hegerl, and S.-K. Min, Attributing intensification of precipitation extremes to human influence, Geophysical Research Letters, 40(19), 5252–5257, 2013.

Zhao, A. D., D. S. Stevenson, and M. A. Bollasina, The role of anthropogenic aerosols in future precipitation extremes over the asian monsoon region, Climate Dynamics, 52(9), 6257–6278, 2019.

Zheng, F., S. Westra, and M. Leonard, Opposing local precipitation extremes, Nature Climate Change, 5(5), 389–390, 2015.

Zhou, S., A. P. Williams, A. M. Berg, B. I. Cook, Y. Zhang, S. Hagemann, R. Lorenz, S. I. Seneviratne, and P. Gentine, Land–atmosphere feedbacks exacerbate concurrent soil drought and atmospheric aridity, Proceedings of the National Academy of Sciences, 116(38), 18,848–18,853, 2019.

Zhou, T., A. Turner, J. Kinter, B. Wang, Y. Qian, X. Chen, B. Wang, B. Liu, B. Wu, and L. Zou, Overview of the global monsoons model inter-comparison project (gmmip), Geosci. Model Dev. Discuss, 2016, 1–25, 2016.

Ziese, M., A. Rauthe-Schöch, A. Becker, P. Finger, A. Meyer-Christoffer, and U. Schneider, Gpcc full data daily version.2018 at 1.0: Daily land-surface precipitation from rain-gauges built on gts-based and historic data, doi:doi.org/10.5676/DWD_GPCC/FD_D_V2018_100, 2018.

Appendices

A

Supplementary tables and figures

Chapter 2

Tables

Model Name	Country	Horizontal resolution (lon x lat)	Variant label
ACCESS-CM2	Australia	1.9° x °1.3	rlilplfl
ACCESS-ESM1-5	Australia	19° x °1.2	rlilplfl
BCC-CSM2-MR	China	1.1° x °1.1	rlilplfl
CESM2	USA	2.8° x °2.8	rlilplfl
CESM2-WACCM	USA	1.3° x °0.9	rlilplfl
CMCC-CM2-SR5	Italy	1.25° x °1.0	rlilplfl
CMCC-ESM2	Italy	1.25° x °0.9	rlilplfl
CNRM-CM6-1	France	1.4° x °1.4	rlilplf2
CNRM-CM6-1-HR	France	0.5° x °0.5	rlilplf2
CNRM-ESM2-1	France	1.4° x °1.4	rlilplf2
CanESM5	Canada	2.8° x °2.8	r[1-25]ilplfl
EC-Earth3	Europe	0.7° x °0.7	rlilplfl
EC-Earth3-CC	Europe	0.7° x °0.7	rlilplfl
EC-Earth3-Veg	Europe	0.7° x °0.7	rlilplfl

EC-Earth3-Veg-LR	Europe	1.1° x °1.1	rlilp1f1
FGOALS-g3	China	2° x °2.3	rlilp1f1
GFDL-CM4	USA	2.5° x °2.0	rlilp1f1
GFDL-ESM4	USA	1.3° x °1	rlilp1f1
HadGEM3-GC31-LL	UK	1.86° x °1.25	rlilp1f1
HadGEM3-GC31-MM	UK	0.8° x °0.5	rlilp1f1
IITM-ESM	India	1.8° x °1.8	rlilp1f1
INM-CM4-8	Russia	2° x °1.5	rlilp1f1
INM-CM5-0	Russia	2° x °1.5	rlilp1f1
IPSL-CM6A-LR	France	2.5° x °1.3	rlilp1f1
KACE-1-0-G	South Korea	2.5° x °2.5	rlilp1f1
KIOST-ESM	South Korea	2.5° x °2.0	rlilp1f1
MIROC-ES2L	Japan	2.8° x °2.8	rlilp1f2
MIROC6	Japan	1.4° x °1.4	rlilp1f1
MPI-ESM1-2-HR	Germany	0.9° x °0.9	rlilp1f1
MPI-ESM1-2-LR	Germany	1.9° x °1.9	rlilp1f1
MRI-ESM2-0	Japan	1.1° x °1.1	rlilp1f1
NESM3	China	1.9° x °1.9	rlilp1f1
NorESM2-LM	Norway	2.5° x °1.9	rlilp1f1
TaiESM1	Taiwan	1.25° x °0.9	rlilp1f1
UKESM1-0-LL	UK	1.9° x °1.3	rlilp1f2

Table A.1: List of all CMIP6 models used in the study, along with their native horizontal resolution, country of origin, and the ensemble variant used

CT categories	27 original weather types	11 merged weather types
Low flow	LF	LF
Anticyclone	A	
Hybrid anticyclones	AN	A
	ANE	
	AE	
	ASE	

	AS ASW AW ANW	
Cyclone	C	C
Hybrid cyclones	CN CNE CE CSE CS CSW CW CNW	
Pure directional	N NE E SE S SW W NW	NW N E SE S SW W NW

Table A.2: Description and acronyms of the original 27 circulation types, obtained from the classification, and resulting merged 11 types

Figures

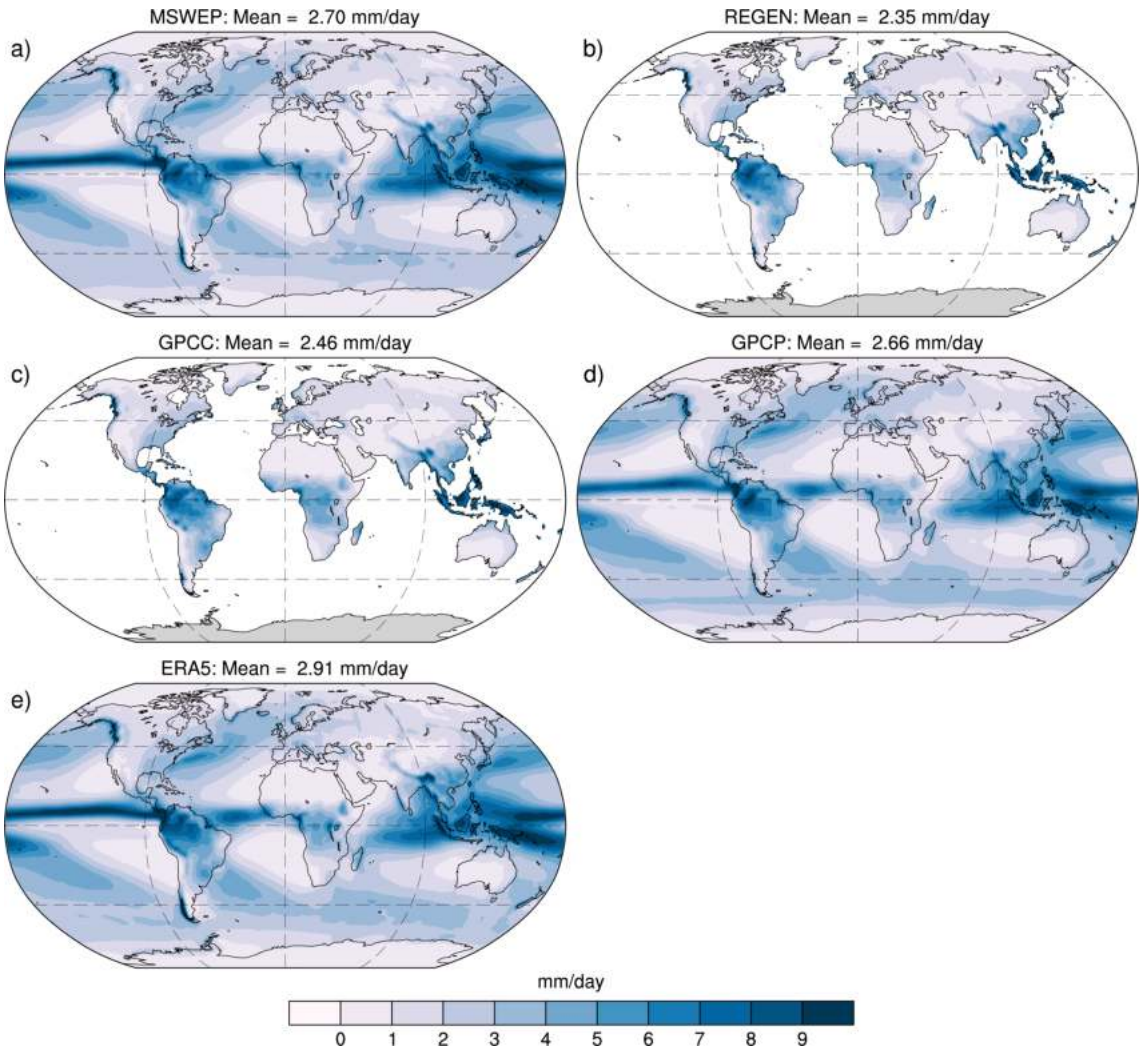

Figure A.1: Mean annual precipitation from the different observational products discussed in chapter 2. The period of evaluation is different among the datasets, and depends on the availability of the data (cf. Table 2.1). Unit is mm/day.

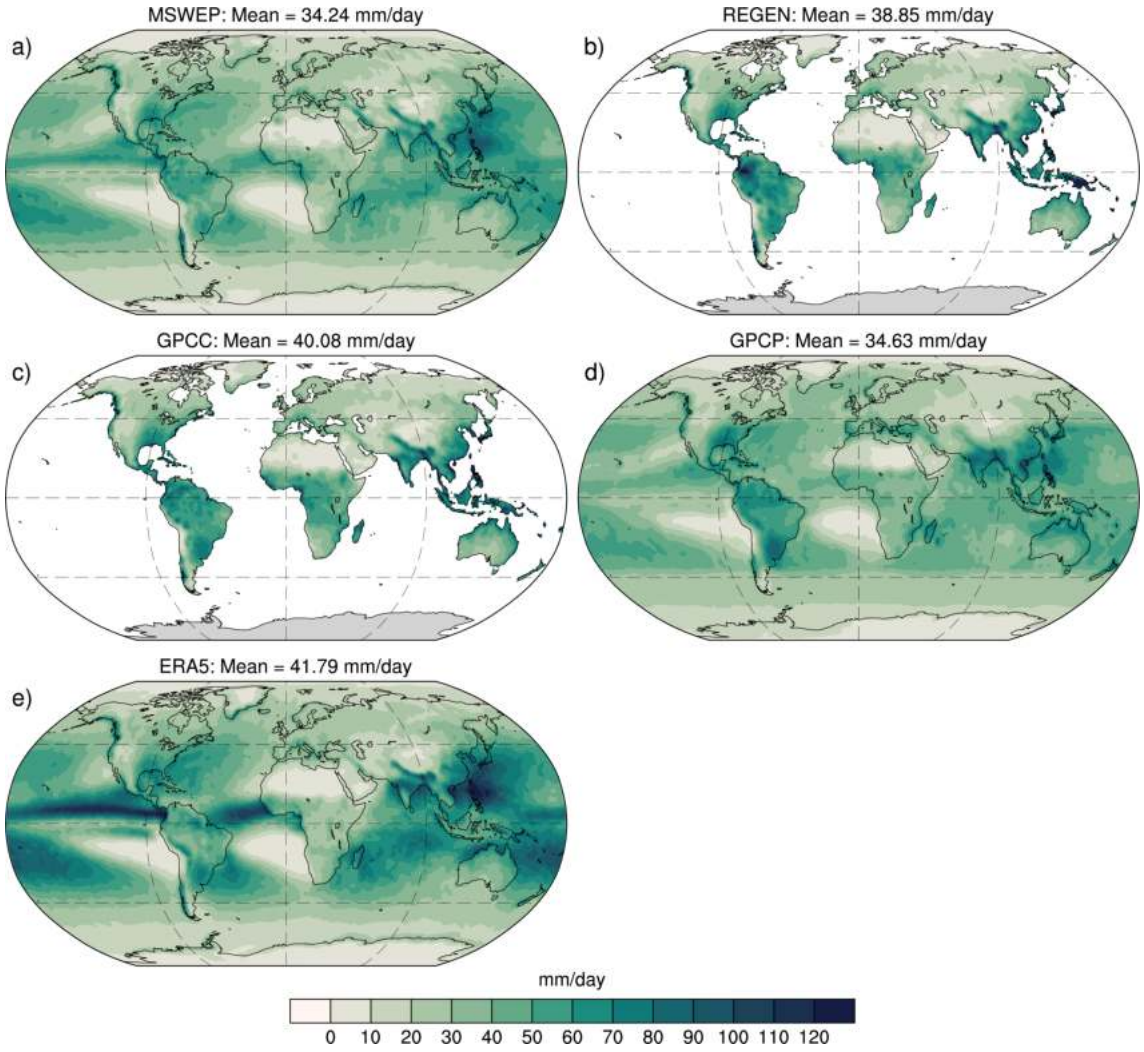

Figure A.2: Same as Figure A.1, but for the mean annual maximum one-day precipitation (RX1DAY).

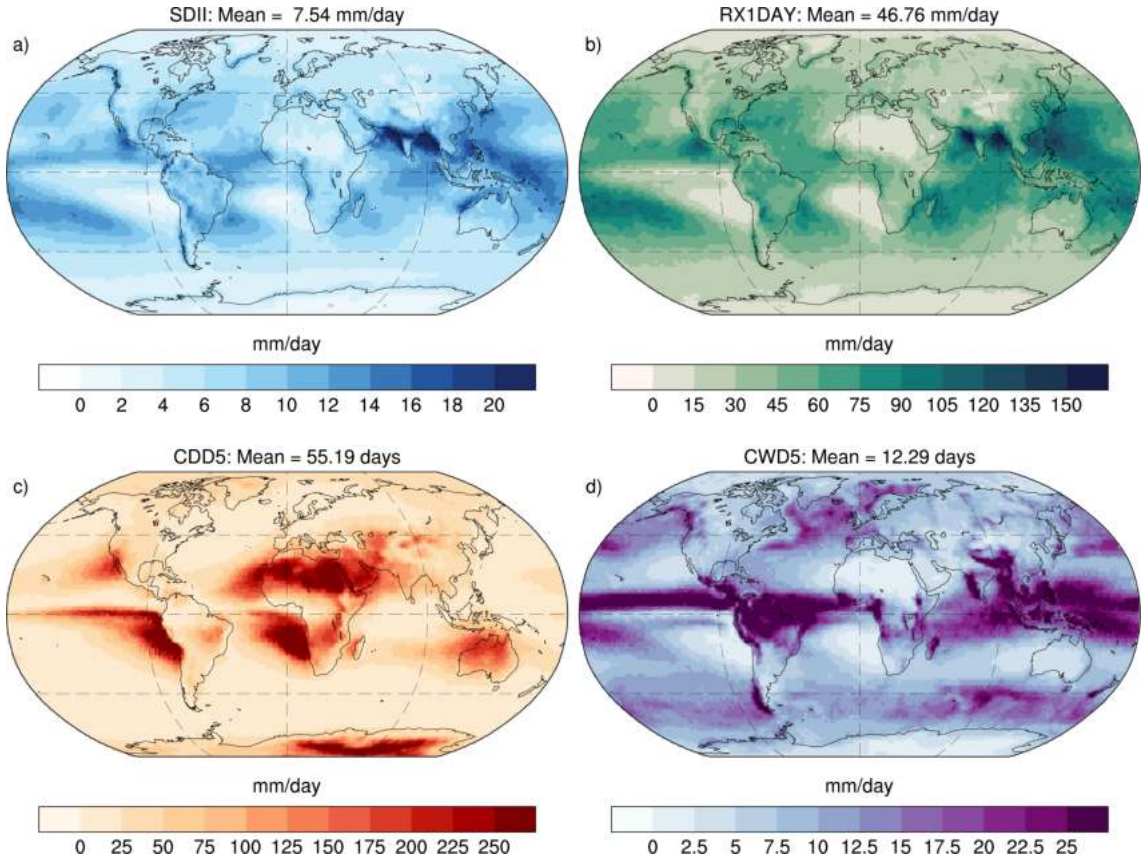

Figure A.3: Global mean maps for the extreme indices a) SDII, b) RX1DAY, c) CDD, and d) CWD simulated by the CNRM-CM6-1 in the GMMIP experiments for the period 1979-2014.

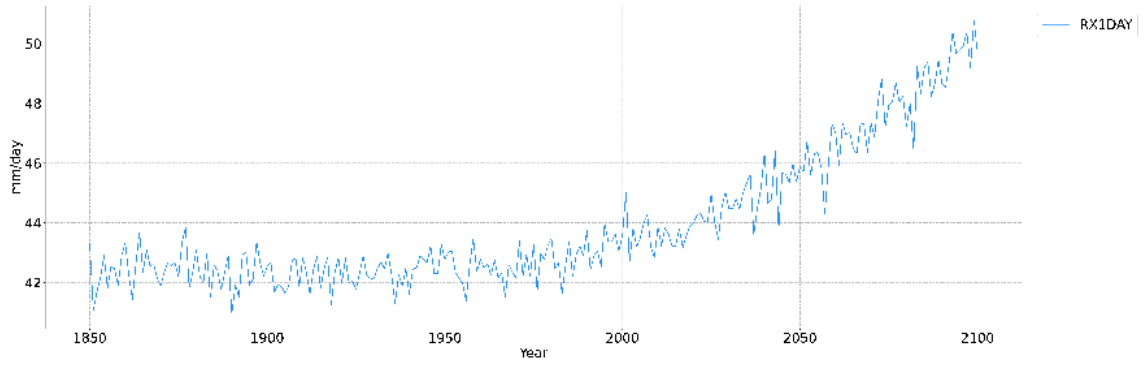

Figure A.4: Timeseries showing the yearly globally averaged RX1DAY values. This figure is produced using the Scenario SSP5-8.5 from the CNRM-CM6-1 model.

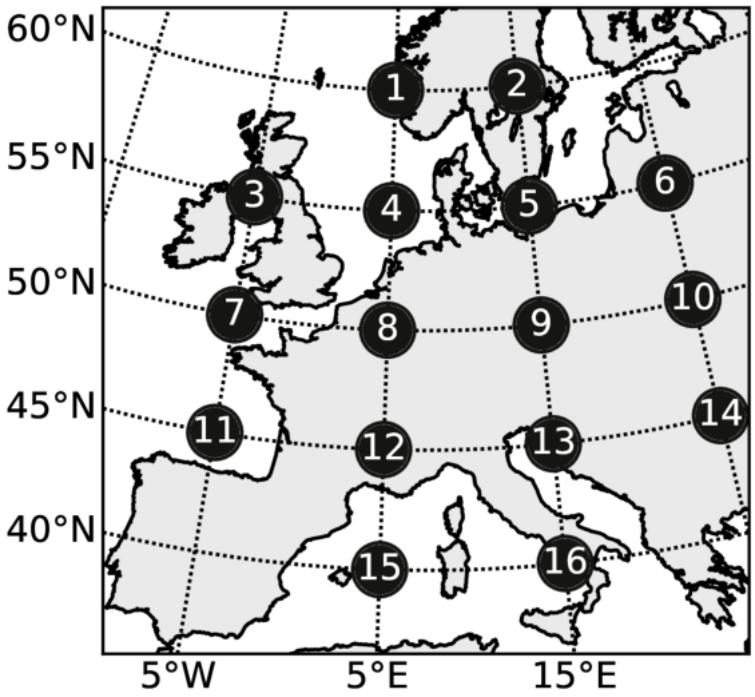

Figure A.5: Example figure showing the 16-grid points around a central-grid point used for the computation of a moving JC classification of circulation types.

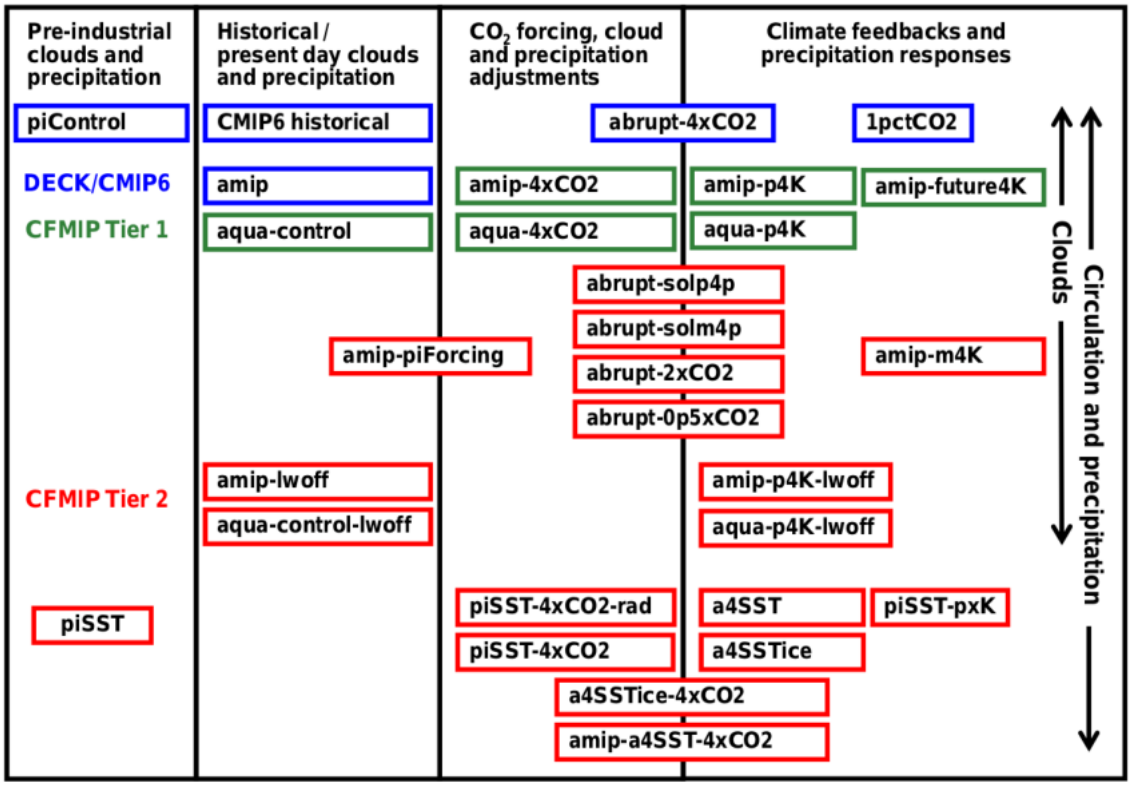

Figure A.6: Summary of CFMIP-3/CMIP6 experiments and DECK +CMIP6 Historical experiments. Source: Webb et al. (2017)

Chapter 3

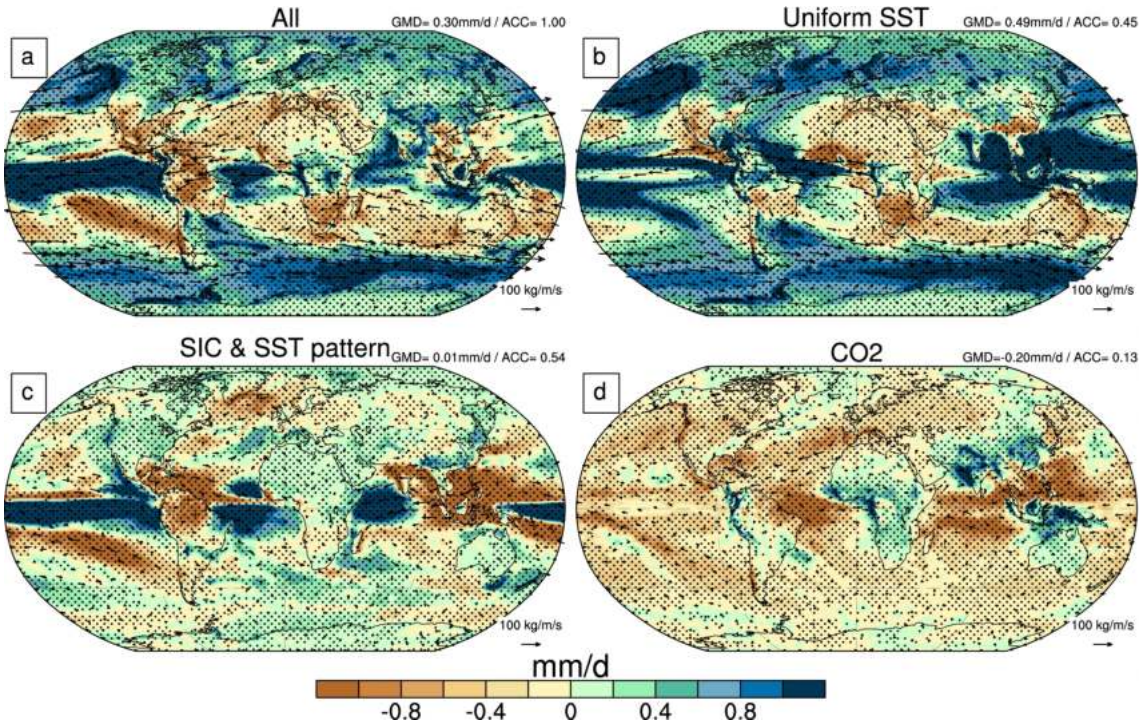

Figure A.7: Replication of the Figure 3.2, but with the vectors indicating the integrated moisture transport overlayed.

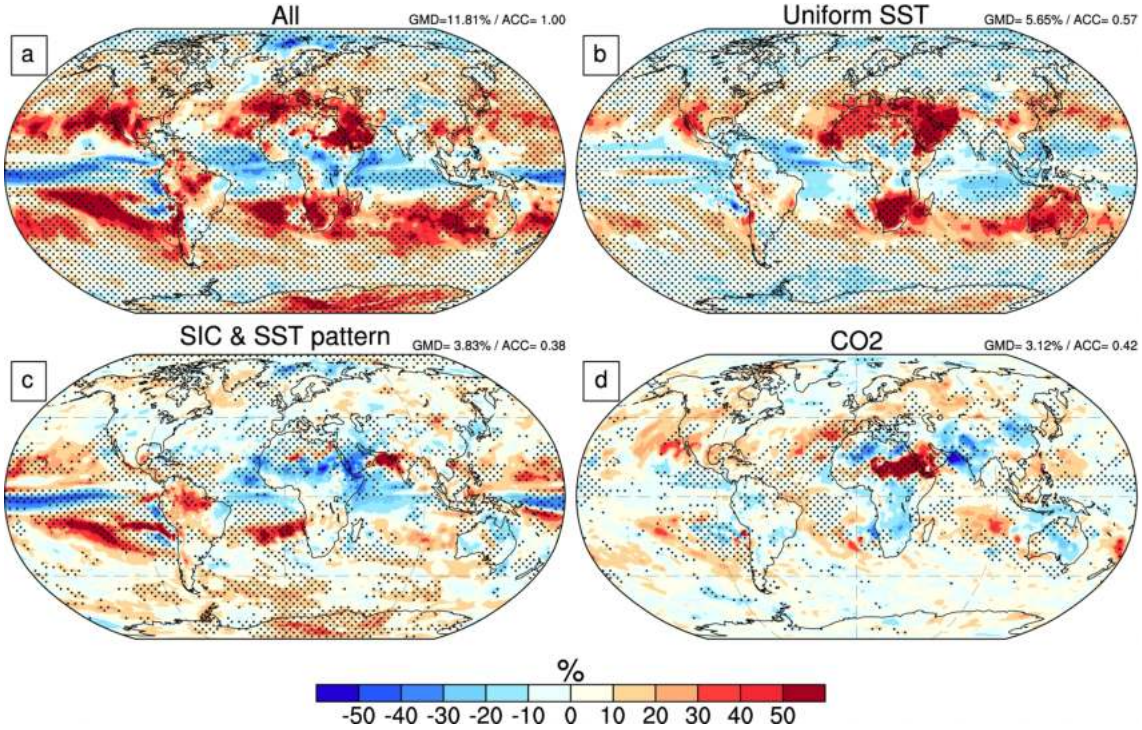

Figure A.8: Same as Figure 3.2, but for relative changes (%) in interannual precipitation variability, which is simply defined as the ratio between the standard deviation and the mean of annual precipitation

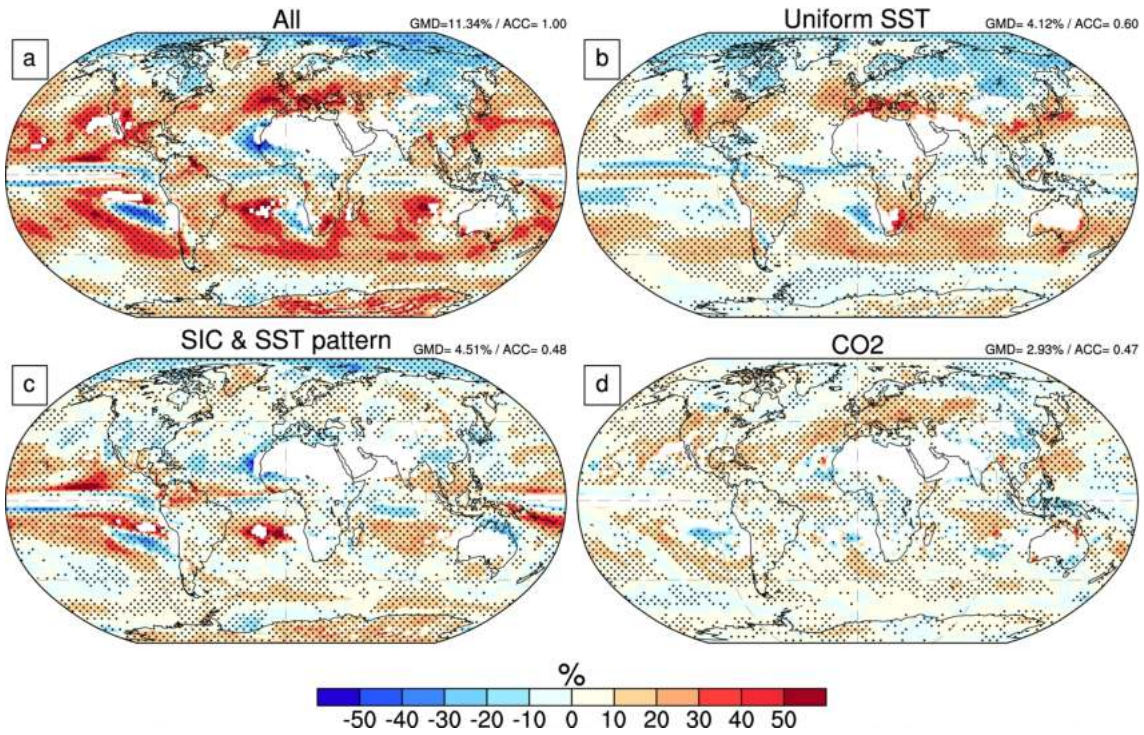

Figure A.9: Same as Figure 3.2, but for relative changes (%) in precipitation seasonality, which is simply defined as the sum of the absolute deviations of mean monthly rainfalls from the overall monthly mean, divided by the mean annual rainfall

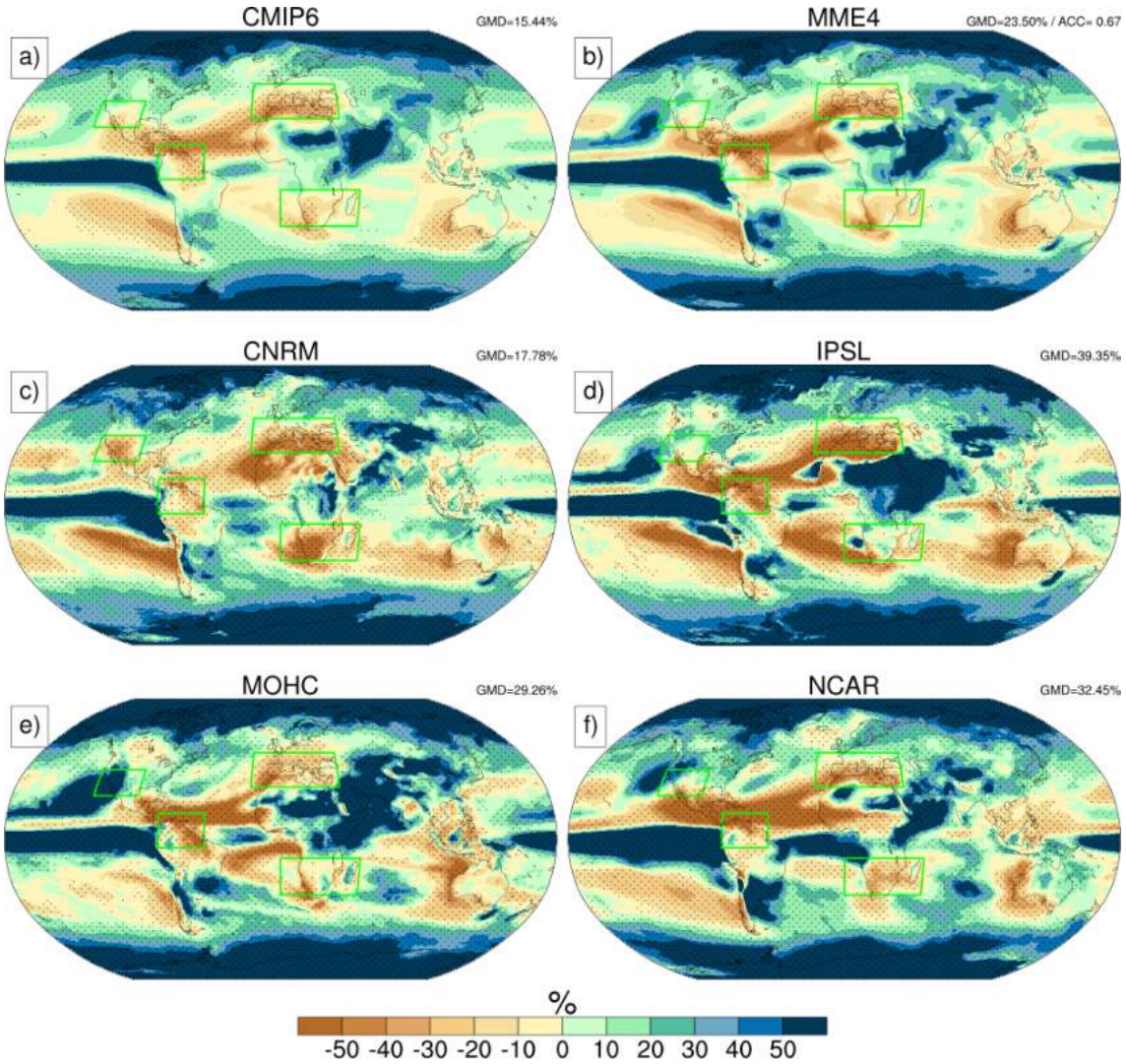

Figure A.10: AOGCM intercomparison of relative changes (%) in annual mean precipitation: a) CMIP6 ensemble mean, b) subset ensemble mean, c) CNRM, d) IPSL, e) MOHC, f) NCAR. All changes are estimated as annual mean differences between year 111-140 of abrupt-4xCO2 versus piControl respectively. In each panel, stippling highlights areas where the difference is significant at the 10% level, GMD denotes the global mean difference and green lines delineate regional domains that will be further discussed for the future studies. In panel b), ACC denotes the spatial anomaly correlation coefficient between CMIP6 and MME4 as a measure of the representativity of our subset of four AOGCMs.

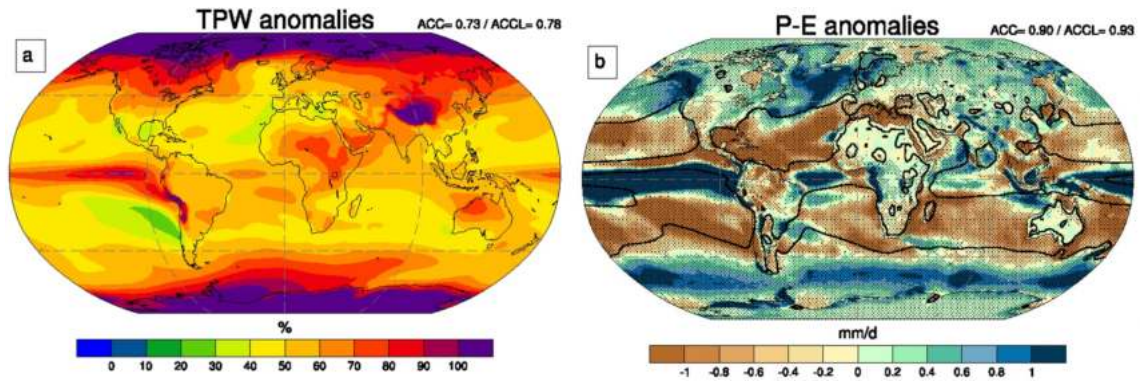

Figure A.11: Annual mean response to abrupt 4xCO2 simulated in atmosphere-only mode (a4SSTice-4xCO2 minus piSST): a) relative anomalies (%) in total precipitable water (ACC/ACCL denotes the global/ global land spatial anomaly correlation coefficient with the relative precipitation anomalies; b) anomalies of moisture convergence (P-E, (mm/day) (ACC/ACCL denotes the global/global land spatial anomaly correlation coefficient with the precipitation anomalies. Stippling in panel b highlights areas where the differences are significant at the 5% level.

Chapter 4

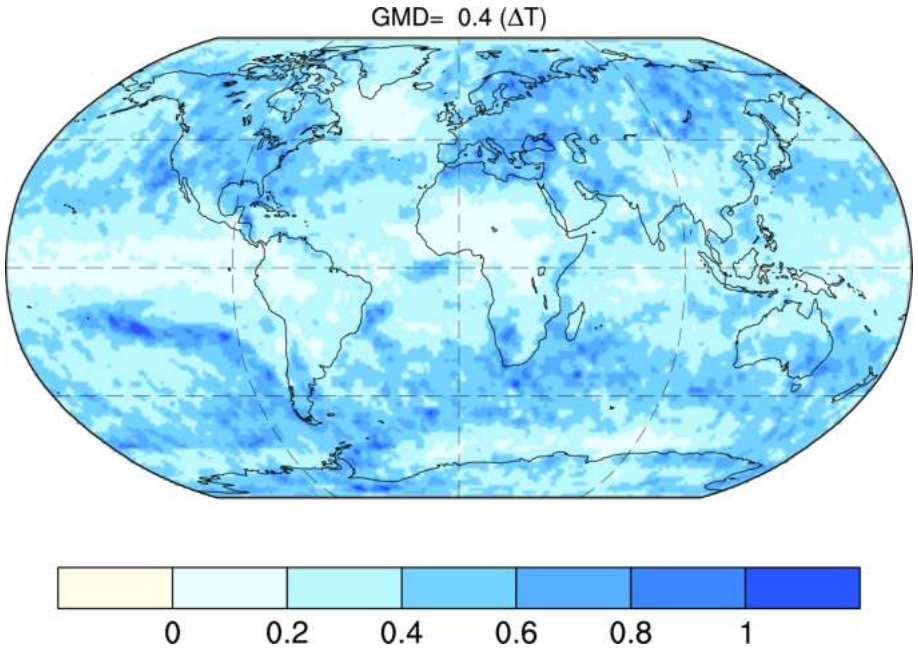

Figure A.12: The ratio of the width of confidence range of extreme precipitation in large ensemble CanESM5 to the CMIP6 multi-model ensemble. The result shown here is scaled with the local temperature change (ΔT).

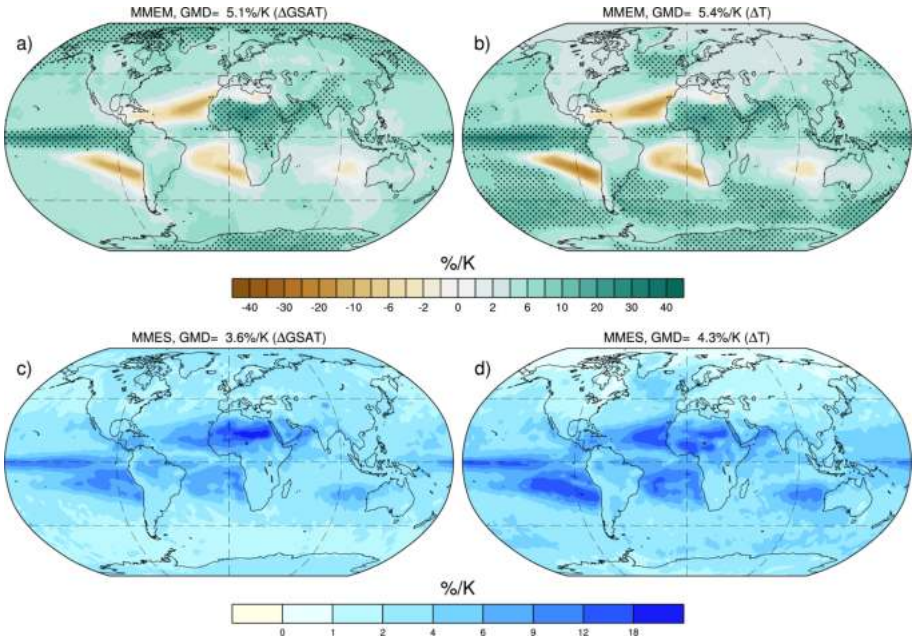

Figure A.13: Projected relative changes (%/K) in 20-yr return values of RXIDAY scaled by both global mean surface temperature change (ΔGSAT in K, left panel) and local mean surface temperature change (ΔT in K, right panel). The changes are calculated for the future period of 2051-2100 relative to the historical period of 1951-2014 using the SSP5-8.8 scenario. (a),(b) show the multi-model mean (MMEM) maps, and (c),(d) show the multi-model standard deviation (MMES) maps using the CMIP6 multimodel ensemble. Stippling highlights the grid cells where the percentage response of the changes is more than 7%/K. GMD denotes the global mean differences.

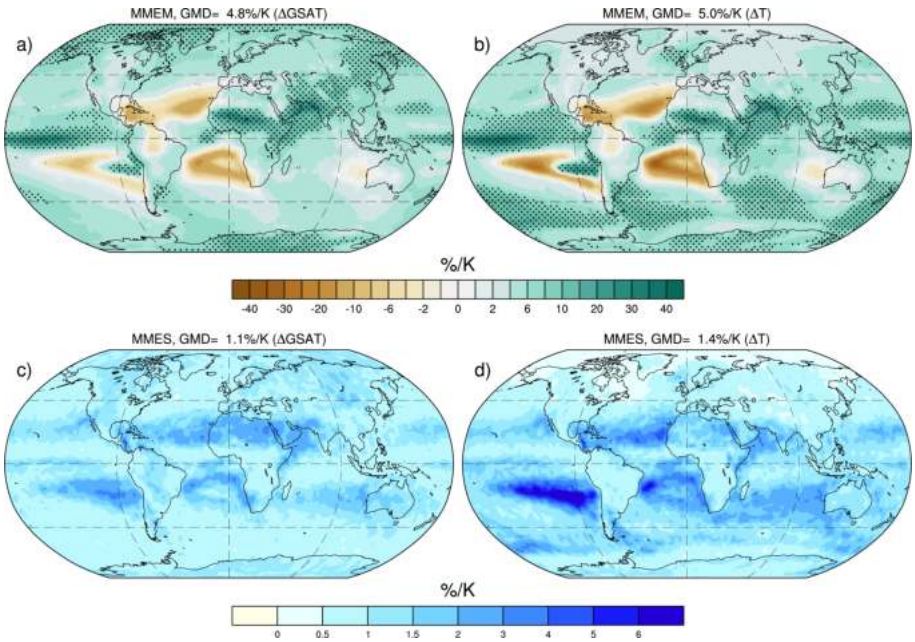

Figure A.14: Same as the Figure A.13, but for the ensemble of 25 individual members of CanESM5 model.

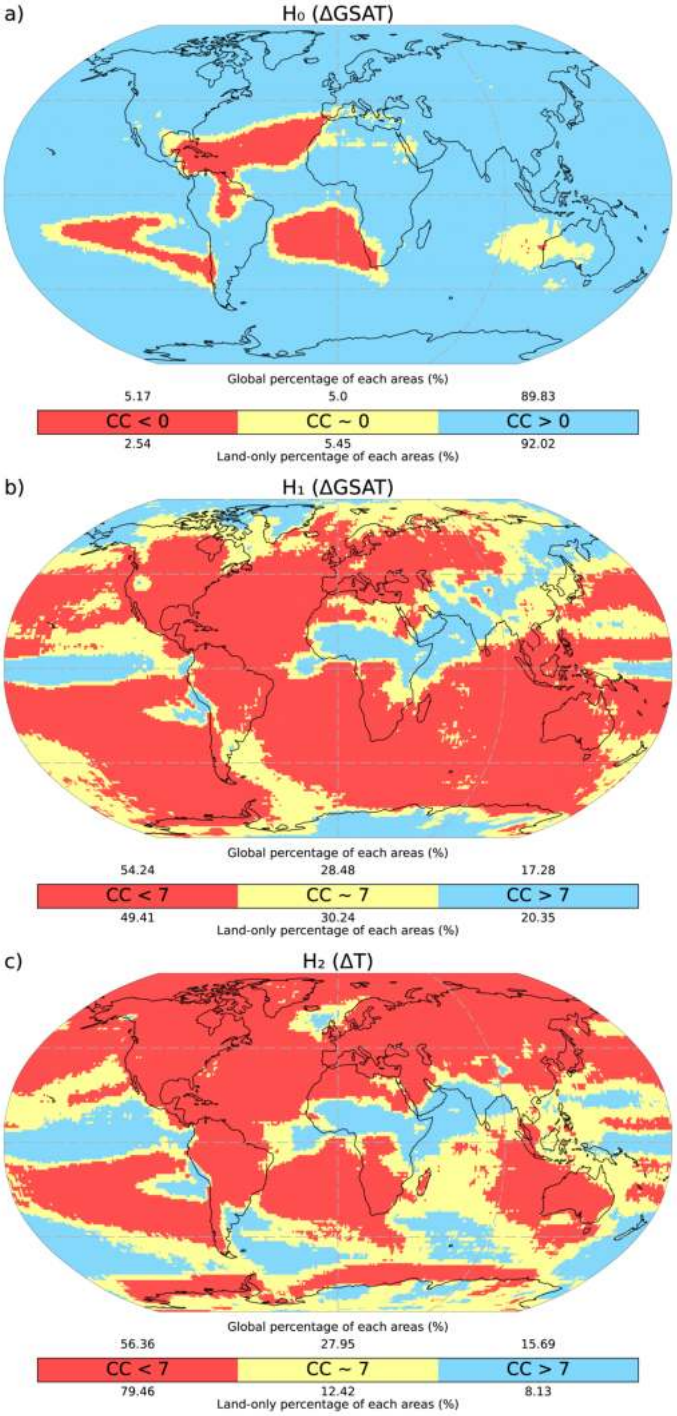

Figure A.15: Global maps of confidence areas (80% confidence interval) for the CanESM5 large ensemble using 25 individual members. The maps show where the rate of extreme precipitation changes is consistent with constant rates of ≈0%/K or ≈7%/K. Red color denotes the regions where the changes are always less than the constant, yellow denotes areas where the constant falls within the confidence interval and blue denotes areas where the rates are always greater than the constant. Map (a) shows the areas where the rate of changes in extreme precipitation remains unchanged or consistent to 0%/K when scaled with ΔGSAT. Maps (b), (c) show the global areas where the rate of changes are consistent with the CC rate of ≈7%/K with respect to ΔGSAT and ΔT.

Chapter 5

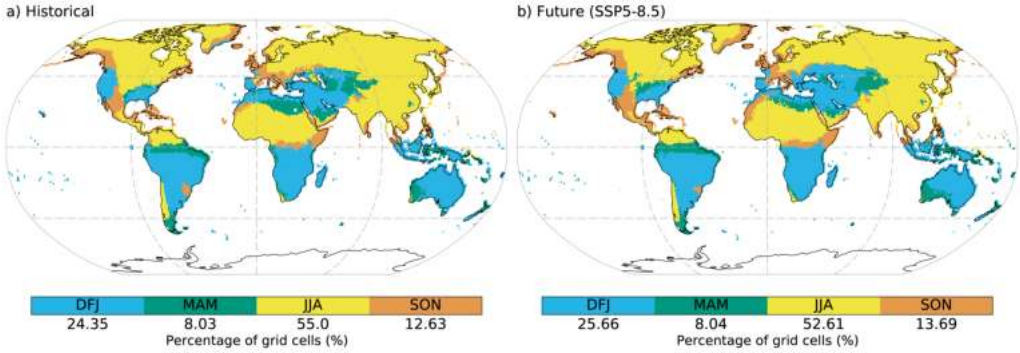

Figure A.16: Season of the median day of year of extreme daily precipitation in the multi-model CMIP6 ensemble; a) for the historical period (1951-2014) and b) for the future period (2051-2100), using the SSP5-8.5 scenario. Four colors in the colorbar represent four different seasons; blue for DJF = December-January-February; green for MAM = March-April-May; yellow for JJA = June-July-August; orange for SON = September-October-November. The numbers provided below colorbar indicates the percentage of the total land areas covered by each seasons when the extremes occurs.

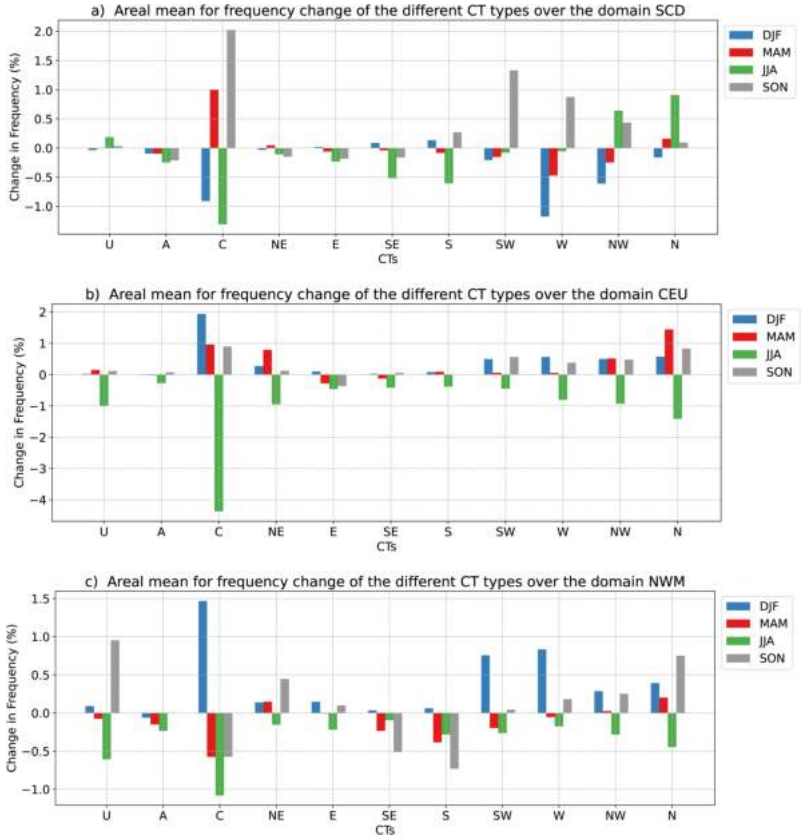

Figure A.17: CMIP6 multimodel mean changes in the seasonal frequency of the 11 different circulation types (CTs) that occurred for the RX1DAY days during the period 1951-2014 relative to 2051-2100. The bars indicate the average values of the occurrences of CTs; a) over Scandinavia (SCD); b) over Central European domain (CEU); c) over North-West Mediterranean (NWM). Different seasons are indicated by the colors as shown in the legend.

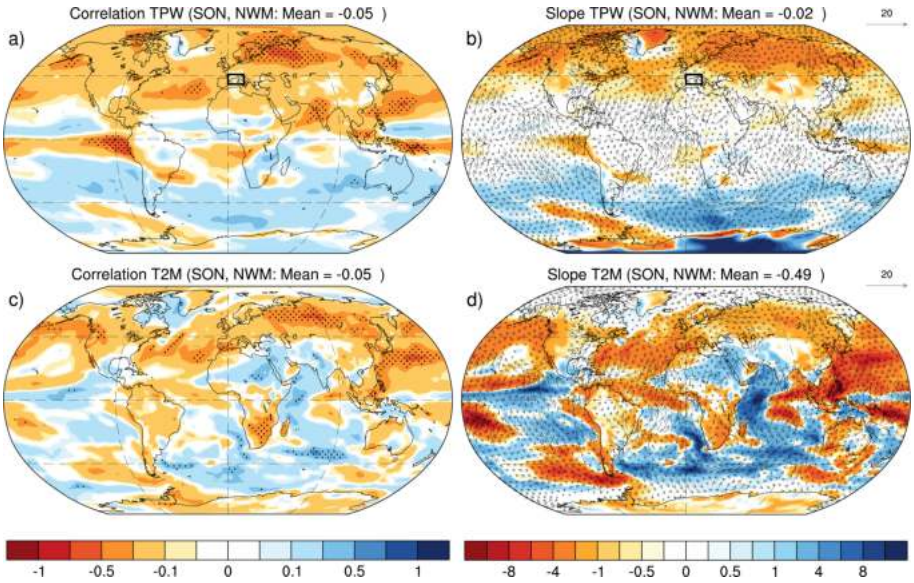

Figure A.18: Maps showing the correlation (a, c) and slope (b, d) from the cross-model regression of the between class values across models from the North West Mediterranean (NWM) subdomain with the global anomalies (with annual mean removed) of total precipitable water (TPW; a and b), surface temperature (T2M; c and d) and low level wind flux (overlayed vectors in b and d). The top panel is for the TPW and the bottom panel for the T2M. The stippling over the correlation maps indicate the significant areas with P-value less than 0.05. The vectors overlayed over the panels b and d are the 850 hPa wind flux slopes.

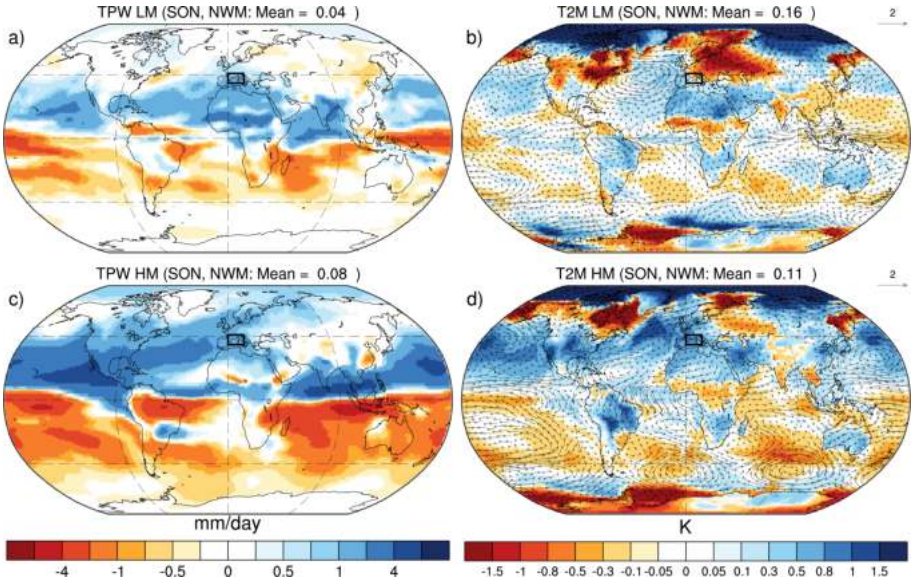

Figure A.19: Maps illustrating the anomalies of the change in the available total precipitable water (a, c), surface temperature (b, d) and the low level wind fluxes (overlayed vectors in b, d) among the extremes models based on the within class (WC) values from the North West Mediterranean (NWM). The top panel is for the model with the lowest WC (LM) and bottom for model with the highest WC (HM).